UNIVERSITY OF TRENTO

DOCTORAL THESIS

Linear, nonlinear and quantum optics in Silicon Photonics

Author:
Massimo Borghi

Supervisor:
Lorenzo Pavesi

March 2016

Contents

Abbreviations

sFWM	Spontaneous Four Wave Mixing
SFWM	Stimulated Four Wave Mixing
FWM	Four Wave Mixing
MMFWM	Multi Modal Four Wave Mixing
MMPM	Multi Modal Phase Matching
TOE	Thermo Optic Effect
TPA	Two Photon Absorption
SPM	Self Phase Modulation
XPM	Cross Phase Modulation
MZI	Mach Zehnder Interferometer
BS	BeamSplitter
AWG	Arrayed Waveguide Grating
AP	All Pass
AD	Add Drop
SCISSOR	Side Coupled Integrated Spaced Sequences Of Resonators
CROW	Coupled Resonator Optical Waveguide
WDM	Wavelength Division Multiplexing
NIR	Near Infra-Red
MIR	Mid-Infrared
PBG	Photonic Band Gap
SPDC	Spontaneous Parametric Down Conversion
IC	Integrated Circuit
OEIC	Opto-Electronic-Integrated-Circuit
DUV	Deep Ultra Violet
LE	Lyapunov Exponent
LLE	Largest Lyapunov Exponent
CMOS	Complementary Metal Oxide Semiconductor
SOI	Silicon On Insulator
VLSI	Very Large Scale Integration
ONoC	Optical Network on Chip
TE	Transverse Electric
TM	Transverse Magnetic
GVD	Group Velocity Dispersion
FEM	Finite Element Simulation
OSA	Optical Spectrum Analyzer

FWHM	Full Width at Half Maximum
FSR	Free Spectral Range
FE	Field Enhancement
EDFA	Erbium Doped Fiber Amplifier
VOA	Variable Optical Attenuator
VNA	Vector Network Analyzer
FPR	Free Propagation Region
CRIT	Coupled Resonator Induced Transparency
PPLN	Periodically Poled Lithium Niobate
SHG	Second Harmonic Generation
XPA	Cross Photon Absorption

Chapter 0

The SIQURO project and thesis outline

This thesis work has been largely carried out within the framework of the project SIQURO, which started in 2013 funded by the Provincia Autonoma di Trento (PAT) [1]. SIQURO covers both fundamental aspects of quantum physics and experimental applications. Theory of quantum fluids of photons, experimental generation of rotating photon gasses, phenomenology of strongly correlated photon gasses in silicon waveguide are some examples of the first. The original milestones of the project were the demonstration of entangled photon pairs and heralded photon generation in strained Silicon waveguides, the development of a new Mid Infrared (MIR) detector based on up-converted photons, the fabrication of an heterogeneous mode-locked III-V laser on Silicon and the engineering of a quantum random number generator based on spontaneous emission of radiation in Silicon. The various building blocks for an integrated quantum photonic circuit should all be demonstrated in SIQURO. The eventual further step is their integration in a single circuit where the heterogeneous integrated mode-locked laser acts as a pump to induce second order or third order parametric processes in suitably designed silicon waveguides which generate the correlated photon pairs or single heralded photons. These photons, with Mid Infrared (or near infrared, if produced by Spontaneous Four Wave Mixing (sFWM) wavelength, will then propagate in a Silicon quantum circuits. Then, the MIR photons will be upconverted to a spectral region suitable for being absorbed by a Silicon photomultiplier. Therefore, from the quantum optics circuit, an electronic signal will be generated which will be easily processed by standard microelectronics circuits. To help the reader to understand the main tasks of the project and their connections, the network of concepts are illustrated in Fig.1. This picture highlights also the topics covered by this thesis work, and indicates their link with the SIQURO project.

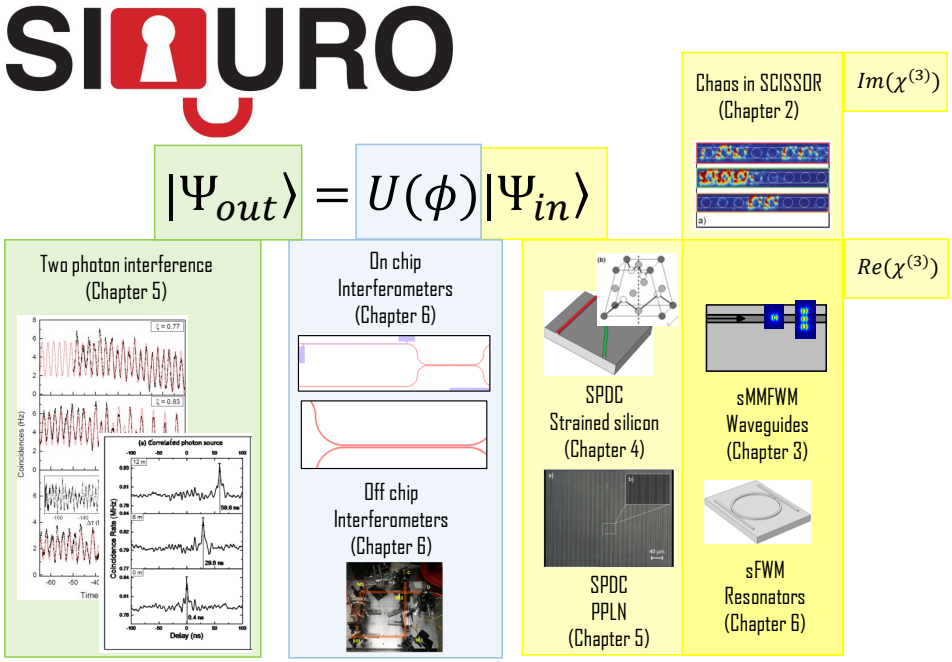

Figure 1: Illustration of the milestones of the project SIQURO and the thesis chapters in which these are covered. The research on quantum sources is represented by the input state $|\Psi_{in}\rangle$, their manipulation by the operator $U(\phi)$ and the detection of the output state by $|\Psi_{out}\rangle$.

Except for chapter 2, the research activities of all the other chapters have been carried out within the framework of the SIQURO project. By the way, chapter 2 covers a different aspect of the same nonlinearity which will be the subject of chapter 3. The first is indeed focused on TPA, which is mediated by the imaginary part of the complex $\chi^{(3)}$ tensor, while the second deals with FWM, which is instead related to the real part. By virtue of this fact, and by following the logical streamlines of the project SIQURO, this thesis work will be organized as follows:

- Chapter 1 gives an introduction to Silicon Photonics, which is the platform over which the SIQURO project aims to realize the integrated quantum circuits. In the first part of this chapter, some historical remarks and a general overview of the subject are presented. Then, the chapter focuses on the basic building blocks of a photonic integrated circuit, like waveguides, splitters, resonators, modulators, lasers and photodetectors. This section is intended to offer a brief insight on the physics of the devices that will be implemented in the experiments described in the following chapters, as well to review the state of the art of these components.

- Chapter 2 is linked to thermal and free carrier nonlinearities activated by TPA in single and coupled resonator sequences. In the first part of the chapter, the theory of resonators under thermal and free carrier effects is presented, and the solutions to the dynamical field equations inside the resonator are presented. These include optical limiting, bistability and self pulsing. All these phenomena are successively experimentally validated in a single ring resonator. Particular attention will be devoted to the self pulsing regime, which is literally the conversion of a continuos pump beam into a pulsed one by the periodic interplay of thermal and free carrier nonlinearities. This concept will be extended to a sequence of coupled resonators organized in the SCISSOR geometry. In the latter, the optical feedback between many cavities under self pulsing provides a route to the instauration of a chaotic regime. The latter is exploited for the generation of random bit sequences, thus paving the way for an all optical,

all passive, CMOS compatible random number generator.

- Chapter 3 is devoted to the study of Multi Modal Four Wave Mixing (MMFWM) in straight Silicon waveguides. The final goal of this study is the engineering of multimode waveguides for the efficient generation of entangled photon pairs through sFWM. These will constitute a possible on chip integrated source of nonclassical states of light, through which multiphoton manipulation and quantum interference is made possible. Despite the fact that this phase matching technique directly comes from earlier studies in optical fibers [2], only few and very simple examples have been reported on a chip [3]. To my knowldge, examples of wavelength conversion in which the pump, the signal and the idler wave propagates in different mode orders have never been reported in literature. In chapter 3, MMFWM will be experimentally demonstrated for several modal combinations and waveguide widths. Different setups for selective mode excitation will be discussed.

- Chapter 4 focuses on the investigation of $\chi^{(2)}$ nonlinearities in strained Silicon waveguides. Within the framework of the project SIQURO, the final aim of this work is to exploit the induced second order nonlinearities to generate entangled photon pairs through SPDC. The process would convert a pump photon at $1.55\,\mu m$ into two twin photons at MIR wavelengths. These will constitute a possible source of nonclassical states of light integrated on a Silicon chip, through which multiphoton manipulation and quantum interference is made possible. To probe the existence of $\chi^{(2)}$ effects, the linear electro optic effect (or Pockels effect) is investigated in strained racetrack resonators using an homodyne detection based on Lock In amplifiers. In comparison with previosly reported works, which rely on the static Pockels effect in strained Mach Zehnder interferometers, this technique offer enhanced sensitivity and immunity to noise sources. During this activity, it has been found that free carrier accumulation and depletion at the waveguide boundaries in response to an applied voltage, was the main source of electro optic modulation, which masked any $\chi^{(2)}$ contribution. These observations have been validated by high frequency measurements, which allowed to disentangle $\chi^{(2)}$ effects from free carrier ones on the basis of the different timescales at which the modulation is performed.

- Chapter 5 reports on a quantum optic experiment performed by using Infra-Red entangled photon pairs produced by SPDC in a Periodically Poled Lithium Niobate (PPLN) crystal. Such experiment has been preparatory for the future implementations of integrated interferometric structures on a Silicon chip, which is outlined as one of the main goals of the SIQURO project. In the first part of the chapter, the SPDC source has been characterized. In the second part, the theory of entangled photon propagation in an amplitude unbalanced free space Mach Zehnder interfefometer is presented and experimentally validated. Novel two photon interference effects, which arise from the asymmetric excitation of the device, have been observed. The experiment was preparatory in the sense that the whole theoretical framework can be straightforwardly applied to integrated circuits, provided that the refractive index of the medium in which light propagates is replaced by the effective modal index.

- Chapter 6 concerns the future perspectives of the SIQURO project. In particular, the designs of the main elements which compose a complete integrated quantum network are presented and validated through simulations. Such elements include quantum sources based on sFWM in waveguides and resonators, phase shifters and delay lines, pump suppression filters and arrayed waveguide gratings. The main goal of this chapter is to propose an optical nework which includes all the functionalies required to perform a complete quantum optics experiment on a Silicon chip. Only the pump laser and the photodetectors are not integrated and have to be supplied from the outside.

- The concluding remarks, the list of the publications and the appendices are given at the end of the text.

In appendix A, the theory of optical resonators under the simultaneous action of thermal, free carrier and $\chi^{(3)}$ nonlinearities is presented. The coupled wave equations for the resonator modes involved in the FWM process are derived. In appendix B, the relation between bulk refractive index perturbations and modal effective index variations in straight waveguides are derived.

Chapter 1

Introduction

The global data traffic is steadly growing [4, 5, 6, 7]. This massive traffic is generated by enterprises, governments, universities and individuals. In the last decade, the rapid diffusion of cloud computing for data storage, entertainment and social media, significantly contributed to the increasing demand of bandwidth for data transmission and computing. A feeling on the orders of mangnitude involved can be get by looking at Fig.1.1, which shows the North American internet traffic during the last three decades.

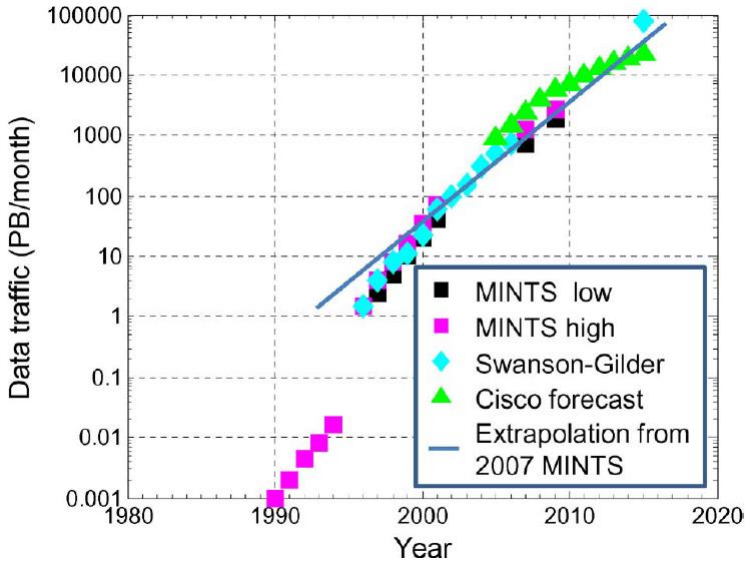

Figure 1.1: Amount of internet traffic in the North America in the last three decades. $1\,PB = 10^{15}$ bytes. Datas taken from [7].

All data sources, among which the influential Minnesota Internet Traffic Study (MINTS), show very similar trends. The linear projection extrapolated from the MINT data of 2007 has been respected during the years: from a data traffic of $10^3\,PB/month$ in 2007 , it was reached a volume of $10^4\,PB/month$ in 2016. Following this extrapolation, the projection for 2020 are of $10^5\,PB/month$. Needless to say, this rapid growth was possible through a concurrent technological improvement which sends, receives and routes the data. Up to now, the technological improvement occurred at all scales, from big data centers grouping thousands of clusters, to commercial devices of everyday use [8, 5]. Progress has been made in the communication protocols [9], in the physical medium through which data is sent [10], and in the performances of the transceiving stations [11]. A clear example of technological evolution is constituted by the optical fiber communication

link. Nowadays, long haul connections, ranging from tens to hundreds of kilometers, are based on optical fibers. Since the early 1970s, the system capacity, i.e., the maximum amount of bits that can be sent in one second in a single fiber, has improved by a factor of 10^5 [7]. On one side, this has been possible by the introduction of Wavelength Division Multiplexing (WDM) at the beginning of the 1990s, which consists in the encoding data streams in different wavelengths which simultaneously travel along the same fiber without interference [12]. WDM improved the aggregate bitrate by a factor of 10^3 [7] On the other side, also the spectral efficiency (SE), i.e., the number of bits per second per channel bandwidth (typically measured in $b/s/Hz$), increased by a factor 10^2 [7]. These trends are shown in Fig.1.2.

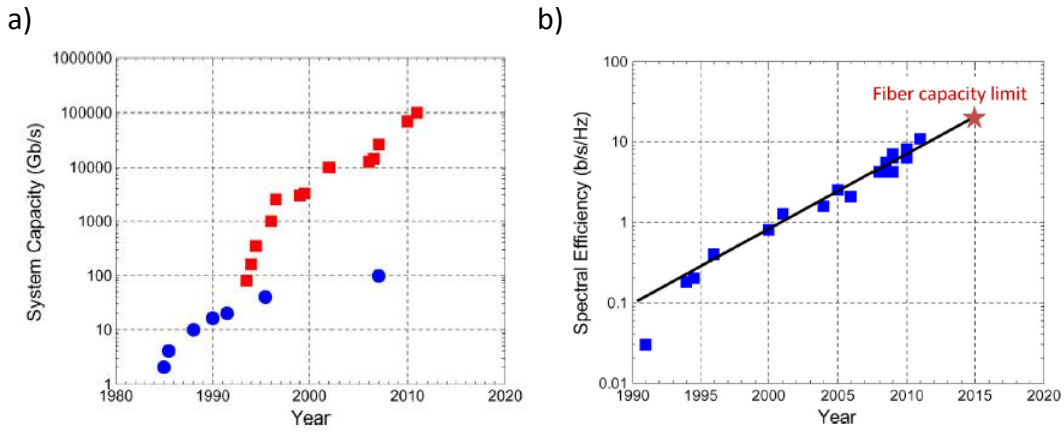

Figure 1.2: (a) Fiber system capacity during the years. Blue circles represent single mode fibers for Time Division Multiplexing (TDM), while red rectangles represent fibers engineered for WDM applications. Picture from [7]. (b) Spectral efficiency (SE) of a single fiber as a function of the years. The red star corresponds to the maximum SE according to Shannon's limit, which is set by the nonlinear effects occurring in optical fibers [7]. Picture taken from [7].

Progress in the fabrication technology of optical fibers has been of paramount importance as well. There has been a continuous effort in material science to realize low loss optical fibers. Since their introduction in the early 1960s, when signal attenuation exceeded $1000\,dBkm^{-1}$, losses have been constantly decreased to less than $0.2\,dBkm^{-1}$ at a wavelength of $1.55\,\mu m$ [2]. The simultaneous reduction of the modal birifrangence and the engineering of the chromatic dispersion to tailor the group velocity dispersion contributed to increase the bitrate, to improve the signal integrity and to decrease the numbers of repeaters. The hardware which handles the microelectronic interfaces of the transceiving stations has followed similar progress during those years. In this technological challenge, a key role has been played by Very Large Scale Integration (VLSI), that is the continuos reduction of the size of the electronic and optical components. Smaller dimensions imply higher component density and enhanced computing capabilities. This concept is well exemplified by the famous Moore's law, introduced for the first time in 1965, and which states that the number of functions per microelectronic chip would double every two years [13]. As shown in Fig.1.3, Moore's predictions were right, and the transistor counts in a microprocessor steadily increased during the years.

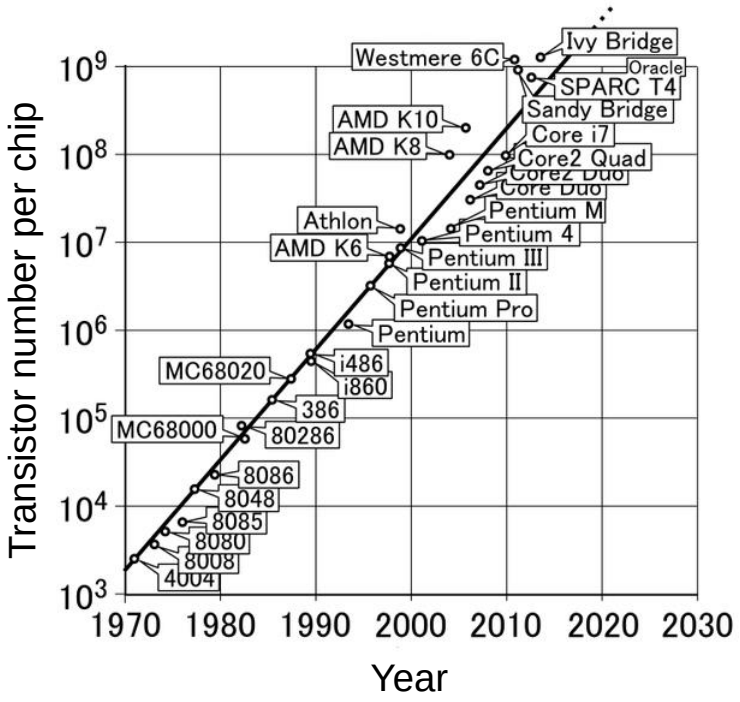

Figure 1.3: Transistor count in processors during the years. The solid black curve represent the Moore's prediction of 1965. Picture taken from [14].

As reported in Fig.1.4, the gate width of the transistor was approximately $1.3\,\mu m$ wide at the beginning of the 1970s, and stacked to a constant value of $\sim 25\,nm$ during the last few years. Recent reports show that $15\,nm$ transistors are being implemented in low power microprocessor for smartphone applications.

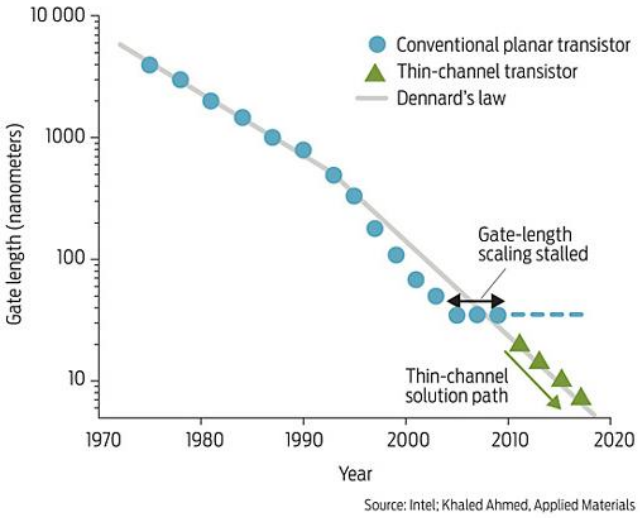

Figure 1.4: The evolution of the gate length of a transistor during the years. Picture taken from [15].

Miniaturization has been possible by the huge investments of the semiconductor companies in Integrated Circuit (IC) facilities, which in turn have been motivated by the increasingly demandes of the market. VLSI has been pursued to reduce the production cost. A synergy between different industries declared the success of VLSI. Indeed, the realization of an IC requires a series of complex operations such as photolithography, etching and metal deposition [16]. In case that each of these operations were performed by specialized

machines built by a variety of commercial companies, it would be difficult for the industry to advance, since in many cases it would not be ideal for one company to introduce a new product if the other needed machines are not available around at the same time. A shared roadmap to plan and control the technological needs of IC production and to anticipate the evolution of the market was needed. This task has been fulfilled by the institution of the IndustrialTechnology Roadmap for Semiconductors (ITRS), a set of documents produced by a group of semiconductor industry experts [17].
By the way, the continuos race toward more complex and performant architectures, which shall meet the increasing demand in computation, data traffic, bandwidth and storage, hardly will follow the Moore's law in the very near future, if a new paradigm will not support or even replace the one of miniaturization. Indeed, the density of the electrical components has reached a so high level of packaging and integration that the operation frequency of a single processing unit has levelled to few GHz over the last decade. This was due to heat dissipation, signal attenuation and Resistor-Capacitance (RC) delays associated to the copper lines used for the interconnections [18, 19]. Heat dissipation occurs because the metals have a finite resistance, which increases as the cross section diminuishes. Large scale integration implies an increased number of wires, with smaller dimensions, which goes in the opposite direction with respect to heat reduction . Energy is also required every time that a capacity, which can be associated to a transistor or to a connection line of similar length (these are almost the same and equal to $\approx 1\,fF$ for state of the art electronic design and fabrication [18]), has to be charged or discarged. On average, the switching of a transistor, which can be roughly assimilated to the processing of one bit, consumes about $1\,pJ$ of energy [18]. The trends in heat dissipation over the last three decades are shown in Fig.1.5.

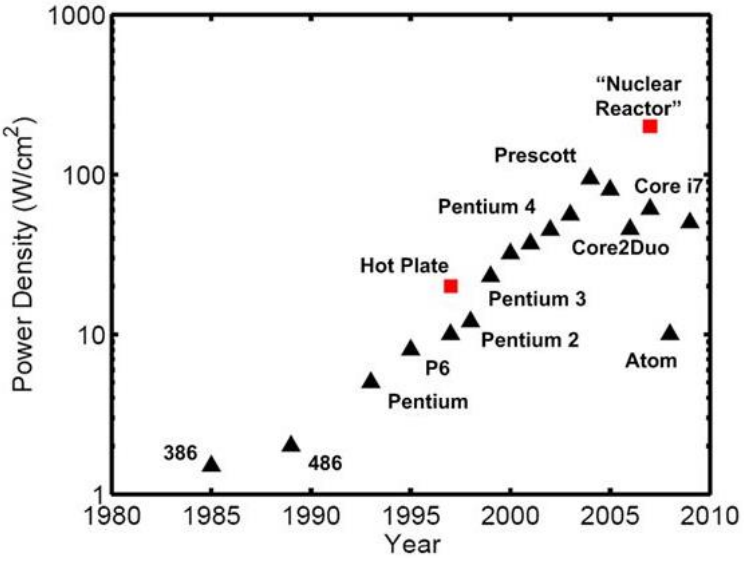

Figure 1.5: Power density developed inside a single core microprocessor during the years. Picture taken from [19].

The dielectric support where the ICs are fabricated, which has a poor heat conduction, sets a threshold to the maximum dissipated power density slightly above $100\,Wcm^{-1}$. If one thinks that $200\,Wcm^{-1}$ is the power generated by a nuclear reactor, it can be seen that this is a huge amount of power. Power loss is also induced by radio frequency (RF) signals which are radiated from the interconnection lines when they operate at GHz frequencies [20]. Miniaturization also crashes with the problem of RC delays. The resistance-capacitance product is the characteristic time which limits the speed of the processor. Scaling does not help to reduce the time constant. Indeed, it can be demonstrated that the uniform scaling along the three dimensions of a copper

wire does not alter its RC constant [18]. By looking at Fig.1.3, one may wonder how it has been possible to follow the Moore's law in the last decade, if miniaturization suffers for all the problems cited above. The answer relies in the introduction of the multi-core paradigm. Instead of increasing the processing capability of a single CPU, many of them, called cores, have been connected together in a single microprocessor and made to work in parallel to increase the overall computational power. By the way, as a natural consequence of coworking, more and more interconnections are needed to let the cores to communicate and exchange data, with the consequence that this approach will soon face the same heat dissipation problems encountered in single CPU units. The only viable solution is the use of optical interconnections instead of copper wires [21, 22, 8, 5, 11, 6]. This is not a completely new paradigm, since it has been already applied at the macro-scale level with the introduction of optical fibers for long and medium distance telecommunications. As exemplified in Fig.1.6, in the last 20 years, copper cables were progressively replaced by optical links.

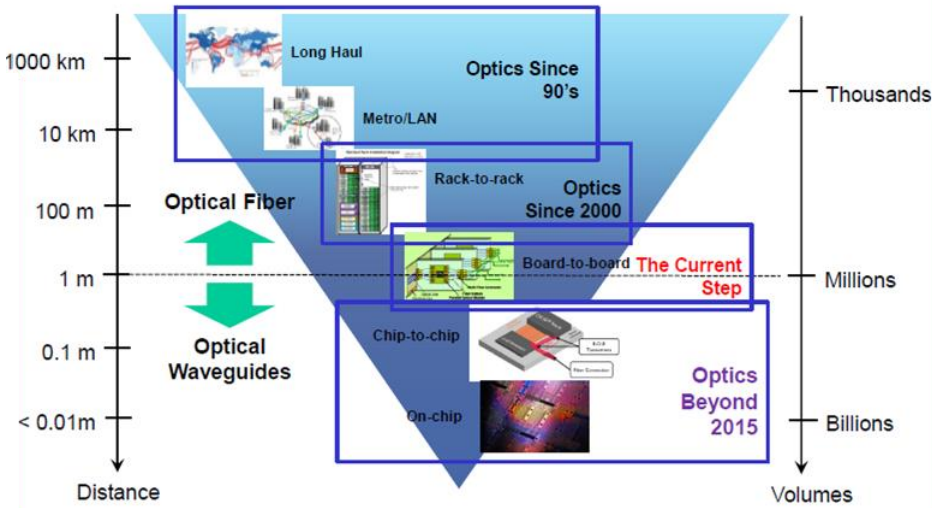

Figure 1.6: The progressive replacement of copper interconnection with optical ones as the length scale of the communication link decreases. Picture taken from [23].

The length scale of interconnections progressively moved from long haul ($> 100\,km$), to rack-to-rack ($100\,m$) and even to board to board ($< 1\,m$) connections. The challenge of the next few years will be the implementation of optical interconnections at the chip-to-chip ($< 1\,cm$) or even intra-chip ($< 10\,\mu m$) scale. There are several advantages of using light instead of electrons for the transfer of data. Light is made by photons, which travels at the speed of light with zero rest mass, which implies that no energy is wasted for line charging or for sending/retriving bits. This aspect is significant if one thinks to the typical matrix organization of a dynamic random access memory (DRAM). Here, for accessing to the single content of a memory cell, whole sets of lines are continuosly charged and discharged. As it will be discussed later, losses in sub-wavelength nanophotonic wires are associated to light which is scattered away from the wire itself, and thus do not contribute to material heating. In a fully optoelectronic network, in which electronic components are connected by optical links, the heat sources would be mostly localized in light sources, detectors and switching elements like electro optic modulators and memories, which are associated to a finite capacitance and resistance, but not from the interconnections. The reduction of the power consumption, hence in the power dissipation, will be enormous. Indeed, the dominant energy dissipation in the core operations is linked to the actual logic switching, or in the energy stored in the memory cells which hold the information. However, of these three core operations, it is the interconnect that accounts for most of the energy dissipation, and that the energy is almost entirely used by charging and discharging the capacitance of signal lines [18]. The zero capacitance

of the nanophotonic wires allows also to eliminate the RC time constant required to shift from an Off to an On state and vice versa. In the optical domain, the fundamental limit to the maximum achievable bitrate is the Nyquist limit, which however is very far from being reached, as it lies in the hundreds of THz regime. Photonic chips are also immune to electromagnetic interference and do not suffer from antenna's effects.
The most promising platform for on chip optical interconnections is Silicon Photonics [24, 25, 21, 26]. The latter is the technology of integrating electronic and photonic functionalities with processing tools currently used in the microelectronic industry. Silicon Photonics is fabbricated by the well-developed infrastructure of Complementary Metal Oxide Semiconductor (CMOS) technology, which allows for VLSI in a cost-effective and monolithic manner. Silicon Photonics started in the 1980s, with the pioneering works of R. Soref et. al. At that time, the first structures for guiding and splitting light on Silicon waveguides have been proposed and demonstrated [27]. In 1993, following the early ideas of Abstreiter about an OptoElectronic Integrated Circuit (OEIC) [28], Soref proposed the concept of "superchip" [29]. That visionary idea, whose original sketch is shown in Fig.1.7, was incredibly close to the state of the art Optical Networks On Chip (ONoC) produced today.

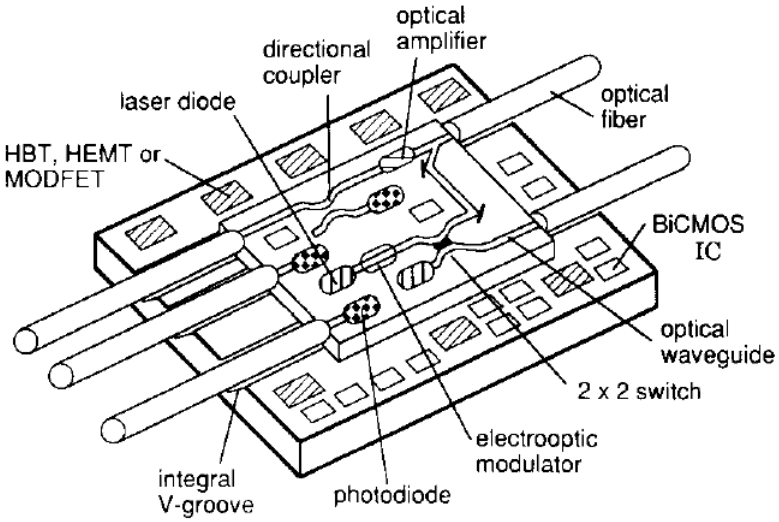

Figure 1.7: The idea of optoelectronic "superchip" proposed by Soref in 1993. Picture taken from [29].

The idea of Soref was to realize a chip which merges and combines the potential of electronics and photonics on the same substrate, which is the Silicon platform. In the superchip of Fig.1.7, it is possible to recognize all the fundamentals building blocks which are now part of a typical ONoC: etched V-grooves for on chip fiber coupling, splitters, combiners, amplifiers and modulators, switches, photodiodes and so on. The ten years following 1993 were not of such big impact for Silicon Photonics as the last ten years. The scene of integrated photonic devices was dominated by semiconductors belonging to the III-V groups like $AlGaAs/GaAs$ and $InGaAsP/InP$. The main reason was that the III-V platform was already well understood for the realization of active devices like Light Emitting Diodes (LEDs), amplifiers or lasers . Silicon, being an indirect bandgap material, has an intrinsic low radiative recombination probability, which makes it not suitable for the fabrication of active sources [30]. What is also relevant is that Silicon is a centrosymmetric material, therefore it lacks of the electro optic effect, which is at the basis for the realization of fast electro optic modulators [31]. During those years, it was thought that these fundamental limitations would never promote Silicon as the primary material for the realization of opoelectronic devices. However, already in 1993, Soref stated that "*the performance of Si-based OEIC's will eventually surpass that of III-V's in niche areas, yielding a shared dominion of IV's and III-V's. Si-based OEIC's should have economic advantages over their III-V*

counterparts. The multi-billion dollar Silicon VLSI industry has given an immense knowledge of how process silicon circuits at low cost. Much of that know-how can be adapted for optoelectronic processing, putting us part-way up to the learning curse of Silicon optoelectronics" [30]. The Soref's predictions were right. The year 2004 represented a turning point for Silicon Photonics. A ramping up of the investments to promote research and developement has been done by governments and industries [30]. A big effort was done by the DARPA microelectronics technology office with the four year project on electronic and photonic integrated circuits (EPIC) in Silicon at $1.55\,\mu m$. On the other side, Europe lauched the MELARI initiative at the end of the $1990s$, which founded several projects on Silicon Photonics (PICMOS, WADIMOS, SYNERGIA, HELIOS). Starting from 2004, the path of Silicon Photonics never stopped, as it is witnessed by the steadily increasing number of publications and citations over the years [22](see Fig.1.8).

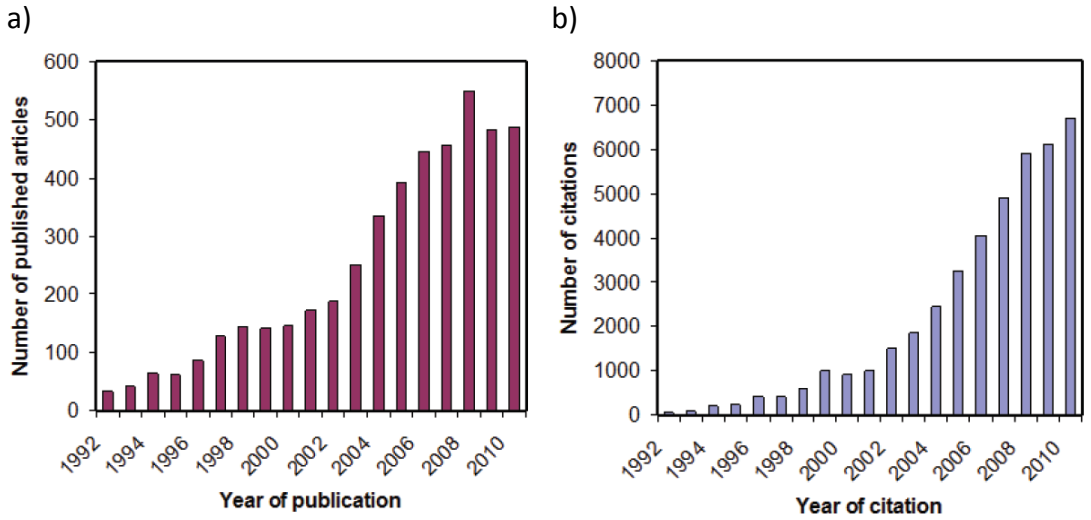

Figure 1.8: (a) Number of published articles per year having as a keyword "Silicon" or "waveguide" . (b) Number of citations per year to articles having as a keyword "Silicon" and "waveguides". Picture taken from [22].

Silicon Photonics was able to follow the same steps which decretated the leadership of CMOS microelectronics. This is schematically shown in Fig.1.9.

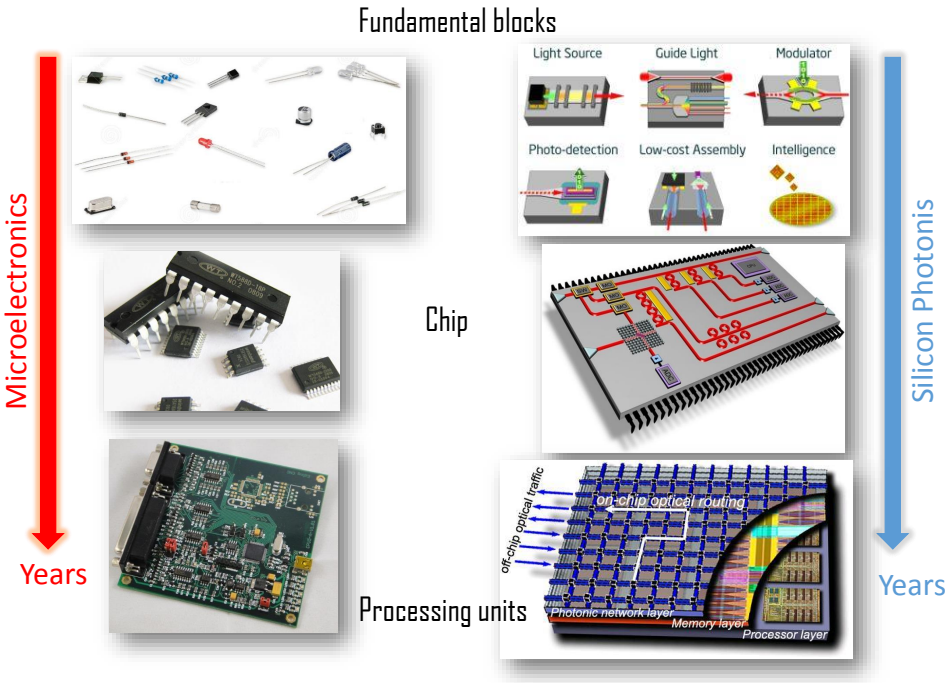

Figure 1.9: The similar path followed by Silicon Photonics with respect to microelectronics during the years. From the basic building blocks, progressively more complex circuits have been realized by connecting together several components.

At first, the basic bulding blocks have been demonstrated and progressively optimized. These includes both passive devices, as waveguides, splitters, grating couplers and interferometers, and active ones, like modulators, hybrid lasers and photodetectors. Then, these building blocks have been connected together, and assembled in networks to realize more complex functions. As a last step, photonic networks have been compatibily integrated with electronic ones to realize optoelectronic circuits. All these steps have been done under the same paradigms which moves the IC industry: miniaturization and standardization. The latter can be defined as the attempt to realize all the functionalities using only a limited number of materials (mainly Silicon and Silica, but also other group IV compounds and metals) and only one processing technology, which is CMOS. In particular, the CMOS processing technique was already available to Silicon Photonics for low-cost mass production, so no investments were required. With the introduction of Silicon On Insulator (SOI) wafers in the late 1980's and in the middle of 1990's to decrease the parasitic capacitance of ICs, the index contrast between the core and the cladding material increased, shrinking the dimensions of the photonic devices [32] . The first waveguides were fabricated in Silicon on heavily doped Silicon, with poor refractive index contrast, of the order of $0.01 - 0.1$ [27, 33]. The guided modes were weakly confined within the waveguide, with considerable energy leakage into the substrate. Large radius ($> 100\,\mu m$) was required to bend the waveguides without significant radiative losses. The use of SOI wafers permitted to use Silica as the cladding material, boosting the refractive index contrast to ≈ 2.92 at a wavelength of $1.55\,\mu m$. As a result, modes are more confined, and waveguides can be bent with lower radii [34]. The shift from the $850\,nm$ band to the O-band ($1.26\,\mu m - 1.36\,\mu m$) and C-band ($1.53\,\mu m - 1.565\,\mu m$) for fiber-optics communication; which are spectral regions where Silicon is highly transparent, contribuited to promote Silicon Photonics as the leading technology for small scale optical interconnections. The spread of Silicon Photonics is not limited to datacom and telecom application. The versatility of the building blocks has been exploited for applications in medical diagnostics [35], lab-on-chip [36, 37], spectrometer-on-a-chip [38], environamental monitoring [39],

neural networs [40, 41, 42] and so on. Today, Silicon Photonics can be considered as a mature technology, which is the subject of many books [25, 24] and enstablished international conferences [43, 44]. ONoC moved from the laboratories to the market, which is projected to increase from US$-25M in 2013 to more than US$-700M in 2024 [23]. Fig.1.10 reports an example of a commercial device fabbricated by Intel labs and named the Silicon Photonic link [45].

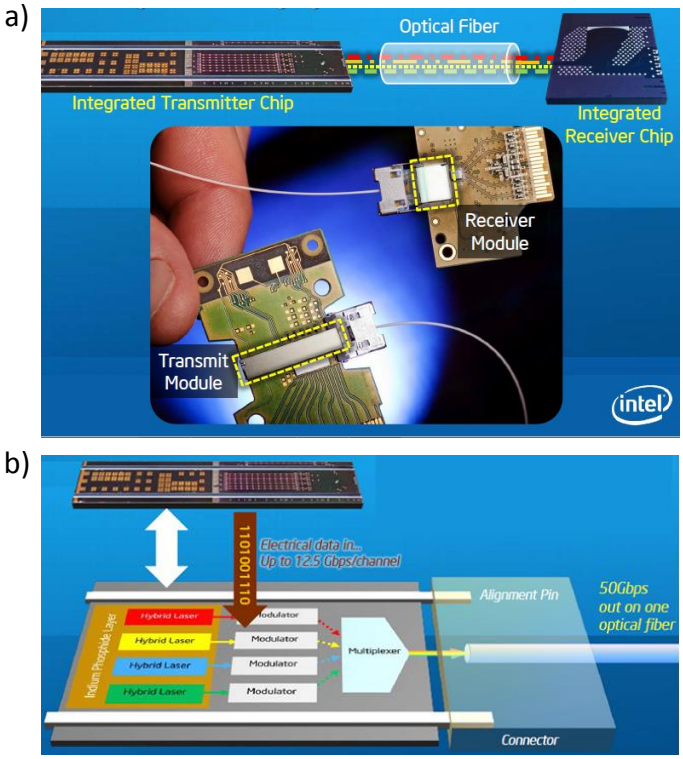

Figure 1.10: (a) The Silicon photonic link developed by Intel. (b) Schematic of the operation of the Silicon Photonic link. Pictures taken from [46].

It is a transceiver which operates at 50 *Gbps* using 4 hybrid Silicon laser sources which fed a WDM stage and are coupled to a fiber link. It has been launched on the market in 2015. Another example, which outlines the high level of complexity and co-integration with electronics reached by Silicon Photonics today, comes from the matrix router shown in Fig.1.11. This chip is being fabbricated by the Integrated Reconfigurable sIlicon phonic Switch (IRIS) european project, coordinated by Ericsson, one of the world-leading provider of communications technology and services [47].

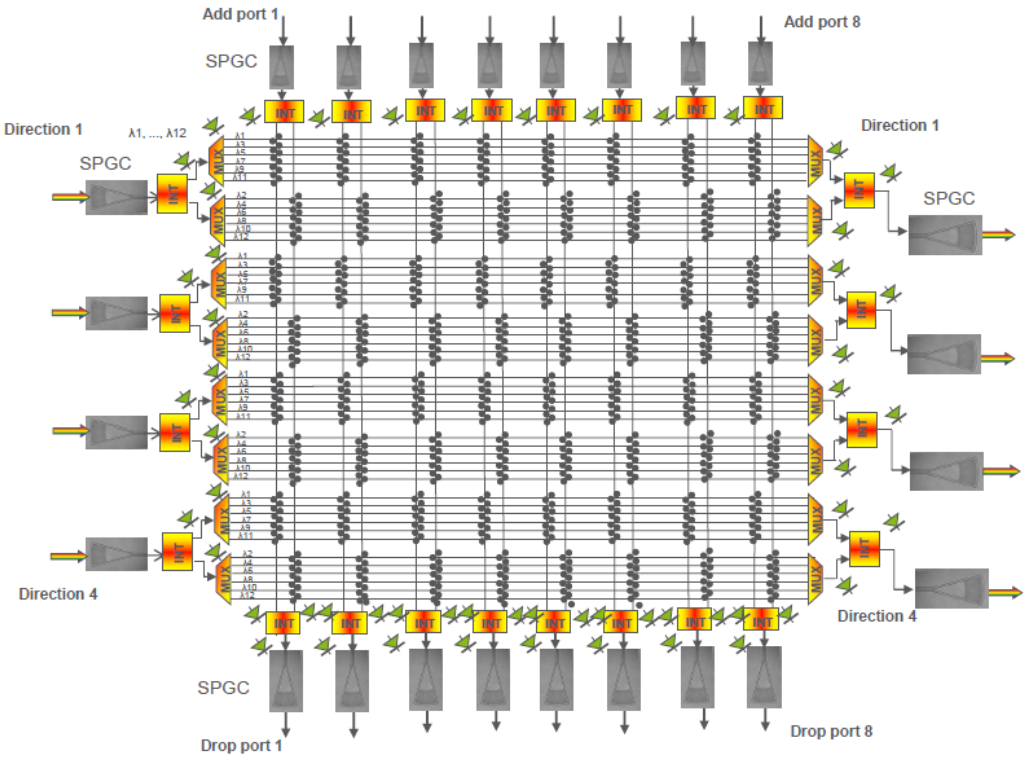

Figure 1.11: A schematic of the layout of the transponder aggregator developed within the european project IRIS. Picture taken from [47].

If successfully demonstrated in 2016, the router will pave the way for a new generation of optical systems integrated in a single chip (more than 10^5 photonic components and 48 WDM channels in less than $30\,mm^2$ of chip area). Such a chip will enable network operators to enhance the network performance, increasing node capacity as required by future 5G networks and Cloud.
Some challenges are, however, still open. As already introduced before, Silicon is mainly a passive material due to its indirect bandgap, and the realization of active devices still mainly proceed through the hetero-integration of III-V semiconductors [48]. These processes are expensive and not always compatible with the CMOS fabrication. Monolithic integration would be desired, but still much work has to be done in this direction. The same does not hold for photodetectors at $1.55\,\mu m$. Silicon is transparent in the O and C telecom bands, thus can not be used for photodetection and needs the hetero-integration of narrow bandgap semiconductors like Germanium [49]. There are also some technical aspects that need to be solved. For example, almost every Silicon Photonic company has its own Computer Aided Design (CAD) suite, and the diffusion of common Process Design Kits (PDK) are not so popular, even if lot of efforts has been done to invert this trend . In general, today's design methods and tools are not up to the task, mainly for what concernes the co-integration of photonics and electronics blocks. More on this subject can be found in Ref.[50]. Last, but surely not least, the cost of a photonic device is still too high. This is because the production volumes are still too low for bringing down the market prices, and because most of the foundries have been focused on developing individual Silicon Photonics elements, rather than complete ONoC.

1.1 Silicon photonics building blocks

In the next sections, the main building blocks of a Silicon Photonic network are introduced and briefely reviewed. The first block which will be presented is the waveguide, then couplers and splitters will be discussed. Next, more advanced devices will be reported, like optical resonators, sequence of coupled resonators, electro optic modulators and active sources.

1.1.1 Waveguides

Waveguides are probably the most important elements of photonic networks, since they carry the optical signal from one block to the other. Light is confined inside the waveguide by Total Internal Reflection (TIR), which requires a cladding material of lower refractive index than the one of the core, as shown in Fig.1.12(a). Light travels in the form of discrete modes of electric field profile $\mathbf{e}_m(x, y, \omega)$, which are solution of the Helmoltz equation [51]:

$$\left(\nabla_{xy}^2 + \beta_m^2\right) \mathbf{e}_m(x, y, \omega) = \frac{\omega^2}{c^2} n^2(x, y) \mathbf{e}_m(x, y) \tag{1.1}$$

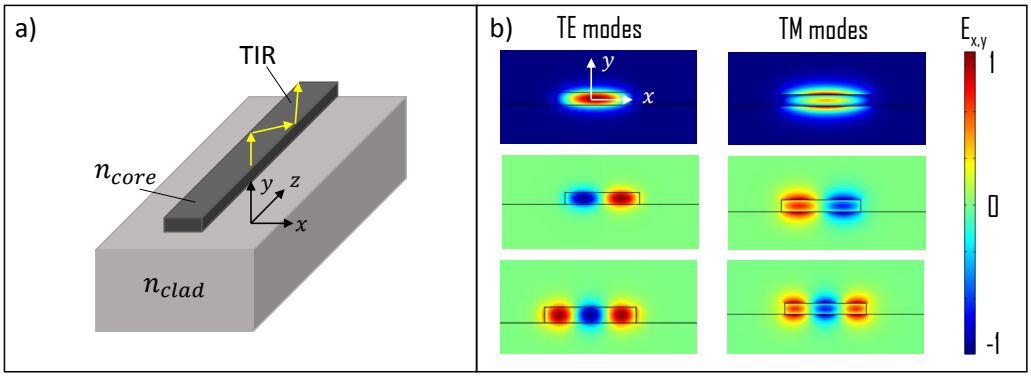

Figure 1.12: (a) Schematic of a channel waveguide. The index of refraction of the cladding material is n_{clad} while the one of the core is n_{core}. The propagation direction is z. (b) Distribution of the dominant electric field component (E_x for TE modes, E_y for TM modes) for the three lowest order TE and TM modes of a waveguide with cross section $1.6\,\mu m \times 0.25\,\mu m$.

Due to the invariance of the refractive index distribution $n(x, y)$ along the propagation direction z, the dependence on this coordinate is on the form $e^{-i\beta_m z}$, where $\beta_m = \frac{\omega}{c} n_{eff,m}$ is called the modal propagation constant (or wavevector), and $n_{eff,m}$ the effective index. In general, $n_{eff,m}$ is a complex quantity. As for plane waves, the real part is associated with propagation, while the imaginary one to losses. The field intensity exponentially decreases along z as $e^{-\alpha z}$, where the attenuation coefficient α is given by $\alpha = \frac{2\omega}{c} Im(n_{eff,m})$. Fig.1.12(b) shows an example of the electric field distribution $\mathbf{e}_m(x, y)$ for three lowest order solutions of Eq.1.1. Each solution is associated to a different number of nodal points n, in which the electric field is equal to zero. In what follows, the modal order m will be defined as $m = n + 1$. As the modal order increases, the modal confinenement, defined as:

$$\Gamma_m = \frac{\int_{wg} n^2(x, y) |\mathbf{e}_m(x, y)|^2 \, dxdy}{\int n^2(x, y) |\mathbf{e}_m(x, y)|^2 \, dxdy} \tag{1.2}$$

in which the integral at the numerator is performed only in the core region, decreased. As a consequence, the effective index monotonically decreases as the modal order increases, because the optical field senses less

the refractive index of the core. Given the geometry of the waveguide, the maximum number of supported modes is limited. Apart from very simple geometries, as the slab one [52], no analytical expression exists for determining this number. For the channel waveguides implemented in this work, it is possible to take as a rough rule the fact that light of wavelength λ can not be confined to features which are lower than $\frac{\lambda}{2}$ due to the diffraction limit. The maximum number of supported modes (for a fixed polarization) can then be approximated as $\sim \frac{4wh}{\lambda^2}$. Modes can be classified also on the basis of their polarization. In general, for waveguides of sub-wavelength dimension, the electric and the magnetic fields are not transverse to the propagation direction and neither orthogonal to each other. The classification between Transverse Electric (TE) and Transverse Magnetic (TM) modes is done on the basis of their dominant electric feld component, which for the reference frame of Fig.1.12(b) concides with the x direction in case of TE modes, and y for TM modes. The effective index of each mode depends on wavelength. As the latter increases, the mode get less confined due to diffraction, and the effective index decreases. The way this occurs strongly depends on the mode order, the waveguide geometry, the polarization and the core and cladding chromatic dispersion. In micron size waveguides, it is the geometric dispersion which dominates over chromatic one, in opposition with what happens in an optical fiber [2, 53]. A measure of the effective index dispersion is given by the high order dispersion coefficients $\beta_m^{(j)} = \frac{d^j \beta_m}{d^j \lambda}$. For $j = 1$, this is given by:

$$\beta_m^{(1)} = \frac{d\beta_m}{d\lambda} = \left(n_{eff,m} - \lambda \frac{dn_{eff,m}}{d\lambda} \right) \frac{1}{c} = \frac{n_{g,m}}{c} \tag{1.3}$$

and represents the inverse of the group velocity $v_{g,m} = \frac{c}{n_{g,m}}$, where the group index is defined as $n_{g,m} = n_{eff,m} - \lambda \frac{dn_{eff,m}}{d\lambda}$. For $j = 2$, the quantity $\beta_m^{(2)}$ is called Group Velocity Dispersion (GVD), and for $j > 2$ the terms are in general referred as j^{th} order dispersions. Another important property is the mode effective area $A_{eff,m}$, defined as:

$$A_{eff,m} = \frac{\left(\int |\mathbf{e}_m(x,y)|^2 \, dxdy \right)^2}{\int |\mathbf{e}_m(x,y)|^4 \, dxdy} \tag{1.4}$$

which is a measure of the effective extension of the optical mode into the core and cladding regions. Higher order modes, being less confined, have larger effective areas than the lower order ones.

The first Silicon waveguides, reported in 1980, were fabricated on the Silicon-On-Silicon platform, in which the crystalline Silicon core was deposited on a substrate of heavily doped one. The process of doping lowers the index of refraction of the material through plasma carrier dispersion, thus creating the conditions for waveguiding [33]. However, the index contrast was of the order of 0.01, so the mode was highly delocalized and suffered from leakage of energy into the substrate. In the late 1980s, SOI wafers were introduced in the microelectronic industry, offering an improved refractive index contrast. Wafers were developed with methods like SIMOX, BESOI and SmartCut [24]. Waveguide fabrication requires definition of their edges in a photoresist (through deep UltraViolet (DUV) or electron beam lithography) and subsequent dry etch. The process naturally introduces roughness on the side walls of the waveguide, which is source of scattering. As a consequence of the enhanced refractive index contrast, the spatial mode profile got tightly confined inside the core. On one side, this allowed to shrink the waveguide dimensions and to realize smaller bends, and on the other side to avoid energy leakage into the cladding material. The first fabricated SOI waveguide was characterized by $0.5\,dBcm^{-1}$ of propagation loss, but this was due to the fact that it had several microns of cross section, so the modal overlap with side wall roughness was negligible. During the following years, lots of efforts have been done in the design and fabrication of low cross section and low loss waveguides. To reduce the side wall roughnesses, post-etch thermal oxidation has been introduced. Using this technique, Lee et. al. demonstrated that it was possible to reduce the losses at $1.55\,\mu m$ of a $500\,nm \times 50\,nm$ Silicon wire from $32\,dBcm^{-1}$ before thermal oxidation, to $0.8\,dBcm^{-1}$ after post etch oxidation [54]. Local oxidation of Silicon

(LOCOS), a technique firstly reported at the Carleton University, allowed to realize etchless ridge Silicon waveguides by the local oxydation of Silicon, which resulted in $0.3\,dBcm^{-1}$ of propagation loss in a $1\,\mu m$ wide waveguide with a rib height of $70\,nm$ [55]. For small scale production, the use of electron beam lithography has proven to be a very effective tool for the realization of low loss Silicon waveguides. For example, Gnan et. al. reported about photonic wires formed by electron beam lithography with $0.92\,dBcm^{-1}$ of loss [56]. The current record of propagation loss at $1.55\,\mu m$ is $0.27\,dBcm^{-1}$, achieved by Bogaerts and Selvaraja using hybrid ridge-channel waveguides [57].

1.1.2 Couplers

One of the biggest challenges in realizing photonic chips relates to the efficiency of the coupling of light in the waveguide by an input fiber. The difficulties arise from the huge mismatch between the effective area of the mode which propagates in the fiber and the one in the waveguide. A standard single mode Silica fiber has a core with a typical dimension of $\sim 10\,\mu m$, and an effective mode area of $\sim 315\,\mu m^2$, while the one of a waveguide is of the order of $1\,\mu m^2$, which is more than two orders of magnitude lower. It comes out that if the two cores are brought into contact (edge coupling), more than $20\,dB$ of power is lost. Tapered lensed fibers, which are fibers in which one of the two ends are progressively reduced in size to $\sim 2\,\mu m$, offer better performances by focusing light to an effective area of $\sim 10\,\mu m^2$, thus reducing the coupling losses at a value close to $10\,dB$. If lower losses are needed, the input facet of the waveguide havs to be engineered. Two approaches have been developed during the years: tapering, which consists in enlarging or reducing the size of the waveguide core as it approaches to the fiber, or patterning subwavelength periodic structures at the waveguide extremities called grating coupler. Both are schematically shown in Fig.1.13.

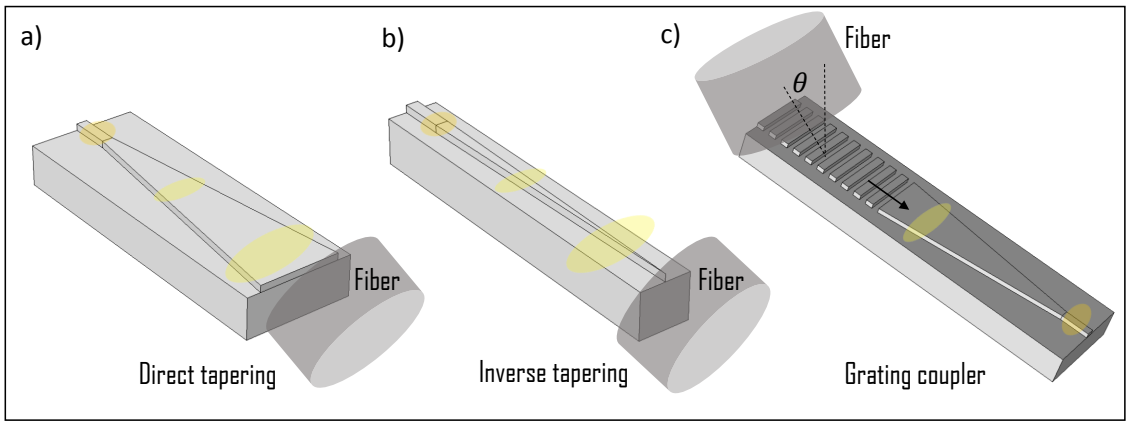

Figure 1.13: (a) Direct tapering of a waveguide. (b) Inverse tapering of a waveguide. (c) Grating coupler, with the fiber tilted by an angle θ with respect to the normal of the grating. In all panels, the yellow circle sketches the modal intensity of the propagating light. Fiber is not to scale.

Tapers are also called Spot Size Converters (SSC). Tapering can be direct if the end of the waveguide is smoothly increased to match the dimension of the spot of the fiber, or inverse, if the end of the waveguide is progressively reduced to delocalize the modal profile outside the core. The performances are quite similar. By using direct tapering, in which both the width and the thickness of the waveguide were increased, Day et. al. demonstrated coupling losses of less than $0.5\,dB$ in $1\,mm$ of taper length [58]. M.Pu et. al. reported on inverse tapers in which a $450\,nm$ width waveguide was reduced to only $15\,nm$ using thermal oxydation, achieving an ultra low value of $0.36\,dB$ of coupling loss [59]. Grating couplers relies instead on a completely different working principle. In the most simple implementation, they are structures in which Silicon is periodically

etched with a period Λ, creating alternating regions of different index of refraction. As a consequence of the periodicity, the mode of propagation constant β is converted into a wave which is diffracted into the cladding with an angle θ with respect to the propagation direction [60]. This occurs if the period Λ satisfies the following phase matching relation:

$$\sin\theta = \frac{\Lambda n_{eff} - \lambda_0}{\Lambda n} \tag{1.5}$$

where n_{eff} is the effective index of the mode which diffracts light, λ_0 is the wavelength and n is the refractive index of the medium in which the wave is radiated. A fiber placed at an angle θ can than collect the diffracted light. The reverse process can be exploited to couple light from the fiber into the mode of the waveguide. Starting from the most simple implementation described above, the effort to reduce the coupling losses in grating couplers produced a wide variety of structures. Coupling efficiencies of 37% have been demonstrated using shallow-etched gratings [61], 42% using photonic crystal structures within the grating [62], 64% using apodization [63], and 69% using backside reflectors [64]. The current record of couplig losses is $0.58\,dB$, achieved by Ding et. al. in a fully etched apodized grating coupler using sub-wavelength photonic crystals and a bonded aluminum mirror [65].

1.1.3 Splitters and combiners

Light which propagates in a waveguide can be split into one or more waveguides and vice-versa. Several structures allow achieving this: Y-junctions [66], Multi Mode Interference (MMI) devices [67] and directional couplers [68]. Only the latter will be briefely discussed here, due to its use in the designs shown in the rest of this thesis. As sketched in Fig.1.14(a), a directional coupler if formed by two waveguides which are brought in close proximity. Their separation is the coupling gap c_g, which is few hundreds of nanometers long [51]. The region where the two waveguides are close is long L.

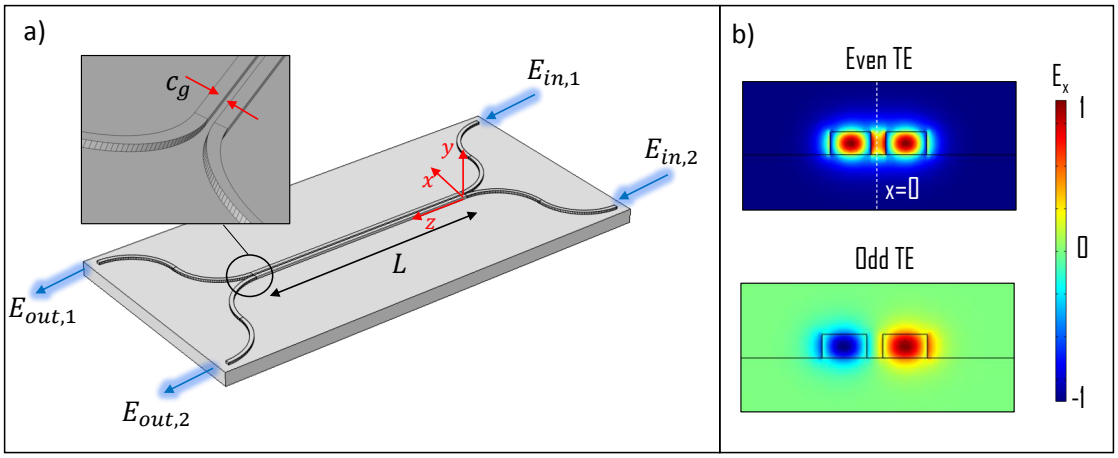

Figure 1.14: (a) Sktech of a directional coupler of length L and coupling gap c_g. Electric fields $E_{in,1}$ and $E_{in,2}$ represent the inputs, while $E_{out,1}$ and $E_{out,2}$ represent the outputs. (b) Dominant electric field component (E_x) for the even and odd TE supermodes of the two coupled waveguides.

The gap is so narrow that the evanescent tail of the optical mode of each waveguide penetrates, through the cladding, into the core of the neighboring one, thus allowing cross talk between the two. In the most simple case of two identical parallel waveguides, if some power P_{10} is launched into waveguide 1 while waveguide 2 is not excited, after a certain propagation distance $z = L$, the powers in the two waveguides $P_1(L)$ and $P_2(L)$ become [52, 51]:

$$P_1(L) = P_{10}\cos^2\left(\frac{\pi}{2}\cdot\frac{L}{L_c}\right) = |r|^2 P_{10} \tag{1.6}$$

$$P_2(L) = P_{10}\sin^2\left(\frac{\pi}{2}\cdot\frac{L}{L_c}\right) = |\kappa|^2 P_{10} \tag{1.7}$$

where r and κ are called the reflection and the transmission coefficient of the coupler respectively. κ and r for a lossless system satisfy $|r|^2 + |\kappa|^2 = 1$. In Eqs.1.6-1.7, the quantity L_c is called the transfer length, and coincides with the length of the coupler which realizes a complete transfer of power from waveguide 1 to waveguide 2. It can be demonstrated that L_c is given by [52]:

$$L_c = \frac{\lambda}{2(n_o - n_e)} \tag{1.8}$$

where n_o and n_e are the effective indexes of the "supermodes" of the combined structures, shown in Fig.1.14(b). The subscripts o and e stand for odd and even respectively, and refer to the parity of the electric field distribution with respect to the $x = 0$ axes of Fig.1.14(b). In general, if both waveguide 1 and waveguide 2 are excited at the input, the system is described by a 2×2 unitary matrix M which maps the input electric field vector $E_{in} = (E_{in,1}, E_{in,2})$ at $z = 0$ into the output one $E_{out} = (E_{out,1}, E_{out,2})$ at $z = L$. The matrix M is given by:

$$M = \begin{pmatrix} r & -i\kappa \\ -i\kappa & r \end{pmatrix} e^{-i\beta L} \tag{1.9}$$

where β is the propagation constant of the mode in the waveguides, while κ and r are defined above. If the two waveguides are not equal, and hence a phase mismatch $\Delta\beta$ exists between the propagation constants, the expression for the transfer matrix M gets more complex. When $\Delta\beta \neq 0$, a complete power transfer can no more occur between the two waveguides [51]. Directional couplers are fabricated through patterning of the photoresist and subsequent etching. Coupling gaps as low as $160\,nm$ can be fabricated using $193\,nm$ DUV lithography and dry etching. For lower gaps, electron beam lithography gives better results. The size of the gap is a critical dimension for the coupler, since the dependence of the coupling and reflection coefficients on the gap is exponential [69]. This is a direct consequence of the fact that the evanescent tail of the optical modes exponentially decreases in the cladding. The ability to fabricate waveguides with tight tolerances on the dimensions is also required to set the phase mismatch $\Delta\beta$ equal to zero, thus allowing a more efficient energy transfer. For these reasons, tapered directional couplers have been proposed, in which the size of one waveguide is intentionally adiabatically swept in the neighboring of the nominal one. This trick allows to relax the fabrication tolerances on the final waveguide dimensions to tens of nanometers [70, 71].

1.1.4 Microresonators

Microresonators are ones of the most important, multi purpose and versatile tools in Silicon Photonics [72, 73, 74]. They can be realized in very different geometries, as, for example, microrings, racetracks, microdisks and microtoroids [75, 76, 77, 78]. Some of them are shown in Fig.1.15.

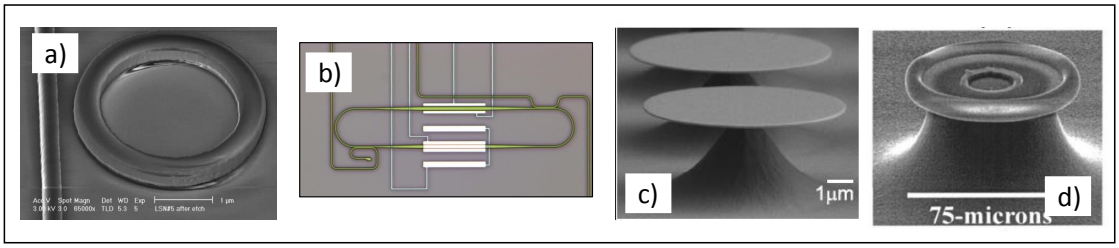

Figure 1.15: (a) Scanning Electron Microscopy (SEM) image of a ring resonator in the All Pass configuration. Picture taken from [76]. (b) Optical microscope image of a racetrack resonator. Picture taken from [79]. (c) SEM image of a suspendend microdisk resonator. Picture from [75]. (d) SEM image of a suspended microtoroid resonator. Picture taken from [77].

Each of these shapes possess its own advantages and disadvantages, so the resonator type has to be choosen to best match the purposes of the experiment. The common feature of each resonator is that light is made to travel in a closed path, and, as a consequence, only certain wavelengths λ_m can be supported. For travelling wave resonators, as microrings or racetracks, these wavelengths are the ones which satisfy the resonance condition [74]:

$$n_{eff}p = m\lambda_m \tag{1.10}$$

where n_{eff} is the effective index of the waveguide, p is the resonator perimeter and m is an integer number. Eq.1.10 has a simple physical interpretation: the perimeter of the resonator has to contain an integer number of wavelengths (in the material), in such a way that the travelling wave, after a roundtrip, can reproduce itself. Alternatively, Eq.1.10 can be cast in the form $\beta p = 2m\pi$, in which β is the propagation constant defined in Section 1.1.1. Given in this form, the resonance condition is met every time that after a complete roundtrip, the light has acquired a phase which is a multiple integer of 2π, so that the wave undergoes constructive interference each time it completes a roundtrip.

1.1.4.1 Add Drop and All Pass configurations

In order to be excited, a resonator requires to be coupled to a bus waveguide. When only one waveguide is used, the resonator is said to be in the All Pass (AP) configuration. When two waveguides are coupled, the configuration is called Add Drop (AD). As sketched in Fig.1.16(a), the AP configuration possess an input and an output port.

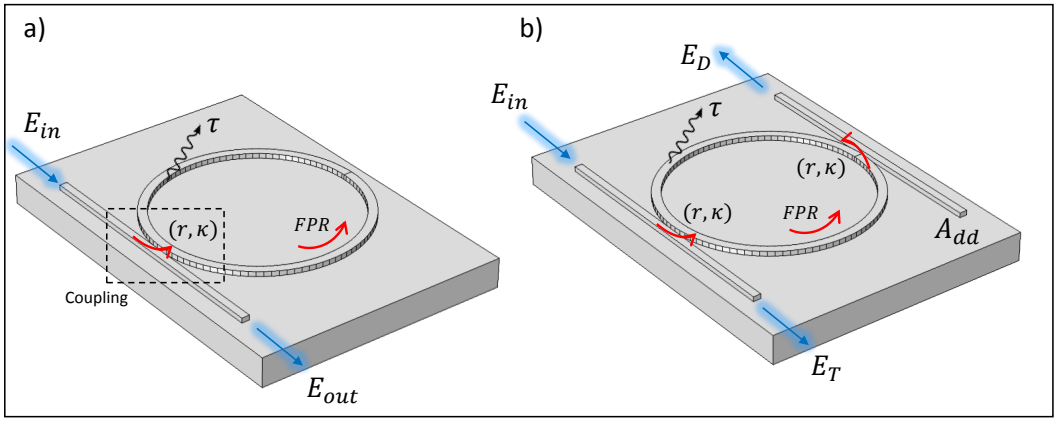

Figure 1.16: (a) Ring resonator in the All Pass configuration. The coupling region and the Free Propagation Region (FPR) are explicitally indicated. The reflection and transmission coefficients of the coupler are r and κ respectively. Scattering losses are indicated as τ. (b) Ring resonator in the Add Drop configuration. The meaning of the parameters are the same as for panel (a).

The electric field amplitude at the input port E_{in} is connected to the one at the output port E_{out} by the transfer function $H_{AP}(\omega)$, which is a complex function that depends on the light frequency ω. An expression for $H_{AP}(\omega)$ can be derived using the Transfer Matrix Method (TMM) [80]: the two sections of the resonator, which are the coupling region CR and the free propagation region FPR in Fig.1.16(a), are treated as four and two port systems respectively, whose outputs are connected to the inputs by linear matrix relations. A system of equations is then derived which can be solved for E_{out}, once that E_{in} is known. The transfer function $H_{AP}(\omega)$ can be demonstrated to be [81, 80]:

$$H_{AP}(\omega) = \frac{\tau - re^{-i\phi(\omega)}}{r\tau - e^{-i\phi(\omega)}} \tag{1.11}$$

where $\tau = e^{-\alpha p}$ (α is the scattering loss coefficient) represents the roundtrip losses, r is the reflection coefficient of the coupler and $\phi(\omega) = \frac{\omega}{c} n_{eff}(\omega) p$ is the roundtrip phase. The quantity $|H_{AP}(\omega)|^2$ is plotted in Fig.1.17 as a function of ϕ.

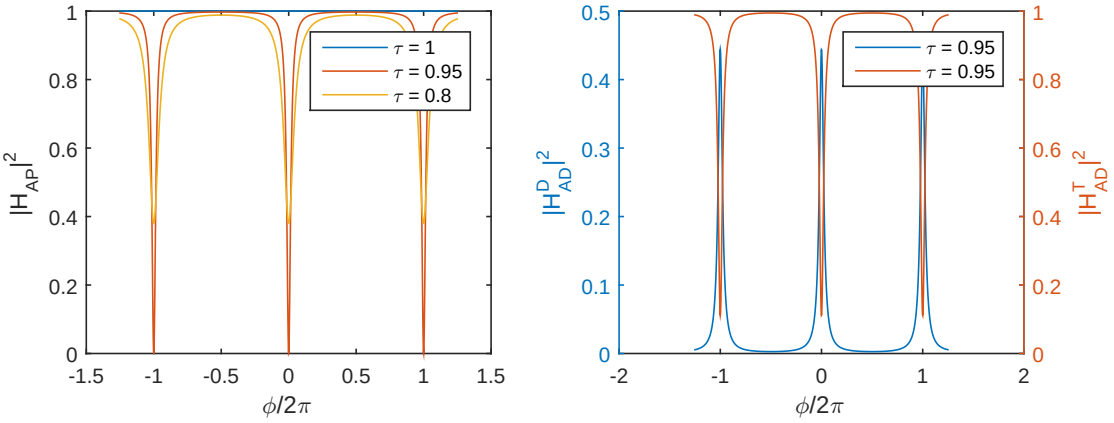

Figure 1.17: Plot of the quantites $|H_{AP}|^2$, $|H^D_{AD}|^2$ and $|H^T_{AD}|^2$ as a function of the roundtrip phase ϕ. For all the curves, the reflectance of the coupler is set to $r = 0.95$.

As already introduced above, each time that $\phi = 2m\pi$, the resonance condition is met, and a transmission dip appears in the spectral response. When this occur, energy is accumulated inside the resonator and a fraction τ is lost (for example, from scattering with the side walls roughness), resulting in a lack of power in the transmission. Outside the resonance condition, the resonator behaves as a straight waveguide, and no light is coupled. It is worth to note that when $\tau = 1$, i.e., no losses are present, $H_{AP} = 1$ independently on the phase. This comes directly from energy conservation.
The AD resonator has instead two input ports, conventionally named Input and Add, and two output ones, named Drop and Through. These are sketched in Fig.1.16(b). If only the Input port is excited, the transfer function $H^D_{AD}(\omega)$, which express the ratio between the input field E_{in} and the dropped field E_D, is given by [81]:

$$H^D_{AD}(\omega) = \frac{\kappa^2\sqrt{\tau}e^{i\phi(\omega)/2}}{r^2\tau - e^{i\phi(\omega)}} \tag{1.12}$$

where κ is the transmission coefficient of the coupler (for simplicity, the two coupling regions are assumed to be symmetric). The transfer function of the Through port $H^T_{AD}(\omega) = \frac{E_T}{E_{in}}$ is instead given by [81]:

$$H^T_{AD}(\omega) = \frac{r\left(e^{i\phi(\omega)} - \tau\right)}{e^{i\phi(\omega)} - r^2\tau} \tag{1.13}$$

The quantities $|H^T_{AD}(\omega)|^2$ and $|H^D_{AD}(\omega)|^2$ are plotted in Fig.1.17 as a function of $\phi(\omega)$. As for the AP configuration, everytime that $\phi = 2m\pi$ a resonance occurs, which is manifested in a peak in the Drop signal and in a dip in the Through one. When the Add port is simultaneously excited, it is possible to exploit the linearity of the system to calculate the expressions for the dropped and transmitted powers. The key parameters which characterize a resonator are the quality factor Q, the Free Spectral range (FSR) and the Field Enhancement factor FE. The quality factor of the m^{th} resonance order is defined as the ratio between the resonant wavelength λ_m and the Full Width at Half Maximum (FWHM) $\Delta\lambda_m$ of the peak, i.e., $Q = \frac{\lambda_m}{\Delta\lambda_m}$. It can be shown, by expanding the exponential terms in Eq.1.12 to the first order in $\omega - \omega_m$ (ω_m is the resonance frequency), that the the peak is actually a lorentzian function. The FSR is defined as the distance between two adjacent resonance wavelengths, while the FE factor is the ratio between the field inside the resonator and the one in the input waveguide. The expressions for these quantities are reported in Table 1.1. The interested reader can refer, for example, to Ref.[82], for a complete derivation.

Parameter	**All Pass**	**Add Drop**
Q	$\frac{\pi n_g(\lambda_m)p\sqrt{r\tau}}{(1-r\tau)\lambda_m}$	$\frac{\pi n_g(\lambda_m)pr\sqrt{\tau}}{(1-r^2\tau)\lambda_m}$
FSR	$\frac{\lambda_m^2}{n_g(\lambda_m)p}$	$\frac{\lambda_m^2}{n_g(\lambda_m)p}$
FE	$\frac{i\kappa}{1-r\tau e^{-i\phi(\omega)}}$	$\frac{i\kappa}{1-r^2\tau e^{-i\phi(\omega)}}$

Table 1.1: Main parameters which characterize the performances of a resonator expressed as a function of the coupler parameters r and κ, the perimeter p, the resonant wavelength λ_m and the group index n_g.

By looking at Table 1.1, some general considerations can be made:

- The quality factor is inversely proportional to the transmittance of the coupler κ and to the roundtrip losses τ. Hence, high Q resonators are characterized by weak coupling with the waveguide and low losses.
- The FSR is inversely proportional to the resonator perimeter. The average spectral distance between two resonances thus decreases as the resonator is made bigger.

- For small losses, the on resonance FE is given by $FE \sim 1/\kappa$. Hence, if the resonator is weakly coupled to the waveguide, and has very low losses, the field inside the resonator is greately enhanced with respect to the one in the bus waveguide. For example, if $\kappa^2 = 0.01$, the power inside the resonator is 100 times higher than in the bus waveguide. As described later and in Chapter 6, this feature can be exploited for nonlinear optics applications.

Another important quantity is the group delay τ_g. The latter is defined as the derivative of the phase $\delta(\omega)$ of the transfer function with respect to the frequency, i.e., $\tau_g = \frac{d\delta(\omega)}{d\omega}$. As derived in Chapter 6, it represents the time delay that is imparted to an incoming electric field envelope when passing through the resonator. Fig.1.18(left panel) shows the phase δ for an AP filter in the neighboring of a resonance.

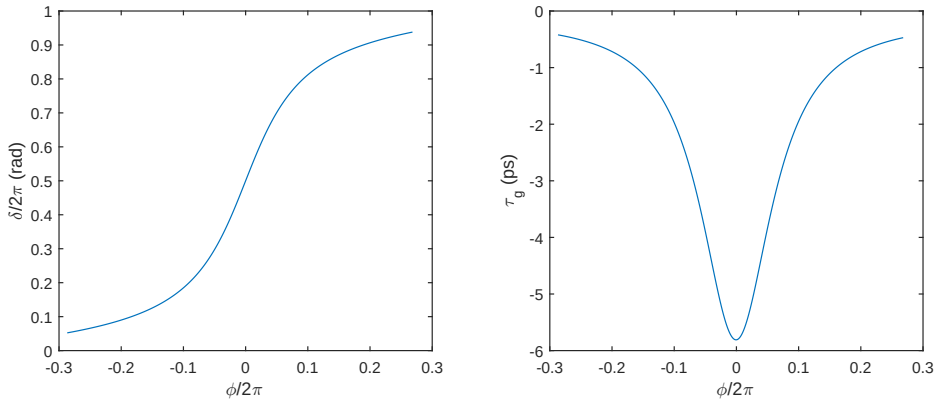

Figure 1.18: Left: Phase δ of the transfer function H_{AP} as a function of the roundtrip phase ϕ. Right: group delay τ_g as a function of the rountrip phase ϕ. The parameters used in the simulation are the ones of the All Pass filters implemented in the delay line for the broadband design of Section 6.4, which are reported in Table 6.2.

As it can be appreciated, the curve is very steep in proximity of the resonance, which means that the group delay is quite high in this region. The derived group delay is shown in Fig.1.18(right panel). The slow light properties of the resonator can be more appreciated through an example. As shown in Fig.1.18(right panel), if the carrier frequency of the incoming field lies near resonance, delays at the order of $\sim 6\,ps$ can be achieved. The size of the resonator used for this simulation is $50\,\mu m$. If the resonator would be replaced by a straight waveguide of group velocity $v_g = 75\,\frac{\mu m}{ps}$ (a waveguide of cross section $400\,nm \times 250\,nm$ fullfils this requirement) and having the same length, the group delay would be $\tau_g = \frac{50}{75} \sim 0.75\,ps$, i.e, 8 times shorter. The speed of light is then reduced by a factor 8 by using the resonator.

1.1.4.2 Sequence of coupled resonators: CROW and SCISSOR

The slow light property of single resonators can be enhanced by N times if N cavities are connected in series to form, for example, an AP chain. Indeed, sequence of resonators have been widely used as optical delay lines due to their slow light properties [83, 84]. Different geometries have been explored, among which the most implemented was the Coupled Resonator Optical Waveguide (CROW) [85, 86], and the Side Coupled Integrated Spaced Sequence Of Resonators (SCISSOR) [87, 78, 82]. Both are sketched in Fig.1.19.

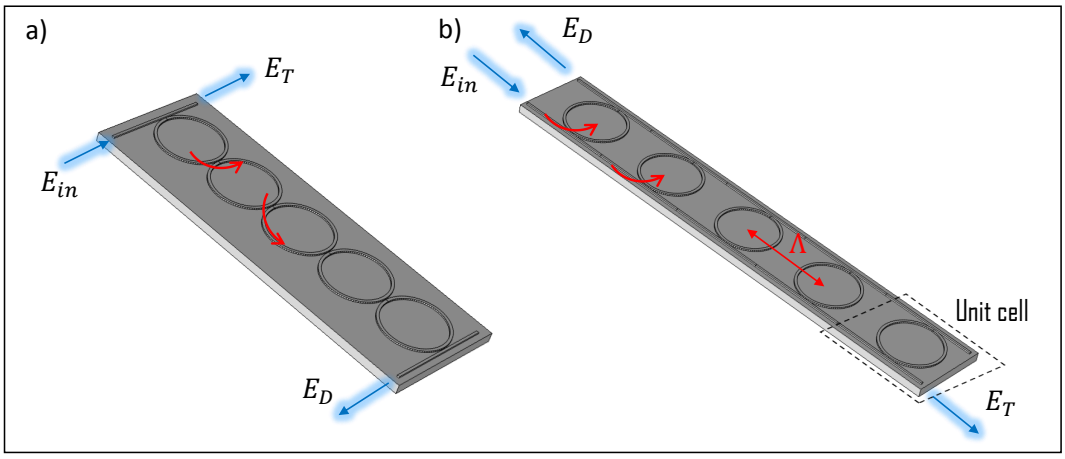

Figure 1.19: (a) Sketch of a CROW made by 5 coupled resonators. The input, Drop and Through ports E_{in}, E_D and E_T are also indicated. (b) Sketch of a SCISSOR made by 5 side coupled resonators. The input, Drop and Through ports E_{in}, E_D and E_T are also indicated. The lattice periodicity of the unit cell is indicated by Λ.

In the CROW geometry, resonators are directly coupled, and only the first and the latter resonators of the sequence are coupled to the bus waveguides. On the contrary, in the SCISSOR geometry, resonators are all coupled to two straight side waveguides. Due to the implementation of the ring-based SCISSOR geometry in Chapter 2, a brief discussion of its spectral properties is now outlined. The SCISSOR is actually a one dimensional photonic crystal made by the repetition of a unit cell constituted by an AD filter. From the theory of light propagation in periodic media [51, 88], it results that there are some frequency ranges in which light can not penetrate in the structure, which are called Photonic BandGaps (PBG). PBGs manifest themselves in dips in the transmission spectra (Through port) and peaks in reflectance (Drop port) spectra. An example of the latter is shown in Fig.1.20.

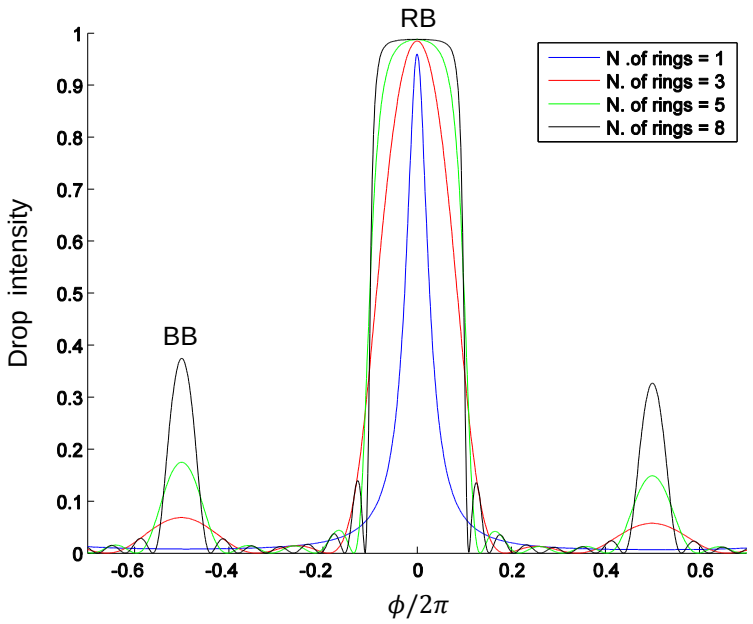

Figure 1.20: Drop spectral response of a SCISSOR as a function of the number of rings which compose the sequence.

The SCISSOR configuration has two types of PBGs, one is called the Resonator Band (RB) and the other the Bragg Band (BB) [78]. The RB is due to the response of each resonator of the chain. Indeed, it occurs when the input wavelength satisfies the condition in Eq.1.10. The BB is due to the coherent, constructive superposition, of all waves which are back reflected by each resonator. Infact, even when the input wavelength is off resonance, a small portion of electric field is coupled into the Drop port (back reflected). If the resonator distance Λ satisfies $\Lambda\beta = q\pi$, in which q is an integer number, then all the reflected waves superimpose contructively, and significant power can be build up into the drop port. If the SCISSOR is designed to have $\Lambda = \pi R$, in which R is the radius of the rings, the RB and the BB overlap for all orders. From Fig.1.20, it is possible to notice that as the number of resonators increase, the bandwith of the filter both flattens and increases, becoming very similar to a box-like response. One may wonder what happens if the resonators which compose the sequence are not all equal, i.e., they have resonant frequencies which are slightly detuned between each other. This situation can be intentionally induced already at the design stage [87], or it can be an undesired consequence of defects in the fabrication process [89]. What happens is that defect states, in which the energy is mosty localized in the neighborhood of the defects, are created. These manifest in the spectral response as narrow transparency peaks inside the PBGs of the Through port, or equivalently in dips into the Drop one. The phenomenon is called Coupled Resonator Induced Transparency (CRIT) and is widely discussed in Refs.[87, 78, 82]. By virtue of the intrinsic link between CRIT and defects, a device which quantifies the amount of fabrication disorder in a SOI wafer by exploiting the CRIT effect has been proposed [89].

1.1.4.3 Tuning of microresonators

The resonance wavelength of a microresonator is very sensitive to fabrication imperfections. By differentiating both sides of Eq.1.10, it is derived that a small change in the effective index Δn is reflected in a shift in the resonance wavelength of $\Delta\lambda = \lambda_m \frac{\Delta n}{n_g}$. For example, a variation of $5\,nm$ in the width of a waveguide of cross section $450\,nm \times 250\,nm$, which corresponds to a realistic value for both DUV and electron beam lithography [90, 91], implies $\Delta n \sim 0.01$ (calculated from a Finite Element Method simulation), and a consequent wavelength shift of $\Delta\lambda \sim 3.8\,nm$ (in the calculation, $\lambda_m = 1550\,nm$ and $n_g \sim 4$). For resonators implemented in WDM applications, this quantity is typically much higher than the FWHM of the resonace [74], with the consequence that if the filter is designed to drop all the power at λ_m, no power will be actually dropped when fabricated. It comes naturally that a trimming mechanism is required for aligning the resonance at the wavelength where the filter has been designed to operate. Two tuning mechanisms are typically implemented: thermal [92, 93] and plasma carrier tuning [94, 95]. The first exploits the thermo optic coefficient of Silicon, which is $\frac{dn}{dT} = 1.86 \cdot 10^{-4} K^{-1}$ [96], to change the effective index of the mode by inducing a temperature variation of ΔT into the waveguide core. The relation is linear, i.e, $\Delta n = \frac{dn}{dT}\Delta T$. At this purpose, a metallic heater can be placed on top of the resonator, optically isolated from the mode by hundreds of nanometers of cladding. When a current flows in it, the metal increases its temperature, and by conduction the heat flows through the cladding and reaches the waveguide core. For example, for correcting the effective index by 0.01, a temperature increase of the core of the order of $\sim 55\,K$ is required, which can be easily achieved using an Aluminium or a Titanium Nitride (TiN) metal stripe of less than $1\,\mu m^2$ of cross section and few mW of electrical power [82]. Since the sign of the thermo optic coefficient is positive, temperature tuning only acts in one direction. For realizing a wavelength shift in the opposite direction, free carrier injection can be used. When electrons and holes are injected into the Silicon core at concentrations above equilibrium, indicated as ΔN and ΔP respectively, both the refractive index n and the absorption coefficient α of the material change. The variations Δn and $\Delta\alpha$ are given by [97]:

$$\Delta n = \sigma^e_{FCD}\Delta N + \sigma^h_{FCD}\Delta P^{0.8} = -8.8 \cdot 10^{-22}\Delta N - 8.5 \cdot 10^{-18}\Delta P^{0.8} \tag{1.14}$$

$$\Delta \alpha = \sigma_{FCA}(\Delta N + \Delta P) = 1.45 \cdot 10^{-17}(\Delta N + \Delta P) \tag{1.15}$$

In the relations (1.13) and (1.15), the carrier concentrations have been expressed in cm^{-3}. For example, to change the refractive index of 0.01, an electron concentration of $\Delta N \sim 10^{19}\, cm^{-3}$ is required. A wide variety of geometries have been implemented to achieve this goal. One of the most popular and effective one consists in embedding a rib waveguide into the intrisinc region of a PIN diode, and by connecting the n and p regions to metal electrodes [98]. In this way, the optical mode propagates without significant attenuation, because it has negligible overlap with the highly doped regions (which are source of losses, as indicated by Eq.1.15). Thermal and free carrier effects are the most important and more effective tools for tuning the spectral response of resonators. Their main limitation relies on the fact that they are quite slow tuning mechanisms. Thermal effects have a slow dynamics because of the quite high heat capacity of Silicon and the very low thermal conductivity of the Silica cladding. Typically involved timescales lie in the μs range [96, 99]. Free carriers are limited by the recombination time, which is of the order of $500\, ps - 5\, ns$ for micron size Silicon waveguides [100, 101, 102], and by the charging and discharging of the junction and diffusion capacitances of the PIN diodes [103].

1.1.4.4 Applications of Silicon microresonators

Originally, microresonators have been conceived for WDM applications. The ability to send a specific set of wavelengths into the Drop port make resonators natural building blocks for filtering applications. The characteristics which are required to efficiently route different channels are a very high FSR, low insertion loss, steep roll off of the transmittance and high extinction. Typical values for C band telecom applications are tens of nanometers for the FSR, $\sim 0.2\, dB/GHz$ for the transmittance roll off, and $< -30\, dB$ for the extinction [72]. Usually, these requirements are too high to be fulfilled by a single resonator, so high order filters like CROWs or SCISSORs are implemented. The reader can refer to Ref.[103]for a state of the art review about this subject. Resonators can be organized in matrix of elements for bidirectional routers. An example is the one by D. Sherwood et. al., who demonstrated a 4×4 nonblocking Silicon optical router using thermo optic switching, with a footprint of $0.07\, mm^2$ [104]. Their design enabled bidirectional communications among the four input ports and the four output ports. Each communication path demonstrated a maximum extinction of $-20.79\, dB$ and a bandwidth of $38.5\, GHz$. The biggest, and most complex matrix router is the one developed within the project IRIS, and discussed at the beginning of the chapter, with more than 10^5 photonic components, 4 directions of operation and 48 WDM channels. Resonators are also the building blocks of optical modulators (discussed in Section 1.1.5) and laser cavities (discussed in Section 1.1.6).
Silicon resonators have been demonstrated to be very effective tools for sensing and biomolecule recognition. The optical mode inside the resonator evanescently extends into the cladding, where the target molecule/protein can be trapped by surface functionalization [105, 106]. The mode is then able to sense the external environment, and, as a consequence, its effective index is altered. From Eq.1.10, this implies a shift of the resonant wavelength, which constitutes the transduced signal. The shift is proportional to the amount of biomolecule that is trapped on the surface, so not only the concentration, but also the kinetics of the binding reaction can be tracked [107]. The parameters which quantify the performances of the sensor are the sensitivity and the limit of detection. The sensitivity S is defined as the nanometers of resonance shift as a consequence of a unit change of the refractive index (RIU). The limit of detection, LOD, is the minimum detectable refractive index shift, and is given by $LOD = \frac{3\sigma}{S}$, where $\sigma$is the uncertainty given by repeated

measurements of the same blank solution (when no analyte is present). A review on the state of the art of resonators for biosensing is given in Ref. [72].
Due to the ability of optical microresonators to enhance the power which is sent into the input waveguide, a wide variety of nonlinear optical phenomena have been demonstrated. Examples are wavelength conversion through Stimulated Four Wave Mixing (SFWM) [108, 109], optical frequency combs through Spontaneous FWM (sFWM) [110, 111, 112], optical parametric oscillators and amplifiers (OPO and OPA) [113, 114, 115]. Some of them are reviewed in Section 1.2. Nonlinearities associated to Two Photon Absorption (TPA) have been used for all optical switching[116, 117]. Thermal effects induced by nonlinear absorption, which drive the resonator into a bistable state, have been proposed for the realization of all optical memories [118]. Dynamical effects induced by the interplay of thermal and free carrier nonlinearities have been demonstrated to produce the self pulsing [96, 119, 120]of the transmitted signal or even chaos [99]. This part will be investigated in depth in Chapter 2.

1.1.5 Modulators

Modulators are used to convert an electrical signal into an optical one and vice versa. Through modulators, it is possible to encode data into the optical signal. Their working principle is depicted in Fig.1.21.

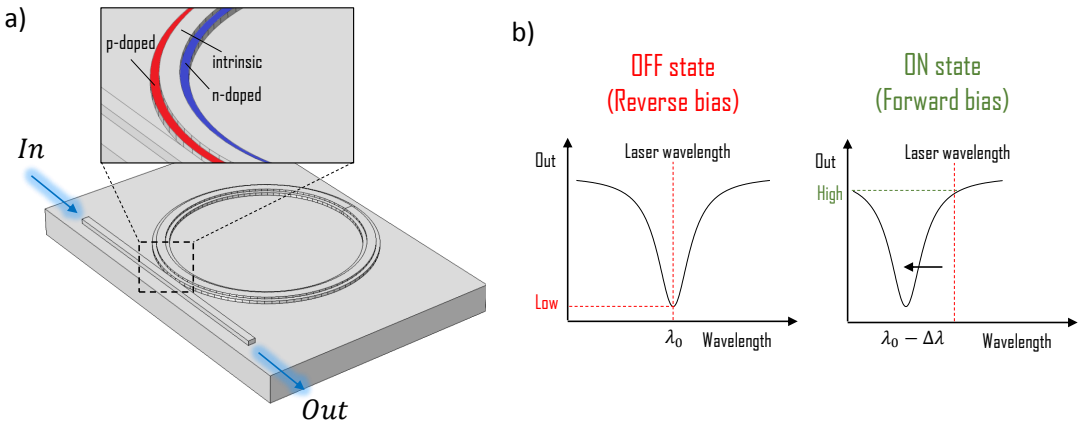

Figure 1.21: (a) Sketch of a ring resonator realized using a rib waveguide which embeds a PIN junction (shown in the inset). The input light is constant, while the output one depends on the bias of the junction. (b) Relative position of the resonant wavelength λ_0 and of the input laser wavelength in case of reverse and forward bias of the PIN junction. In the latter case, the injection of free carriers in the intrinsic region determines a shift of the resonance wavelength of $\Delta\lambda$.

The resonance wavelength of a microresonator, in this example an AP filter, is initially aligned with the carrier wavelength λ_0 of the WDM channel that has to be modulated (Fig.1.21(b)). The waveguide which forms the resonator is embedded into a PIN junction, which can inject carriers into the core when the junction is forward biased. When this occurs, the modal effective index changes through plasma carrier dispersion (see Eq.1.14), and the resonance position accordingly shifts by a quantity $\Delta\lambda$. The carrier wavelength is no longer on resonance, so the transmitted intensity switches from a low value to an high one. The voltage which forward bias the junction is applied until the bit is processed, and then the bias turns to off, waiting for the next bit. In this way, electrical bits, which are encoded in low/high state voltages, are transduced into the optical domain through high and low intensity signals. Needless to say, there has been a a steady growth of modulator designs through the years, with the attempt to lower the voltage and the power required to switch the modulator state. There are several figures of merit that are used to characterize a modulator: modulation

speed and depth, optical bandwidth, insertion loss, area efficiency (footprint) and power consumption. An excellent review on the state of the art of optical modulators is given in Ref.[103]. Basically, two big lines of research developed during the years. Both rely on plasma carrier dispersion, but the first class is based on carrier injection while the other one on carrier depletion. In general, modulators based on carrier injection have a very good extinction ($\sim -8\,dB$ at maximum operating speed), but low bandwidth ($\sim 10\,GHz$). The speed is mainly limited by the diffusion times of the carriers from the highly doped regions into the intrinsic one [103]. On the contraty, modulators based on carrier depletion have poor extinction ($\sim -1\,dB$ at maximum operating speed) but high bandwith ($\sim 30\,GHz$). In this class of modulators, the optical mode propagates in the junction region of a reverse biased PN diode, and the modulation is achieved by changing the depletion width of the juction. The extinction is limited by the amount of carriers which can be depleted between the on and the off states. State of the art modulators based on carrier accumulation are represented by the work of Liao et. al., in which it is reported $10\,Gbps$ operation with an extinction ration of $-3.8\,dB$ [121], and by Lightwire, which achieved the same bandwith but with the improved extinction ratio of $-9\,dB$ [122]. The fastest reported Silicon modulators are based on carrier depletion and are the ones of Liu et. al., which operates at $40\,Gbps$ [123], and the modulators of T.Baba et. al. [124] and D.Thomson et.al. [125], with $50\,Gbps$ operation.

1.1.6 Lasers and photodetectors

As introduced at the beginning of Chapter 1, one of the still open questions of Silicon Photonics is the lack of efficient monolithic laser sources, which could be easily integrated using the standard CMOS process flow. In fact, Silicon is a very good passive optical material, but, due its indirect bandgap, it is very inefficient for light emission, which are necessarily phonon mediated [25]. Different approaches to the problem have been afforded to overcome this intrinsic limitation. One of these is Stimulated Raman Scattering (SRS) [2, 126]. SRS relies on the interaction of photons with the optical phonons inside the material, which is described by the Raman contribution to the third order optical nonlinearity $\chi^{(3)}$ of Silicon [127]. A pump wave can be scattered by an optical phonon into two waves, called Stokes (or signal) and Anti-Stokes (or idler) waves. The spectral separation between the Stokes and the Anti-Stokes wave is determined by the energy and the wavevector of the involved phonon. If a signal wave is added to the pump, and tuned at the Stoke frequency, the material can exhibit a net gain at the idler frequency. By exploting this fact, Raman lasing on Silicon has been demonstrated in 2004 [128]. Recently, fivefold enhancement of the gain has been demonstrated in Silica waveguides which embeds Silicon nanoparticles [129]. However, lasers based on SRS require intense pump fields, which are naturally subject to TPA and Free Carrier Absorption (FCA) (both discussed in detail in Chapter 2), which are limiting the maximum gain [130]. Other approaches than SRS make use of epitaxial growth of III-V compounds on Silicon. Such materials have a direct bandgap, so they can be electrically pumped to obtain amplification and then lasing. One example are the on-chip $InGaAs$ nanopillar lasers reported by Chen et. al., which are grown efficiently on Silicon using the bottom-up self-organized technique [131]. The advantge of these nanopillars is that they can be integrated onto Silicon after a single growth step. In addition to III–V materials, Germanium also attracted increasing interest in making lasers on Silicon. Although Germanium is an indirect bandgap semiconductor, it has a direct bandgap at $0.8\,eV$, which is close to the indirect bandgap at $0.66\,eV$. The first Germanium on Silicon continuos wave laser, working at room temperature, was demonstrated by the MIT in 2010 [132]. Recent works towards more efficient Germanium lasers are mainly focused on bi-axially tensile strained quantum wells and quantum dots [133]. The applied strain has seen to reduce the size of the indirect bandgap faster than the direct one, and in generally it is believed that $1.7\% - 2.5\%$ of biaxial tensile strain will turn Germainium into a direct bandgap material [134]. Hybrid Silicon lasers also increased their popularity in the last few years [135]. These classes of lasers are

made by a complex combination of active III-V materials which are firstly fabricated on a separate substrate, more suited for the growth and deposition processes, and then bonded on the Silicon chip. The output coupler of the heterointegrated laser can be directly aligned to the input Silicon waveguide, or the laser cavity can be evanescently coupled to the latter [136].
Photodetectors for telecom applications have to be necessarily made by a different material than Silicon, since the latter is transparent at such wavelengths. Materials with lower bandgaps have to be grown on Silicon or bonded as it is made for lasers. Among these, Germanium based photodetectors played a primary role. This is due to their excellent optoelectronic properties: high responsivity from visible to near-infrared wavelengths, high bandwidths, and compatibility with CMOS technology. A comprehensive review on Germanium photodetectors is presented in Ref.[49].

1.2 Nonlinear Silicon Photonics

The nonlinear optical properties of any material are described by the fundamental relation between the macroscopic polarization P and the applied electric field E:

$$P = \epsilon_0(\chi^{(1)} \cdot \mathbf{E} + \chi^{(2)} \cdot \mathbf{EE} + \chi^{(3)} \cdot \mathbf{EEE} + ...) \tag{1.16}$$

where $\chi^{(j)}$ are tensors of rank $j+1$. Depending on the order of magnitude of the various terms, only some of them are significant for the problem considered. In general, $\chi^{(j+1)} < \chi^{(j)}$, but this is not an universal relation and strongly depends on the geometry of the unit cell of the material. For an extended class of materials, which are centrosymmetric, any susceptibility of even order vanishes due to symmetry considerations [137]. In such class of materials, each unit cell possess a geometrical point from which the whole lattice is invariant under the inversion operation, which accounts in inverting the position vectors of each atom from r to $-r$. This aspect will be covered in detail in Chapter 4. Silicon belongs to the class of centrosymmetric materials, so it has no native $\chi^{(2)}$. Since also $\chi^{(4)}$ vanishes, it comes out that the dominant nonlinearity is the third order non linear susceptibility $\chi^{(3)}$. The order of magnitude of the field polarization P due to the $\chi^{(3)}$ in bulk Silicon is $8.85{\cdot}10^{-30}\, Fm^{-1}$ [137] for an electric field of amplitude $1\, Vm^{-1}$, which is twenty orders of magnitude lower with respect to the one induced by the linear susceptibility $\chi^{(1)}$ ($\chi^{(1)} \approx 13$). It is worth to note that a $\chi^{(2)}$ can be induced in Silicon by breaking the centrosymmetry of the unit cell. This has been accomplished in many works by applying a strain gradient to the material [138, 139, 140, 141, 142]. Connected to that, chapter 4 is focused on the investigation of strain induced second order nonlinearities in strained Silicon waveguides. The large $\chi^{(3)}$ of Silicon enables several effects, like Self Phase Modulation (SPM), Cross Phase Modulation (XPM), Four Wave Mixing (FWM), Two Photon Absorption (TPA) and Stimulated Raman Scattering (SRS) [53, 127]. The interested reader can refer to Ref. [143] for a comprehensive review of each of these processes. Two key parameters, which quantify the strength of the nonlinear processes are the nonlinear coefficient γ and the Figure of Merit FOM. These are defined as:

$$\gamma = \frac{\omega n_2}{A_{eff}} \tag{1.17}$$

$$FOM = \frac{n_2}{\beta_{TPA}\lambda} \tag{1.18}$$

where n_2 is called the nonlinear index ($n = n_0 + n_2 I$, where n_0 is the low power refractive index and I the field intensity) and β_{TPA} the TPA coefficient ($\alpha = \alpha_0 + \beta_{TPA} I$, where α_0 is the low power attenuation constant). These are connected to the real and the imaginary part of the $\chi^{(3)}_{iiii}$ tensor element as [127]:

$$\chi^{(3)}_{iiii} = \frac{4}{3}\epsilon_0 n_2 n_0^2 c + i\frac{2}{3\omega}\beta_{TPA}\epsilon_0 n_0^2 c^2 \tag{1.19}$$

In writing Eq.1.19 it has been assumed that the i^{th} direction coincides with one of the equivalent directions [100], [010] or [001] of the Silicon unit cell. As it will be shown in Chapters 3 and 2, the n_2 coefficient is responsable for FWM (and in general for all the other $\chi^{(3)}$ effects listed above), while the β_{TPA} term is associated to nonlinear absorption. The FOM, which is proportional to their ratio, gives a method for comparing the performances of different nonlinear optical materials. A typical value for Silicon is ~ 0.4 at a wavelength of $\lambda = 1.55\,\mu m$ [144]. From Eq.1.17, it can be seen that the magnitude of nonlinear effects is inversely proportional to the modal effective area. The factor $\frac{1}{A_{eff}}$ is, on average, greater by a factor $100 - 1000$ with respect to the one in optical fibers [53, 143]. This is a direct consequence of the fact that the same power is confined to flow in a smaller core area than the one of optical fibers. The use of resonators can further reduce the power which is needed to activate nonlinearities because of their ability to enhance the stored field with respect to the exciting one. Power enhancements of 100 can be achieved using high Q cavities, corresponding to γ values which are 10^5 times greater than in optical fibers. Compactness and power enhancement make Silicon Photonics a very attractive platform for nonlinear optics applications. These are so many that they are subject of many review papers [53, 145, 143, 146]. Some examples, which will not be discussed here, include supercontinuum generation [147, 148], wavelength conversion [108, 109], optical parametric amplification and oscillation [113, 114, 115], Stimulated Raman Scattering [149, 150], frequency comb generation [111], optical soliton generation [151, 152] and third harmonic generation [153]. Most of the parametric processes cited above requires a phase matching condition to be satisfied in order to be efficient. For example, as demonstrated in Section 3.1, wavelength conversion from an idler wave at λ_i into a signal wave at λ_s through the use of a strong pump at λ_p occurs via FWM if the following phase matching relation is satisfied: $2\omega_p n(\omega_p) = \omega_s n(\omega_s) + \omega_i n(\omega_i)$ [2]. Waveguides fabricated on SOI can be easily engineered to tailor the effective index dispersion in order to fullfil this requirement [53]. The opportunity to control and precisely tune the geometric dispersion by engineering the waveguide cross section or shape, is one of the major advatages of using Silicon Photonics for parametric processes over bulk media.

In this thesis work, particular attention will be devoted to Four Wave Mixing. As discussed in Section 3.1, when FWM is stimulated by random vacuum fluctuations (Spontaneous FWM, or sFWM), it can produce pairs of energy-time entangled photons [154, 155, 156]. As detailed in the next section, these are nonclassical states of light which are of valuable interest for the emerging field of Quantum Silicon photonics.

The $\chi^{(2)}$ nonlinear optics of Silicon is quite a new field of research, which acquired increasingly growing attentions from the seminal paper of R.S.Jacobsen et.al. in 2006 [142]. The interests mainly lie on the possibility to promote Silicon as CMOS compatible electro optic material. The latter is the ability of a material to change its refractive index when a static electric field is applied. When this is induced by second order nonlinearities, it is referred as Pockels effect. The amount of index change is linear with the applied field, and what is most important, is instantaneous up to optical frequencies. This means that ultrafast optical modulators, with improved speed and power consumption with respect to the ones based on plasma carrier dispersion, can be implemented. The all Silicon modulators could replace the ones based on Lithium Niobate [31]. Methods for breaking the centrosymmetry of the Silicon unit cell mainly rely on the application of stressing materials, like Silicon Nitride, on the top of Silicon waveguides [139, 140]. As a consequence of the applied stress, a non uniform strain is induced in the crystal unit cell, and the inversion symmetry is removed. By doing that, Second Harmonic Generation (SHG) [157, 158, 159] and electro optic modulation [142, 139, 138] have been demonstrated , and some of the $\chi^{(2)}$ tensor elements have been extracted, with values ranging from $40\,pmV^{-1}$ at optical frequencies [157], to $336\,pmV^{-1}$ in static regime [138]. In parallel, lots of efforts have been dedicated to find a theoretical link between the strain distribution and the magnitude of the

$\chi^{(2)}$ components [160, 161]. Recent works, demonstrated that the injection of free carriers accumulated at the interfaces between Silicon and the straining material as a consequence of an applied voltage, significantly masks the electro optic modulation due to the Pockels effect [162, 163]. A method for distinguishing the two contributions has been implemented on the basis of the different timescales over which free carrier and $\chi^{(2)}$ nonlinearities act [79]. This work proved that, at DC regime, the value of the $\chi^{(2)}$ should lie below $(8 \pm 3)\, pmV^{-1}$ with $-0.48\, GPa$ of applied compressive strain in a $1.6\, \mu m \times 0.25\, \mu m$ cross section waveguide. Chapter 4 will present this method in detail.
The enabling of $\chi^{(2)}$ nonlinearities in Silicon is important also for quantum photonics applications. The process of Spontaneous Parametric Down Conversion (SPDC), which is mediated by $\chi^{(2)}$ nonlinearities, converts a pump photon at frequency ω_p into two energy-time entangled photons whose frequencies are simmetrically located with respect to the pump one [164, 165]. The produced quantum state has correlation properties which are very similar to the ones of the entangled state produced by sFWM. This aspect will be covered in depth in Chapter 5.

1.3 Quantum Silicon Photonics

It is a well know fact that quantum mechanical effects can dramatically improve the performance for certain tasks in communication, computation and measurement [166]. Of the various physical systems being pursued, single particles of light (photons) have been widely used in quantum communication [167], quantum metrology [168], and quantum lithography [169]. Photons are subjected to low decoherence effects, which means that once a quantum state is prepared, the statistical uncertaintly on the final state produced by stochastic interactions with the environment is very low [170, 171]. For this reason, photons are attractive quantum bits (or qubits), and they have emerged as a leading approach to quantum information processing. Although a number of photonic quantum circuits have been realized for quantum metrology [172, 173], lithography [174], quantum logic gates [175, 176], and other entangling circuits [177, 178], these demonstrations have relied on large-scale (bulk) optical elements bolted to large optical tables, thereby making them inherently unscalable. In the last few years, Silicon photonics has been proposed as the ideal platform for the realization of integrated quantum photonic circuits [171]. The latter are realized using the standard bulding blocks already implemented in ONoC, like waveguides and directional couplers, but which operate at the single photon level. Integration and light confinenement provide natural tools for subwavelength stability of the optical paths, complete mode overlap between interferring beams, and low propagation loss, which are the most challenging task for the realization of high visibility classical and quantum interference. Practically all the optical elements and the functionalities currently implemented in free space quantum photonic circuits can be integrated on a single chip, even if only a limited set, like quantum sources, beasmplitters and interferometers have been integrated at the same time. The first integrated quantum lightwave circuits have been demonstrated on the Silica On Silicon (SOS) platform, rather than on SOI [171]. Waveguides were patterned using standard photolithographic techniques on a Germanium and Boron Oxide doped Silica layer deposited by flame hydrolysis. With a refractive index contrast between the core and the cladding of $\sim 0.5\%$, single mode operation at a wavelength of $800\, nm$ was realized using waveguides with a cross section of $3.5\, \mu m \times 3.5\, \mu m$. The SOS platform was chosen because of the transparency at $800\, nm$, which lies in a spectral region where Silicon Avalanche Photodiode Single-Photon Counting Modules (SPCMs) have their peak efficiency ($\sim 70\%$). The first demonstrations, dated 2008, rely on Hong Ou Mandel (HOM) quantum interference with $(94.8 \pm 0.5)\%$ visibility, controlled-NOT quantum gates with an average logical basis fidelity of $(94.3 \pm 0.2)\%$ and a path-entangled state of two photons with fidelity $> 92\%$ [171] . Later, in 2009, J.C.F Matthews et. al. succesfully demonstrated multiphoton entanglement, and performed quantum metrology

experiments using two and four photon entrangled states [179]. The visibility of the two and four photon interference patterns were $(97.2 \pm 0.4)\%$ and $(92 \pm 4)\%$ respectively. Hong Ou Mandel interference with reconfigurable visibility up to $(98.2 \pm 0.9)\%$ has been also demonstrated using resistive elements for changing the phase of an interferometer.

The developement of increasingly bright quantum sources at $1.55\,\mu m$ from sFWM or from SPDC of $775\,nm$ pump photons allowed to promote Silicon has the core material of the waveguides. SOI wafers gradually replaced the SOS ones, and fully CMOS compatible quantum circuits were then fabricated. In 2013, J.W. Silverstone et. al. published a seminal work in which photon pairs produced by sFWM in two Silicon spiral sources were directly manipulated on the same chip to deterministically prepare quantum states of light [180]. By using a thermal heater to tune the phase of one of the two sources, one could choose wheater the output state is a split state, in which the photons travel into two different spatial modes, or a N00N state, in which both photons travel in the same spatial mode. Off chip HOM experiments were performed to test the degree of entanglement of the pair and the purity of the split state, yelding visibilities of the two photon interference fringes as high as $(100.0 \pm 0.4)\%$.

Chapter 2

Chaotic dynamics in coupled resonator sequences

In chapter 1, the thermo optic and the free carrier dispersion effects have been introduced as the main mechanisms which affect the spectral response of Silicon resonators. Strictly speaking, these do not belong to the class of linear effects. A shift in the refractive index induced by a change in temperature ΔT or by a change in the free carrier concentrion ΔN (for simplicity, assumed unipolar) is reflected in a perturbation of the linear susceptibility $\Delta\chi^{(1)}$ given by:

$$\Delta\chi^{(1)} = \Delta n_{th} + \Delta n_{FC} = 2n_0\frac{dn}{dT}\Delta T + 2n_0\sigma_{FC}\Delta N \tag{2.1}$$

where n_0 is the unperturbed refractive index, and $\sigma_{FC} = \sigma_{FCD} + i\frac{c}{2\omega}\sigma_{FCA}$ is the complex free carrier dispersion coefficient. The excess polarization $\Delta\mathbf{P}$ is then $\Delta\mathbf{P} = \epsilon_0\Delta\chi^{(1)}\mathbf{E}$, where $\mathbf{E}$ is the electric field. Thus, the relation between $\mathbf{P}$ and $\mathbf{E}$ is still linear, even in presence of thermal and free carrier effects. This is why they can not be classified as nonlinear effects. However, if the change in temperature or in the free carrier concentration is induced by the nonlinear material absorption, both ΔT and ΔN become dependent on the light intensity, and the relation between $\mathbf{P}$ and $\mathbf{E}$ becomes nonlinear [181]. Only in this case, it is possible to refer to thermal and free carrier nonlinearities. This fact can have important consequences on the dynamics of the field inside optical resonators, since a nonlinear dynamic is often associated with chaos and turbulence.

In this chapter, the impact of thermal and free carriers which are generated by TPA inside a chain of coupled resonators is investigated. It will be demonstrated, both theoretically and experimentally, that when the sequence of resonators is excited by a continuos wave pump beam, the intensity of the light at the output can become unstable in time, showing a periodic self pulsing or chaotic fluctuations. While the first dynamics can be observed even in single resonator, the latter is seen to be an effect of the coupling between several resonators. The chapter is divided as follows: in the first section, the theory of the field dynamics in single resonators under the action of thermal and free carrier nonlinearities is presented. Next, the experimental evidence of unstable regimes is presented for both single and coupled resonators, and their connection with the input exciting conditions is analyzed. In the rest of the chapter, the sensitivity of the system to small changes in the initial conditions is tested, and the shape of the phase space reconstructed. From these analyzes, the presence of chaotic instabilities are found. As a last step, it is investigated the possibility to engineer a simple system constituted by three coupled optical cavities, in order to tune the onset of chaotic oscillations by changing the device geometry.

The experiments described in this chapter have been done in collaboration with Dr. Mattia Mancinelli and Dr. Fernando Ramiro Manzano. Prof. Leonardo Ricci gave also an important contribution through helpful discussions and hints.

2.1 Theory of optical resonators under thermal and free carrier nonlinearities

As discussed in Section 1.1.4.3, the temperature and the free carrier concentration in a resonator can be altered through the use of heaters or PN junctions. However, as described above, these mechanisms do not break the linear relation between the polarization P and the electric field E. This can only be done if the temperature or the free carrier concentration are changed by nonlinear absorption. At a wavelength of $1.55\,\mu m$, the photon energy is $\sim 0.81\,eV$, which is less than the Silicon energy bandgap ($1.1\,eV$). Due to this fact, linear absorption, that is the direct creation of an electro-hole pair by the absorption of one photon, has vanishing probability. However, TPA, that is the simultaneous annihilation of two photons to promote the transition of an electron from the valence band to the conduction band, is not forbidden by energy conservation. As it will be shown later, TPA is a phenomenon which is mediated by the imaginary part of the $\chi^{(3)}$ of the material, and is only significant when the optical intensity circulating in a waveguide becomes of the order of the tens of mW [181, 96], a value easily achievable in an optical resonator. The energy diagram of the TPA process is sketched in Fig.2.1(b). When two photons at a wavelength of $1.55\,\mu m$ are simultaneously absorbed, the sum of their energies exceed the Silicon bandgap, but their momentum is not sufficient to perform the transition towards the conduction band. This is because the top of the valence band does not have the same crystal momentum as the bottom of the conduction band. The transition becomes possible if at the same time a phonon is created. The latter gives the required momentum to complete the transition. As a consequence, the TPA process simultaneously promotes the creation of electron/hole pairs and contributes to heat the material (phonons are created). The excess of carriers is itself a source of losses, a phenomenon known as Free Carrier Absorption (FCA). In this process, sketched in Fig.2.1(c), the absorption of a photon from an electron in the conduction band (or in the valence band) induces an intraband transition to the quasi-continuum of energy states at higher energies. As before, the transition requires the creation of phonons to conserve the momentum, and the temperature of the material raises.

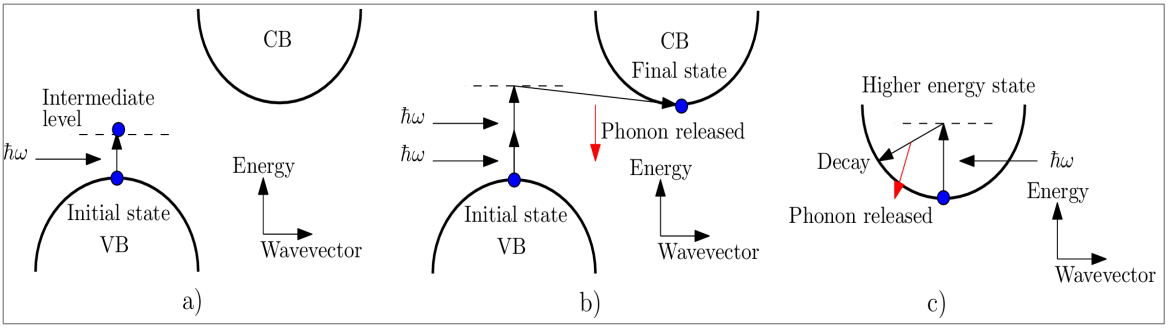

Figure 2.1: Different absorption mechanisms in Silicon at a wavelength of $1.55\,\mu m$. (a) Linear absorption is not allowed since the photon energy lies below the bandgap. (b) Two Photon Absorption. The energy of two photons is used to overcome the energy gap, while the creation of a phonon allows to acquire the momentum necessary to complete the transition toward the conduction band. (c) Free Carrier Absorption. An electron in the conduction band absorbs a photon with the simultaneous excitation of a phonon. The same process can occur for an electron in the valence band.

In the next section, it is derived the equation of motion of the field inside an optical resonator under the action of temperature and free carrier induced refractive index changes. The latter are caused by the field itself through TPA and FCA. A full and more general derivation of the equation of motion is given in Appendix A.

2.1.1 Equation of motion for the field

In what follows, the resonator is assumed to have a cylindrical symmetry. Without losing of generality, the latter will be assumed to be a ring resonator of perimeter L. The j^{th} eigenfrequency relative to the m^{th} spatial mode (indicated as ω_{mj}) satisfies the equation:

$$\left(\nabla^2 + \omega_{mj}^2 \frac{n^2(\mathbf{r})}{c^2}\right) \tilde{\mathbf{u}}_{mj}(\mathbf{r}) = 0 \tag{2.2}$$

which is the Helmoltz equation in absence of material nonlinearites [182, 183] . In Eq.2.2, $\tilde{\mathbf{u}}_{mj}(r)$ is the modal electric field distribution associated to the eigenfrequency ω_{mj}, while $n(\mathbf{r})$ is the refractive index of the whole structure. In the experiments described later, the resonator supports only the fundamental spatial mode, and the coupling between different eigenfrequencies will not be considered. The opposite situation will be considered in Chapter 6. In this case, it is possible to remove all the subscripts from both ω_{mj} and $\mathbf{u}_{mj}$, and write them as simply ω and $\mathbf{u}$. The total electric field $\mathbf{E}$, which is solution of Eq.2.2, can be written as:

$$\mathbf{E}(\mathbf{r}, t) = \frac{1}{2} A_0 \mathbf{u}(\mathbf{r}) e^{i\omega t} + c.c \tag{2.3}$$

where A_0 is a constant amplitude. In order to simplify further, the field is assumed to be polarized mainly in one direction of space, so Eq.2.2 is reduced to a scalar equation.
When a nonlinear polarization δP^{NL} is induced as a consequence of the material nonlinearities, and at the same time a refractive index change $\Delta n = \Delta n_{th} + \Delta n_{fc}$ occurs due to thermal and free carrier effects (described by a change in the linear polarization δP^L), the unperturbed field of Eq.2.3 is no more solution of the (now) nonlinear wave equation [182, 183]. If the perturbation is small, it is possible to assume that only the amplitude A_0 is altered in the new solution, and replace it with a slowly varying envelope $A(t)$. The latter has the property that $\frac{d^2A(t)}{dt^2} \ll \omega^2 A$. Using this approximation, the equation of motion for the modal amplitude $A(t)$ reduces to (see Appendix A):

$$\frac{dA(t)}{dt} = \frac{i\mu_0 c^2}{\omega} e^{-i\omega t} \frac{\partial^2}{\partial^2 t} \int u_q^*(\mathbf{r}) \left(\delta P^L + \delta P^{NL}\right) d\mathbf{r} \tag{2.4}$$

where $\delta P^{NL}(\mathbf{r}, t)$ and $\delta P^L(\mathbf{r}, t)$ are given by:

$$\delta P^L = 2\epsilon_0 n_0 (\Delta n_{th} + \Delta n_{fc})(E + c.c) \tag{2.5}$$

$$\delta P^{NL} = \frac{3}{8} \epsilon_0 \chi^{(3)} |E|^2 E \tag{2.6}$$

In writing Eq.2.6, the value of the $\chi^{(3)}$ is an average of the projected tensor components along the radial direction. Eq.2.4 can be rewritten in terms of the total energy $U_{int} = |u_{int}|^2$ stored inside the resonator by using the fact that (see Appendix A):

$$u_{int} = \sqrt{\frac{\epsilon_0}{2}} A(t) \tag{2.7}$$

By inserting the expression for δP^L and δP^{NL} in Eq.2.4, and by including the fact that the resonator is excited from an external bus waveguide with an energy exchange rate η , one obtains (see Appendix A for

the full derivation):

$$\frac{d\tilde{u}_{int}}{dt} = i\left[\omega(1-\Delta(t)) - \omega_p\right]\tilde{u}_{int} - \frac{\tilde{u}_{int}}{\tau_{tot}(t)} + i\sqrt{\frac{2}{\tau_{ext}}}P_0 \tag{2.8}$$

in which the internal energy amplitude has been expressed in terms of a slowly varying envelope $\tilde{u}_{int}$ and a carrier term $e^{i(\omega-\omega_p)}$ as $u_{int}(t) = \tilde{u}_{int}(t)e^{-(\omega_p-\omega)t}$. In Eq. 2.8, $|P_0|^2$ is the power of the incident laser, which has a frequency ω_p. The most important quantity in Eq.2.8 is the frequency perturbation $\Delta(t)$, which is given by:

$$\Delta(t) = \frac{\sigma_{FCD}}{n_0}\bar{\Delta N} + \frac{1}{n_0}\frac{dn}{dT}\bar{\Delta T} + \gamma^R|u_{int}(t)|^2 \tag{2.9}$$

The definitions of $\bar{\Delta N}$,$\bar{\Delta T}$,τ_{tot}, τ_{ext} and γ^R can be found in Appendix A.
It can be noticed that Eq.2.8 is the energy equation of a damped harmonic oscillator of fundamental frequency ω that is perturbed in time by a quantity $\Delta(t)$. The latter is the sum of three contributions: a thermal induced resonance shift, a free carrier based resonance shift and a Kerr shift [184, 99, 82]. The oscillator is driven by an external force at frequency ω_p , and has a variable decay time τ_{tot}. An efficient coupling of energy into the cavity is then possible only when the exciting frequency ω_p is close to $\omega(1-\Delta(t))$. If one neglects the contribution of thermal, free carrier, and TPA effects, and solve Eq.2.8 for a steady state solution $\tilde{u}_{int}(t) = \tilde{u}_{int0}$, one gets:

$$\tilde{u}_{int0} = \frac{-i\sqrt{\frac{2}{\tau_{ext}}}P_0}{i(\omega-\omega_p) - \frac{2}{\tau_{ext}}} \tag{2.10}$$

The modulus square of the expression above, which gives the total stored energy $U_{int} = |\tilde{u}_{int}|^2$, then reads:

$$U_{int} = \frac{\frac{2}{\tau_{ext}}|P_0|^2}{(\omega-\omega_p)^2 + \left(\frac{2}{\tau_{ext}}\right)^2} \tag{2.11}$$

which is the lorentzian lineshape of the resonance. In the denominator, one can indentify $\frac{1}{\tau_{ext}}$ as the FWHM of the resonance, from which the quality factor is given by $Q = \frac{\omega}{FWHM} = \omega\tau_{ext}$. Eq.2.8 depends on $\bar{\Delta N}$ and $\bar{\Delta T}$, so it can not be solved if the temperature and the free carrier dynamics inside the resonator is not known. This is why two additional equations have to be provided. This is the subject of the next section.

2.1.2 Rate equations for the carriers and temperature

Let's concentrate first on free carriers. These are created by TPA, so their generation rate G_{TPA} will be given by the power per unit time absorbed by TPA divided by $2\hbar\omega$. Once a concetration ΔN is created above equilibrium, the recombination process takes place to restore the initial concentration. The timescales at which recombination acts is strongly dependent on the waveguide geometry, the quality of the interfaces and the doping of the material. For Silicon nanowires with submicron dimensions, free carriers lifetimes are typically of the order of $\tau_r = 500\,ps - 1\,ns$ [100, 101, 102]. The equilibrium concentration when simultaneously TPA and recombination act will be the result of the balance between the two. In appendix A, the rate equation is derived, which yields:

$$\frac{d\bar{\Delta N}(t)}{dt} = -\frac{\Delta\bar{N}(t)}{\tau_r} + G_{TPA}(t) \tag{2.12}$$

where the generation rate G_{TPA} is given by:

$$G_{TPA}(t) = \frac{c^2 \beta_{TPA} \Gamma_{FCA}}{n_0^2 (2\hbar\omega) V_{FCA}^2} |\tilde{u}_{int}(t)|^4 \tag{2.13}$$

The carrier confinement factor Γ_{FCA} and the FCA effective volume V_{FCA} are defined as:

$$\Gamma_{FCA} = \frac{\int_{wg} n(r,z)^6 |u(r,z)|^6 \, dr dz}{\int n(r,z)^6 |u(r,z)|^6 \, dr dz}; \qquad V_{FCA}^2 = \frac{L^2 \left(\int n(r,z)^2 |u(r,z)|^2 \, dr dz \right)^3}{\int n(r,z)^6 |u(r,z)|^6 \, dr dz} \tag{2.14}$$

The quartic dependence of G_{TPA} on the internal energy amplitude $\tilde{u}_{int}$ means that free carriers are mainly generated when the optical power circulating in the resonator is high. This happens only when the input laser frequency is very close to the resonance frequency.

A similar equation as the one of Eq.2.12 can be derived for the temperature dynamics. All the power which is absorbed by the material contributes to raise its temperature. Different contributions to the total absorbed power come from TPA (P_{TPA}) and FCA (P_{FCA}). At the same time, the thermal energy of the resonator can decay into the surrounding medium through conduction at the interfaces. The characteristic time scale τ_{th} at which this occurs, depends on the geometry of the resonator and on the materials. The balance between the absorbed power and the dissipated one governs the dynamics of the temperature, which can be demonstrated (see Appendix A) to be given by:

$$\frac{d\Delta T}{dt} = -\frac{\Delta T}{\tau_{th}} + \frac{P_{TPA} + P_{FCA}}{M_{res} c_p} \tag{2.15}$$

where M_{res} is the mass of the resonator and c_p is the specific heat at constant pressure. The expressions for the absorbed powers P_{TPA} and P_{FCA} are given by:

$$P_{TPA} = \frac{\beta_{TPA} c^2}{n_0 V_{TPA}} |\tilde{u}_{int}|^4 \tag{2.16}$$

$$P_{FCA} = \frac{\sigma_{FCA} c |\tilde{u}_{int}|^2 \bar{\Delta N}}{2 n_0} \tag{2.17}$$

with the TPA effective volume defined as:

$$\frac{1}{V_{TPA}} = \frac{\int_{wg} n^4(r,z) |u(r,z)|^4 \, dr dz}{L \left(\int n^2(r,z) |u(r,z)|^2 \, dr dz \right)^2} \tag{2.18}$$

In deriving Eq.2.15, the temperature profile has been assumed constant inside the waveguide core. This is a good approximation since Silicon has an high thermal conductivity with respect to the Silica cladding. The assumption of a constant profile allows to write $\bar{\Delta T} = \Gamma \Delta T$, where the confinement factor Γ is defined in Eq.1.2.

From the analysis of the above equations, it comes out that temperature and free carrier variations are maximized when the ratio between the optical energy and the effective modal volumes (V_{FCA} and V_{TPA}) is high. This is why thermal and free carrier nonlinearities are enhanced in high Q resonators, where the optical energy is confined in small modal volumes.

2.1.3 Qualitative discussion of the solutions of the field equation

The field equation in (2.8) can be solved together with the temperature and the free carrier equations (2.15) and (2.12) provided that a set of initial conditions is given. Depending on the relative orders of magnitude between the time decay constants $\tau_{ext}, \tau_{th}, \tau_r$, the frequency of the input laser and the modal volume of the resonator, Eq.2.8 can have a wide variety of solutions. The stability analysis of the latter has been

widely investigated in the literature [120, 82, 185], so it will not be performed here. In this section, only the qualitative features of the solutions are discussed.
As a first step, the different types of solutions of Eq.2.8 can be roughly classified on the basis of the position of the input laser frequency ω_p with respect to the resonance frequency ω. This is schematically shown in Fig.2.2.

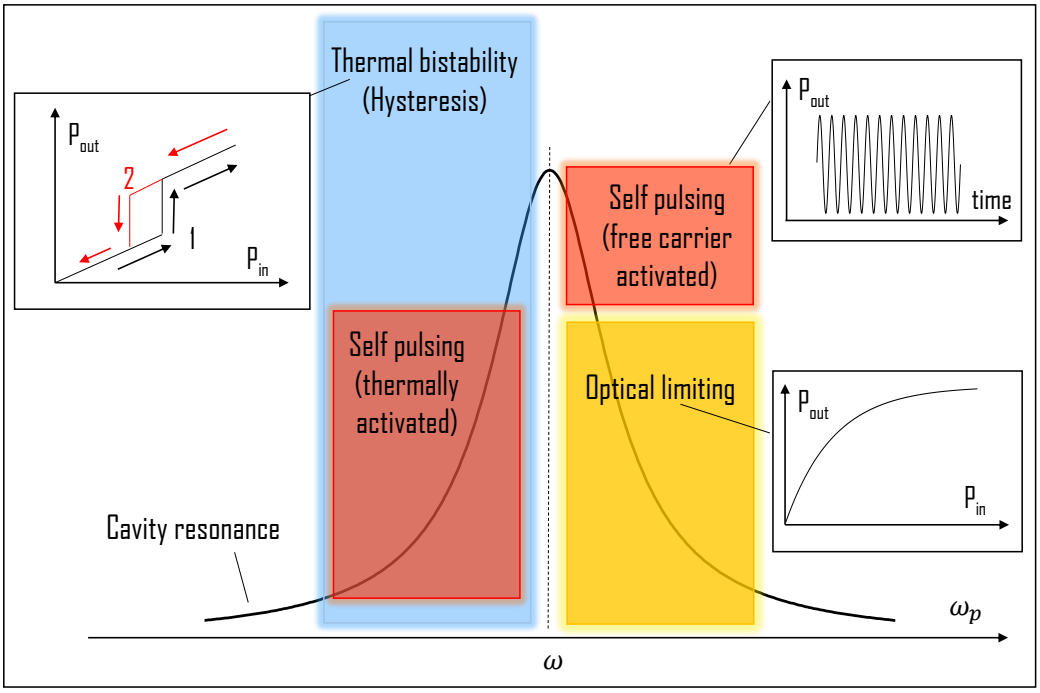

Figure 2.2: The different regimes that can be observed in a resonator under thermal and free carrier nonlinearities as a function of the input laser frequency ω_p. At $\omega_p < \omega$, thermal bistability and self pulsing occur. The corresponding inset shows the hysteresis loop connected to thermal bisability. At $\omega_p > \omega$, the two regimes are optical limiting and self pulsing. In all the cases, the solution choosen by the system depends on the cavity geometry and on the input power and wavelength conditions.

If ω_p lies within the FWHM of the resonance, and on the blue side of ω ($\omega < \omega_p$), Eq.2.8 can have three solutions: a stable, a bistable and an unstable one. The stable solution is found at low input powers, where the device response is linear. The bistable and self pulsing ones manifest at higher powers, since they are the result of a nonlinear regime. The type of solution which is enstablished depends on different factors, which include the ratio between the quality factor Q and the modal volume V_{eff}, the input laser wavelength and the input pump power. In general, if $\frac{Q}{V_{eff}}$ is sufficiently high, a thermal bistability creates the initial conditions which are necessary for activating the self pulsing regime, otherwise only a bistable behaviour is registered. Here, sufficiently high means that the field enhancement factor should be enough to generate a number of free carriers which is capable to activate, after the thermal bistability, a subsequent free carrier bistability, as it will be discussed in Section2.2. In the bistable regime, the output is always constant in time but an hysteresis cycle is exhibited as the pump power is increased and decreased (see corresponsind inset in Fig.2.2). Optical bistability is a direct manifestation of the thermo optic effect: consider for example a ring resonator in AD conguration, and a frequency that initially is smaller than the resonance frequency; when the input power is increased, the optical intensity in the resonator begins to grow, heating the material through TPA. This decreases the spectral distance $\omega - \omega_p$, since the correction Δ of Eq.2.9 is negative. In other words, the resonance frequency is pushed toward the one of the pump. A consequent enhancement of the internal

energy occurs, which in turn heats further the resonator. When the input power reaches a threshold, this leads to a positive feedback mechanism that makes the resonance locking with the laser frequency (slightly red detuned), determining a steep increase of the transmission intensity (point 1 in the inset of Fig.2.2). At this point a further increase of the input power no longer leads to a positive feedback, so the output power will again increase linearly with the input one. Then, when the input power is reduced, the transmitted intensity decreases linearly up to a second threshold (point (2) in Fig.2.2). This is due to the fact that on the right shoulder of the resonance, the feedback between the input power reduction and the internal energy is negative. At the same input power the internal energy is now higher than it was at point 1, because the resonator frequency is locked to the one of the laser. The negative feedback turns to positive at point 2, where a steep decrease of the transmitted signal is observed and the original path is recovered, closing the hysteresis loop. It is worth to note that a thermal hysteresis loop can only occur if at the beginning $\omega < \omega_p$, becuse it is the only condition to achieve a positive feedback. The threshold power at point (1) in the hysteresis loop depends on the initial spectral distance $|\omega_p - \omega|$. The more the spectral distance is increased, the higher is the threshold power. This is because as $|\omega_p - \omega|$ increases, a larger resonance shift (i.e. higher temperature) is needed to lock the resonance to the input wavelength.
If the laser frequency ω_p is initially tuned on the red side ($\omega > \omega_p$), Eq.2.8 still has three different solutions. One solution is stable, one is associated to optical limiting and the other one to self pulsing. The type of regime which is entablished depends on the same factors which regulates the boundary between thermal bistability and thermally induced self pulsing. In the optical limiting regime, as the input power is increased, thermal effects dominate, with the result that the spectral distance $\omega - \omega_p$ increases. This in turn decreases the Drop transmittance at the laser frequency (see inset which corresponds to optical limiting in Fig.2.2). It comes out that after a first linear increase of the transmitted power, the latter saturates to a constant value due to the continuos decrease of the transmittance at the laser frequency. The probability of activating a self pulsing regime when $\omega > \omega_p$ is much lower than in the opposite case. This is because, as it will be discussed in the next section, the activation of self pulsing requires a free carrier bistability. However, thermal effects are stronger than free carrier ones, so if $\omega > \omega_p$ they will more likely set the system into the optical limiting regime. In contrast to optical limiting and thermal bistability, in which the output power is constant in time, the self pulsing regime is characterized by a periodic modulation of the transmitted intensity.

2.2 Hysteresis, optical limiting and self pulsing of a single cavity

In this section, the self pulsing of a single cavity is firstly introduced from an experimental point of view. Then, the behaviour will be interpreted using the theoretical model developed in Section 2.1. The use of the model will be essential for connecting the time varying shape of the transmitted power to the internal dynamics of carriers and temperature. At first, the different regimes which are solution of Eq.2.8 are validated by the experiment. Since only the self pulsing regime will be of interest for the following sections, the hysteretic behaviour and the optical limiting one will be briefly covered and not discussed in detail.
The resonator under test is shown in the inset of Fig.2.3. The ring is made by a bent waveguide with a width of $500\,nm$ and a inner radius of $7\,\mu m$. The resonator is realized on the SOI platform using $193\,nm$ DUV lithography by CEA Leti [186]. The thickness of the Silicon layer is $220\,nm$, while the lower and upper SiO_2 cladding have a thickness of $1.5\,\mu m$ and $750\,nm$ respectively. The ring geometry is an AD configuration. Two $500\,nm$ wide bus waveguides are evanescently coupled to the ring by means of a $160\,nm$ gap. The time and spectral response of the resonator are investigated using the setup shown in Fig.2.3.

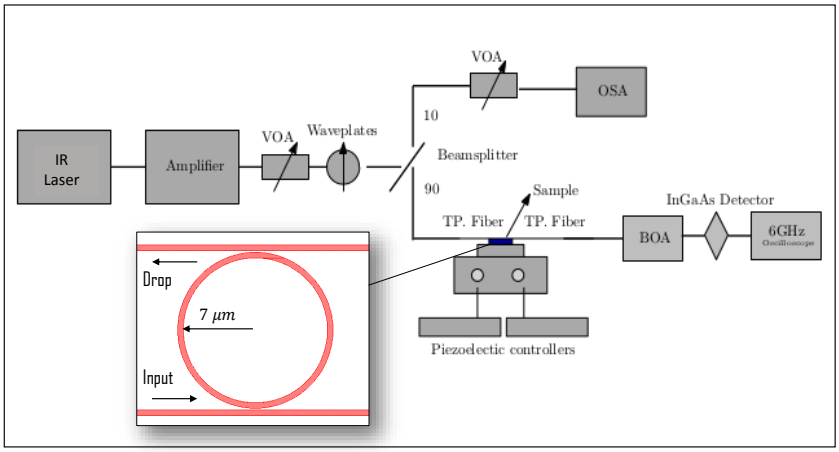

Figure 2.3: Sketch of the experimental setup used to investigate the different regimes shown in Fig.2.2. The geometry of the resonator is shown in the inset.

A tunable infrared laser of $10\,dBm$ of maximum output power is fiber coupled to an Erbium Doped Fiber Amplifier (EDFA), which can deliver more than $30\,dBm$ of power. The output of the EDFA is sent to a variable optical attenuator (VOA). A polarization controller sets the polarization to TE. The input signal is then split by a fiber beamsplitter: 10% goes to an Optical Spectrum Analyzer (OSA) which gives a feedback on the input power, while 90% goes to the sample. The coupling of light to the sample is made by using a tapered lensed fiber of $2\,\mu m$ tip width and $16\,\mu m$ of working distance. To minimize the coupling losses, a micrometric XYZ alignment stage is used. The fine tuning of the alignment is done using piezoelectric controllers. The whole coupling is monitored by an Infra-Red camera. A lensed fiber collectes the light from the output, which is amplified by $28\,dB$ using a Booster Optical Amplifier (BOA) before feeding a photodiode. The latter has a bandwidth of $1\,GHz$. The output of the photodiode is monitored in time using an oscilloscope with more than $40\,GHz$ of bandiwidth. As shown in Fig.2.4, the hysteretic regime is investigated by tuning the laser wavelength at $\lambda_p = 1549.72\,nm$, at $+60\,pm$ of spectral distance with respect to the selected resonance order (centered at $\lambda_0 = 1549.66\,nm$ and with $Q \approx 10800$).

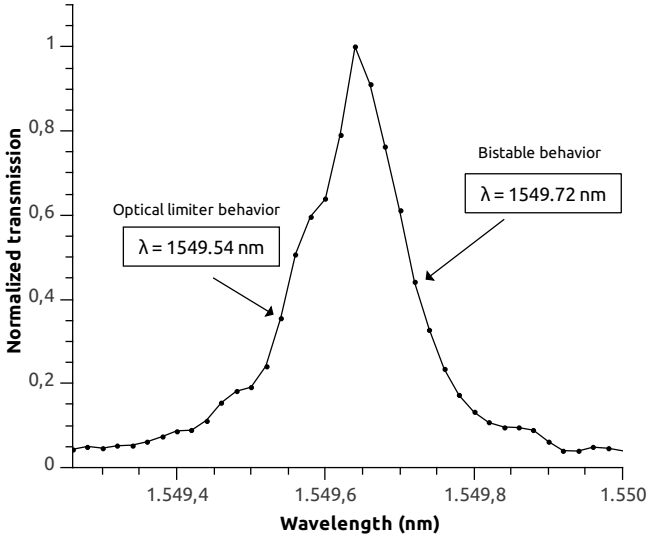

Figure 2.4: Normalized drop spectral response of the resonator at the resonance under test. The arrows indicate the wavelengths of the input laser where the bistable and the optical limiting regimes are investigated.

Using the VOA, and $\lambda_p = 1549.72\,nm$, the pump power is slowly increased from $0\,mW$ to $1.5\,mW$ (effectively coupled into the waveguide), and the output power in the drop port is monitored. As it can be seen from Fig.2.5, when the power is raised (black curve) the bistability occurs nearly at $0.7\,mW$, and is manifested by the steep increase of the transmitted power. The hysteretic behaviour is evidenced by the fact that the jump in the transmittance occurs at a lower power than before ($\approx 0.6\,mW$), when the power is successively decreased (red curve), The black and the red curves in Fig.2.5 do overlap, a part between $0.6\,mW$ and $0.7\,mW$ where two stable states are allowed, one at low transmitted power and the other one at high transmitted power.

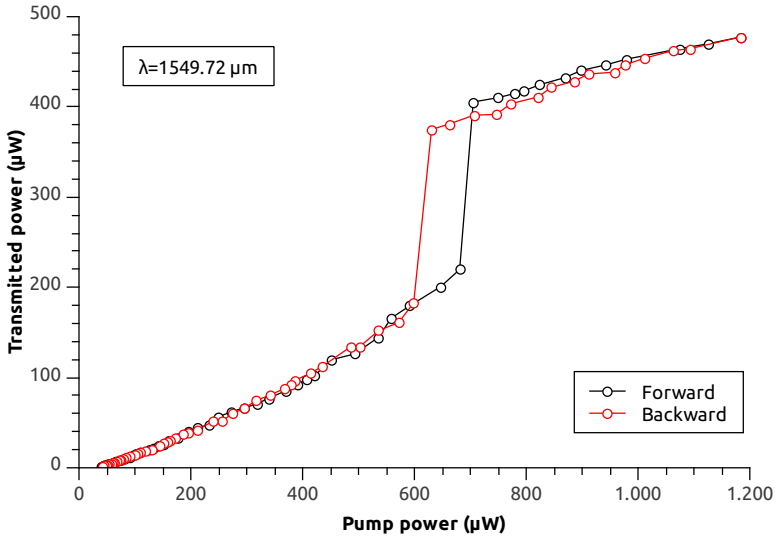

Figure 2.5: The hysteresis loop found when the input laser wavelength is tuned at $\lambda_p = 1549.72\,nm$, which is at $+60\,pm$ of spectral distance with respect to the selected resonance order. The black line indicates the transmitted power in the Drop port when the input power is raised. The red line indicated the transmitted power in the Drop port when the input power is decreased.

The system is then bistable, and sets to one or to the other state depending on the history, which would allow realizing all optical memories [118]. The optical limiting regime is observed when the laser wavelength is tuned at $\lambda_p = 1549.54\,nm$, at $-120\,pm$ from the resonance. As it can be noticed from Fig.2.6, as the input power is increased, the transmitted power initially grows linearly, but after a certain threshold of about $0.2\,mW$, it saturates to a constant value.

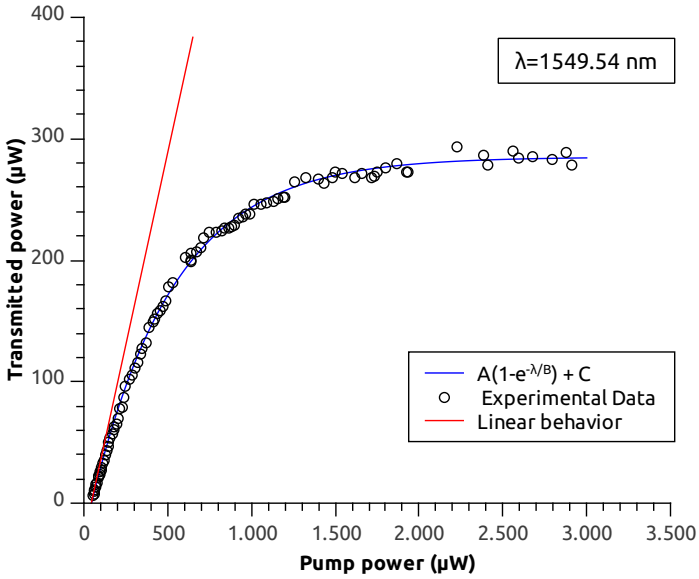

Figure 2.6: The cavity in the optical limiting regime: the solid red curve is added to show the linear regime, and its tangent to the blue curve at zero pump power. The blue curve is fittted on experimental data using the function $a(1-e^{-\frac{x}{b}})+c$, in which $a=(3.13\pm0.03)\cdot10^2\,\mu W$, $b=(4.94\pm0.06)\cdot10^2\,\mu W$, $c=(-28\pm1)\,\mu W$.

It is worth to note that in both the optical limiting regime and in the hysteretic one, the time trace recorded at the output of the photodiode is constant in time. This is not the case for the self pulsing regime, which is registered at $\lambda_p = 1549.84\,nm$. As shown in Fig.2.7, the transmitted intensity is periodically modulated in time, even if the input laser is continuous wave. The period and the shape of the oscillations depend on the level of the input power. As the latter is raised, the period grows.

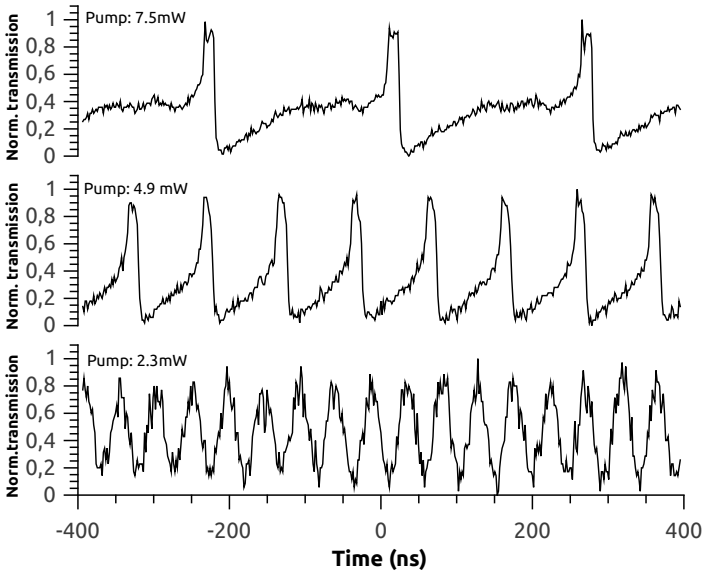

Figure 2.7: Power tuning of the oscillation period at fixed wavelength, in this case $\lambda_p = 1549.6\,nm$. The period and the shape of the oscillations become progressively similar to a sinusoid as the power is decreased.

In Fig.2.8, it is analyzed in detail the shape of a single period of oscillation, from which four different features emerged. These are labelled from (i) to (iv), and are characterized by different shapes and time scales.

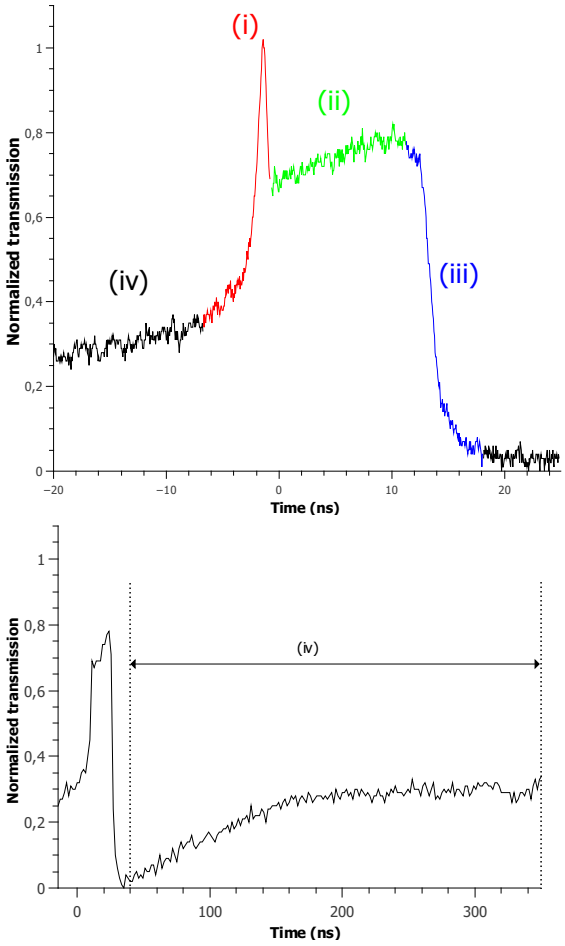

Figure 2.8: The period of the waveform is divided in four distinct regions (from (i) to (iv)). Each of these corresponds to a different physical process, as described in the text.

In order to understand the physical mechanisms which are responsable of self pulsing, the system is simulated through Eq.2.8 by using parameters which are as close as possible to the ones of the experiment. Fig.2.9 shows a comparison between simulation and experiment, and Table 2.1 summarizes the parameters of the simulation.

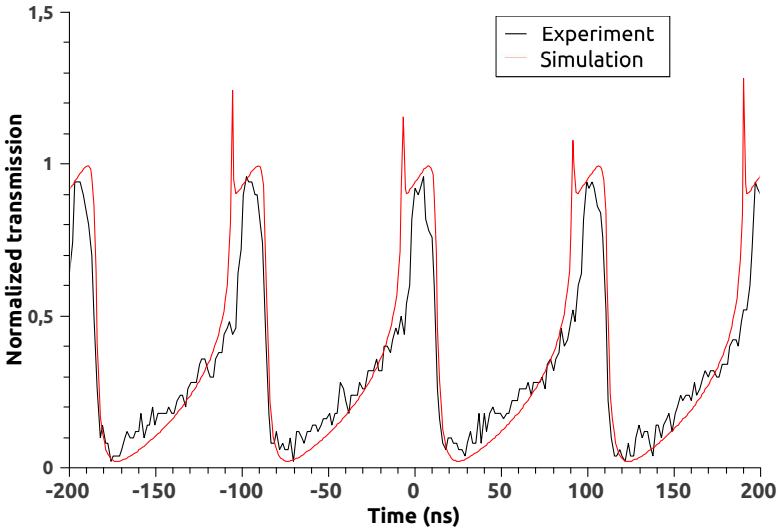

Figure 2.9: Comparison between theory and experiment when the cavity is in the self pulsing regime. The red curve is obtained from the numerical integration of Eqs.2.12, 2.15, 2.8 using the parameters listed in Table 2.1.

Parameter	Value	Source	Unit
$1/\tau_{ext}$	(51 ± 2)	Experiment	GHz
$1/\tau_0$	(0.33 ± 0.10)	Experiment	GHz
$\frac{dn}{dT}$	$1.86 \cdot 10^{-4}$	[96]	K^{-1}
σ_{FCD}	$-1.73 \cdot 10^{-27}$	[96]	m^3
σ_{FCA}	$1.1 \cdot 10^{-15}$	[96]	m^2
β_{TPA}	$0.79 \cdot 10^{-11}$	[187]	$\frac{m}{W}$
n_2	$0.45 \cdot 10^{-17}$	[187]	$\frac{m^2}{W}$
Γ_{FCA}	0.99	FEM simulation	-
Γ	0.92	FEM simulation	-
n_0	3.485	[96]	-
V_{FCA}	5.331	FEM simulation	μm^3
V_{eff}	4.34	FEM simulation	μm^3
M_{res}	$1.013 \cdot 10^{-11}$	Experiment	g
c_p	0.7	[96]	$\frac{J}{gK}$
$\frac{1}{\tau_{th}}$	7.5	Fit	MHz
$\lvert P_0\rvert^2$ (exp.)	(4.92 ± 0.01)	Experiment	mW
$\lvert P_0\rvert^2$ (sim.)	4.92	Fit	mW
$\frac{1}{\tau_{fc}}$	250	Fit	MHz
λ_p (simulation)	$1550\,nm$	Fit	nm
λ_p (experiment)	$(1549.84 \pm 0.01)\,nm$	Experiment	nm
λ_0	$(1549.66 \pm 0.01)\,nm$	Experiment	nm

Table 2.1: Parameters used in the numerical integration of Eq.2.12,2.15 and 2.8.

From the analysis of the temperature and of the free carrier dynamics shown in Fig.2.10(a), and from the corresponding induced resonance shifts with respect to the input wavelength (Fig.2.10(b)), it is now possible to identify the origin of the unstable regime and associate each of the four regions in Fig.2.8 to a specific physical situation.

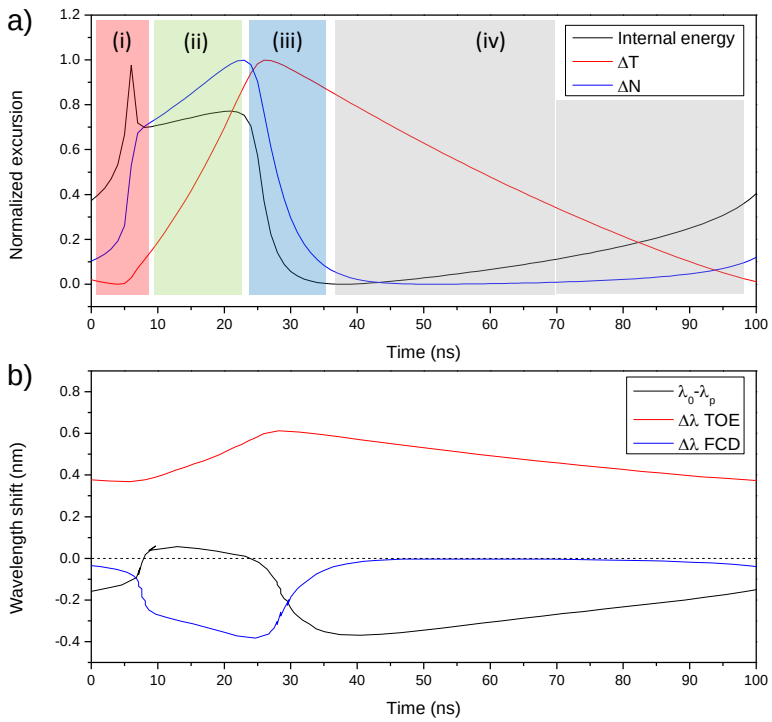

Figure 2.10: (a) Normalized energy amplitude U_{int} (black curve), temperature variation ΔT (red curve) and free carrier concentration ΔN (blue curve) during an oscillation cycle. The ranges of variation are $[3 \div 57]\, fJ$ for U_{int} , $[5 \div 8.3]\, K$ for ΔT and $[5 \cdot 10^{15} \div 5.6 \cdot 10^{17}]\, cm^{-3}$ for ΔN. Regions from (i) to (iv) in the coloured rectangles have the same meaning of the ones in Fig.2.8. (b) Total detuning (black) of the resonance wavelength λ_0 with respect to the one of the input pump λ_p, decomposed into the thermo optic (red) and into the free carrier (blue) induced resonance wavelength shifts $\Delta\lambda_{TOE}$ and $\Delta\lambda_{FCD}$ respectively. The total detuning is the sum of the initial detuning, the thermo optic contribution and the free carrier contribution.

Region (i): the resonance is initially slightly red detuned from the input wavelength, and a large number of free carriers are generated through TPA due to the high internal energy density, determining a blue shift of the resonance and a consequent free carrier bistability. The temperature grows at slower rate, making the free carrier dispersion dominating at this stage. This process continues until the resonance is slightly blue detuned from the input wavelength. At this point, the positive feedback that achieved bistability turns to negative. The result of these steps is a first steep increase of the Drop transmitted intensity, followed by a smaller rapid reduction when the maximum of the transmittivity is passed.

Region (ii): at this stage, the resonance wavelength is blue detuned with respect to the one of the input laser, a condition which is favorable for thermal bistability. Thus, when the slow increase in temperature is sufficient to activate a positive feedback mechanism, the resonance red shifts toward the input wavelength, crossing the resonance peak and increasing again the transmittivity.

Region (iii): Once the resonance peak has crossed the input wavelength, the decrease of the internal energy causes a fast decay of the free carrier population which further pushes away the peak, determining a steep decrease in transmission and a large residual detuning.

Region (iv): Temperature now slowly decreases, and a consequent blue shift of the resonance is achieved, until it is so close to the pump wavelength that the oscillation starts again.

The involved time scales are $\sim 6\, ns$ for the fast increase in the transmission of region (i), then $\sim 12\, ns$ for region (ii), $\sim 6\, ns$ for region (iii) and $\sim 32\, ns$ for region (iv).

Even if in the above description the cycle starts when the resonance wavelength is slightly red detuned with respect to the input wavelength, this does not correspond to the true experimental situation. In fact, as it

can be noticed in Table 2.1, $\lambda_p > \lambda_0$. The reason why this occurs, is that the starting conditions of region (i) are reached by a prior thermal bistability. The latter will set the resonance slightly red detuned from the input wavelength. At this point, thermal effects no more contribute to shift the resonance, and a free carrier bistability can occur. On the contrary, if at the beginning $\lambda_p < \lambda_0$, thermal effects will in general dominate over free carrier ones, and this will set the system into the optical limiting regime.
An illustrative and exemplifying view of what happes during an oscillation cycle is shown in Fig.2.11(a-c).

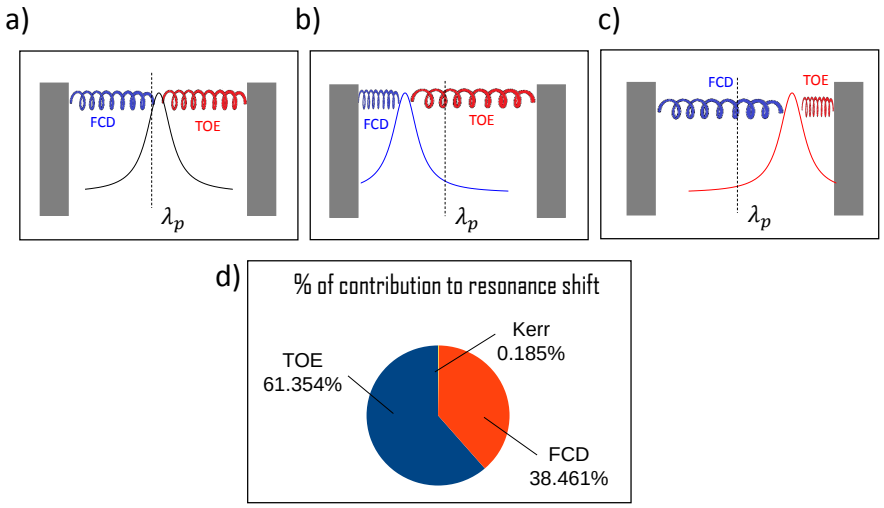

Figure 2.11: From (a) to (c): different frames in time illustrating the position of the resonance wavelength with respect to the laser wavelength λ_p. The thermo optic effect (TOE) and the free carrier dispersion effect (FCD) both contribute to shift the resonance wavelength by changing the modal effective index through Eq.2.1. The shifts have opposite signs. This is illustrated by two springs which are locked to the resonance and pull it into opposite directions. (d) Percentage contribution to the total shift of the resonance during one cycle of oscillation. This has been split into TOE, FCD and Kerr contributions.

Two springs, corresponding to thermal and free carrier effects, pull the resonance wavelength in opposite directions. Carriers pull toward the blue side with respect to the initial, or "cold" resonance wavelength, while temperature pull on the red side. The two springs have different damping times, in particular the one representing free carriers damps much faster than the one representing temperature, even if the latter is stronger (higher elastic constant). As a result, there is an interplay of the dominating dispersion mechanism, with the result that the resonance oscillates back and forth with respect to the input laser wavelength, determining a periodic modulation of the transmitted intensity. During the description of the physical processes involved from region (i) to (iv) in Fig.2.10, only thermal and free carrier effects have been considered, even if from Eq.2.9 it is evident that also the Kerr effect partecipates in the dynamics. In particular, the latter pulls the resonance wavelength on the same side as the temperature. However, the strength of this shift is very small compared to the ones induced by temperature and carriers. This becomes evident from Fig.2.11(d), where the average strength of the resonance shifts occurring in one oscillation cycle is evaluated. This is defined as the ratio between the resonance shift induced by a specific dispersion mechanism (temperature, carriers, Kerr) over the total resonance shift $\Delta(t)$, which is then averaged in time. The Kerr effect partecipates only for the 0.19% of the total shift, which is a negligible contribution compared to the ones due to thermal effects (61.35%) and due to carrier effects (38.46%).

2.3 Periodic self pulsing and chaos in coupled resonator sequences

The main feature shared by all the waveforms shown in Fig.2.7 is that they are all periodic. The period and the shape of the oscillations can be modified by changing the input exciting conditions or the resonator geometry, but nevertheless the system will never show aperiodic outputs. It has been theoretically proved, on the basis of the stability analysis of the solutions of Eq.2.8, that a system composed by a single cavity will never show a chaotic regime, regardeless of the input conditions [82, 99]. This is true provided that the only nonlinearites which act are of thermal and free carrier origin. The question which naturally arise is: can a single cavity show a chaotic output under the action of some nonlinear dispersion mechanism? The questions has been addressed in many works. For examples, in many of them chaos is achieved by the inclusion of a cm-size external cavity to a distributed feedback (DFB) III-V laser [188, 189], thus forming a multi-cavity system. An alternative solution exploits Kerr nonlinearities in mm size silicon microresonators. In this way, Armaroli et. al. predicted a chaotic regime in single resonators with short photon lifetime through an exotic non instantaneous Kerr effect [185]. Nevertheless, in order to achieve such a slow $\chi^{(3)}$ relaxation time (at ps scale), the addition of metals and liquids to the silicon device has been suggested, which limits the resonant cavity feasibility and the industrial manufacturing process.
These technical issues could be only faced by employing multi-cavity systems. In fact, there are some theoretical studies that predict a broad chaotic regime for passive coupled cavities, like Coupled Resonator Optical Waveguides (CROW) [190] or inline photonic crystal (PhC) nanocavities [191]. However, such models consider the Kerr effect as the only intensity dependent perturbation to the refractive index, neglecting thermal and free carrier ones. This is no longer valid in the continous wave regime, where, as shown in Fig.2.11, free carriers and temperature effects dominate over Kerr ones. Therefore, the demonstration either theoretically or experimentally of a Silicon-based device showing chaos is still open. In the next sections, it is studied the nonlinear dynamics of a SCISSOR under thermal and free carrier nonlinearities. It is demonstrated, both theoretically and experimentally, that the intracavity feedback of optical energy provides the necessary input for the onset of chaotic oscillations.

2.3.1 System geometry

The schematic of the resonator sequence under study is shown in Fig.2.12(a). The SCISSOR device has been fabricated on a $200\,mm$ wafer using $193\,nm$ DUV lithography. The SOI wafer consists of $220\,nm$ thick Silicon layer laid on top of a $2\,\mu m$ thick buried oxide (BOX) layer with underlying the Silicon substrate. After patterning and etching, a $745\,nm$ thick Silica layer was deposited to form buried single mode (in TM polarization) channel waveguides of $500\,nm \times 220\,nm$ cross section. The SCISSOR is composed by a sequence of 8 ring resonators. The latter has a nominal inner radius of $R = 7\,\mu m$ and are separated by a distance$L = 22\,\mu m$. They are evanescently coupled to the waveguides by means of a $300\,nm$ gap. The number of resonators is determined by the amount of power which can be coupled into the Drop port by each ring. With the considered design parameters, TMM simulations reveal that the input pump power is almost totally depleted after 10 rings, so adding more cavities does not significantly change the device performance. The number of rings has then been fixed to 8. At a wavelength of $1.55\,\mu m$, each resonator is designed to have a resonance linewidth of $0.8\,nm$, corresponding to a Q of ~ 1900. The ratio between the resonator separation and its perimeter is ~ 0.5, a value which ensures the maximum feedback between the cavities [82]. To probe the device spectral response, both in the high power and low power regime, it has been implemented the experimental setup sketched in Fig.2.12(b). A near Infra-Red tunable laser amplified by an EDFA was end-fire coupled to the input waveguide through a lensed optical fiber. The position of the input (output) lensed

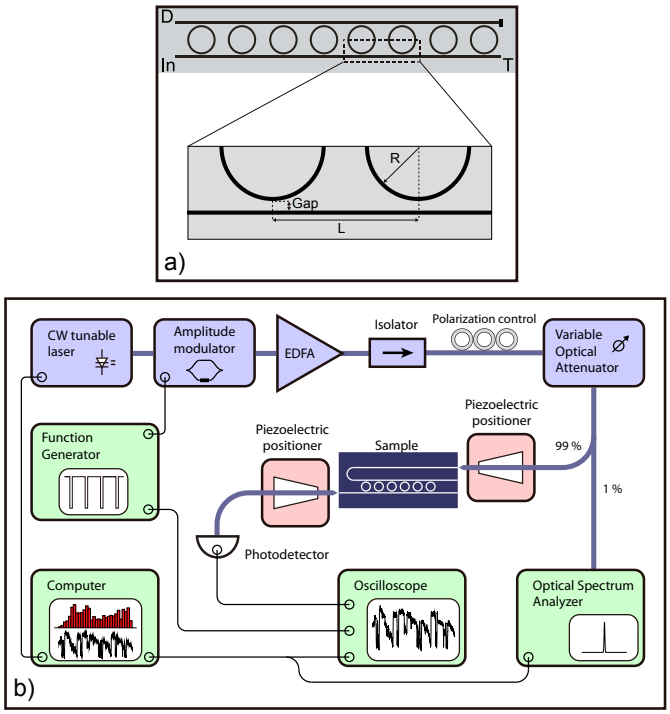

Figure 2.12: (a) Sketch of the device geometry. The values of the parameters R and L are indicated in the text. The SCISSOR is excited from the Input (In) port. Dropped and transmitted signals are recorded in the Drop (D) and Through (T) ports, respectively. (b) Schematic of the experimental setup.

fiber is controlled with a closed-loop three-axis piezoelectric stage ensuring accurate and stable alignment conditions. TM polarization was used. The signal power was controlled and monitored by using a VOA and an Optical Spectrum Analyzer respectively. In addition, an external $38\,dB$ fiber optic isolator blocked the light back reflected from the sample facet avoiding spurious effects in the EDFA. The signal polarization was controlled employing two quarter-wave and one half plates placed in an U-bench module before inserting the light into the input waveguide. An $InGaAs$ camera with a $20\times$ objective and $16\times$ zoom lens recorded the radiation scattered out of the surface of the SCISSOR. The output signal from the drop port was collected with another lensed fiber and connected to a detection system, composed by a $1\,GHz$ photodetector and a $40\,GHz$ digital oscilloscope. To study the time evolution of the system, a $10\,GHz$ amplitude modulator was employed to switch off the input signal for a period of $1\,ms$ prior to the signal acquisition. This modulator and the oscilloscope were electrically driven/triggered by an arbitrary function generator. The scattered light from the top of the sample as a function of the input power and wavelength, and the time evolution of the output signal, were remotely acquired by a computer.

2.3.2 Dynamic time response of the SCISSOR

At first, the low power spectral response of the device in the Drop port has been recorded to track the position of the resonances. As already introduced in section 1.1.4.2, the Through spectra consists of a sequence of regions of low transmissivity, where the input signal is resonantly coupled to the ring sequence and is directed to the Drop port. Such wavelength regions represent the PBGs. The spectral response is shown in Fig.2.13(a). From the zoom of one of the PBGs, shown in Fig.2.13(b), it is possible to notice the presence of narrow transparency peaks inside the bandgap.

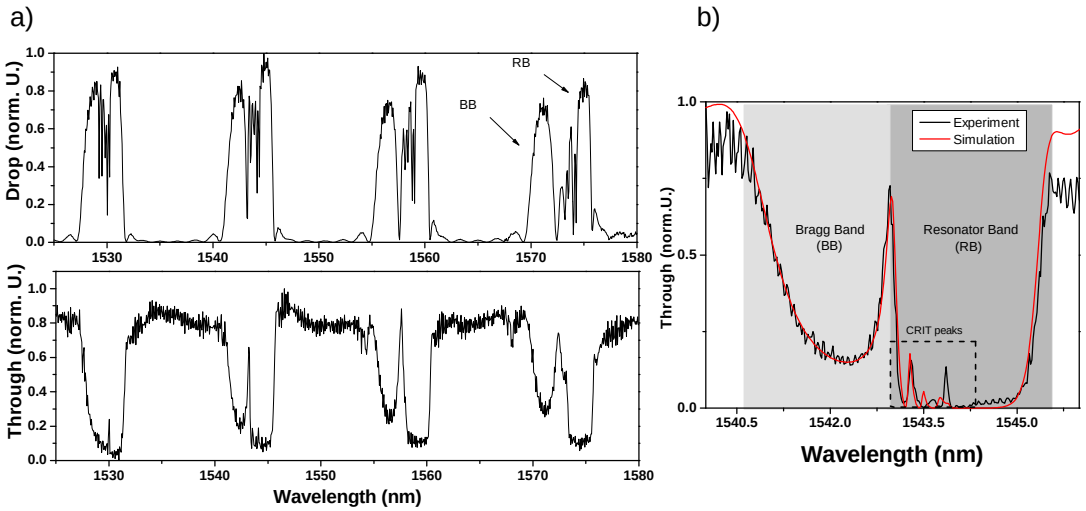

Figure 2.13: (a) Spectral response of the SCISSOR at $1\,mW$ of pump power. The Drop transmitted intensity is shown in the upper panel while the Through one is shown in the lower panel. The arrows indicate the Resonator Band (RB) and the Bragg Band (BB) position. (b) A zoom of the PBG centered at $1542.75\,nm$. The RB and the BB are indicated with two coloured rectangles. CRIT peaks lie inside the dashed ractangle. The solid red line is a fit of the experimental spectral response obtained using a Transfer Matrix simulation.

It is well known that these states are created by defects in the resonator sequence (CRIT effect) [87, 78, 82]. The observation of CRIT reveals that the rings in the sequence have optical paths slightly different from each other. As a consequence, the resonances of each cavity are not perfectly overlapped.

If the input power coupled into the waveguide is kept lower than $1\,mW$, the output power in the Drop port is found constant in time, which means that the system has still a linear behaviour. However, after a certain threshold input power, this is no more true: depending on the input wavelength, a transition from a static output to an unstable one is observed, exactly as it has been described for the single cavity of section 2.2. When this occurs, the Drop(Through) intensity switches from its high(low) constant amplitude to a time varying value. The phenomenon is resonance assisted since it only occurs when the input signal wavelength lies in one of the PBGs. Fig.2.14 reports some of the observed Drop signal waveforms in the $1542.5\,nm - 1545.5\,nm$ PBG.

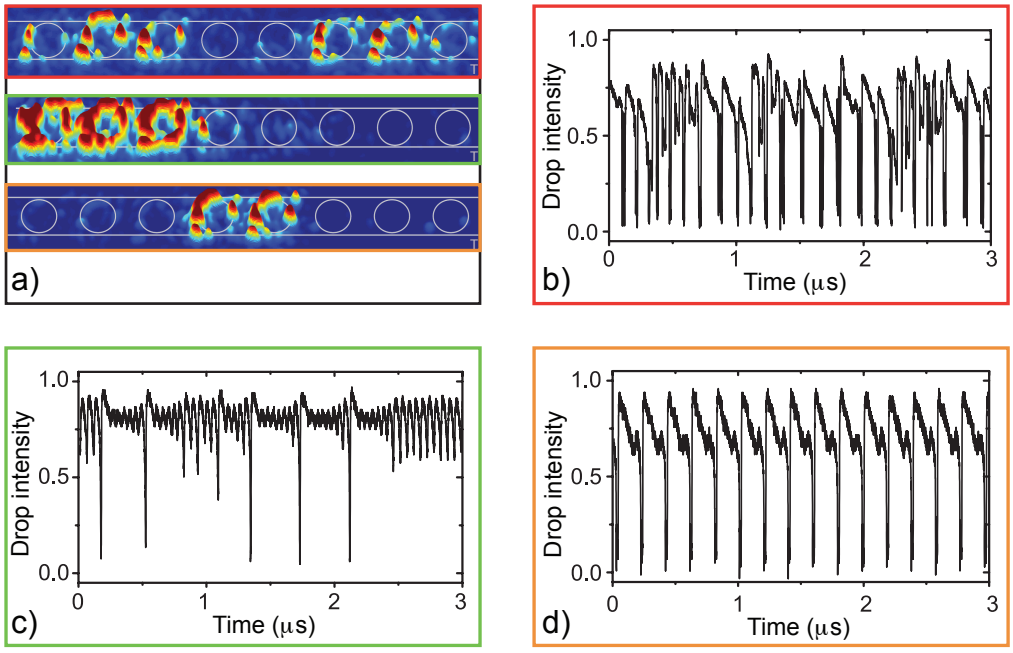

Figure 2.14: (a) Top scattered light from the SCISSOR associated to the three waveforms shown in (b-d), respectively. A schematic of the device geometry (white line on the scattering images) illustrates the position of the rings in the chain. (b-d) Drop signal waveforms at different input powers (P_{in}, coupled in the waveguide) and wavelength (λ_p) combinations - (b) $P_{in} = 20\,mW$; $\lambda_p = 1543.225\,nm$, (c) $P_{in} = 13\,mW$; $\lambda_p = 1543.17\,nm$, (d) $P_{in} = 14.5\,mW$; $\lambda_p = 1543.99\,nm$ - showing six (b), three (c) and two (d) hot resonators.

A common feature is the presence of sharp transitions from an high transmission state to a lower one and back, creating short time intervals of low intensity separated by transient regions of slowly varying high intensity. Typical time scales are $5\,ns$ for the sharp features and $70\,ns$ for the transient ones. The involved time scales are the same of the self pulsing experiment described in Section 2.2, so the instabilities can be still associated to thermal and free carrier effects. The out of plane scattered light signal shown in Fig.2.14(a) reveals that, during the unstable regime, the energy is mostly localized in a limited number of resonators. The number of resonators to which the input signal efficiently couples is power and wavelength dependent. The complexity of the Drop signal waveforms scales with this number, that can be defined as the number of "hot" cavities. The term hot is here used since it corresponds to ring resonators where a high internal energy is accumulated due to the resonant coupling with the input light signal. In Fig.2.14(a-d) it is shown that periodic outputs are observed when a maximum of two resonators become hot. For more hot resonators, the output signal shows complex aperiodic waveforms. The light pattern associated to the waveform in Fig.2.14(b) shows one of the peculiarities of the SCISSOR geometry compared to that of a CROW or to a sequence of inline PhC nanocavities. Even if the two central resonators are off resonance due to fabrication defects, the energy flow along the chain is not interrupted and reaches the last three cavities.

2.3.3 Comparison between periodic and chaotic waveforms

The different unstable regimes shown in Fig.2.14 are now analyzed from a more quantitative point of view. In particular, some tests are performed to assess if the complex patterns as the one in Fig.2.14(b) are truly chaotic or simply aperiodic. Indeed, the aperiodicity of some physical observable (the light intensity in this case) is not always related to chaos. For example, the time evolution of the distance between two pendulums which independently oscillate at frequencies ω_1 and ω_2, can be aperiodic if the ratio $\frac{\omega_1}{\omega_2}$ is not

commensurable. By the way, the described system is clearly not chaotic. This can be easily detected from a Fast Fourier Transform (FFT) of the signal, which would reveal the two main frequencies at ω_1 and ω_2. In Fig.2.15, two Drop signal waveforms of Fig.2.14, one periodic and one aperiodic, are analyzed. This is done to compare the distinguishing features of chaos to the ones of a periodic regime.

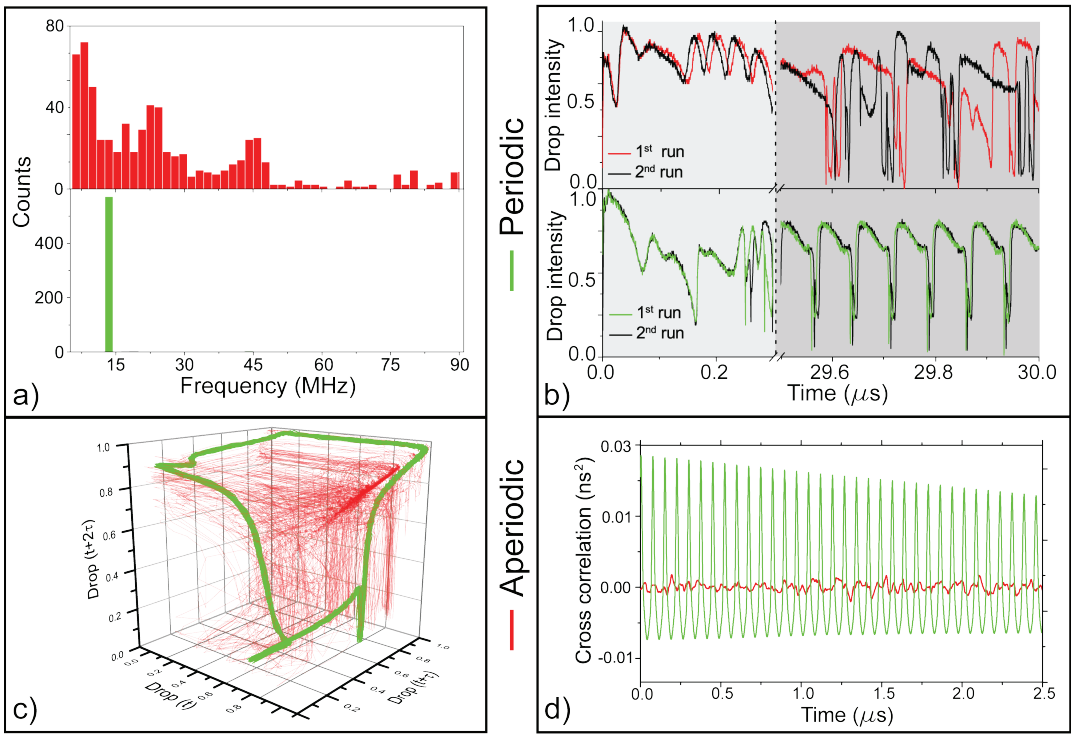

Figure 2.15: (a) Frequency distributions of the periodic and of the aperiodic Drop signal waveforms shown in Fig.2.14(d) and in Fig.2.14(b). (b) Time evolution of two periodic (aperiodic) signals, indicated as run 1 and 2, which start from slightly different initial conditions. Input powers and wavelength positions are the same as in (a). (c) Reconstructed phase spaces of the system for the periodic and the aperiodic outputs in (b). The reconstruction makes use of the Taken's theorem with $m = 2$ and $\tau = 8\,ns$. (d) Cross correlation between the two periodic (aperiodic) Drop signal waveforms in (b).

At first sight, the main difference between the waveforms in Fig.2.14(d) and in Fig.2.14(b) is the spectral content. To extract the frequencies with which the sharp transitions recur, the two $50\,ms$ long sequences are converted into binary ones by a digital Schmitt trigger ($10\,ns$ of hysteresis time). In Fig.2.15(a) the histograms of the inverse of the time lags between two subsequent rising edges are reported. The periodic sequence has only one predominant frequency at $15\,MHz$, while the aperiodic one is characterized by a wider distribution in the $0.5\,MHz - 90\,MHz$ range. Similar considerations can be done by comparing the FFT of the two time sequences (not shown in Fig.2.15). The FFT of the periodic sequence is made by a comb of equidistant frequency peaks, spaced by the fundamental frequency of $15\,MHz$. The FFT of the aperiodic sequence is white, in the sense that there are not dominant frequencies. The complete lack of regularities and the wide spectral content of the aperiodic sequence suggests the presence of chaos. One of the distinguishing features of a chaotic dynamical system is the high sensitivity to the initial conditions. Two trajectories which start from slightly different initial conditions rapidly lose correlation as the system evolves. The sensitivity to the initial conditions is proven as follows: the input signal of a given wavelength is square wave modulated with a 2% duty cycle. The off duration is nearly $1\,ms$, which is sufficient to let the SCISSOR to relax and thermalize with the environment. The experimental noise (chip temperature and pump intensity fluctuations)

makes the initial conditions slightly different every square wave edge front. The similarities of the generated waveforms are monitored as a function of time by studying their cross correlation. Fig.2.15(b) shows that two periodic sequences with small different initial conditions evolve towards two identical signals that are again periodic and slightly delayed. The case of two aperiodic outputs is different: after few microseconds ($\sim 30\,\mu s$), the waveforms completely lose their similarity. As shown in Fig.2.15(d), the cross correlation between the two aperiodic sequences vanishes, meaning that the small perturbations of the initial state are modifying the evolution of the system. To further investigate the presence of chaos, the concept of phase space has to be introduced.

Given a system with Hamiltonian $H(\mathbf{q}, \mathbf{p}, t)$ with R generalized coordinates q and R conjugate momentum p, this generates a $2R-$ dimensional space, called the phase space, in which the system evolves. Each time, the state of the latter is defined by a point in that space corresponding to the vector $\mathbf{x} = (\mathbf{q}, \mathbf{p})$. Given the initial conditions $\mathbf{x}_0 = (\mathbf{q}_0, \mathbf{p}_0)$, the vector $\mathbf{x}(t)$ will evolve in time following the Hamilton's equation of motion, and it will generate a sequence of points in the phase space. The latter is called the trajectory of the system. These concepts are illustrated in Fig.2.16, where the system is constituted by a simple pendulum subjected to gravity.

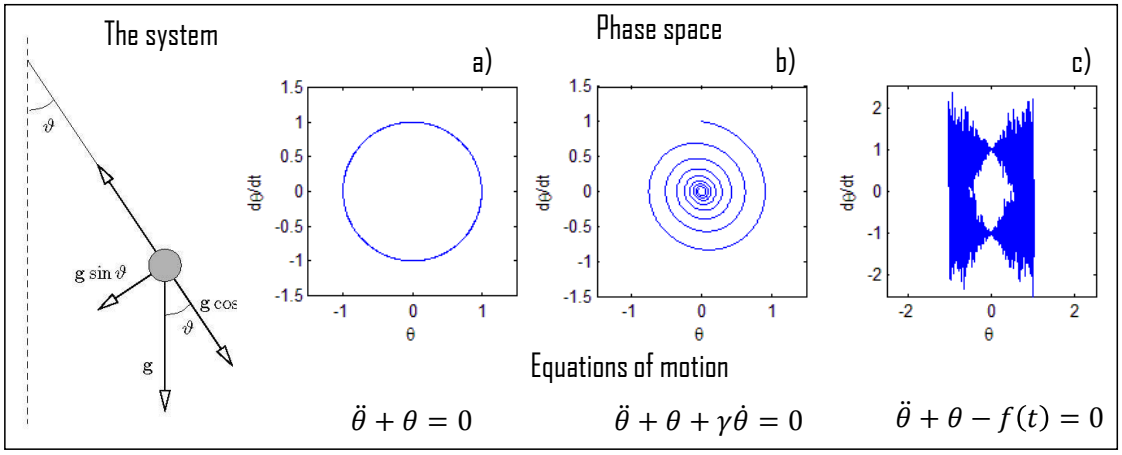

Figure 2.16: Examples of phase space trajectories for a system constituted by a simple pendulum. The phase space vector has two coordinates, $q = \theta$ (angular position) and $p = \frac{d\theta}{dt}$ (angular velocity). (a) Phase space of an undamped pendulum. The trajectory is a closed curve. (b) Phase space of a damped pendulum. The trajectory collapses toward a stable point. (c) Phase space of a pendulum which is driven by a stochastic force $f(t)$. In this example, at each time t the value of f is normally distribuited around zero. The equation of motion associated to each phase space is shown at the bottom of each panel.

From panel (a) of Fig.2.16, which corresponds to the phase space associated to a periodic motion, it can be noticed that the trajectory is a closed curve. When the system is purely dissipative, as in the case of the damped pendulum in panel (b), the trajectory evolves toward a point, which is an equilibrium point for the system. When the system is chaotic, as in the case of a pendulum subjected to a stochastic force $f(t)$ (panel (c)), some regions of the phase space get densely covered with points. Such regions are called attractors. Intuitively, this happens because the stochastic force kicks the pendulum into random directions. The pendulum is nevertheless forced by the gravity, by the length of the wire and by its inertial mass to explore limited regions of space. Of course, the concepts of phase space, density of points and sensitivity to initial conditions introduced above are very simplicistic. They have been introduced only to offer a direct insight to the qualitative features which distinguish a chaotic motion from a not chaotic one. In this sense, they are not rigourous and do not pretend to offer a complete comprehension of the concept of chaotic

systems. This lies well outside the scope of this work.
From a more practical point of view, the phase space trajectory can not be traced except for very simple systems. This is because it requires the knowledge of all the internal degrees of freedom of the system, and usually most of them are not accessible. As explained in detail in section 2.3.5, in the present experiment the dimension of the phase space is $R = 24$. However, the only (easily) measurable quantities are the Through and Drop signal intensities. Given in this terms, it seems that it is not possible to extract any information concerning the properties of the phase space. However, with the help of the Taken's theorem [192], it is possible to construct an equivalent $m-$dimensional space by using m delayed versions of the same system observable, which in this case is the Drop(Through) intensity. For $m = 2$ the generated space is two-dimensional, while for $m = 3$ the space is three dimensional. It has to be pointed out that the reconstructed space does not correspond to the one spanned by the vector $\mathbf{x}(t)$. Nevertheless, it preserves the properties of the dynamical system. A closed trajectory in the original space will be mapped into a closed trajectory in the reconstructed one, and an attractor will be mapped into an attractor of a different shape. In Fig.2.15(c), the reconstructed phase space is obtained for both aperiodic and periodic Drop signals. The trajectory is traced by the vector $\mathbf{x}(t) = (D(t), D(t+\tau), D(t+2\tau))$, in which $D(t)$ is the Drop intensity at time t, while $\tau = 8\,ns$ is the delay time. There is no a general rule for choosing τ, even if some choices of the latter allow to reconstruct the properties of the original space with more efficiency and less data [193]. The same holds for the dimension m. The use of $8\,ns$ ensures that the information carried by the fastest features in the generated waveforms are correctly reproduced in the reconstructed space. As it can be seen from Fig.2.15(c), the periodic sequence (green line) always retraces the same trajectory. The aperiodic sequence has a trajectory that folds on itself several times with no preferential directions and results in a phase space which is dense of points.
The high sensitivity to the initial conditions and the dense phase space are strongly indicators of chaos.

2.3.4 Influence of the input initial conditions on the onset of chaos

The transitions between stable, periodic and chaotic regimes are seen to be regulated by the input signal wavelength and power. The onset of the various regimes are studied in detail by performing an input power scan from $5\,mW$ to $23\,mW$ (coupled in the waveguide) in the $1542.5\,nm - 1545\,nm$ range. The Drop signal is recorded at each combination of input power and wavelength, then the phase space density is calculated using a 2D reconstructed space with $m = 2$ and and $\tau = 8\,ns$. The computation of the phase space density proceeds as follows (refer to Fig.2.17 for the illustration of the method):

1. The Drop signal $D(t)$ is recorded .

2. The 2D projection of the phase space is reconstructed using Taken's theorem and two delayed versions of the recorded output, $D(t)$ and $D(t+\tau)$, with $\tau = 8\,ns$. The final result is a plot which has $D(t)$ on the x-axis and $D(t+\tau)$ on the the y-axis.

3. The signals $D(t)$ and $D(t+\tau)$ are normalized to one, in order that the whole phase space has unit volume.

4. The phase space is divided into a 100×100 matrix ρ. The element ρ_{mn} is set equal to one if the corresponding element of the phase space grid contains at least one point of the plane trajectory $(D(t), D(t+\tau))$, otherwise is set to zero.

5. The density is calculated as $\left(\sum_{mn} \rho_{mn}\right)/10^4$. The quantity 10^4 corresponds to the total number of phase space accessible points.

Results are shown in Fig.2.18(b).

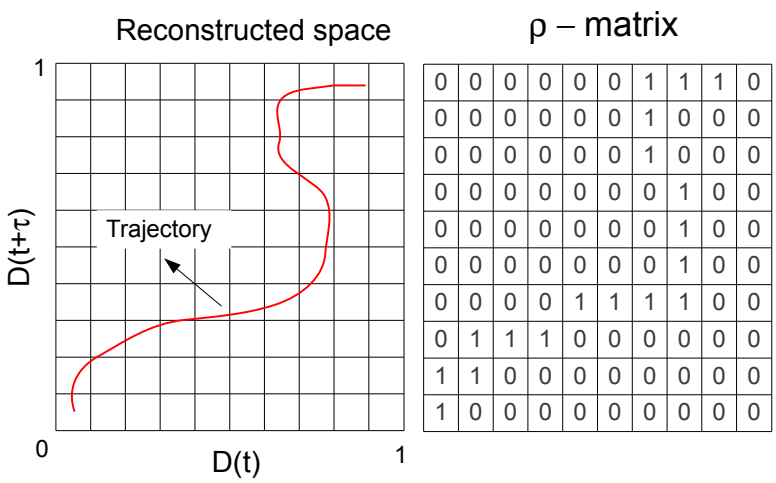

Figure 2.17: Illustration showing how the phase space density is calculated starting from a single recorded Drop intensity $D(t)$.

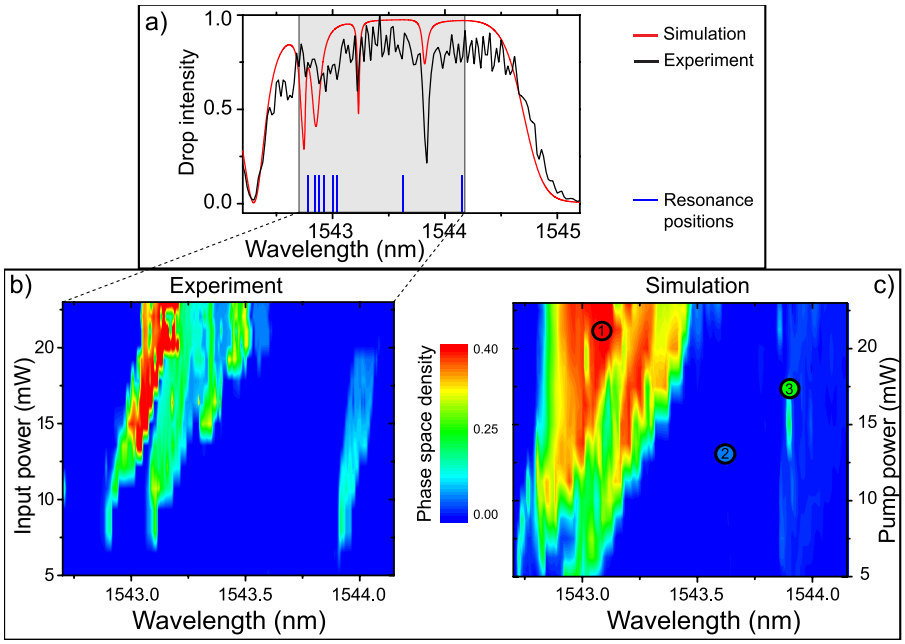

Figure 2.18: (a) Experimental (black) and simulated (red) low power ($< mW$) spectral response of the SCISSOR in the $1542.5\,nm - 1545\,nm$ range. The resonance positions of each ring in the SCISSOR are indicated with a vertical blue line. (b) Experimental phase space density as a function of the input power and wavelength. (c) Simulated phase space density as a function of the input power and wavelength. Density is computed as in (b) using simulated Drop signals. Colored dots indicate the combinations of input power and wavelength at which the Lyapunov exponents, reported in Fig.2.21, are computed. Dots coordinates are ($21.0\,mW$, $1543.11\,nm$) for the red one, ($17.8\,mW$, $1543.91\,nm$) for the green one and ($13.3\,mW$, $1543.59\,nm$) for the blue one.

High density regions, associated to the most complex and irregular Drop signal waveforms, are found at high input powers and in the wavelength ranges where the ring resonances lie close together (Fig. 2.18(a)). The approximate wavelength position of the latter are found by using a Transfer Matrix code to simulate the SCISSOR's Drop spectra. Transitions towards lower density areas are smooth, indicating that chaotic

outputs adiabatically turn to periodic ones before reaching stable states. No oscillations in the Drop signals are observed for input powers below $5\,mW$. It can be noticed that the densest regions resemble a triangle whose basis is tilted toward larger wavelengths. In this way, the wavelength range in which complex oscillations are found is more extended at higher powers rather than at lower ones. This can be understood from the fact that, as described in Section 2.2, each oscillation starts with a thermal bistability, and the latter can be activated at progressively larger spectral distances, between the pump and the resonance wavelength, as the input power is increased. The information coming from the shape of the phase space density of Fig.2.18(b) and from the scattered light patterns of Fig.2.14(a) can be merged together to qualitatively interpret the role of the input exciting conditions on the onset of unstable regimes. The input wavelength selects which rings in the sequence are on resonance, i.e the spectral position of the hot resonators. The increase of the input power induces a resonance oscillation in the hot resonators similar to the one described in Section 2.2 for a single cavity. As a consequence, the spectral response of the SCISSOR, which depends on the actual position of all the resonances, gets time dependent. When many rings have close resonance positions, collective oscillations can be activated at high input powers, which are associated to the localized scattering patterns of Fig.2.14(a). The higher the number of hot cavities, the more the spectral response gets distorted and complex waveforms are generated. In some cases, the effect of coupling leads to chaos. In principle, the presence of fabrication defects is detrimental for the creation of collective excitations, since it limits the number of cavities having overlapping resonances. Hovewer, defects can also induce localized states in which energy is trapped and enhanced, leading to higher nonlinear effects [82, 99, 78].

2.3.5 Theoretical model of the coupled cavity system and computation of the Lyapunov exponents

The theoretical model presented in Section 2.1 for a single cavity is extended to the system constituted by 8 coupled cavities. This is done in order to validate the qualitative deductions of the previous section and to analyze the stability of the solutions. With reference to Fig.2.19, the internal energy amplitude $\tilde{u}^j_{int}$ of the j^{th} cavity evolves following the differential equation:

$$\frac{d\tilde{u}^j_{int}}{dt} = i\left[\omega_j(1-\Delta_j(t)) - \omega_p\right]\tilde{u}^j_{int} - \frac{\tilde{u}^j_{int}}{\tau^j_{tot}(t)} + i\sqrt{\frac{2}{\tau_{ext}}}(P^j_H(t) + P^j_L(t)) \tag{2.19}$$

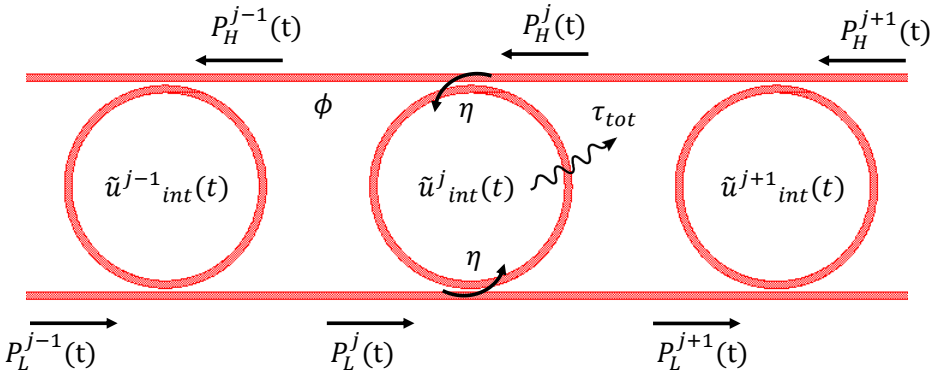

Figure 2.19: Schematic of the coupled cavity system. Only three cavities are shown. Each resonator stores an internal energy $|\tilde{u}^j_{int}(t)|^2$, with $j = 1, ..., 8$, and is excited from both the upper and the lower waveguides. The straight waveguides make the light experience a phase ϕ during the propagation from one resonator to the other. The energy is coupled from the bus waveguides to the resonator with a rate η, and at the same time it is dissipated through scattering loss, TPA and FCA. This results in a total photon lifetime of τ_{tot}.

Eq.2.19 has exactly the same form of Eq.2.8 but now the external excitation is provided both from the upper and from the lower waveguides. The incoming power amplitudes are $P_H^j(t)$ and $P_L^j(t)$ respectively, and are given by:

$$P_H^j(t) = e^{-i\phi}\left(P_H^{j+1}(t) + i\sqrt{\frac{2}{\tau_{ext}}}\tilde{u}_{int}^{j+1}(t)\right) \tag{2.20}$$

$$P_L^j(t) = e^{-i\phi}\left(P_L^{j-1}(t) + i\sqrt{\frac{2}{\tau_{ext}}}\tilde{u}_{int}^{j-1}(t)\right) \tag{2.21}$$

in which $\phi = \frac{2\pi}{\lambda} n_{eff} L$ is the phase acquired during the propagation in the straight waveguide sections connecting the adjacent cavities. The coupling rate is assumed to be the same for all the cavities and equal to $\eta = \sqrt{\frac{2}{\tau_{ext}}}$. Each cavity has a different resonant frequency ω_j due to the presence of fabrication defects, a fact supported by the observation of CRIT peaks inside the PBG. The propagation and bending lossess have been measured to be $2\,dBcm^{-1}$. Needless to say, in addition to Eq.2.19, each cavity comes with two more equations, one for the internal temperature and one for the free carrier concentration. The global system is then described by 24 differential equations (Eq.2.19 is complex, so it has to be counted twice, one for the real part and one for the imaginary part). The model consider a strictly unidirectional propagation, backward waves generated by surface roughness have not been considered. The set of equations has been integrated using a variable order solver. At $t = 0$, which corresponds to the initial step, all the cavities are assumed to have internal energy equal to zero. The same is true for ΔT and ΔN in each cavity. The accuracy of the model is tested by comparing simulations with experiment at the same input power and wavelength conditions. Most of the simulation parameters were found by fitting the low power spectral response of Fig.2.18(a). The complete list of the simulation parameters is presented in Table 2.2. Fig.2.20 shows the agreement between a simulated periodic Drop signal waveform and an experimental one.

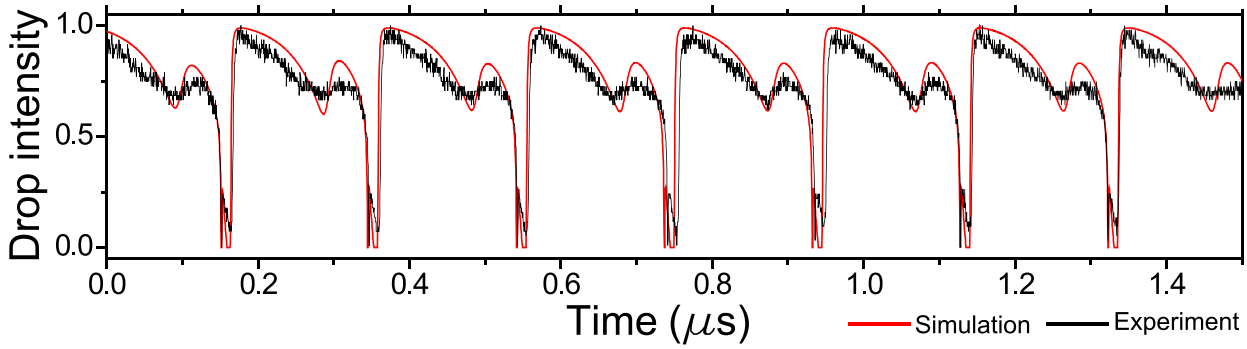

Figure 2.20: Comparison between simulation (red line) and experiment (black line) for an input power of $14.5\,mW$ and an input wavelength of $1543.99\,nm$.

The perodicity of the signal is a fundamental requirement for a correct comparison. In fact, it relaxes the choice of the initial conditions in the neighborhood of the ones of the experiment, which are not exactly known. This would not be possible for chaotic outputs due to the high sensitivity to the input initial conditions. Using simulated Drop signals, the phase space density diagram in Fig.2.18(c) is generated, which closely resembles the one of Fig.2.18(b). High density areas distribution, intensity and shape are in agreement with the experiment.

To theoretically prove the existence of a chaotic regime, the stability of the solutions of Eq.2.19 is evaluated by calculating the Lyapunov exponents (LE) by integrating the Jacobian of the system of equations (2.19)

Parameter	Value				Source
$\lambda_i = \frac{2\pi c}{\omega_{0i}}$	i		i		Fit of spectra in Fig.2.18(a)
	1	$1543.00\,nm$	5	$1544.21\,nm$	
	2	$1542.92\,nm$	6	$1542.83\,nm$	
	3	$1542.80\,nm$	7	$1542.79\,nm$	
	4	$1543.67\,nm$	8	$1543.06\,nm$	
$1/\tau_{ext}$	$(107 \pm 5)\,GHz$				Experiment
$1/\tau_0$	$(17 \pm 1)\,GHz$				Experiment
$1/\tau_{fc}$	$220\,MHz$				Fit
$1/\tau_{th}$	$7.2\,MHz$				Fit
L	$22.03\,\mu m$				Fit
n_{eff}	1.78				FEM
V_{eff}^2	$8.85\,\mu m^3$				FEM
V_{FCA}^2	$49.47\,\mu m^3$				FEM
Γ	0.58				FEM
Γ_{FCA}	0.99				FEM
λ_p^{exp}	$(1543.91 \pm 0.01)\,nm$				Experiment
λ_p	$1543.99\,nm$				Fit
$\lvert P_L^0\rvert^2$ (experiment)	$(13.33 \pm 0.01)\,mW$				Experiment
$\lvert P_L^0\rvert^2$ (simulation)	$14.5\,mW$				Fit

Table 2.2: Values of the simulation parameters used to generate the red curve in Fig.2.20.

using a QR factorization algorithm [194]. The latter are indicators on how fast two phase space trajectories $x_{x_0}(t)$ and $x_{x_0+\Delta}(t)$, which start from slightly different initial conditions x_0 and $x_0 + \Delta$, separate from each other. In order to get an immediate feeling on the concept of LE without developing a full theory (which lies outisde the scope of this work), it is possible to consider a more simple one dimensional problem. Given again two solutions $x_{x_0}(t)$ and $x_{x_0+\Delta}(t)$, which are generated by the hamiltonian of the system starting from two slightly different initial conditions, their separation $d = |x_{x_0}(t) - x_{x_0+\Delta}(t)|$ can be demonstrated to evolve in time as $d(t) = \Delta e^{\lambda_e t}$ [195]. The quantity λ_e is called the Lyapunov exponent of the system. It comes out that a positive LE implies ultra-sensitivity to the initial conditions, since the distance between the two trajectories exponentially increases with time. This is why positive LE are often associated to chaotic regimes. A LE which is equal to zero implies that the system dynamics is not influenced by the choice of the initial conditions, because $x_{x_0+\Delta}(t)$ will keep the same initial distance Δ from $x_{x_0}(t)$. The two trajectories will stay very close to each other as the time evolves. A negative LE implies that $x_{x_0+\Delta}(t)$ and $x_{x_0}(t)$ will collapse to the same trajectory or toward a fixed point as the time evolves. This is the case of dissipative systems. If the system has dimension R, it will have R Lyapunov exponents [195]. In this case it is the sign of the Largest Lyapunov exponent (LLE) which determines the system dynamics, while the very same considerations done for the unidimensional system still apply. LEs are evaluated at three different combinations of power and wavelength, corresponding to regions of low, medium and high phase space density, respectively (colored dots in Fig.2.18(c)). Figure 2.21 reports the six LLEs for each combination. The lowest density region has all the LLEs lower than zero, which is associated to a stable output. The medium density one has the maximum LE equal to zero, which implies a stable periodic motion. Finally, the region of highest density admits a positive LE. This constitutes another demonstration that a chaotic regime is allowed in the SCISSOR device.

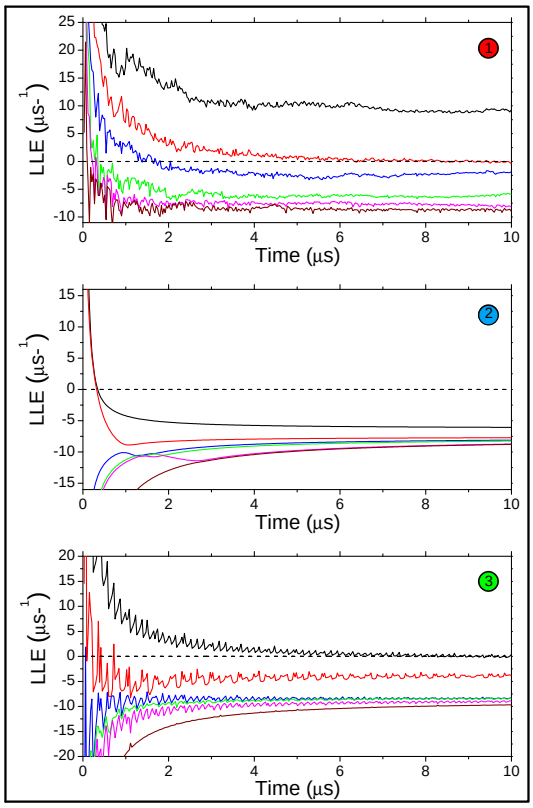

Figure 2.21: System stability analysis through Lyapunov Exponents (LE). At each combination of input power and wavelength position, indicated with colored dots in Fig.2.18(c), the spectrum of Lyapunov exponents of the SCISSOR is computed. As the time evolves, curves in each panel converge to the values of such exponents. Only the largest six LEs are plotted in each panel. The Drop signal waveforms (not shown) is constant in the case of the blue dot, periodic for the green one and chaotic for the red one.

2.3.6 Tuning the onset of chaos with the device geometry

Up to now, chaos has benn reported for a given SCISSOR geometry with 8 resonators. A reliable relation between the SCISSOR parameters and chaos would be of much more interest for device engineering. However, an 8 cavity system has too many degrees of freedom to easily derive a relationship between the onset of chaos and the device parameters, or with the combinations of input power and wavelength. To achieve this goal, it is convenient to reduce the number of coupled resonators. The computation of Lyapunov exponents did not reveal any positve LE up to three coupled cavities. It comes out that the minimum number of coupled resonators required to generate chaos in the SCISSOR configuration is three. The investigated geometry is shown in Fig.2.22(a).

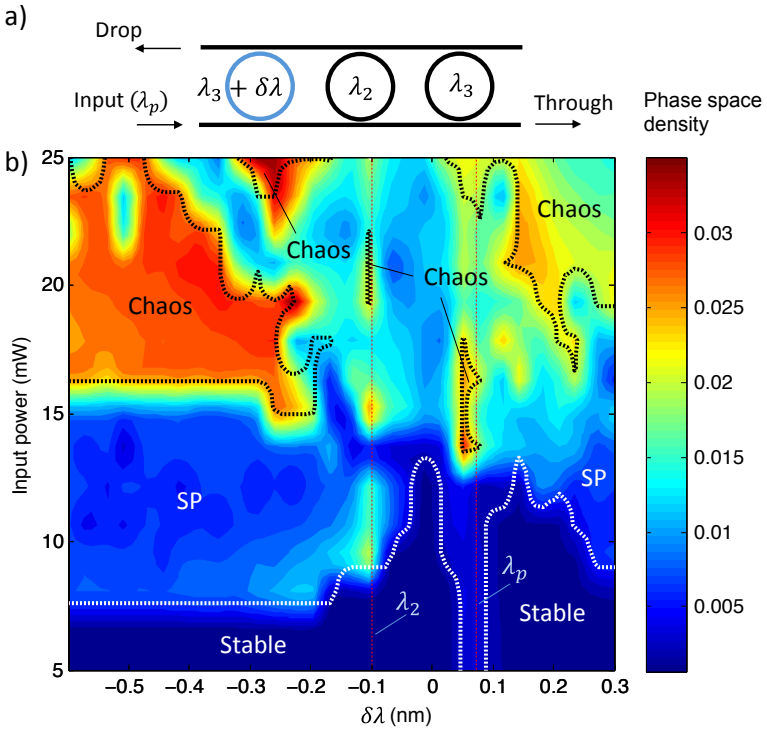

Figure 2.22: (a) Sketch of the device geometry. By moving from left to right, the three rings have resonance wavelength $\lambda_1 = \lambda_3 + \delta\lambda$, $\lambda_2 = \lambda_3 - 0.1\,nm$ and λ_3 respectively. The input signal wavelength is set to $\lambda_p = \lambda_3 + 0.075\,nm$. Vertical red lines show the input wavelength λ_p and λ_2, respectively. The ring separation is chosen to give a phase delay of π to light which propagates in the straight waveguide sections. Each cavity has a linewidth of $0.8\,nm$. (b) Phase space density as a function of the parameter $\delta\lambda$ and of the input power. Contour lines separate the regions where the largest Lyapunov exponent turns from negative (labelled Stable) to null (labelled SP, for Self Pulsing regime), null to positive (labelled Chaos) and vice versa.

To further simplify the model, the resonant wavelength of the first ring and the input power were set to be the only variables, as depicted in Fig.2.22(a). The first cavity, being directly connected to the input port, plays a crucial role in the dynamics of the whole structure. The input wavelength λ_p has been set slightly red detuned with respect to the third cavity resonance λ_3. At each combination of input power and first resonance position $\lambda_1 = \lambda_3 + \delta\lambda$, the density of the phase space and the corresponding spectrum of Lyapunov exponents have been computed. Contour lines separating regions of positive (chaotic), null (stable oscillation) and negative (stable state) LLEs are then superimposed to the phase space density plot. The result is shown in Fig.2.22(b). Chaos is found, at similar powers, both on positive and negative $\delta\lambda$, but with the important difference that the associated phase space densities, hence the complexity of the output waveforms, are higher at negative detunings. This is due to the fact that at positive $\delta\lambda$, the first cavity gets red detuned with respect to the input wavelength, and then works in the optical limiting regime. Its resonant wavelength is then pushed away from the other two, reducing the optical feedback that provides. The power threshold for the onset of chaos is also much more irregular at positive $\delta\lambda$, while it is quite flat on the other side. Therefore, in spite of the simplicity of the model, a reliable recipe to achieve chaos is found: to obtain a uniform threshold power for a complex chaotic output, all the three cavities must be blue detuned with respect to the input signal wavelength.This is not surprising since the chaotic regime requires the self pulsing of resonators, and, as it has been described in Section 2.2, this will most likely occur when the input wavelength is red detuned with respect to the cavity resonance.

2.4 Generation of random bit sequences using chaotic waveforms

The observation of chaos in a SCISSOR could be relevant for the generation of random data sequences, both in the electrical and in the optical domain. In this context, a SCISSOR based random number generator will be conceptually simple and easy to fabricate while preserving the flexibility of Silicon Photonics, which allows integrating them with other photonic components to realize complex optical functions in a single chip. In order to demonstrate the capability of the SCISSOR to generate a random bit sequence, the same data post processing discussed in the work of Kanter et.al. is applied to a chaotic signal seed [196]. The post processing consists in computing the n^{th} numerical derivative of the signal, then converting each point into a binary value (using a 8 bit (32 bit) ADC), and assembling the final sequence by taking the 5 (15) less significant bits (LSB) from each point. In what follows, the rough chaotic signal has been recorded at an input power of $15\,mW$ and at an input wavelength of $1543.848\,nm$. The sequence is $5\,ms$ long and has been sampled with a $20\,GS$ digital oscilloscope with $5\,ns$ of temporal resolution, yelding a total number of 10^7 sampled points. Since the derivative stage enhances the high frequency electronic noise superimposed to the deterministic signal, a moving average filter has been used on the rough sequence to increase the signal to noise ratio (SNR). With this step, the random properties of the final bit sequence would arise mostly from the deterministic part of the signal and less from the stochastic noise. The filter allows to achieve a SNR of ≈ 16 (on the derived sequence) and at the same time does not tailor the sharp spikes of the deterministic signal. The randomness of the final sequence is evaluated using the statistical test suite provided by the National Institute of Standards and Technology (NIST) [197]. This consist in a series of tests that a sequence of bits has to pass in order to be classified as a random sequence. In a perfectly random bit sequence, each bit has an equal probabily to be zero or one. The highest bitrate that passed all the NIST tests is $1\,Gbps$, and has been reached using the post processing parameters listed in Table 2.3. The reports of the statistical tests are shown in Table 2.4. It has been found that the sampling rate of $200MHz$ was too high to generate uncorrelated points, so the latter has been halved. To verify that the SNR iwas sufficiently high to exclude any contribution from the stochastic noise to the randomicity of the final bit sequence, the NIST tests were performed on the electronic noise alone, using the same post processing parameters of Table 2.3. As it can be seen from the report of Table 2.4, the electronic noise did not pass three tests, meaninig that the noise level superimposed to the deterministic signal was indeed very low after the averaging stage. Furthermore, to also exclude that the randomicity of the sequence may have originated from the post processing steps, the NIST tests have been performed on a quasi-periodic signal, recorded at an input wavelength of $1543.893\,nm$ and at $15\,mW$ of input power. The signal is quasi-periodic in the sense that a small jitter ΔT on the period T is present, but $\Delta T/T \ll 1$ holds. The post processing parameters were again the ones listed in Table 2.3. The reports of Table 2.4 show that the bit sequence did not pass many tests, meaning that the random properties of the bit sequence arised from the chaotic nature of the signal seed.

Post processing parameter	**Value**
Temporal resolution of derivatives points	$10\,ns$
Number of derivatives	4
Total bits of the digital ADC	13
LSB	10

Table 2.3: Values of the post processing parameters used to generate the $1\,Gbps$ sequence. The digital ADC has 13 bits instead of the 8 of the oscilloscope which recorded the rough sequence. However, as discussed in [196], the derivative stage ensures that no redundancy is introduced in the sequence in the case of higher resolutions.

Test description	Chaotic sequence	Noise sequence	Quasi-periodic sequence
Frequency	Passed	Passed	Not passed
Block Frequency	Passed	Passed	Passed
Cumulative Sums	Passed	Passed	Not passed
Longest runs of ones	Passed	Passed	Passed
Runs	Passed	Not passed	Passed
Rank	Passed	Passed	Passed
FFT	Passed	Passed	Not passed
Non overlapping template	Passed	Not passed	Not passed
Overlapping template	Passed	Passed	Passed
Random excursions	Passed	Passed	Not passed
Random excursions variant	Passed	Passed	Passed
Universal test	Passed	Passed	Passed
Approximate entropy	Passed	Not passed	Not passed
Serial test	Passed	Passed	Passed
Linear complexity test	Passed	Passed	Passed

Table 2.4: List of the results of the NIST statistical tests performed with the chaotic signal, the electronic noise and the quasi periodic sequence. The tests have been performed analyzing 98 sequences of 1 $Mbit$ each.

The fact that it has not been possible to raise the bitrate over 1 $Gbps$ was due to the intrinsic timescales of thermal and free carrier nonlinearities. The thermal decay of region (iv) in Fig.2.10 has a characteristic time scale at the order of $\sim 30\,ns$, which correspond to a decay rate of $\sim 30\,MHz$. This means that the waveform has a finite correlation time, which limits the time interval over which two sampled points can be considered to be completely independent. The use of increasingly complex post processing algoritms help to decrease the correlation time of the original sequence, but of course there will be some maximum achievable bit rate. The latter is dictated by the timescales of the orginal process. In order to further increase the bitrate, faster chaotic waveforms are required, which means that one has to look for other modulation mechanism rather than thermal and free carrier ones.

2.5 Conclusions

In this chapter, the influence of thermal and free carrier effects on the temporal response of Silicon resonators have been studied. When the variation in the temperature, or in the free carrier concentration, arises from TPA, the associated refractive index changes become dependent on the light intensity. As a consequence, the dynamics governing the internal energy can be strongly nonlinear, even if $\chi^{(3)}$ effects are negligible. In a single optical resonator, several regimes can be enstablished. The one which sets in is determined by the characteristics of the cavity as well as from the input exciting conditions. On the same ring resonator, with $Q = 10800$ and modal volume $V_{eff} \approx 5\,\mu m^3$, a bistable output, an optical limiting regime and a self pulsing one. The latter consists in a periodic modulation of the transmitted intensity in time, even if the input excitation is continous wave. Self pulsing is seen to arise as a consequence of the periodic interplay between the resonance shifts induced by thermal and free carrier effects. The signs of the thermo optic shift and of the free carrier dispersion coefficient are opposite, so the resonance wavelength is made to oscillate with respect to the initial position in time. If the laser wavelength is tuned near resonance, also the transmittivity follows the oscillation, modulating the transmitted power. When many resonators are coupled together in the SCISSOR configuration, a new dynamic and chaotic regime enstablishes together with self pulsing. When this occurs, the light intensity at the output of the device randomly fluctuates and becomes unpredictable. The system possesses very high sensitivity to initial conditions and the generated waveforms completely lack of self similarities as the time evolves, creating a phase space which is dense of points and whose shape

resembles that of a strange attractor. All these features are strongly indicators of the presence of chaos. The conditions which regulate the onset of chaos are studied. The input laser wavelength and the input power must be chosen to set as many cavities as possible in the self pulsing regime. When a joint oscillation of three or more cavities is activated, the intracavity feedback of optical energy turns the independent self pulsing of each cavity into a collective chaotic oscillation. The system geometry has also a strong influence on chaos. If the resonances of the coupled resonators do not overlap, the collective oscillation is limited to few cavities, which does not result in a chaotic motion. Cavities have also to be designed with a sufficiently high Q/V_{eff} ratio to let self pulsing to occur. At the end of the chapter, it has been explored the possibility to use the chaotic waveforms as input seeds for the generation of random bit sequences. Using a post processing algorithm on a rough chaotic waveform, it has been possible to generate a $1\,Gbps$ random bit sequence which passed all the NIST test of randomness. The bitrate of the SCISSOR based random number generator is fundamentally upper limited by the timescales of thermal and free carrier nonlinearities, which are at the order of $\sim 30\,ns$. The corresponding raw bitrate, which is $\sim 30\,MHz$, has been enhanced by two orders of magnitude with the use of a post processing algorithm. Nevertheless, it seemed that this is the maximum achievable value. To further increase the bitrate, intrinsically faster nonlinearities are required.

Chapter 3

Multimodal Four Wave Mixing in Silicon waveguides

This chapter addresses the study of Multimodal Four Wave Mixing (MMFWM) in straight Silicon waveguides. Together with Chapter 4, it belongs to that part of the project SIQURO which aims to the realization of integrated sources of correlated photon pairs. In the first part, the concepts of Stimulated and Spontaneous FWM (sFWM and SFWM respectively) are introduced. The technique of MMFWM is then discussed as a tool for achieving an efficient process at large spectral distances from the pump, a task which will be difficult to realize using standard FWM in which all the fields involved in the process propagate in the same spatial mode order. Since the MMFWM technique requires the ability to selectively excite specific mode orders in the waveguide, the problem will be faced using two different approaches. The first method exploits the interference of two oblique beams to create a standing wave pattern at the waveguide input facet which selectively excites a specific mode order in the waveguide. Unfortunately, this method proved to be not efficient for observing MMFWM. For this reason, a second approach has been developed. The latter relies on the excitation of higher order modes in the waveguide using tilted lensed fibers. Using this method, Stimulated MMFW will be demonstrated for several modal combinations and for different waveguide widths. Even if the tilted fiber approach has been sufficient for observing Stimulated FWM, the losses were still too high for observing the spontaneous counterpart. This is why, at the end of the chapter, the design and the simulation of an integrated interferometer which mimics the oblique beam interference is proposed. In the integrated version, losses get greatly reduced, and sFWM could in principle be observed.
The experiments described in this chapter have been done in collaboration with Dr. Mattia Mancinelli and Mr. Stefano Signorini, who also performed the major part of the simulations.

3.1 Stimulated and Spontaneous FWM in straight Silicon waveguides

The process of SFWM is firstly introduced. FWM is a process which is mediated by the $\chi^{(3)}$ nonlinearity of the material, and which couples four waves at frequencies ω_i, with $i = 1, 2, 3, 4$. Suppose that the $\chi^{(3)}$ material, of index of refraction $n(\omega)$, infinitely extends over the transverse dimensions x and y, where the term transverse applies to the z direction, along which light is propagating. The total electric field constituted by the four waves can be written as $E(z,t) = \sum_i \frac{1}{2}\left(A_i(z)e^{i(\omega_i t - k_i z)} + c.c\right)$, in which $k_i = \frac{\omega_i}{c}n(\omega_i)$ is the wavevector and $A_i(z)$ is a slowly varying envelope. The latter condition implies that $\frac{d^2 A_i}{d^2 z} \ll \omega_i^2 A_i$. The amplitudes A_i

are normalized in such a way that the light intensity $|I_i|^2$ is given by $|I_i|^2 = \frac{1}{2Z}|A_i|^2$ ($Z = \sqrt{\frac{\mu_0\mu_r}{\epsilon_0\epsilon_r}}$ is the characteristic impedance of the medium). In absence of $\chi^{(3)}$ nonlinearities, each of the four waves evolves following the Helmoltz equation:

$$\left(\nabla^2 + k_i^2\right) E_i = 0 \tag{3.1}$$

which gives $A_i(z) = C_i$, where C_i are constants which depend on the value of the field at $z = 0$. In other terms, each wave evolves freely and they are not coupled. In particular, if the initial amplitude $C_i = 0$, then there is no possibility that such frequency will be generated inside the material. The picture changes when a $\chi^{(3)}$ nonlinearity is present. In this case, the Helmoltz equation modifies to the more general wave equation [51, 2]:

$$\left(\nabla^2 - \frac{n(\omega)^2}{c^2}\frac{\partial^2}{\partial^2 t}\right) E = \mu_0 \frac{\partial^2 P^{NL}}{\partial^2 t} \tag{3.2}$$

where the nonlinear polarization P^{NL} is given by:

$$\begin{aligned} P^{NL} &= \epsilon_0 \chi^{(3)} E^3 \\ &= \epsilon_0 \chi^{(3)} \sum_{ijk} \left(\frac{1}{8} A_i A_j A_k e^{i(\omega_i+\omega_j+\omega_k)t} e^{-i(k_i+k_j+k_k)z} + \frac{3}{8} A_i A_j^* A_k e^{i(\omega_i-\omega_j+\omega_k)t} e^{-i(k_i-k_j+k_k)z} \right) + c.c \end{aligned} \tag{3.3}$$

Each of the index i, j, k runs from 1 to 4. From Eq.3.3, it can be seen that new frequencies are created. These are $\omega_{ijk} = \omega_i + \omega_j + \omega_k$ and $\omega'_{ijk} = \omega_i - \omega_j + \omega_k$. Both terms involve the interaction of four waves $(\omega_{ijk}, \omega_i, \omega_j, \omega_k)$, reason why they are called Four Wave Mixing terms. The left hand side of Eq.3.2 has terms which oscillate in time as $e^{i\omega_l t}$, so they are coupled only to those terms at the right hand side which oscillate at the same frequency. Since, in general, $\omega_{ijk} \neq \omega'_{ijk}$, only one of the two terms of Eq.3.3 has to be considered. If $\omega_l = \omega_i + \omega_j + \omega_k$, then the coupled term is the one at ω_{ijk}, otherwise if $\omega_l = \omega_i - \omega_j + \omega_k$, only the term at ω'_{ijk} has to be kept. In what follows, it is assumed that only the term at ω'_{ijk} partecipates to the FWM process. In general, it is customary to refer as FWM the interaction of four waves which satisfy $\omega_l = \omega_i - \omega_j + \omega_k$, while the process $\omega_l = \omega_i + \omega_j + \omega_k$ is called sum frequency generation. Third harmonic generation is a special case of sum frequency generation, in which $\omega_i = \omega_j = \omega_k$. The equality:

$$\omega_l = \omega_i - \omega_j + \omega_k \tag{3.4}$$

is called the energy conservation relation. In a quantum mechanical description, Eq.3.4 corresponds to the annihilation of two photons at frequencies ω_l and ω_j with the simultaneous creation of two photons at frequencies ω_i and ω_k. This is sketched in Fig.3.1(a).

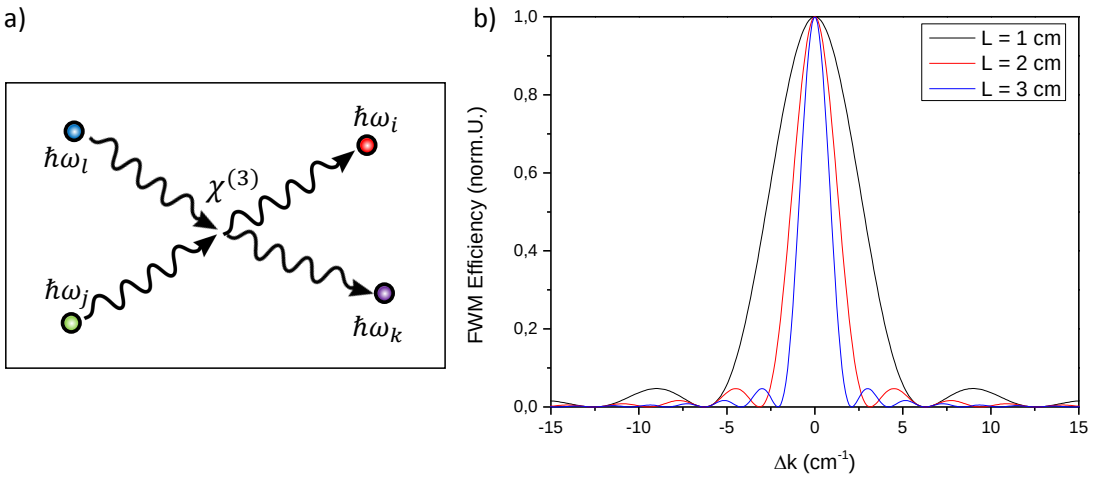

Figure 3.1: (a) Description of FWM in terms of photons. Two photons at frequencies ω_l and ω_j are annihilated for creating other two photons at frequencies ω_i and ω_k. (b) Efficiency of the FWM process as a function of the phase mismatch parameter Δk for different values of sample length L.

Without losing in generality, it is possible to set $\omega_l = \omega_1$, $\omega_i = \omega_2$, $\omega_j = \omega_3$ and $\omega_4 = \omega_k$ into Eq.3.4. By inserting the expression for the field E into Eq.3.2, and by using the slowly varying envelope approximation introduced above, one obtains the set of coupled equations:

$$\frac{dI_1}{dz} = -i\gamma_1 \left[(2|I_2|^2 + 2|I_3|^2 + 2|I_4|^2 + |I_1|^2)I_1 + 2I_2 I_3^* I_4 e^{-i\Delta kz}\right] \tag{3.5}$$

$$\frac{dI_2}{dz} = -i\gamma_2 \left[(2|I_1|^2 + 2|I_3|^2 + 2|I_4|^2 + |I_2|^2)I_2 + 2I_1 I_4^* I_3 e^{-i\Delta kz}\right] \tag{3.6}$$

$$\frac{dI_3}{dz} = -i\gamma_3 \left[(2|I_2|^2 + 2|I_1|^2 + 2|I_4|^2 + |I_3|^2)I_3 + 2I_2 I_1^* I_4 e^{-i\Delta kz}\right] \tag{3.7}$$

$$\frac{dI_4}{dz} = -i\gamma_4 \left[(2|I_2|^2 + 2|I_3|^2 + 2|I_1|^2 + |I_4|^2)I_4 + 2I_1 I_2^* I_3 e^{-i\Delta kz}\right] \tag{3.8}$$

where $\gamma_i = \frac{2n_2\omega_i}{c}$ and:

$$\Delta k = k_2 - k_3 + k_4 - k_1 \tag{3.9}$$

The quantity Δk is called the phase mismatch parameter. The various terms on the right hand side of Eqs.3.5-3.8 have different meaning:

- The term proportional to $|I_i|^2$ in the equation for I_i is called Self Phase Modulation (SPM). For example, if Eq.3.5 is solved neglecting the term $I_2 I_3^* I_4 e^{-i\Delta kz}$ and the ones proportional to $|I_j|^2$ with $j \neq 1$, one gets $I_1(z) = I_{10} e^{-i\gamma|I_{10}|^2 z}$. Then $|I_1|^2$ inflluences the phase of the same I_1. This is why it is called SPM.

- The term proportional to $|I_j|^2$ in the equation for I_i, with $i \neq j$, is called Cross Phase Modulation (XPM). For example, if Eq.3.5 is solved neglecting the term $I_2 I_3^* I_4 e^{-i\Delta kz}$ and the one proportional to $|I_1|^2$, one gets $I_1(z) = I_{10} e^{-i2\gamma(|I_{20}|^2 + |I_{30}|^2 + |I_{40}|^2)z}$ (the fields I_j with $j \neq 1$ have been assumed in the form $I_j = I_{j0} e^{i\phi_j}$, i.e, they do not change their amplitude during propagation. This is an approximation.). The intensity of the fields 2, 3 and 4 ($|I_2|^2, |I_3|^2$ and $|I_4|^2$ respectively) inflluences the

phase of the field 1. This is why it is called XPM.

- The term proportional to $2I_iI_j^*I_ke^{-i\Delta kz}$ is called the FWM term, and acts as a polarization source for the field at frequency $\omega_l = \omega_i - \omega_j + \omega_k$.

The FWM process which is of interest for the generation of photon pairs is the one in which $\omega_1 = \omega_3 = \omega_p$, and it is sketched in Fig.3.2 (non degenerate FWM).

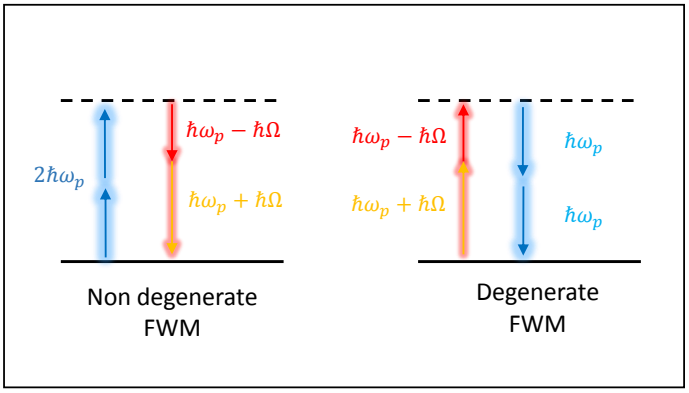

Figure 3.2: Non degenerate and degenerate FWM. In the first case, two equal photons annihilates to produce two photons at different frequncies. In the second case, two photons at different frequency annihilates to generate two photons at equal frequency.

The wave at ω_p is called the pump wave. For historical reasons, the fields at ω_2 and ω_4 are called the signal and idler waves respectively. By using this convention, it has been assumed that $\omega_2 = \omega_s > \omega_4 = \omega_i$, since the signal has higher frequency than the idler. The energy conservation relation of Eq.3.4 becomes $2\omega_p = \omega_s + \omega_i$, and the corresponding phase matching relation:

$$2\omega_p n(\omega_p) = \omega_s n(\omega_s) + \omega_i n(\omega_i) \tag{3.10}$$

By writing $\omega_s = \omega_p + \Omega$, it comes out from Eq.3.4 that the idler frequency is $\omega_i = \omega_p - \Omega$, i.e., the signal and idler frequencies are simmetrically located with respect to the one of the pump. The reverse FWM process, shown in Fig.3.2 (degenerate FWM), is also possible. In this case, two pump fields, one at $\omega_{p1} = \omega_p - \Omega$ and one at $\omega_{p2} = \omega_p + \Omega$ can be combined to produce two waves at the degenerate frequency ω_p [198].
The set of equations from (3.5) to (3.8) can be solved under some approximations. At first, the pump field is considered more intense than the signal one, which in turn is considered much stronger than the idler, i.e, $|I_p|^2 \gg |I_s|^2 \gg |I_i|^2$. As a consequence, the FWM and the XPM term can be neglected in the pump equation. The solution for the pump field is then $I_p(z) = I_{p0}e^{-i\gamma_p|I_{p0}|^2 z}$. This is usually called the undepleted pump approximation, since only the phase changes during propagation. In the equation for the signal, the FWM term is neglected and only the SPM and XPM terms are kept, giving as solution $I_s(z) = I_{s0}e^{-i\gamma_s(|I_{s0}|^2+2|I_{p0}|^2)z}$. Then, by inserting these expressions into the equation for the idler, and by considering only the FWM term, the following expression for the idler intensity $|I_i|^2$ is obtained:

$$|I_i(z)|^2 = \frac{2}{\Delta k^2}|\gamma|^2|I_{p0}|^4|I_{s0}|^2\left(1-\cos(\Delta k' z)\right) \tag{3.11}$$

which for $z \neq 0$ can be rewritten as:

$$|I_i(z)|^2 = |\gamma|^2|I_p|^4|I_s|^2L^2 sinc\left(\frac{\Delta k' z}{2\pi}\right) \tag{3.12}$$

The new phase mismatch parameter becomes:

$$\Delta k' = \Delta k - 2(\gamma_s - \gamma_p)|I_{p0}|^2 - \gamma_s|I_{s0}|^2 \tag{3.13}$$

which takes into account the wavevector correction due to XPM. In what follows, these corrections will be neglected since, for the experiment described in section 3.4, they are several orders of magnitude lower than Δk. Several considerations can be done by looking at Eq.3.12. The first is that the generated idler wave increases quadratically with the pump intensity (hence the pump power) and linearly with the signal intensity (hence the signal power). The second, and most important, is that the efficiency of the process depends quadratically on the sample length and on the phase mismatch parameter Δk. Fig.3.1(b) plots the $sinc^2$ term as a function of Δk when the length of the material is fixed to L. It can be seen that the efficiency is maximum at $\Delta k = 0$ and decreases to zero as the mismatch approaches $\Delta k = \frac{2\pi}{L}$. The condition $\Delta k = 0$ is called perfect phase matching, and is a direct consequence of the wavevector conservation of all the waves involved in the FWM process. In a quantum mechanical description, this corresponds to the momentum conservation between the two annihilated pump photons and the generated signal and idler photons. As the phase mismatch increases, the maximum length over which the process is efficient inversely decreases. This length is called the FWM coherence length and is given by $L_c = \frac{2\pi}{\Delta k}$. It comes out that for achieving an efficient FWM, which scales as L^2, the condition $\Delta k = 0$ has to be satisfied. As indicated by Eq.3.10, the phase matching relation reduces to energy conservation if the refractive index of the material does not depend on frequency, i.e., the medium is not dispersive. Since Eq.3.4 is naturally satisfied, perfect phase matching is always achieved in a non dispersive medium. However, this condition is just an idealization, since every material has a refractive index which depends on the frequency. As a consequence, some techniques have to be used in order to realize the condition $\Delta k = 0$. One of the most implemented exploits the birifrangence of the material [137]. The pump and signal waves propagate on different directions, which corresponds to the ordinary and the extraordinary waves. The latter experiences a refractive index which depends on the direction of propagation, which is then chosen to satisfy Eq.3.10. Another technique, named periodically poling [165], will be discussed in Chapter 5. These techniques are not easily scalable to integrated Silicon devices, because they are affected from both fundamental issues and fabrication problems. For example, the elements of the $\chi^{(3)}$ tensor of Silicon which couples cross polarized fields (the case of ordinary and extraordinary waves) are in average one third of those which couple copolarized ones [127], so the use of birifrangence is intrinsically not efficient in Silicon. In order to overcome these difficulties, the method of MMFWM in Silicon nanowires is developed (Section 3.2).

The starting point for the derivation of Eqs.3.5-3.8 is the wave equation (3.2) for a medium which infinitely extends over the transverse dimensions x and y. As a consequence of this, the solutions are plane waves in which the amplitude and phase only change along z, the direction of propagation. In a waveguiding geometry, modal confinenement has to be considered. The electric field of the j^{th} waveguide mode can be written as $E_j = \frac{1}{2}\left(E_{0j}A_j(z)u_j(x,y)e^{-i(\beta_j z - \omega_j t)} + c.c\right)$, where E_{0j} is a constant amplitude, $u_j(x,y)$ is the transverse profile, A_j a slowly varying envelope and $\beta_j = \frac{\omega_j n_{eff,j}(\omega_j)}{c}$ is the propagation constant. The corresponding set of FWM equations for the coupled waveguide modes representing the pump, the signal and the idler (see full derivation in [2]) is:

$$\frac{dA_p}{dz} = \frac{in_2\omega_p}{c}\left(f_{pp}|A_p|^2 + 2f_{ps}|A_s|^2 + 2f_{pi}|A_i|^2 + f_{ppsi}A_sA_iA_p^*e^{-i\Delta kz}\right) \tag{3.14}$$

$$\frac{dA_s}{dz} = \frac{in_2\omega_s}{c}\left(f_{ss}|A_s|^2 + 2f_{sp}|A_p|^2 + 2f_{si}|A_i|^2 + 2fA_p^2A_i^*e^{-i\Delta kz}\right) \tag{3.15}$$

$$\frac{dA_i}{dz} = \frac{in_2\omega_i}{c}\left(f_{ii}|A_i|^2 + 2f_{is}|A_s|^2 + 2f_{ip}|A_p|^2 + 2fA_p^2A_s^*e^{-i\Delta kz}\right) \tag{3.16}$$

where the parameters f_{ijkl} and f_{ij} (with i,j,k,l that can be replaced by p,s,i) are defined as:

$$f_{ijkl} = \frac{\int_{wg} u_i^* u_j^* u_k u_l \, dxdy}{\left[\left(\int |u_i|^2\, dxdy\right)\left(\int |u_j|^2\, dxdy\right)\left(\int |u_k|^2\, dxdy\right)\left(\int |u_l|^2\, dxdy\right)\right]^{1/2}} \tag{3.17}$$

$$f_{ij} = \frac{\int |u_i|^2|u_j|^2\, dxdy}{\left(\int |u_i|^2\, dxdy\right)\left(\int |u_j|^2\, dxdy\right)} \tag{3.18}$$

Essentially, the structure of the FWM equations (3.5)-(3.8) is mantained, but the effect of modal confinement is taken into account by the overlap integrals in the parameters f_{ijkl} and f_{ij}. Diagonal terms such as f_{ii} correspond to the modal effective areas, while the term f_{ijkl} is called the FWM effective area. An important difference with respect the plane wave case discussed before is that the term f_{ijkl} can be zero for certain modal combinations, which means that FWM can not occur even if $\Delta k = 0$. This happens if the product of the four fields in the numerator of Eq.3.17 is an odd function. In this case, the integral over the waveguide cross section gives exactly zero. This fact will strongly influence the choice of the mode order combinations implemented for MMFWM in Section 3.4. The phase mismatch parameter Δk is now given by:

$$2\omega_p n_{eff,p}(\omega_p) = \omega_s n_{eff,s}(\omega_s) + \omega_i n_{eff,i}(\omega_i) \tag{3.19}$$

which is identical to the one of Eq.3.10 except that the material refractive index is replaced by the modal effective index.

Up to now, the set of FWM equations have been derived on the basis of a complete classical treatement, since the starting point was the wave equation of Eq.3.2. In this derivation, the presence of the signal field is necessary for generating the idler, since as it is indicated in Eq.3.12, the idler intensity is proportional to the signal one. In other words, the signal stimulates the process, reason why it is referred as Stimulated FWM. On the contrary, in the Spontaneous case, only the pump fied is required, and the signal and idler photons are spontaneously generated at frequencies $\omega_p \pm \Omega$. As it can be deduced, sFWM must have an intrinsically quantum mechanical explanation. Qualitatively speaking, the input signal can be seen to be provided by the vacuum fluctuations of the quantized electric field. Such a feature can not be explained in classical terms, and one has necessary to refer to quantum electrodynamics. It is possible to prove that, while the mean value of the electric field operator $E(\mathbf{r})$ at a point r of space gives zero if evaluated on the vacuum state $|0\rangle$, i.e, $\langle 0|\, E(\mathbf{r})\, |0\rangle = 0$ [199], the variance does not vanish, and gives [199]:

$$\langle 0|\, E^2(\mathbf{r})\, |0\rangle = \sum_j \frac{\hbar\omega_j}{2\epsilon_0 V} \tag{3.20}$$

where ω_j is the angular frequency of the j^{th} radiation mode of the free space and V is the volume over which the electric field is quantized (in this case it is considered to enclose free space). It can be seen that the variance in Eq.3.20 diverges, since no upper limit exists on the value that ω_j could take. However, since the physical measurable quantity is not the electric field in a single point of space but the average of the electric field over a finite volume r_o^3, it can be proved that in this case the variance becomes finite, and that the electric field fluctuations around the zero mean value possess a characteristic correlation time of $\approx \frac{1}{cr_0}$ [199]. These noise fluctuations can be qualitatively interpreted as the input seed involved in the activation of sFWM process.

Since sFWM will not be touched in the experiments described in Section 3.4, only a brief overview will be given in the following. The electromagnetic field inside the waveguide in absence of $\chi^{(3)}$ effects evolves freely

following the unperturbed hamiltonian H_0:

$$H_0 = \int \left(\frac{1}{2}\mathbf{D}_0 \cdot \mathbf{E}_0 + \frac{1}{2}\mathbf{B}_0 \cdot \mathbf{B}_0 \right) d\mathbf{r} \tag{3.21}$$

in which $\mathbf{E}_0, \mathbf{B}_0$ and $\mathbf{D}_0$ are the unperturbed electric field, magnetic field and displacement vectors inside the waveguide respectively. The hamiltonian operator H_0 in Eq.3.21 represents the total electromagnetic energy which is stored inside the waveguide. By performing a canonical quantization of the modal fields, the operator H_0 can be rewritten in terms of creation and annihilation operators as [200] :

$$H_0 = \int \hbar\omega_k a_k^\dagger a_k \, dk \tag{3.22}$$

in which $\hbar\omega_k$ is the energy of the photon created with wavevector k inside the waveguide by the operator $a_k^\dagger$. Here, the wavevector k uniquely defines the energy of the photon, therefore the waveguide is assumed to support only the fundamental mode. The connection between the electric field operator E_k and the creation/annihilation operators is provided by:

$$E_k = e_k u_k(x,y) e^{-i(\beta_k z - \omega_k t)} a_k + c.c \tag{3.23}$$

where e_k is a normalization constant. Similarly to the quantization of H_0, one can quantize also the nonlinear polarization P^{NL} introduced in Eq.3.3, and write the hamiltonian H under the presence of $\chi^{(3)}$ nonlinearities as $H = H_0 + H^{NL}$, where H^{NL} is given by (see Ref.[180] (supplementary materials)):

$$H^{NL} = -\gamma_0 \int dk_1 dk_2 dk_3 dk_4 a_{k1}^\dagger a_{k2}^\dagger a_{k3} a_{k4} e^{-i(k_1+k_2-k_3-k_4)z} \, dxdy + c.c \tag{3.24}$$

where γ_0 is a constant which includes the nonlinear coefficient γ introduced in Eqs.3.8-3.10. The pump is represented by a coherent state $|\alpha\rangle$ oscillating at ω_p and carrying an average number of photons $|\alpha|^2$. At the same time the initial signal and idler modes at ω_i and ω_s are not occupied. The initial radiation state can then be written as $|\Psi_{in}\rangle = |\alpha\rangle |0_s, 0_i\rangle$, where $|0_s, 0_i\rangle$ denotes the absence of photons in the signal and idler modes. The output state at time t can be evaluated by:

$$|\Psi_{out}(t)\rangle = exp\left[-\frac{i}{\hbar} \int_0^t H^{NL}(t')dt' \right] |\Psi_{in}\rangle \tag{3.25}$$

where H^{NL} is written in the interaction picture [201]. At first order in H^{NL}, the output state after a sufficiently long time interval Δt is given by (see Ref.[180](supplementary materials)):

$$|\Psi_{out}\rangle = |\alpha\rangle |0_s, 0_i\rangle + \frac{\alpha^2 \gamma_0 L}{\sqrt{2}} sinc(\frac{\Delta k L}{2\pi}) |\alpha\rangle |1_s, 1_i\rangle \tag{3.26}$$

where for sufficiently long it means that the corresponding uncertaintly in the energies of the signal and idler photon $\Delta E_{s,i}$ satisfies $\Delta E_{s,i} \Delta t \ll 1$. The phase mismatch is given by $\Delta k = 2k(\omega_p) - k(\omega_s) - k(\omega_i)$. For clearness, in deriving Eq.3.26, it has been assumed that only one signal/idler pair is produced, which is the one that satisfy $\Delta k \approx 0$. Of course this does not correspond to a realistic case, in which pairs are produced in all the frequency range in which $\Delta k < \frac{2\pi}{L_c}$, but it allows to get a direct insight into the physical situation. Eq.3.26 tells that even in absence of a stimulating signal field, a pair of photons symmetrically located with respect to the frequency of the pump are created. The probability of detecting the pair is proportional to $\frac{\alpha^4 \gamma_0^2 L^2}{2} sinc^2(\frac{\Delta k L}{2\pi})$, so the flux of photon pairs is still quadratic in the pump power and in the sample length as in the stimulated case. The photon pair is said to be energy entangled, since the energy of one photon determines the energy of the other and vice versa.

3.2 Multimodal phase matching technique

In the previous section, it was observed that the phase mismatch Δk regulates the efficiency of the FWM process, both in the stimulated and in the spontaneous version. In particular, the efficiency is maximized by making $\Delta k = 0$. Due to the dispersion of the refractive index, in general $\Delta k \neq 0$ and the efficiency of the process is very low. Given a single mode waveguide, with propagation constant $\beta(\omega)$, the phase matching relation of Eq.3.10 can be written up to the second order in the pump detuning Ω as [2]:

$$\Delta k \approx \beta_2(\omega_p)\Omega^2 \tag{3.27}$$

From Eq.3.27 it can be seen that if $\beta_2 \neq 0$, the phase mismatch quadratically grows as the spectral distance Ω between the signal/idler photons and the pump increases. Efficient FWM is then possible only in a narrowband spectral region in the proximity of the pump wavelength. The waveguide can be engineered to achieve $\beta_2 = 0$ at ω_p, in this case the expression in Eq.3.10 has to be expanded up to the fourth order in Ω to give:

$$\Delta k \approx \frac{\beta_4}{14}\Omega^4 \tag{3.28}$$

in which the fourth order dispersion $\beta_4 = \frac{d^4\beta}{d^4\omega}$ has been introduced. Again, the efficiency decreases as Ω increases. Therefore, if one wants to achieve efficient FWM at large detunings from the pump, a possible technique is to engineer the waveguide in such a way that the sign of the GVD is opposite to the one of the β_4 dispersion, in order to obtain $\beta_2\Omega^2 + \frac{\beta_4}{14}\Omega^4 = 0$. This technique has been used in Ref. [108] to achieve a spectral translation from a signal at $2.44\,\mu m$ to an idler at $1.62\,\mu m$ using stimulated FWM in a dispersion engineered single mode waveguide. However, this method possess the drawback of being very sensitive to fabrication defects. Indeed, the value of β_4 is strongly affected by small variations in the waveguide cross section, so even small imperfections could compromise the outcome of the experiment.
Here it is presented a more robust technique, called MultiModal Phase Matching (MMPM). The latter has been already implemented in optical fibers for broadband FWM [2]. The essence of MMPM is to exploit the different effective index dispersion of the optical modes in a waveguide (shown in Fig.3.3) to achieve perfect phase matching. The pump, signal and idler waves are let to propagate in different mode orders, associated to the effective indexes $n_{eff,p}, n_{eff,s}$ and $n_{eff,i}$. The orders are chosen to satisfy Eq.3.19. Fig.3.4 shows an example for a silicon waveguide of cross section $3.05\,\mu m \times 0.25\,\mu m$, in which $\Delta k = 0$ is achieved when the signal propagates into the 2^{rd} order mode at $1.464\,\mu m$, the pump into the 3^{rd} order mode at $1.55\,\mu m$ and the idler into the 4^{th} order mode at $1.644\,\mu m$.

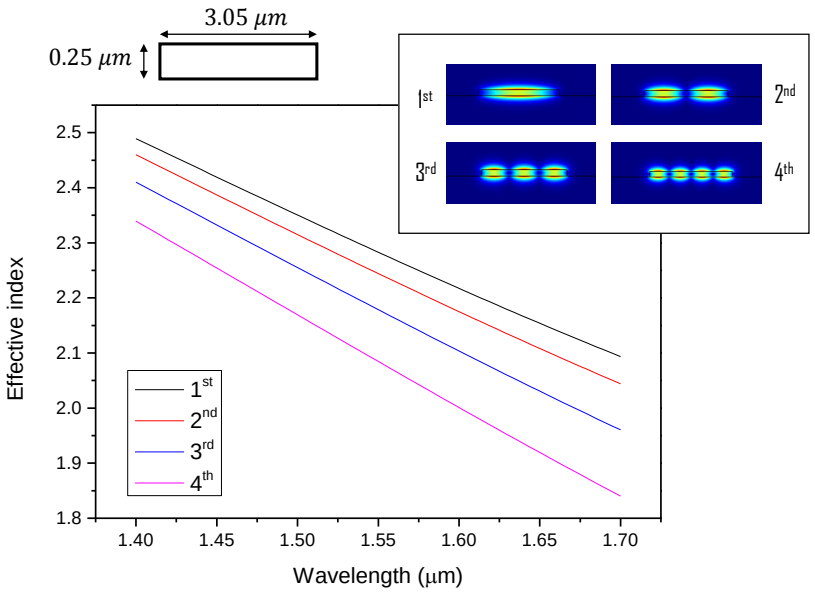

Figure 3.3: Effective index dispersion for the four lowest order modes in TM polarization. The inset shows the intensity patterns of the main component of the electric field for each mode. A sketch of the waveguide cross section is shown in the upper panel.

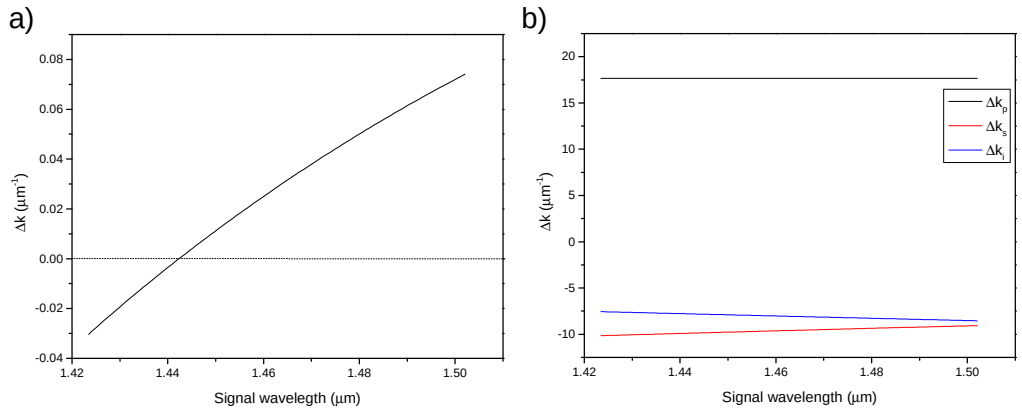

Figure 3.4: (a) Phase mismatch parameter Δk for the mode order combination $(3, 2, 4)$ (pump order, signal order, idler order) in a $3.05\,\mu m \times 0.25\,\mu m$ waveguide. All the modes have TM polarization. The curve crosses the zero at the signal wavelength $\lambda_s = 1.464\,\mu m$. (b) The different contributions to the total phase mismatch Δk given by $\Delta k = \Delta k_p + \Delta k_s + \Delta k_i = \frac{2n_{eff,p}(\lambda_p)}{\lambda_p} - \frac{n_{eff,s}(\lambda_s)}{\lambda_s} - \frac{n_{eff,i}(\lambda_i)}{\lambda_i}$. The idler wavelength is expressed as a function of the signal one as $\lambda_i = \left(\frac{2}{\lambda_p} - \frac{1}{\lambda_s}\right)^{-1}$.

The different dispersion of the mode orders can be engineered by changing the waveguide geometry. The phase matching relation of Eq.3.10 for MMPM can be written up to the first order in the pump detuning Ω as:

$$\Delta k \approx \Delta k_{deg} + \Omega\left(\beta_{1.i}(\omega_p) - \beta_{1,s}(\omega_p)\right) \tag{3.29}$$

in which Δk_{deg} is the phase mismatch at the degenerate pump wavelength, and is given by $\Delta k_{deg} = 2\beta_p(\omega_p) - \beta_s(\omega_p) - \beta_i(\omega_p)$. Note that this term would be equal to zero if all the waves were propagating into the same mode order. The essence of MMFWM is to balance the contribution of Δk_{deg} with the difference in the first

order dispersions of the signal and idler modes. If $\Delta k_{deg} < 0$, then the group velocity of the signal has to exceed the one of the idler in orde to get $\Delta k = 0$, Otherwise, if $\Delta k_{deg} > 0$, it is the group velocity of the idler that has to be greater than the one of the signal. Since the relation in Eq.3.29 only depends on β_1, MMPM is intrinsically less sensitive to fabrication imperfections than the phase matching technique based on the balance between the β_2 and the β_4 term.

3.3 Selective mode excitation in multimode waveguides

In order to implement MMPM, one has to be able to selectively excite specific mode orders. For example, in the combination reported in Fig.3.3, it is required to couple the pump field into the third order mode and the signal field into the second order mode. An easy way to implement selective mode excitation is through an asymmetrical directional coupler [70, 71, 202]. The effective index of a higher order mode is matched to the one of the fundamental mode of a narrower waveguide. When the two waveguides are evanescently coupled, and light is sent into the fundamental mode of the narrower waveguide, after a certain propagation distance the energy gets completely transferred into the higher order mode of the larger waveguide. An example is reported in Fig.3.5.

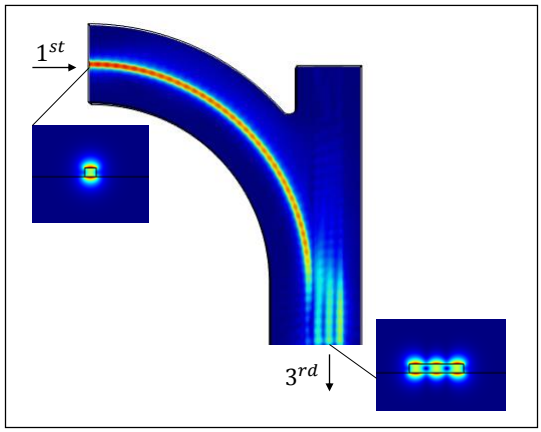

Figure 3.5: Excitation of the third order TM mode using an asymmetric directional coupler. The narrow waveguide has a cross section of $326\,nm \times 220\,nm$ while the multimode waveguide of $1550\,nm \times 220\,nm$. The two waveguides are separated by a gap of $160\,nm$. The effective index of the fundamental mode of the $326\,nm$ wide waveguide is the same as the effective index of the third order mode of the $1.55\,\mu m$ waveguide, and after $5.25\,\mu m$ the power transfer is completed

The weakness of this method is that it requires both high fabrication resolution and tight tolerances in the waveguide size. The resolution is required in order to realize small coupling gaps, while the precision in the waveguide size is required to perfectly match the effective indexes. The photolithographic process implemented for the fabrication of the samples described in Section 3.4 is $293\,nm$ DUV lithography. The minimum allowed coupling gap is $400\,nm$, while the tolerance on the final waveguide dimension is $\pm 20\,nm$. These fabrication limitations make difficult to implement the approach based on the use of directional couplers. In order to overcome this limitation, the higher order modes are directly excited at the input of the multimode waveguide without the use of a directional coupler. This is done by matching the field distribution of the exciting radiation to the one of the optical modes that have to be selectively excited. Fig.3.6 helps to understand why this occurs.

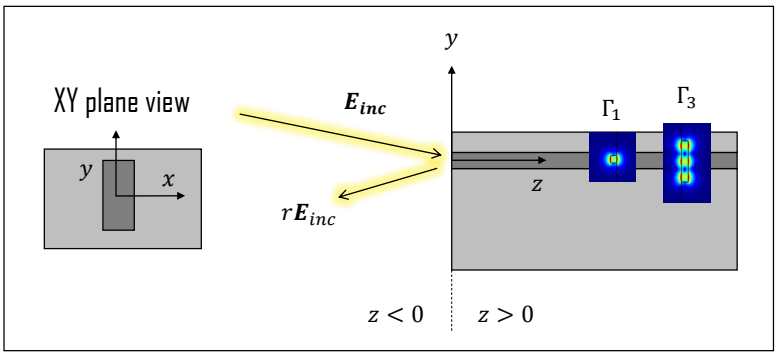

Figure 3.6: Coupling of an incoming electric field E_{inc} into different waveguide mode orders. The reflected field at the interface is $\mathbf{E}_{ref} = r\mathbf{E}_{inc}$. The guided fields inside the waveguide have modal amplitudes Γ_j.

Here, the waveguide input facet is placed in the plane $z = 0$, and the tangential component of the incoming electric field is $\mathbf{E}_{inc}(x, y)$. The tangential component of the electric field inside the waveguide $\mathbf{E}_{wg}$ can be expanded on the basis of its orthogonal guided modes $\mathbf{e}_j$ as:

$$\mathbf{E}_{wg}(x, y) = \sum_j \Gamma_j \mathbf{e}_j(x, y) \tag{3.30}$$

where Γ_j is the modal amplitude. Following the derivation of Ref.[52], the orthogonality relation between two different modes $\mathbf{e}_j$ and $\mathbf{e}_k$ $(j \neq k)$ is given by:

$$\frac{1}{2} \int Re(\mathbf{e}_j \times \mathbf{h}_k^*) \cdot \hat{\mathbf{z}}\, dxdy = 0 \tag{3.31}$$

where $\mathbf{h}_k$ denotes the magnetic displacement vector of mode k. As a consequence of the boundary between the waveguide and the free space region at $z < 0$, a portion $\mathbf{E}_{ref}$ of the incoming field is reflected. As a good approximation, $\mathbf{E}_{ref}$ can be written as $\mathbf{E}_{ref} = r\mathbf{E}_{inc}$, where r is the Fresnel reflection coefficient for a plane wave which impinges at the dielectric boundary between two media [203]. This coefficient depends on the angle of incidence, the polarization of light and on the refractive index contrast. The index of the medium which contains the waveguide is assumed to be the one of Silicon. Since the tangential component of the electric field must be continuos at the interface, one can write :

$$\mathbf{E}_{inc}(x, y)(1 + r) = \sum_j \Gamma_j \mathbf{e}_j(x, y) \tag{3.32}$$

By exploting the orthogonality condition of Eq.3.31, it is possible to isolate the coefficients Γ_j, which then get the following expression:

$$\Gamma_j = \frac{(1 + r) \int \left(\mathbf{E}_{inc} \times \mathbf{h}_j^*\right) \cdot \hat{\mathbf{z}}\, dxdy}{\int \left(\mathbf{e}_j \times \mathbf{h}_j^* \cdot \hat{\mathbf{z}}\right)\, dxdy} \tag{3.33}$$

The ratio between the power coupled into the j^{th} mode $P_j = \frac{1}{2}|\Gamma_j|^2 \int Re(\mathbf{e}_j \times \mathbf{h}_j^*) \cdot \hat{\mathbf{z}}\, dxdy$ and the incident power $P_{inc} = \int Re(\mathbf{E}_{inc} \times \mathbf{H}_{inc}^*) \cdot \hat{\mathbf{z}}\, dxdy$, indicated as $\eta_j = \frac{P_j}{P_{inc}}$, is then:

$$\eta_j = (1 + r)^2 \frac{\left(\int \left(\mathbf{E}_{inc} \times \mathbf{h}_j^*\right) \cdot \hat{\mathbf{z}}\, dxdy\right)^2}{\left(\int \mathbf{E}_{inc} \times \mathbf{H}_{inc}^* \cdot \hat{\mathbf{z}}\, dxdy\right) \left(\int \mathbf{e}_j \times \mathbf{h}_j^* \cdot \hat{\mathbf{z}}\, dxdy\right)} \tag{3.34}$$

As a first approximation, it is possible to consider the guided modes to have a dominant component of the electric field along a specific direction, and neglect all the others in the computation of the numerator in

Eq.3.34. With reference to Fig.3.6, the dominant components are x for TE modes and y for the TM ones. In this way, it is possible to express the magnetic displacement $\mathbf{h}_j^*$ as $\mathbf{h}_j^* = \frac{1}{Z_{eff,j}}\mathbf{e}_j^*$, where $Z_{eff,j} = \frac{c\mu_0}{n_{eff,j}}$ is the effective impedance of the field inside the waveguide. The same approximation can be done for the incoming field $\mathbf{E}_{inc}$, for which it is possible to write $\mathbf{H}_{inc}^* = \frac{1}{Z_{inc}}\mathbf{E}_{inc}^*$ (with $Z_{inc} = \frac{c\mu_0}{n^2}$), thus simplifying Eq.3.34 to :

$$\eta_j = \frac{(1+r^2)Z_{inc}}{Z_{eff,j}} \cdot \frac{\left(\int (\mathbf{E}_{inc} \cdot \mathbf{e}_j^*)\, dxdy\right)^2}{\left(\int |\mathbf{E}_{inc}|^2\, dxdy\right)\left(\int |\mathbf{e}_j|^2\, dxdy\right)} \tag{3.35}$$

which is the quantity that is evaluated for estimating the percentage of power which is coupled from the incident field $\mathbf{E}_{inc}$ to the j^{th} mode of the waveguide. The highest value of η_j is obtained when the ratio between the integral quantities is maximized. This happens when $\mathbf{E}_{inc} = \mathbf{e}_j$. In that case, the integral at the numerator becomes equal to the one at the denominator and their ratio is equal to one. The condition $\mathbf{E}_{inc} = \mathbf{e}_j$ tells that if one wants to selectively excite a specific mode order j inside the waveguide, one has to shape the input field in such a way that its pattern is identical to the one of the guided mode.

3.3.1 Interference of two oblique beams

As can be appreciated from Fig.3.3, the modal field profiles resemble standing wave patterns, in which maxima and minima are separated by nodal points. The period Λ depends on the modal order j and on the width of the waveguide w. For well confined modes (i.e., having a modal confinement factor > 0.9), the period is well approximated by $\Lambda = \frac{w}{j}$. As a natural consequence, if one is able to generate at the input of the waveguide facet a standing wave pattern of the same period, the overlap integral in the numerator of Eq.3.35 will be maximized as the corresponding coupled power. As sketched in Fig.3.7, the standing wave pattern can be created by the interference of two waves which form between them an angle 2θ.

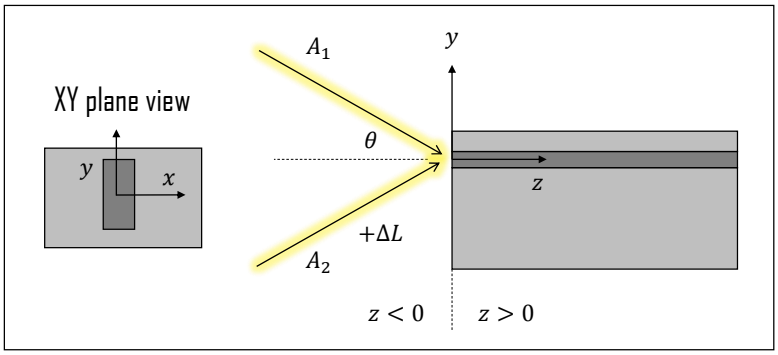

Figure 3.7: Interference of two oblique beams of amplitude A_1 and A_2 which travels at a relative angle 2θ. The plane which contains the waveguide facet is xy. The center of the waveguide facet is placed at $(x, y) = (0, 0)$. The medium at $z < 0$ is uniform and with refractive index n.

For simplicity, the first field is decribed by the plane wave $A_1 = A_{10}e^{-i|k|\sin\theta y}$, while the second by $A_2 = A_{20}e^{i(|k|\sin\theta y + |k|\Delta L)}$, where $|k|\Delta L$ is a phase difference that could exists if the two incoming waves do not travel along paths of equal length. At the plane $z = 0$, where the waveguide facet is placed, the intensity pattern is:

$$I(\theta) = |A_{10}|^2 + |A_{20}|^2 + 2A_{10}A_{20}\cos(2|k|\sin\theta y + |k|\Delta L) \tag{3.36}$$

In Eq.3.36, the wavevector $|k|$ is equal to $|k| = \frac{2\pi}{\lambda}n$, where n is the refractive index of the medium at $z < 0$. Fig.3.8 plots Eq.3.36 along the waveguide cross section (y direction) for different values of θ at the fixed

wavelength of $\lambda = 1.55\,\mu m$. The path length ΔL is chosen equal to zero and the material refractive index n equal to one.

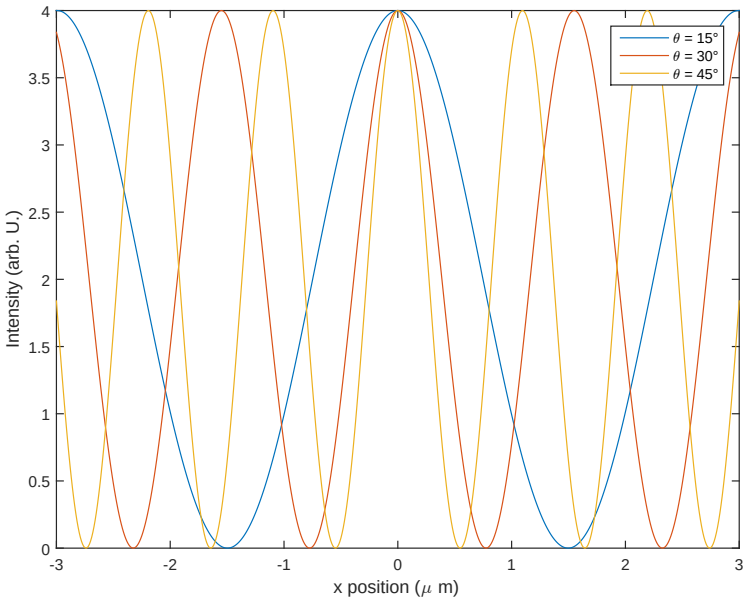

Figure 3.8: Intensity patterns created by the interference of two oblique beams which travels at an angle 2θ between each other. The patterns are evaluated along the y direction of Fig.3.7.

It is seen that the period d of the standing wave pattern can be tuned by changing the angle θ , according to the relation:

$$d = \frac{\lambda}{2n \sin\theta} \tag{3.37}$$

If one want to excite a waveguide mode which has the lobes at a distance Λ, the angle θ has to be chosen in order to satisfy $d(\theta) = \Lambda$. In pratice, the incoming radiation is never in the form of plane waves, but the beams have always a finite size. Fig.3.9(a) shows how the 2D interference pattern on the xy plane looks like when the two beams have a gaussian envelope with waist $10\,\mu m$ and an angle of $\theta = 40^{\circ}$.

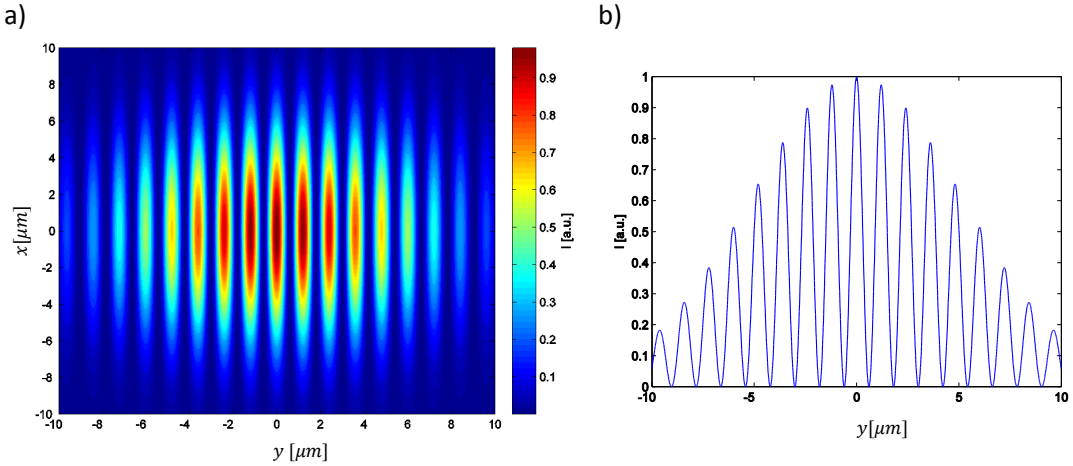

Figure 3.9: (a) Intensity pattern on the xy plane at $z = 0$ of Fig.3.7 when the two waves are described by gaussian beams with waist $10\,\mu m$ and travelling at an angle $2\theta = 80^{\circ}$. The wavelength is set to $1.55\,\mu m$. (b) One dimensional slice of the intensity pattern of panel (a) at $x = 0$.

The maximum intensity is found at $x = 0$ and $y = 0$, reason why it is the point where the waveguide input facet has to be aligned in order to couple the highest fraction of power. The amplitudes of the two beams A_{10} and A_{20} regulate the visibility V of the interference pattern. The latter is defined as:

$$V = \frac{I_{max} - I_{min}}{I_{max} + I_{min}} \tag{3.38}$$

which expressed as a function of A_{10} and A_{20} reads:

$$V = \left(\frac{|A_{10}| + |A_{20}|}{|A_{10}| - |A_{20}|} \right)^2 \tag{3.39}$$

The maximum attainable visibility is achieved when the two beams have equal intensity, i.e, $|A_{10}|^2 = |A_{20}|^2$. In this case $V = 1$. Having a visibility which is close to one is of crucial importance for selective mode excitation. The modal field profile is indeed a standing wave pattern with $V = 1$, and the same must hold for the one created in free space. In order to simulate and evaluate the performances of the method, the following steps have been done:

1. A target waveguide is chosen. The latter has a cross section of $3.6\,\mu m \times 0.25\,\mu m$ and has the center placed at $x = 0$ and $y = 0$. Using a FEM simulator, the modal field profiles $\mathbf{e}_j(x, y)$ of the different orders are computed over the xy plane, where the input facet of the waveguide lies. The field polarization is set to TM.

2. The exciting field $E_{inc}(x, y)$ is calculated as the superposition of two gaussian beams with waist $\sigma_w = 10\,\mu m$, of equal amplitude. The index of the free space propagation region is set to $n = 1$. The field E_{inc} is assumed to be different from zero only inside the simulation window where the waveguide modes are evaluated.

3. The overlap integral in Eq.3.35 is evaluated for different values of θ at the fixed wavelength of $\lambda = 1.55\,\mu m$.

The result is shown in Fig.3.10.

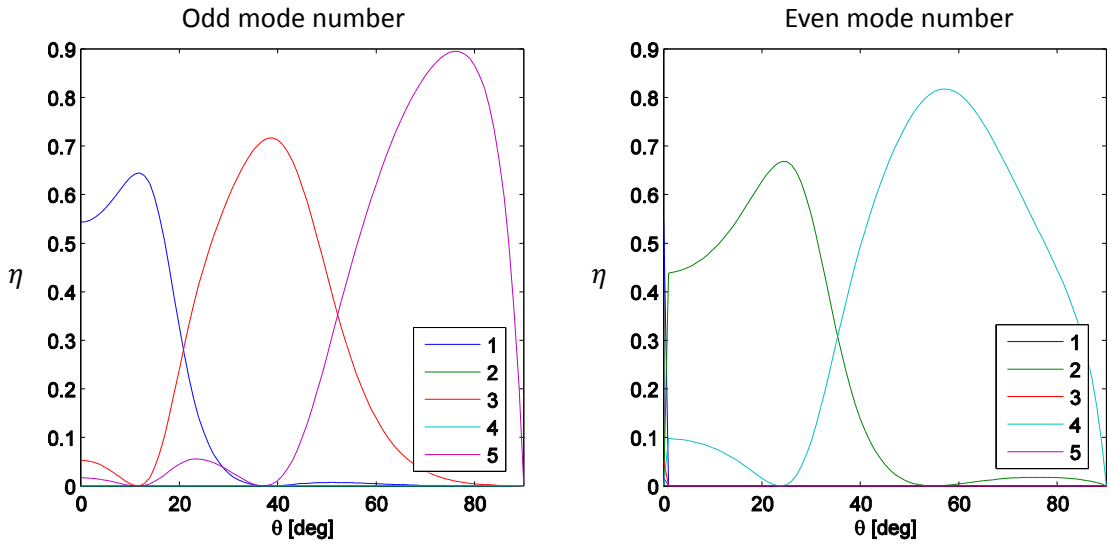

Figure 3.10: Coupling efficiency η for the lowest five modes of a $3.65\,\mu m$ width waveguide in TM polarization. The exciting pattern is obtained by the superposition of two gaussian beams travelling at angle 2θ with waist $\sigma_w = 10\,\mu m$.

Odd mode numbers have even symmetry with respect to $y = 0$, so they can be excited if the path mismatch ΔL is equal to zero. Even mode numbers have odd symmetry with respect to $y = 0$, so the interference pattern has to be shifted by half of the fringe period to maximize the overlap. This can be done by setting $\Delta L = \frac{\lambda}{2}$ in Eq.3.36. From Fig.3.10 it can be seen that in both cases very high mode selectivity is achieved. When the angle is tuned for exciting a specific mode order, the average crosstalk with the other modes is below the 3%. The approach seems to be also robouts against small errors in the angle tuning between the two beams. For example, if the latter differs at about 5° from the optimal one, the percentage of coupled power decreases by less than the 10%, while the crosstalk keeps lower than the 5%. For the excitation of both the even and the odd mode orders, it is always convenient to set the path difference $\Delta L = 0$. In case of modes of odd symmetry, the excitation can be performed by shifting the waveguide center by half of the fringe period, rather than setting $\Delta L = \frac{\lambda}{2}$. If $\Delta L = 0$, the fringe position will not significantly shift with wavelength, thus decreasing the overlap with the desired mode order. This is shown in Fig.3.11, where the the overlap integral, the field profile at $z = 1\,cm$ in a $3.65\,\mu m$ wide waveguide and the interference pattern on the waveguide input facet are shown as a function of wavelength for $\Delta L = 40\,\mu m$ and $\theta = 40°$. As a consequence of the path mismatch ΔL, the coupled mode periodically oscillates between a 3^{rd} order mode, which was the target one, and a 4^{th} order mode. In between, beatings between the two modes are observed.

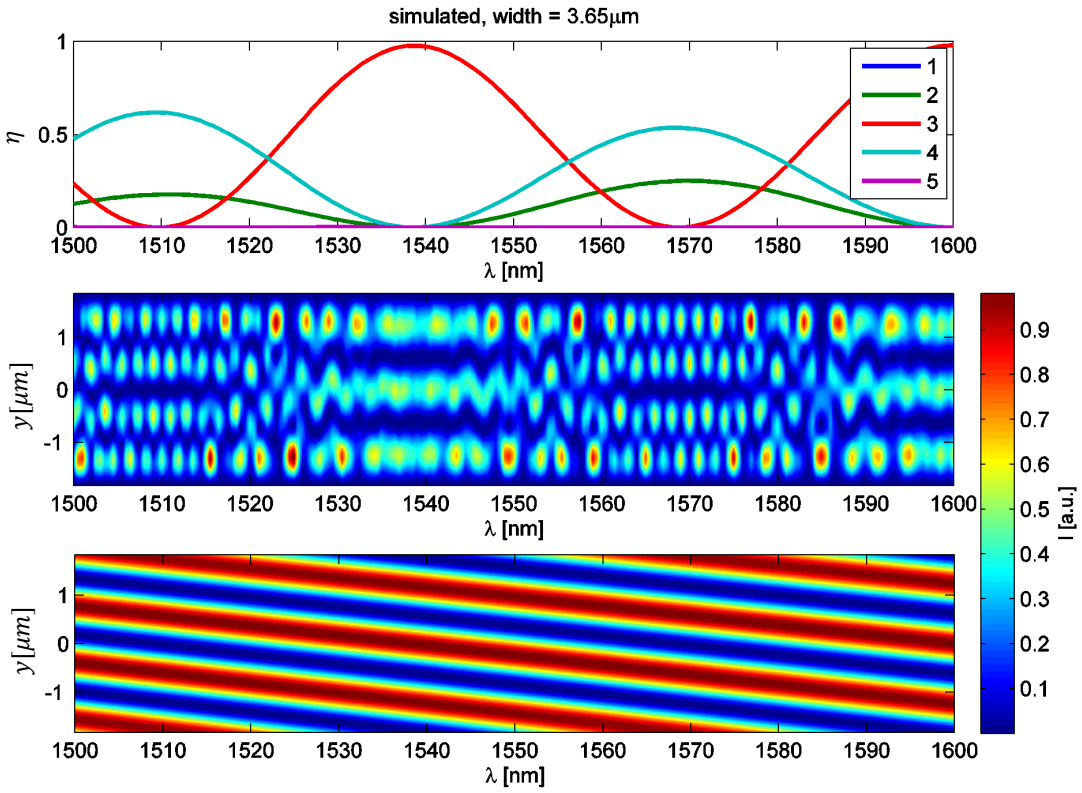

Figure 3.11: From the top panel to the bottom panel: modal coupling efficiency η, field intensity profile at $z = 1\,cm$ along the y direction ($x = 0$) in the $3.65\,\mu m$ wide waveguide and intensity profile along the y direction ($x = 0$) of the incident field $\mathbf{E}_{inc}$. The intensity field profile $|\mathbf{E}_{wg}|^2$ inside the waveguide is calculated using Eq.3.30. The incident field is the superposition of two gaussian beams of waist $10\,\mu m$ travelling at an angle $2\theta = 80°$ and with path difference $\Delta L = 40\,\mu m$.

3.3.2 Experimental realization

The oblique beam interference experiment modeled in the previous section has been implemented using the setup shown in Fig.3.12.

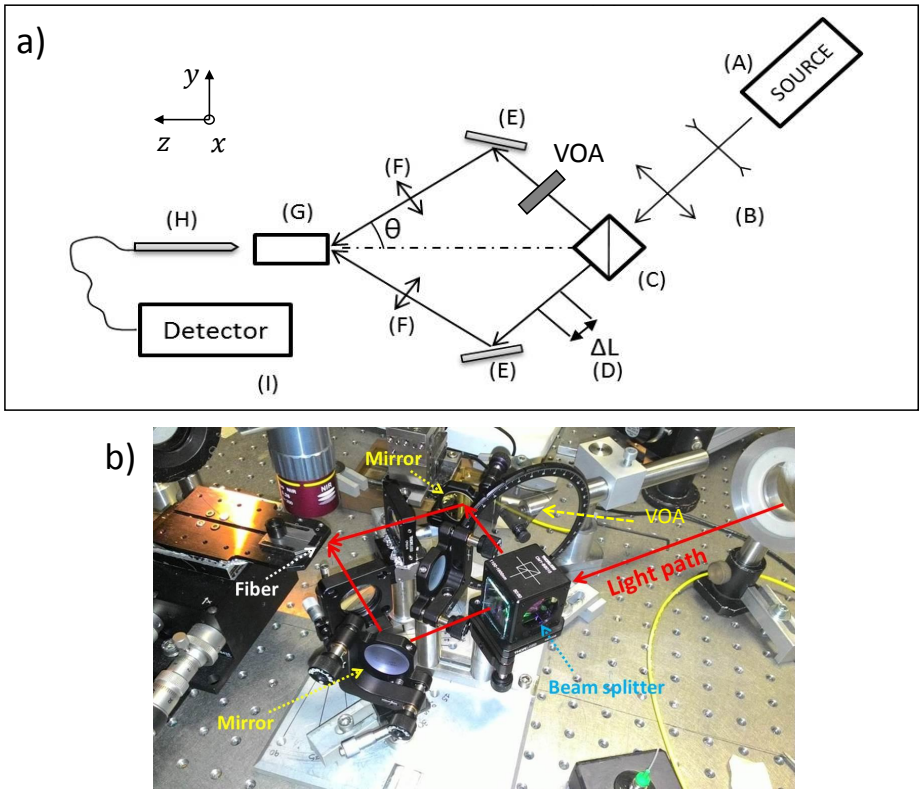

Figure 3.12: (a) Sketch of the experimental setup for oblique beam interference. A = laser source, B = Beam Expander, C = Beamsplitter, D = Translation stage, E = Mirrors, F = Input biconvex lenses, G = sample, H = collecting lensed fiber, I = photodetector. (b) A photograph of the experimental setup sketched in panel (a).

A tunable IR laser is sent into a beam expander which extends the waist of the original beam. Then the latter is split by a 50 : 50 beamsplitter cube and both the outgoing beams are directed toward two gold mirrors. One of the two mirrors is mounted over a micrometric translation stage, which is used to compensate the path length difference ΔL between the two beams. The mirrors direct the beams toward two biconvex lenses which focalize them at the input facet of the waveguide (fabbricated by by Fondazione Bruno Kessler (FBK) [204] using $293\,nm$ DUV lithography). The use of a beam expander allows to reduce the waist of the beam to $\sigma_w = (8.6 \pm 0.2)\,\mu m$. The angle 2θ between the beams can be read directly on a goniometer which is placed below the posts which hold the two mirrors. The sample which contains the straight waveguides engineered for MMFWM is mounted on a XYZ micrometric positioning stage that can perform also nanometric movements using piezoelectric controllers. The output power from the waveguide is collected using a tapered lensed fiber and monitored using a photodetector. Several waveguide widths and the coupling of different mode orders have been tested. In the following, only the results for the coupling of a 3^{rd} order TM mode in a $3.8\,\mu m$ wide waveguide and for the coupling of a 2^{nd} order mode in a $2.45\,\mu m$ wide waveguide are reported. In both cases, the height of the waveguides is $250\,nm$. At first, the angle was chosen. From Fig.3.13, which shows the modal profiles under test, it can be seen that the lobes of the 3^{rd} order mode are spaced by $\Lambda_3 = 1.3\,\mu m$, while the lobes of the 2^{nd} order mode are spaced by $\Lambda_2 = 1.31\,\mu m$.

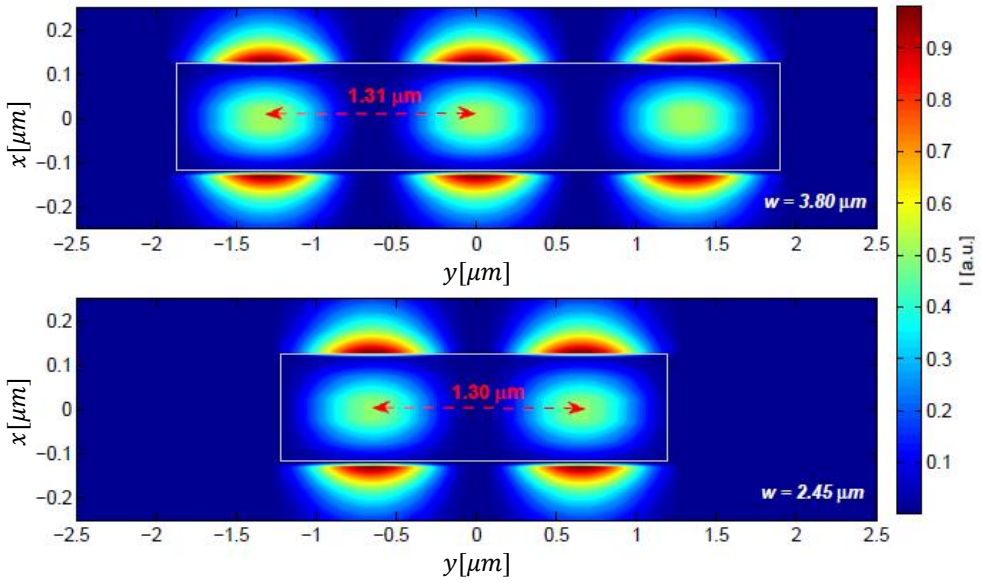

Figure 3.13: Upper panel: electric field intensity distribution of the 3^{rd} order TM mode in the $3.8\,\mu m$ wide waveguide. Lower panel: electric field intensity distribution of the 2^{rd} order TM mode in the $2.45\,\mu m$ wide waveguide.

Then, as a good approximation, $\Lambda_3 = \Lambda_2 = \Lambda$ and a unique angle can be used to excite both of them. This angle can be derived by setting $d(\theta) = \Lambda$, which yelds $\theta = 36.3°$. Once that the angle has been chosen, the visibility of the fringes has to be evaluated. This is done by using a Scanning NearField Optical Microscopy (SNOM) optical fiber with a tip aperture of $100\,nm$. The SNOM fiber tip is placed where the two oblique beams intersects, ideally in the point at coordinates $x = 0$ and $y = 0$ of Fig.3.7. The fiber is then moved along the y direction using a piezoelectric controller, and the coupled power is monitored using a photon counter. The spatial resolution provided by the fiber is of the order of the tip aperture. The recorded pattern in the xy plane is shown in Fig.3.14, while a one dimensional slice of the latter is shown in Fig.3.15.

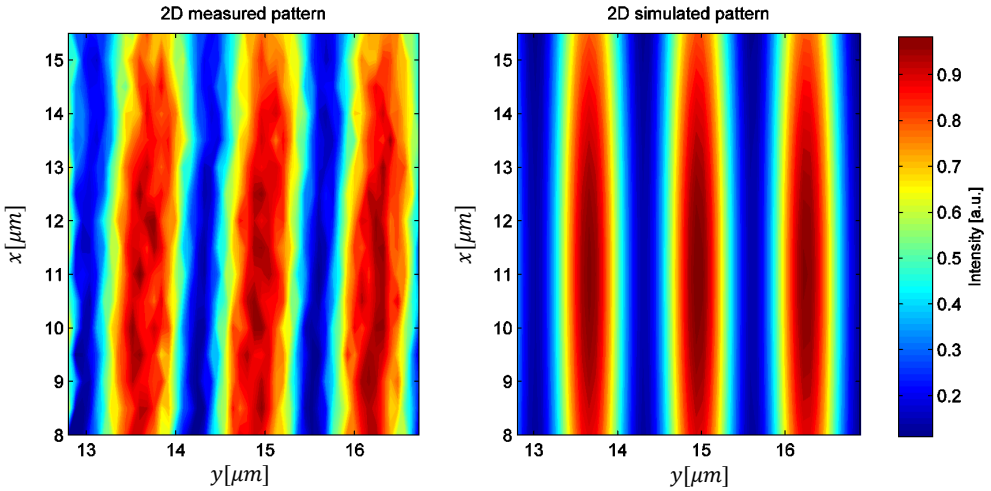

Figure 3.14: Simulated and measured intensity patterns (on the xy plane at $z = 0$ of Fig.3.7) when the angle θ is tuned at $\theta = (36.6 \pm 0.3)°$. Patterns have been recorded using a SNOM fiber coupled to a photon counter. The point $(x, y) = (11.75, 14.9)\,\mu m$ in the picture corresponds to the point $(x, y) = (0, 0)$ in Fig.3.7.

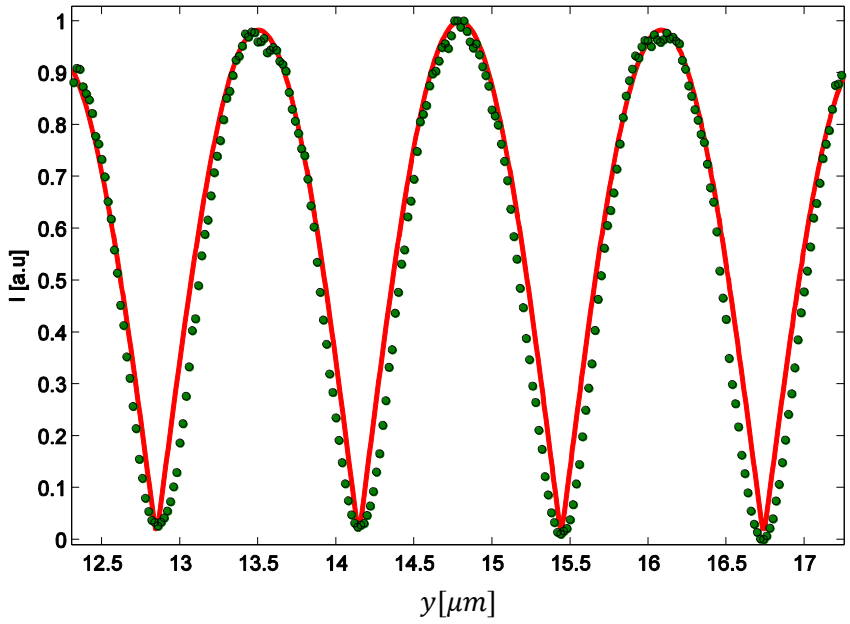

Figure 3.15: A one dimensional slice along the y direction at $x = 11.75$ in Fig.3.14. Green scatters represent experimental data while the solid red line is obtained using Eq.3.36.

From this picture, the fringe period can be extracted and is given by $\Lambda_{exp} = (1.30 \pm 0.01)$, which is compatible with an angle of $\theta_{exp} = (36.6 \pm 0.3)^{\circ}$. The latter is very close to the optimal value of 36.6°. The amplitude of the two beams is made approximately equal using a variable optical attenuator. The maximum obtained fringe visibility is $V = (0.95 \pm 0.02)$. The last step before the coupling of light inside the waveguide is the balance of the path length difference ΔL. This has been done by placing the SNOM fiber at $(x, y) = (0, 0)$ and by monitoring the recorded intensity as the wavelength is changed. Using the micrometric positioning stage mounted on one of the two mirrors, the latter is moved until no fringes are registered as a function of wavelength, which, as indicated by Eq.3.36, implies $\Delta L = 0$. Two examples of patterns, recorded at $\Delta L = (1.47 \pm 0.01)\, mm$ and at $\Delta L = (8 \pm 1)\, \mu m$ are shown in Fig.3.16. The latter condition, which correponds to the smallest path unbalancing that has been possible to realize, will coincide with the working point in the rest of the experiment. The central fringe shows almost constant intensity (3% decrease) in a wavelength range of $1530\, nm - 1550\, nm$.

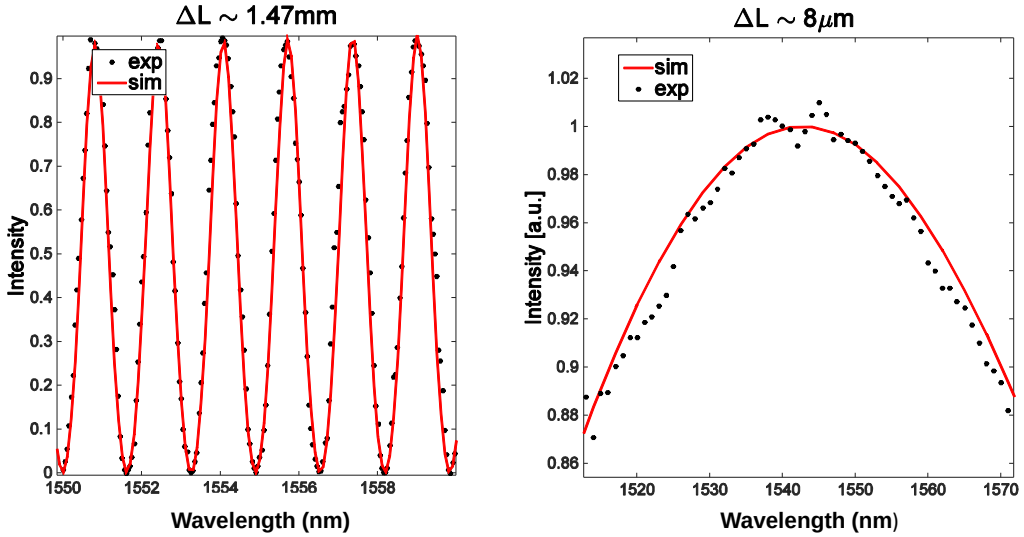

Figure 3.16: Interference fringes recorded at $(x, y, z) = (0, 0, 0)$ (with respect to the reference frame of Fig.3.7) as a function of wavelength. The values of the path unbalancing ΔL have been extracted from the fit (solid red curve) of the experimental data (black scatters). The fit is performed using Eq.3.36.

At this point, the sample has been positioned in such a way that the input facet of the waveguide under test laid as close as possible to the point $(x, y, z) = (0, 0, 0)$ of Fig.3.7. Since this point corresponds to the place of maximum intensity (see Fig.3.9), this task has been achieved by maximizing the power coupled into the waveguide. Fine adjusements have been performed using piezoelectric controllers. In order to evaluate the mode which is coupled into the waveguide, and thus validating the theoretical calculations, the near field profile at the output of the waveguide has been monitored using the SNOM fiber coupled to a photon counter. The recorded field profiles are then compared to the ones in Fig.3.13 obtained using FEM simulations. It is worth to note that even if a certain similarity is found between the experimental and the theoretical patterns, this does not automatically imply that only the target mode is propagating inside the waveguide. This can be understood by looking at Fig.3.11 (middle panel). If the incident field simultaneously excites many modes, these will exhibit beatings during the propagation along the waveguide, which are eventually enhanced by the reflections at the input/output facet of the sample. It may occur that, for a certain wavelength, and for a certain waveguide width, the envelope of the beatings resembles the one of the target mode, even if the modal excitation is far from being selective. A definitive proof that only one mode is propagating in the waveguide, is the observation of a stable pattern as the wavelength is changed. This is because the intensity distribution changes with wavelength if modal beatings are present. Fig.3.17 shows the intensity patterns recorded at the output of the 2.45 μm wide waveguide and of the 3.8 μm wide waveguide as the wavelength is changed.

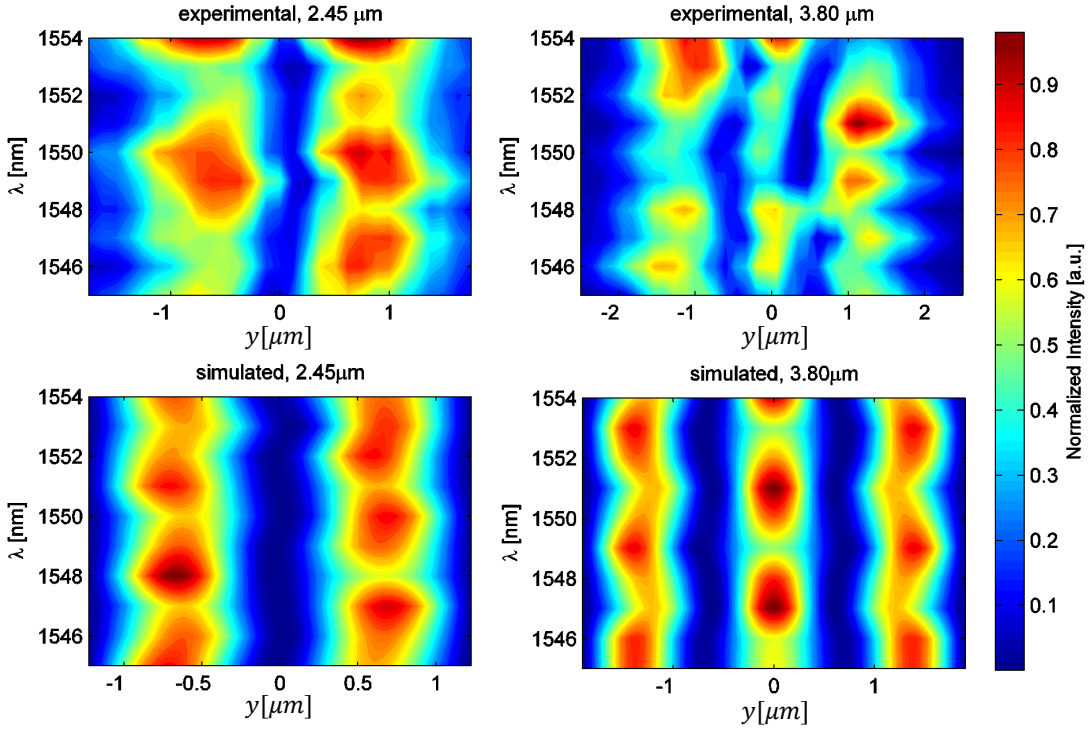

Figure 3.17: Comparison between the simulated and experimentally recorded modal field patterns at the output of a $2.45\,\mu m$ wide waveguide and of a $3.8\,\mu m$ wide waveguide. The target mode orders were the 2^{nd} and the 3^{rd}, respectively. Each slice along y is recorded at a different wavelength λ.

A quite good stability of the patterns is found, which is a clear sign that selective mode excitation has been achieved. Some intensity variations are found as the wavelength is changed, which can be mainly attributed to the reflections at the input/ouput waveguide facets. The system is then capable of performing selective mode excitation by exploiting the interference of two oblique beams. Nevertheless, it has been impossible to use it for probing MMFW due to the high coupling losses between the incoming radiation and the waveguides on the chip. These have been estimated to be $(-25.62 \pm 0.02)\,dB$, which mostly arise from the huge mismatch between the effective area of the waveguide mode $A_{eff,wg}$ and the one of the incoming beam $A_{eff,inc}$. For example, the effective area of the waveguide with cross section $3.8\,\mu m \times 0.25\,\mu m$ is approximately $A_{eff,wg} \approx 0.95\,\mu m^2$, while the one of the exciting radiation is $A_{eff,inc} \approx (2\sigma_w)^2 = (296 \pm 7)\,\mu m^2$, which yelds $10 \log\left(\frac{A_{eff,wg}}{A_{eff,inc}}\right) \approx -25\,dB$ of coupling losses, a value which is very close to the one found in the experiment. Unfortunately, it has been impossible to further reduce the waist of the laser due to some limitations in the implemented optical components. Due to the high coupling losses, an alternative method, which achieves less mode selectivity but ensure lower losses, has been implemented and it will be discussed in the next section.

3.3.3 Tilted fiber approach

A tapered lensed fiber which is tilted by an angle θ with respect to the normal of the waveguide facet can be used to excite higher order modes. The physical situation is the same of the oblique interference experiment described in Fig.3.7, but with the lack of one of the two beams. As a good approximation, the electric field on the (x, y) plane radiated by the fiber can be written as:

$$E_{inc}(x,y) \propto e^{\frac{y\cos\theta + x^2}{\sigma_w^2}} \left[\cos\left(|k| y \sin\theta\right) + i \sin\left(|k| x \sin\theta\right)\right] \tag{3.40}$$

The measured waist σ_w for the fiber implemented in the experiment described in Section 3.4 is $\sigma_w = (0.8 \pm 0.2)\,\mu m$, which is an order of magnitude lower than the ones of the beams implemented in Section 3.3.2. The associated effective area is then two orders of magnitude lower, with the result that the losses should be decreased by approximately $20\,dB$. Indeed, the latter have been measured to be $(7.23 \pm 0.2)\,dB$ for a waveguide of width $2\,\mu m$. Fig.3.18 shows the fraction of coupled power η between different TM modes, calculated as defined in Eq.3.34, when the incident field is given by Eq.3.40 and the target waveguide has a cross section of $3.65\,\mu m \times 0.25\,\mu m$. It can be noticed that the ability to selectively excite only a specific mode order is lower than in the approach based on two beams interference. The maximum fraction of coupled power is about $\eta = 0.5$ for higher order modes, while the cross talk is always higher than the 20%. This is due to the fact that the field in Eq.3.40 does not represent a standing wave pattern, since the intensity does not show interference fringes. Nevertheless, the tradeoff between coupling losses and mode purity is better than in the approach based on two beams interference, so it has been choosen to probe MMWFM. Table 3.1 compares the performances of the two approaches.

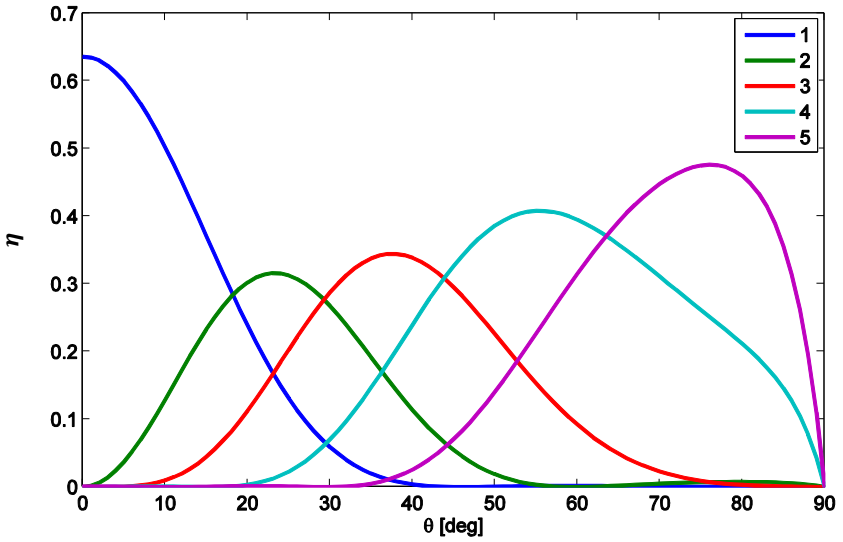

Figure 3.18: Fraction of coupled power η for the five lowest order TM modes of a waveguide with a cross section of $3.65\,\mu m \times 0.25\,\mu m$. The exciting field is given by Eq.3.40.

Parameter	Two beam interference	Tilted fiber
Average modal excitation	$> 75\%$	40%
Modal cross talk	$< 3\%$	$> 20\%$
Beam waist	(8.6 ± 0.2)	$(0.8 \pm 0.2)\,\mu m$
Coupling losses	$(25.62 \pm 0.2)\,dB$	$(7.23 \pm 0.2)\,dB$

Table 3.1: Comparison of the main parameters which characterizes the selective mode excitation based on two beams interference and on the tilted fiber.

3.4 Experimental MMFW in straight Silicon waveguides

The tilted fiber approach to MMFWM described in the previous section has been implemented using the experimental setup sketched in Fig.3.19

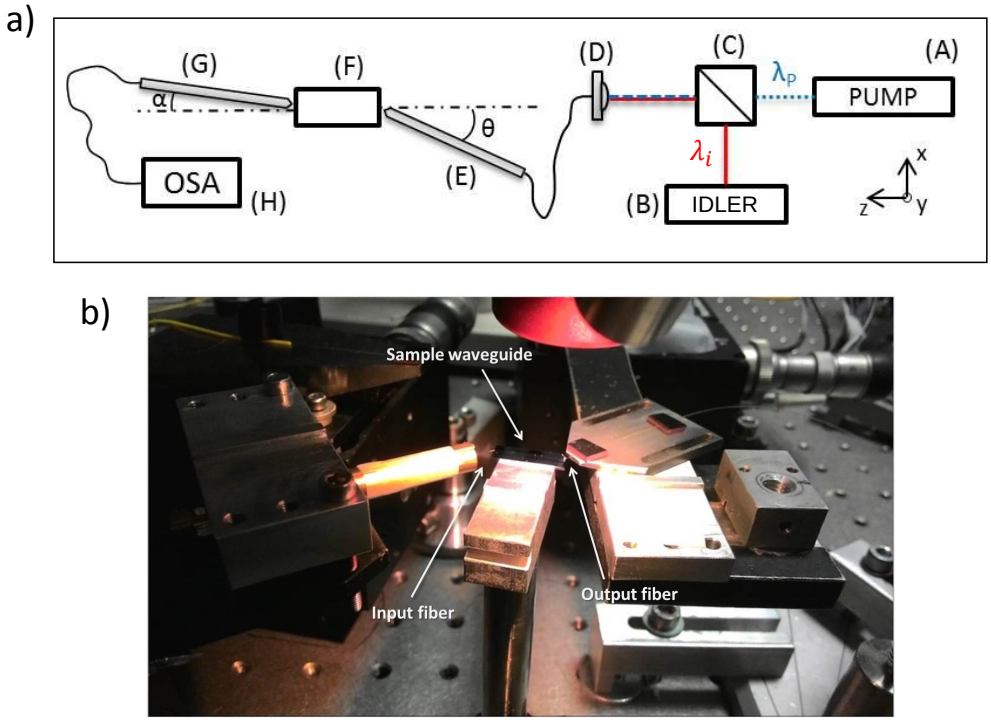

Figure 3.19: (a) Sktech of the experimental setup implementing the tilted fiber approach. A = pump source, B = idler source, C = beam splitter, D = fiber port collimator, E = input tapered lensed fiber, F = sample waveguide, G = output tapered lensed fiber, H = optical spectrum analyzer. The angle between the input(output) fiber and the input(output) waveguide facet is $\theta(\alpha)$.

A pump source constituted by a pulsed Infra-Red laser ($40\,ps$ of pulse width and $100\,MHz$ repetition rate) is combined with the idler, coming from a continuous wave laser, using a beamsplitter. The free space beams are then coupled into a single mode fiber using a fiber port collimator. The polarization of both sources can be controlled using either free space half/quarter waveplates (for the pump) or fiber polarization controllers (for the idler). The input(output) tapered lensed fiber, which lies in the yz plane of Fig.3.19, makes an angle $\theta(\alpha)$ with respect to the normal of the input(output) waveguide facet (directed along the z axis). The tested waveguides have a length of $1.4\,cm$. The output signal is monitored using an OSA. In case that the generated signal power lies below $90\,dBm$, the OSA is replaced by a home made monochromator coupled to a photon counter, which is able to measure up to $-120\,dBm$ of power. The angles α and θ have been chosen in order to maximize the modal collection and excitation efficiency with the mode orders involved in the FWM process. Table 3.2 shows some of the investigated modal combinations. In what follows, each of them will be referred by the vector (m_p, m_p, m_i, m_s), where m_p, m_i and m_s refer to the pump, idler and signal mode order respectively. The expected phase matching point has been calculated using Eq.3.19. The effective index dispersions have been simulated using a FEM solver. As an example of the whole procedure implemented for each combination, in what follows it is reported in detail the case of MMFWM for a waveguide of cross section $3.65\,\mu m \times 0.25\,\mu m$.

Waveguide cross section	Pump	Idler	Signal		Combination
$3.65\,\mu m \times 0.25\,\mu m$	4	3	5	Mode order	$(4,4,3,5)$
	TM	TM	TM	Polarization	
	$1.55\,\mu m$	$1.648\,\mu m$	$1.462\,\mu m$	Wavelength	
$1.85\,\mu m \times 0.25\,\mu m$	1	4	2	Mode order	$(1,1,4,2)$
	TM	TM	TE	Polarization	
	$1.55\,\mu m$	$1.610\,\mu m$	$1.493\,\mu m$	Wavelength	
$1.70\,\mu m \times 0.25\,\mu m$	1	3	3	Mode order	$(1,1,3,3)$
	TM	TM	TE	Polarization	
	$1.55\,\mu m$	$1.665\,\mu m$	$1.450\,\mu m$	Wavelength	
$1.70\,\mu m \times 0.25\,\mu m$	3	3	5	Mode order	$(3,3,3,5)$
	TM	TM	TE	Polarization	
	$1.55\,\mu m$	$1.57\,\mu m$	$1.53\,\mu m$	Wavelength	

Table 3.2: Simulated phase matching points for several modal combinations and waveguide widths.

In this case, the pump and the idler have to be copolarized in TM polarization, travelling into the 4^{th} and the 3^{rd} order mode respectively. Fig.3.20 shows the coupling efficiencies for the five lowest order TM modes as a function of the angle θ.

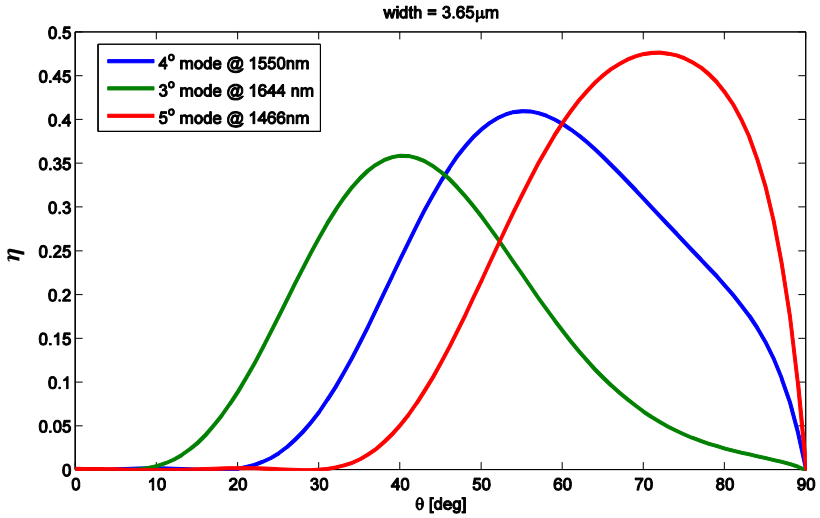

Figure 3.20: Coupling efficiency η as a function of the fiber tilting angle θ for the lowest five TM mode orders in a $3.65\,\mu m$ waveguide.

Since only one fiber is used to excite both the pump and the idler wave, the angle has to be chosen in such a way that both modes are almost equally excited. From Fig.3.20, it can be seen that the 3^{rd} order mode is efficiently excited at $\theta = 39^{\circ}$, while the 4^{th} order mode at $\theta = 55^{\circ}$. The tradeoff angle is the average between the two, which gives $\theta = 45^{\circ}$. The signal will be generated into the 5^{th} order mode, so the output fiber will be tilted by $\alpha = 70^{\circ}$. Once the angles have been fixed, the idler wavelength is spanned in the neighborhood of $1.648\,\mu m$, which is the phase matching wavelength expected from simulations. Fig.3.21 reports the whole spectrum of the transmitted radiation from the waveguide, which shows that a signal peak at $(1466.1 \pm 0.1)\,nm$ is generated due to FWM at $\approx -82\,dBm$.

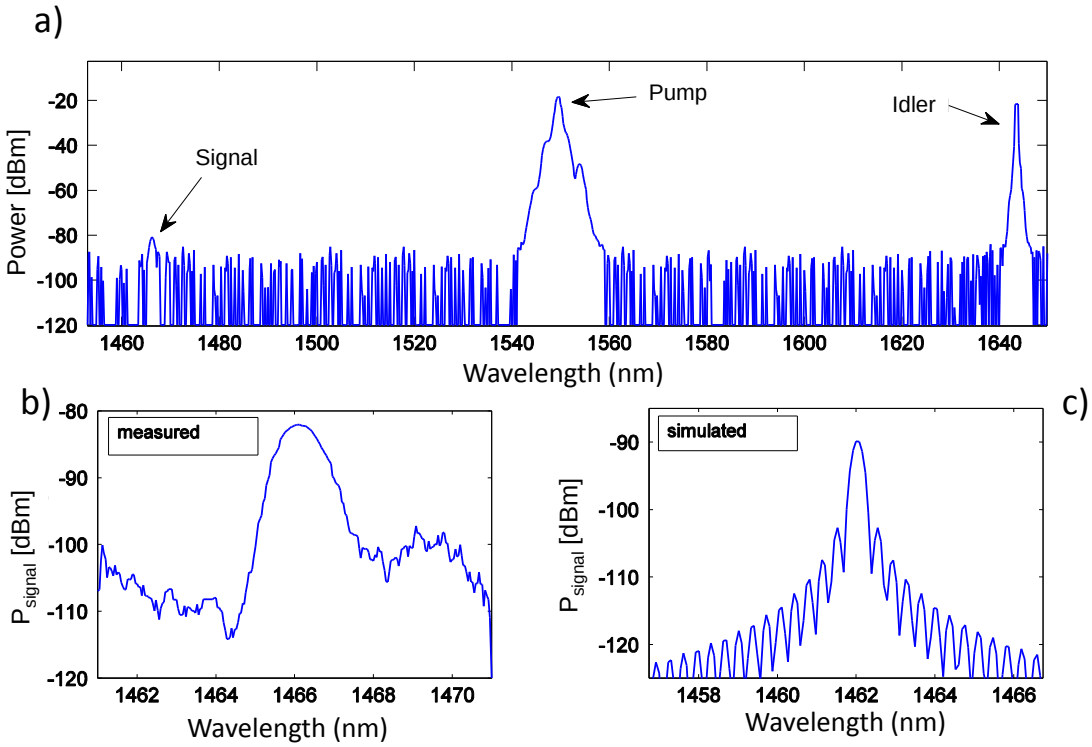

Figure 3.21: (a) Spectrum of the light collected at the ouput of the $3.65\,\mu m$ width waveguide. Arrows indicate the wavelength position of the pump, the signal and idler. (b) A zoom of the spectral region where the signal is generated. (c) Simulated signal bandwidth and efficiency. To obtain this curve, the set of equations from (3.14) to (3.16) has been numerically integrated using the same input conditions of the experiment. The integrals in the definitions of f_{ij} and f_{ijkl} have been computed using a FEM mode solver.

This wavelength is where the maximum of the efficiency is observed (the corresponding idler wavelength is $1644\,nm$). The $3\,dB$ bandwidth of the process, that is the wavelength range in which the generated signal decreases by less than $3\,dB$ from its maximum value, has been measured to be $(1.0 \pm 0.2)\,nm$. In order to evaluate the efficiency of the process, the fact that the pump (hence the signal) is pulsed and that the idler is CW has to be taken into account. The bandwidth of the OSA is $100\,Hz$, which is much less than the $100\,MHz$ of the repetition rate of the pump/signal. As a consequence, the power measured with the OSA is the average power power $\langle P \rangle$ of the pulsed radiation, which is related to the repetition rate R, to the pulse width Δt and to the peak power P_{peak} as:

$$\langle P \rangle = P_{peak} R \Delta t \tag{3.41}$$

The conversion efficiency η_{FWM} is defined as the ratio between the signal peak power $P_{peak}(\lambda_s)$ and the idler peak power $P_{peak}(\lambda_i)$:

$$\eta_{FWM} = 10 \log \left(\frac{P_{peak}(\lambda_s)}{P_{peak}(\lambda_i)} \right) \tag{3.42}$$

By using Eq.3.41 and the fact that for a continuous laser $\langle P \rangle = P_{peak}$, one obtains $\eta_{FWM} = \langle \eta_{FWM} \rangle - 10 \log(R\Delta t)$, where the average efficiency $\langle \eta_{FWM} \rangle = 10 \log \left(\langle P_{\lambda_s} \rangle / \langle P_{\lambda_i} \rangle \right)$ has been introduced.

From Fig.3.21, $\langle \eta_{FWM} \rangle = -60\,dB$, and $10\log(R\Delta t) \approx -23\,dB$, giving $\eta_{FWM} = 37\,dB$. This efficiency has been obtained using a pump peak power of $25\,dBm \approx 316\,mW$ coupled into the waveguide (the fiber to chip coupling losses were $\approx -8\,dB$ for each waveguide facet). In order to be sure that the signal is generated through MMFWM and not from FWM arising between the same mode orders, the expected bandwidths for the combinations (m, m, m, m) with $m = 1, .., 5$ have been simulated using the same parameters of the experiment. The results are reported in Fig.3.22.

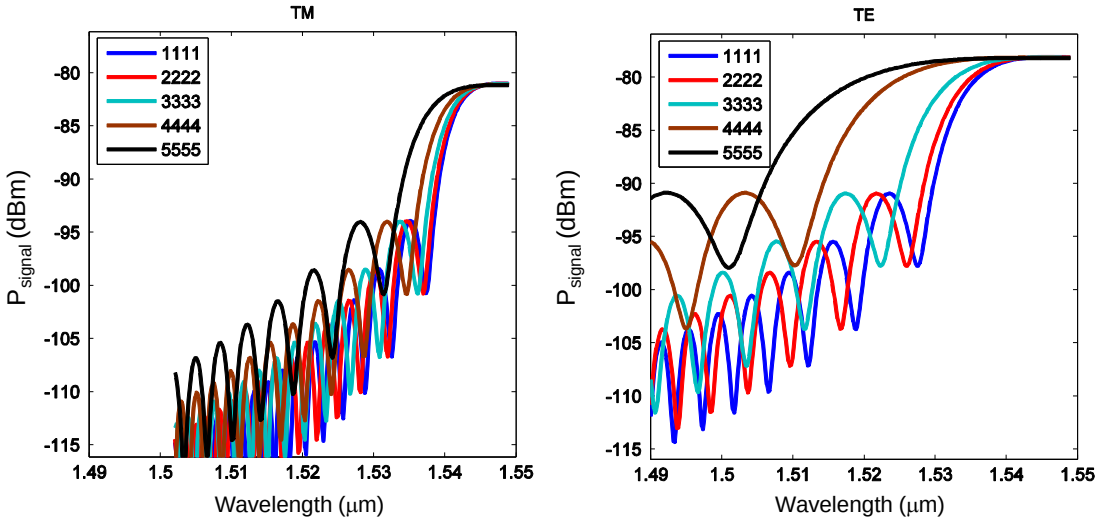

Figure 3.22: Simulated signal power generated through FWM for the combinations (m, m, m, m) with $m = 1, .., 5$. The cases of TE and TM polarizations are reported separately.

It is evident that the signal peak at $1466.1\,nm$ in Fig.3.21 can not be due to any of these combinations. This is because already at $1535\,nm$, the signal intensity lies below $-90\,dBm$, which is the minimum detectable signal by the OSA, and it continues to decrease at shorter wavelengths. Also the $3\,dB$ bandwidths do not agree with the experimental one. The narrowest is about $20\,nm$ for the $(1, 1, 1, 1)$ combination, which is an order of magnitude higher than the one measured in Fig.3.21. The possibility that FWM occurs in the tapered fiber should also be excluded. Fig.3.23 shows the experimental result and the simulation of the FWM experiment performed without the sample, when the input and the output fibers are directly coupled tip to tip.

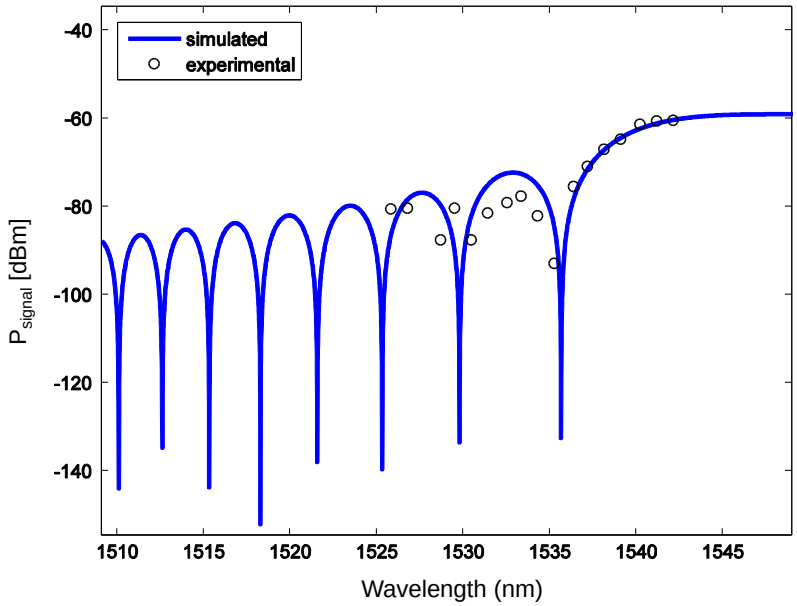

Figure 3.23: Signal power generated through FWM in a single mode Silica optical fiber having a core width of $10\,\mu m$. Black scatters are experimental data while the solid blue line comes from a simulation. The parameters are the same used to simulate the curves in Fig.3.22, except for the modal dispersion and the n_2 coefficient, which are taken from FEM simulations and from [2] respectively.

The parameters of a standard single mode Silica fiber, having a core width of $10\,\mu m$, have been used in the simulation [2]. The generated signal was detectable till $1525\,nm$, while at lower wavelengths it laid below the noise limit of the OSA. This excludes the possibility that the FWM of the fiber was the responsable of the signal peak in Fig.3.21. The dependence of the generated signal in Fig.3.21 on the average pump power and on the idler power is shown in Fig.3.24.

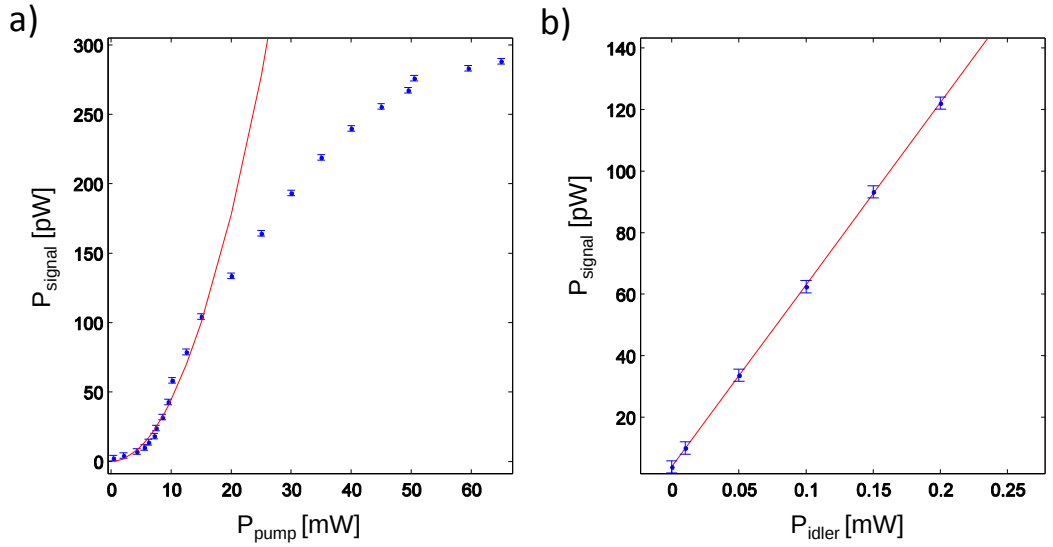

Figure 3.24: (a) Signal power as a function of the average pump power at the fixed idler power of $0.15\,mW$. (b) Signal power as a function of the idler power at the fixed average pump power of $15\,mW$. In both panels, the pump wavelength is $\lambda_p = 1.55\,\mu m$, while the idler wavelength is $\lambda_i = 1.644\,\mu m$.

Before TPA effects occur near $20\,mW$ of average pump power, the relation between the pump and the signal

power is quadratic, as predicted from Eq.3.12. TPA has the effect of saturating the maximum coupled power inside the waveguide, so after a certain threshold the generated signal does not increase anymore even if the pump power is further raised. The relation between the signal and the idler power is linear, which is in agreement with Eq.3.12. The behaviours of Fig.3.24 confirm that the process which creates the signal peak is FWM.

Fig.3.25 shows the generated signal power as a function of the wavelength for the different waveguide widths and modal combinations of Table 3.2. Table 3.3 summarizes the conversion efficiencies, and compares the wavelengths λ_s where the maximum signal is expected from simulations to the ones actually recorded in the experiment.

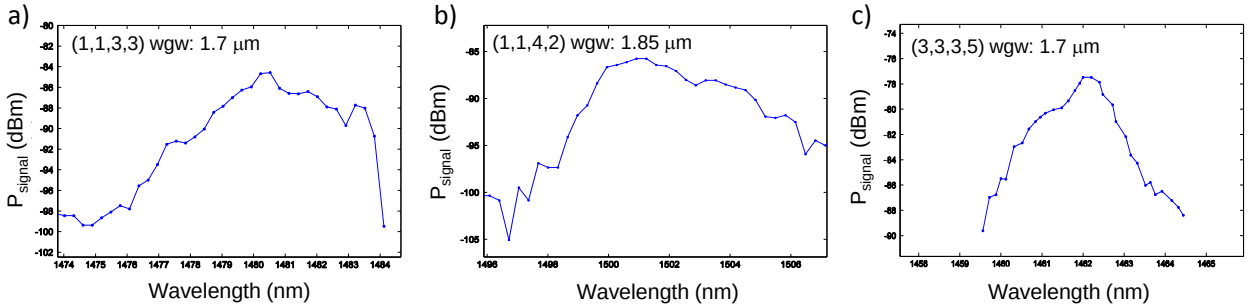

Figure 3.25: (a) Signal power for the combination $(1,1,3,3)$ in the $1.70\,\mu m$ width waveguide. Here, the average pump power is $1.6\,mW$ and the idler power is $40\,\mu W$. (b) Signal power for the combination $(1,1,4,2)$ in the $1.85\,\mu m$ width waveguide. Here, the average pump power is $1\,mW$ and the idler power is $10\,\mu W$. (a) Signal power for the combination $(3,3,3,5)$ in the $1.70\,\mu m$ width waveguide. Here, the average pump power is $1.6\,mW$ and the idler power is $40\,\mu W$.

Combination	**Wg.width** (μm)	λ_s **Simulation** (nm)	λ_s **Experiment** (nm)	**Efficiency** (dB)
$(4,4,3,5)$	3.65	1462.0	1466.1 ± 0.1	-37.4 ± 0.2
$(1,1,4,2)$	1.85	1493.4	1462.1 ± 0.1	-19.4 ± 0.2
$(3,3,3,5)$	1.70	1530.2	1501.0 ± 0.1	-37.8 ± 0.2
$(1,1,3,3)$	1.70	1449.9	1480.5 ± 0.1	-36.3 ± 0.2

Table 3.3: Comparison between the signal wavelengths where the maximum efficiencies are found and the ones predicted from the simulations.

For the combinations which involve cross polarized fields, there is a quite large mismatch, of the order of $30\,nm$, between the wavelength where the maximum efficiency is expected and the ones found in the experiment. This is due to the fact that the widths of the fabricated waveguides may slightly differ from the ones used in the simulations. Indeed, Fig.3.26 shows that the wavelength where the maximum efficiency is expected strongly depends on the width of the waveguide.

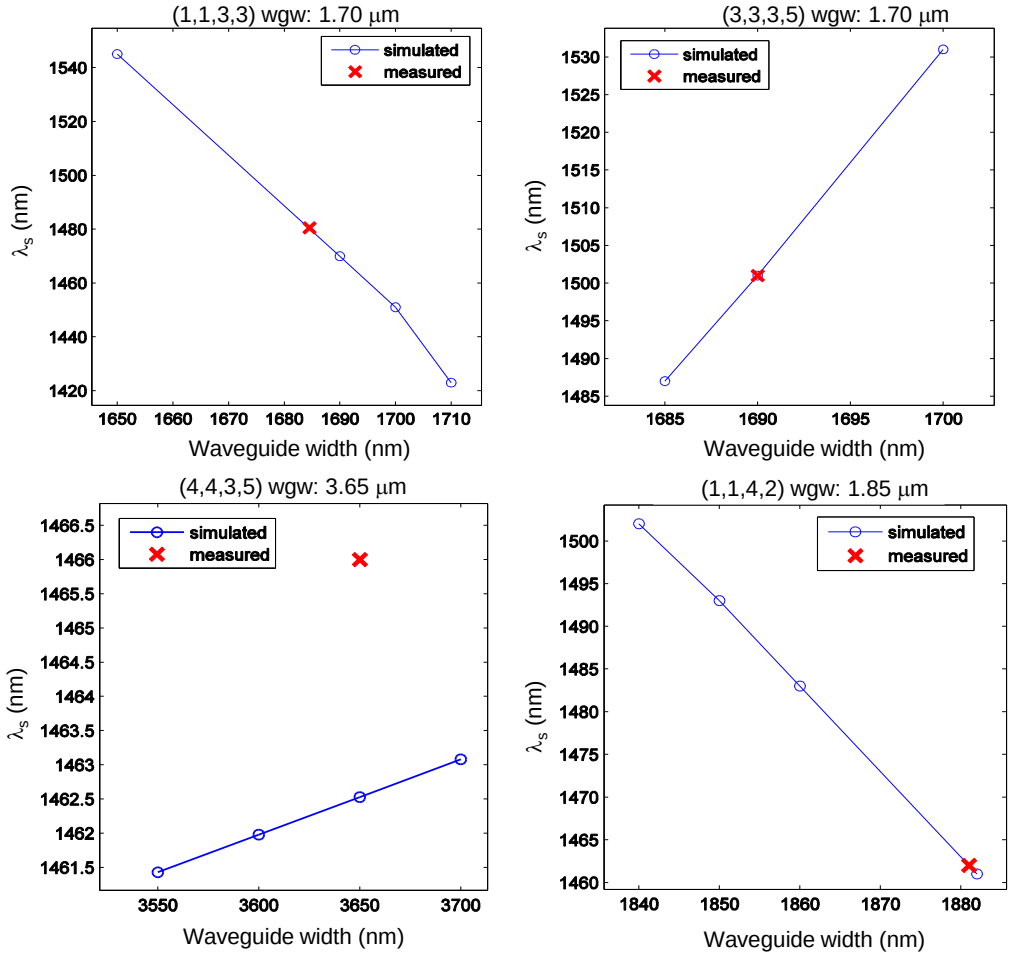

Figure 3.26: Simulated wavelength position of the maximum signal power generated through MMFWM as a function of the waveguide width. The investigated combinations are the same reported in Table 3.2.

This is measured by the parameter $\frac{d\lambda_s}{dW}$, which is the slope of the curve which links λ_s with the waveguide width w, and that is reported in Table 3.4. By matching the experimental value of λ_s with the curves in Fig.3.26, the average width of the fabricated waveguide can be extracted, and is reported in Table 3.5.

Modal combination	$d\lambda_s/dw$
$(4,4,3,5)$	0.01
$(1,1,4,2)$	-1
$(3,3,3,5)$	-2
$(1,1,3,3)$	3

Table 3.4: Slope of the curves in Fig.3.26.

Modal combination	**Nominal width** (nm)	**Fabricated** (nm)
$(4,4,3,5)$	3650	–
$(1,1,4,2)$	1850	1879.3 ± 0.1
$(3,3,3,5)$	1700	1683.8 ± 0.1
$(1,1,3,3)$	1700	1690.7 ± 0.1

Table 3.5: Comparison between the nominal waveguide widths and the values of the fabricated ones.

An average deviation of $(18.4 \pm 0.2)\,nm$ is found between the nominal values of the waveguide widths and the fabricated ones, which is compatible with the tolerances of the photolithographic process ($\pm 20\,nm$). It is interesting to note that the value of $\frac{d\lambda_s}{dW}$ is higher for the combinations which involve cross polarized fields. Qualitatively, this can be explained by the fact that the effective indexes of TE modes are much more sensitive to variations in the waveguide width rather than TM ones. In mathematical terms, if $\Delta\Omega$ denotes the shift of the signal frequency as a consequence of a change Δw in the waveguide width, one can expand the phase matching relation of Eq.3.19 to the first order in Δw to get:

$$\Delta\Omega = (\beta_s(\lambda_p) - \beta_i(\lambda_p)) \left(2\frac{d\beta_p(\lambda_p)}{dw} - \frac{d\beta_s(\lambda_p)}{dw} - \frac{d\beta_i(\lambda_i)}{dw} \right) \Delta w \tag{3.43}$$

which tells that $\Delta\Omega$ depends on the variations of the propagation constants β with respect to the width w. From Fig.3.26, it can be seen that for the combination $(4, 4, 3, 5)$, which involves only TM modes, no matching is found between theory and experiment for any reasonable value of waveguide width. This tells that variations on the waveguide height have to be considered when dealing with only TM modes, due to their high effective index sensitivity to thickness variations. Nevertheless, the height can be controlled with much more tight tolerances than the width. Typically, the height of the Silicon layer of a SOI wafer has inhomogeneities at the order of $\pm 5\,nm$ [90]. This is why the discrepancy between the experimental and the theoretical signal wavelengths is only $(4.1 \pm 0.1)\,nm$.

While the average width of the waveguide has the effect to shift the wavelength position of the signal peak, the inhomogeneities along the propagation direction have the effect to increase the bandwidth of the generated radiation. For example, this can be appreciated from the comparison between the simulated and the experimental signal spectra in Fig.3.21. The predicted bandwidth is $0.3\,nm$, while the experimental one is $(1.0 \pm 0.2)\,nm$, i.e., three times larger. The effect of inhomogeneities in the waveguide width, of amplitude $\Delta w(z)$, is to change the wavevector of the propagating radiation along the length of the waveguide. Each of these wavevectors generaties signal radiation at frequencies which are shifted by $\Delta\Omega(\Delta w)$ from the average one. As a consequence, the bandwidth of the process is increased. In a first approximation the broadening of the signal peak has been computed by writing the modes of the waveguide with a variable width $w(z) = \langle w \rangle + \Delta w(z)$ as:

$$E \approx \frac{1}{2} E_0 e(x, y) e^{-i\beta(w(z))z} + c.c \tag{3.44}$$

where $\beta(w(z))$ is the wavevector associated to the same mode order in a uniform straight waveguide of width $w = w(z)$. Using the same approach which lead to the derivation of Eq.3.5-3.8, the generated signal power P_s is found to be proportional to:

$$P_s \propto \left| \int e^{-i\Delta k(z)z}\, dz \right|^2 \tag{3.45}$$

where the position dependent phase matching $\Delta k(z)$ is written as:

$$\Delta k(z) = 2\beta_p(w(z), \lambda_p) - \beta_s(w(z), \lambda_s) - \beta_i(w(z), \lambda_i) \tag{3.46}$$

In order to calculate the integral in Eq.3.45, the waveguide width variations are modeled as follows :

1. The width variation is assumed to be piecewise constant in sections of length σ_{coh} . The latter is a uniformally distribuited variable between $1\,nm$ and $18\,nm$, which is the maximum correlation length measured from Scanning Electron Microscopy images of the fabricated waveguides. The integration step of Eq.3.45 is $1\,nm$.

2. For each section, the width is constant and given by $w = \langle w \rangle + \Delta w$, where $\langle w \rangle$ is the average value given in Table 3.5 and Δw is a random variable with zero mean value and standard deviation σ_Δ.

The use of this procedure allows to reproduce the more realistic situation where the width of the waveguide randomly changes with a finite correlation length. The results are shown for the combination $(1, 1, 4, 2)$ in Fig.3.27, where the spectrum of the signal power is plotted for different values of σ_Δ.

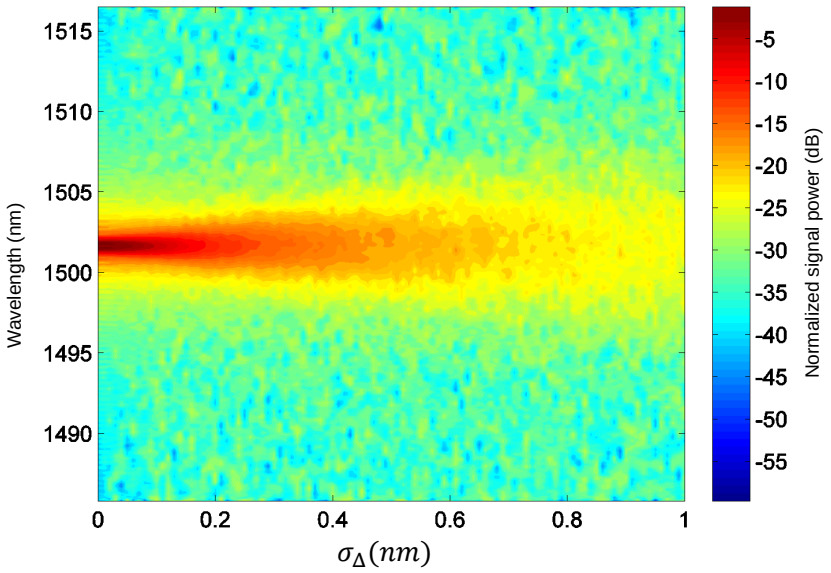

Figure 3.27: Normalized signal power spectrum as a function of the modulation width parameter σ_Δ. The power is normalized with respect to the peak power at $\sigma_\Delta = 0$.

As σ_Δ increases, the FWM peak broadens, and at the same time the efficiency decreases. Note that the wavelength where the signal power is maximum is not affected by the magnitude of σ_Δ, since it is fixed only by the average width $\langle w \rangle$. Using Eq.3.45, the values of σ_Δ are evaluated for all the combinations listed in Table 3.3 by matching the experimental $3\,dB$ bandwidth with the ones from simulations. Table 3.6 summarizes the results.

Modal combination	$\sigma_\Delta(nm)$
$(1, 1, 4, 2)$	0.68 ± 0.2
$(3, 3, 3, 5)$	0.70 ± 0.2
$(1, 1, 3, 3)$	0.51 ± 0.2

Table 3.6: Magnitude of the modulation width parameter σ_Δ for the different combinations reported in Table 3.2.

As a last step, few words have to be spent about the spontaneous version of the MMFWM processes described above. All the combinations reported above have been probed using an idler beam which stimulates the process. Some experiments have been also performed by removing the idler, but no correlated pairs have been detected. The motivation lies in the fact that the generated photon flux was too low for being detected even with a photon counter of $-120\,dBm$ of detection limit. An estimation of the expected flux can be done using the scaling relations provided by the work of G.Helt et.al. [200]. Here, an expression for the idler power P_i generated by sFWM in a straight waveguide has been derived in terms of the efficiency of the stimulated process η_{FWM}, and of a "semi-classical" input signal power P_s, as $P_i = \eta_{FWM} P_s$. The signal power is given by $P_s = \hbar \omega_p B$, where ω_p is the frequency of the pump and B the bandwidth of the process. For example, with

reference to the modal combination $(4,4,3,5)$ in the $3.65\,\mu m$ wide waveguide, $B \approx 124\,GHz$ (corresponding to a linewidth of $\approx 1\,nm$, see Fig.3.21(b)), $P_s \approx -50\,dBm$ and $\eta_{FWM} = -82\,dB$. This has been computed by considering a continuos wave pump power of $0\,dBm$, which corresponds to the realistic value that can be coupled into the waveguide by using the tunable Infra-Red laser of the experiment described in section 3.4. By combining together these factors, the expected idler power is $P_i \approx -132\,dBm$, to which $\approx -8\,dB$ of fiber to chip coupling losses have to be added, with the result that the power to be detected is $\approx -140\,dBm$. This value lies well below the detection limit of the implemented photon counter. In the experimental conditions described in section 3.4, the conversion efficiency is $\eta_{FWM} = (-37.4 \pm 0.2)\,dB$, and is higher than in the continuous case because the peak power of the pulsed laser is $\approx 25\,dBm$. In this case, the detected flux would be $-95.4\,dBm$ (coupling losses have already been taken into account). However, the generated flux comes in temporal pulses of width Δt and repetition rate R, and one has to consider the average flux as the quantity that the photon counters detects. As already discussed in section 3.4, the average flux (expressed in dBm) is lower than the peak flux by a quantity $10\log(R\Delta t)$, which for the parameters of the pulsed laser is equal to $\approx -23\,dB$. The average photon flux is then $P_i = -118.4\,dBm$. This value is very close to the detection limit of the photon counter, which could explain the reason why no sFWM has been detected.

3.5 Future perspectives: use of MMFWM for MIR to NIR conversion

As discussed in Section 3.2, the main feature of the MMFWM approach is its ability to achieve large spectral translations between the signal and the idler signals while keeping the roboustness against fabrication imperfections. Such large wavelength conversions are very difficult to achieve with FWM in which all the waves propagate in the same mode order, due to GVD and to the ultra-high sensitivity of even order dispersions to small changes in the waveguide cross section. Table 3.7 summarizes the efficiencies of the process and the relative spectral translations for the different modal combinations tested in the experiment.

Modal combination	**Polarization**	**Spectral translation** (nm)	**Efficiency** (dB)
$(1,1,1,1)$	(TM,TM,TM,TM)	20	-31.4
$(3,3,3,3)$	(TE,TE,TE,TE)	40	-35
$(4,4,3,5)$	(TM,TM,TM,TM)	178.0 ± 0.2	-37.4 ± 0.2
$(1,1,4,2)$	(TM,TM,TM,TE)	187.0 ± 0.2	-19.4 ± 0.2
$(3,3,3,5)$	(TM,TM,TM,TE)	101.3 ± 0.2	-37.8 ± 0.2
$(1,1,3,3)$	(TM,TM,TM,TE)	145.8 ± 0.2	-36.3 ± 0.2

Table 3.7: Spectral translation (defined as the distance between the signal and the idler wavelength) and associated conversion efficiencies for different MMFWM combinations. The results for the combinations $(1,1,1,1)$ and $(3,3,3,3)$ come from numerical simulations.

In this table, also the single mode combinations $(1,1,1,1)$ and $(3,3,3,3)$ have been included, to emphasize that the conversion efficiency is comparable to the ones achieved using MMFWM at spectral distances which are an order of magnitude larger. This peculiarity can be exploited to realize up conversions from MIR photons to Near Visible ones. The detection of MIR photons is indeed a very difficult task, and requires the use of expensive and not CMOS compatible materials as $HgCdTe$ (Mercury Cadmium Telluride) or $InSb$ (Indium Antimonide) [205]. What is more, these detectors are very bulky due to their internal cooling system which has to keep the operating temperature typically below $70\,K$ [206]. The difficulties in MIR photon detection mainly rely on the fact that the energy of the photons to be detected is comparable to the thermal energy kT of the environment. This fact has the drawback of creating electron hole pairs in

the material due to thermal excitation, thus contributing to the enhance the dark counts of the detector. This is why a cooling system is always required. The blackbody radiation emitted by the detector itself, or from the surrounding environment, has also a not negligible component in the MIR spectral region, which requires filtering to isolate the signal. If MIR photons were converted to NIR or visible ones, one could employ the wide variety of NIR-Vis detectors to detect the up converted radiation. This class of detectors have the advantages of being less expensive that the ones for MIR, and to have higher detection efficiencies, lower dark counts and can operate at room temperature. The principle of up conversion has been already implemented in the work of S.D. Jeppe et. al.[207], where MIR photons are up converted to visible ones using sum frequency generation in a periodically poled Lithium Niobate crystal. A similar approach can be done on a chip by using MMFWM in Silicon waveguides. An illustrative example of a conversion of a MIR idler at $2.88\,\mu m$ to a NIR signal at $1.06\,\mu m$ using a pump at $1.55\mu m$ is given in Fig.3.28.

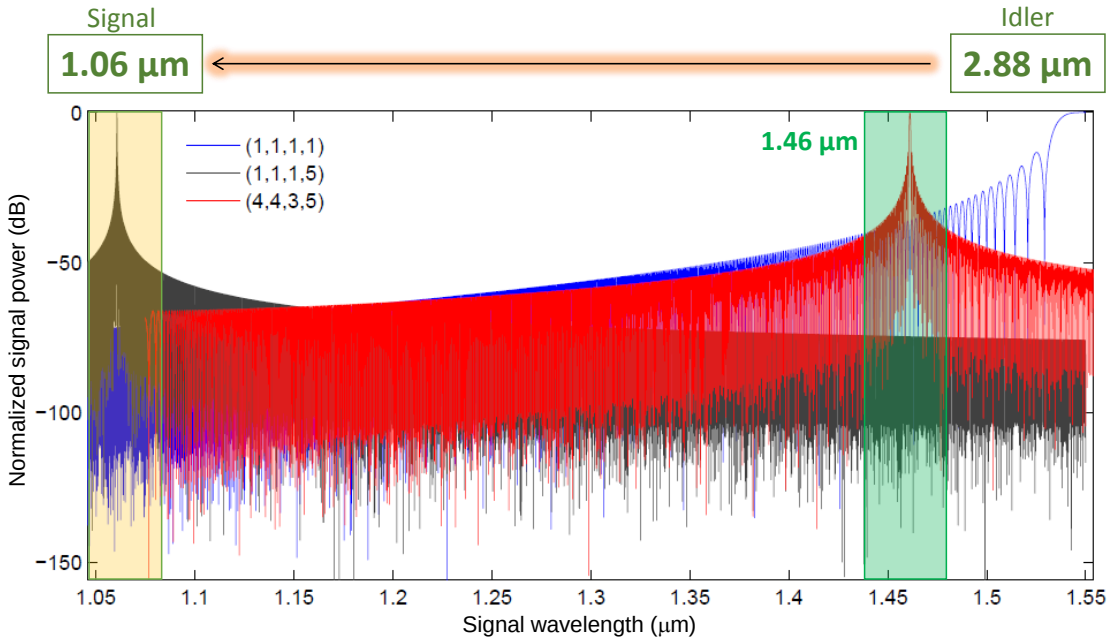

Figure 3.28: Simulation of MMFWM for realizing a spectral translation from an idler at $2.88\,\mu m$ into a signal at $1.06\,\mu m$ using MMFWM in a Silicon waveguide of $3.65\,\mu m \times 0.25\,\mu m$ cross section. The implemented combination is $(1,1,1,5)$, and all the modes have TM polarization. The simulation of the $(4,4,3,5)$ combination, whose feasibility has been experimentally demonstrated in Section 3.4, is also shown in the picture. For each curve, the power is normalized with respect to the maximum value.

This translation is realized by a waveguide of cross section $3.65\,\mu m \times 0.25\,\mu m$ and the modal combination $(1,1,1,5)$, where all the modes have TM polarization. The efficiency of the wavelength conversion could be limited by TPA, which limits the amount of power that can propagate in the waveguide. In order to overcome this limitation, different materials than Silicon can be implemented. For example, Silicon Nitride or Silicon Oxinitride are both CMOS compatible materials whose bandgap is much larger than the one of Silicon. In this way, the threshold for the occurrence of TPA is significantly shifted towards lower wavelengths, with the result that the pump power at $1.55\,\mu m$ can be grately increased without incurring in the problem of nonlinear absorption.

3.6 Future perspectives: on chip implementation of two beams interference

The two beam interference experiment discussed in Section 3.3.2 revealed that the method was effective for selective mode excitation with a very low modal cross talk. The main drawbacks were the high coupling losses and the difficulties to align the input waveguide facet in the point where the two beams interfere. These problems can be solved by integrating the interferometer on a chip. The design of the device which accomplish this task is shown in Fig.3.29(a). Here, the pump and the idler beams are coupled into two single mode waveguides from separate inputs. Both are equally split using a directional coupler and the four outgoing waveguides are directed toward a Free Propagation Region (FPR), where light can freely diffract into a Silicon slab waveguide. The four input waveguides are placed on the circumference of a circle of radius R. The two arms which originate from the pump splitting approach the FPR by making an angle $2\theta_p$, while the two arms which originate from the idler splitting make an angle $2\theta_i$ (see Fig.3.29(b)). These angles are chosen in order to maximize the overlap of the diffracted field with the one of the modes which one wants to selectively excite, and can be extracted from Fig.3.8. Since the transmitted field of a directional coupler is $-\frac{\pi}{2}$ out of phase with respect to the reflected one, attention has to be paid to the symmetry of the mode which one want to excite in the output waveguide. In case of modes with odd symmetry with respect to the center of the waveguide, the relative phase ϕ between the outgoing arms of the directional coupler has to be set to $\phi = \pm\pi$ (see Section 3.3.1). In case of modes with even symmetry, the phase has to be set to $\phi = 0$. A FEM simulation which shows the light propagation into the FPR is shown in Fig.3.29(c). Here, the angle is chosen in order to maximize the overlap with the 3^{rd} order mode of the output waveguide. The size of the four input waveguides w_{in} and the radius R of the FPR have to be optimized in order to maximize the ratio between the power coupled into the output waveguide and the losses due to the portion of the diffracted field which is not coupled. As a general rule, the larger is the radius, the lower is the crosstalk between the excited modes, since the gaussian envelope of the fringes is less marked and the resulting interference pattern is closer to the ones of Fig.3.3. However, larger radius imply more losses, since the field spreads more with distance due to diffraction. This can compensated by enlarging the size of the input waveguides. A tradeoff between all these effects have to be chosen. At the moment of writing this work, the optimization procedure is currently under investigation. The first results reveal that the coupling losses range from a minimum of $1\,dB$ to a maximum of $5\,dB$, depending on the value of R and w_{in}.

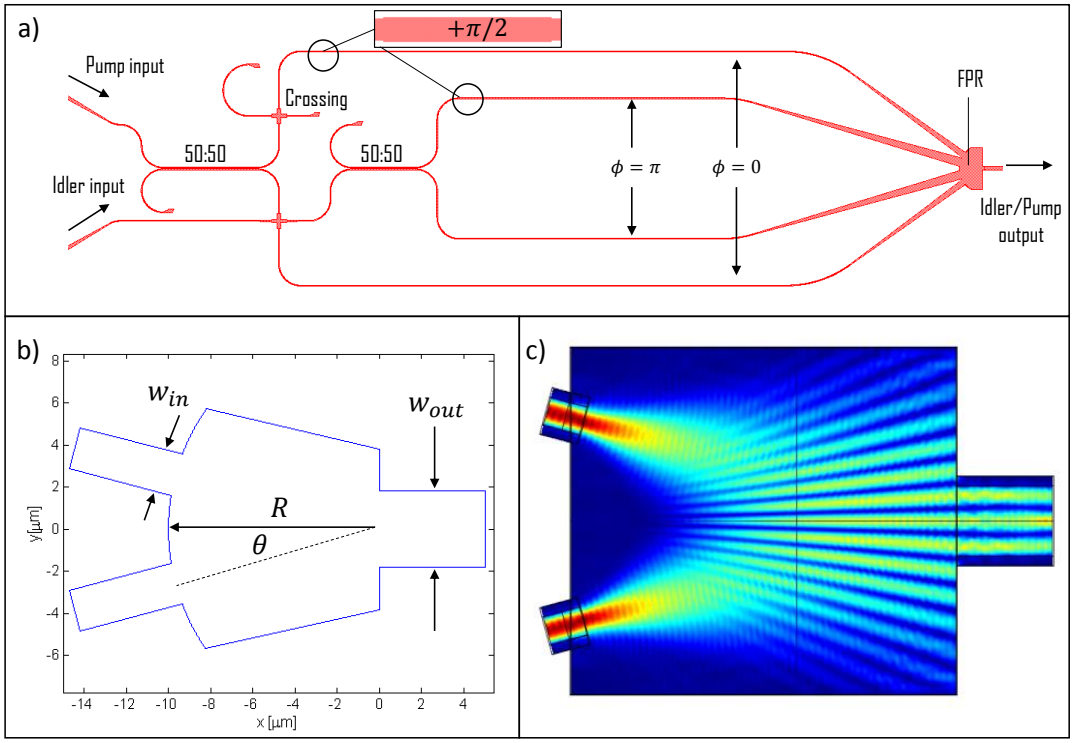

Figure 3.29: (a) Design of the integrated device which realizes the two beam interference experiment of section 3.3.2. In this example, the pump is coupled into a mode of even symmetry ($\phi = 0$), while the idler into a mode of odd symmetry ($\phi = \pm\pi$). (b) Detail of the FPR, indicating the key parameters of the device as the size of the input waveguides w_{in}, the radius R of the Free Propagation Region, the angle θ and the size of the output waveguide w_{out}. Here, only two of the four inputs are shown for clarity. (c) FEM simulation of the light propagation in the FPR.

3.7 Conclusions

In this chapter, the process of Multi Modal Four Wave Mixing has been studied in straight Silicon waveguides. An intense pump and an idler beam have been coupled into a multimode waveguide in specific mode orders, and the generated signal is collected at the output. To this purpose, two methods have been introduced and experimentally characterized. The first exploits the interference of two coherent beams which converges toward the input of the waveguide at an angle θ between each other. The interference pattern created by the crossing of the two beams reproduces the standing wave pattern of the field distribution of the waveguide modes. The angle is tuned to maximize the overlap between the incoming field with the one of the target mode that one wants to selectively excite into the waveguide. Using this procedure, a stable selective mode excitation has been demonstrated. Unfortunately, the method suffered from high coupling losses, which prevented to observe any MMWFM process. Losses mostly originated from the huge mismatch between the modal effective area and the one of the incoming exciting field. The second approach is based on the capability of a tilted tapered lensed fiber to excite higher order modes. The inclination of the fiber with respect to the normal of the waveguide input facet determines the fraction of power which is coupled at the different mode orders. As the angle increases, higher order modes are excited. Thanks to the reduced effective area of the field which exits from the fiber, it has been possible to significantly reduce the coupling losses and to observe MMFWM for different modal combinations and waveguide widths. Several tests have been done in order to demonstrate that the FWM process was realized from a multimode excitation. In

particular, numerical simulations revealed that the measured conversion efficiencies could be only explained if the pump, the signal and the idler waves were propagating in different mode orders. All the main features of the measured FWM spectra have been interpreted with the help of numerical simulations. The discrepancies between the wavelengths where the maximum signal was predicted and the ones found in the experiment were attribuited to the fact that the average waveguide width differed from the nominal ones due to fabrication defects. Random nanometric variations of the width along the propagation direction were seen to broaden the FWM signal peak. The capability of MMFWM to achieve high conversion efficiencies at large spectral distances between the signal and the idler can be exploited to realize an integrated device which up converts MIR photons to NIR ones, or to realize the inverse process in which NIR photons are converted into MIR ones (MIR sources). This would allow to detect MIR photons by using NIR detectors, which are less bulky and expensive than the ones for the Mid Infrared. For all the investigated combinations, the FWM process is stimulated by the presence of the idler wave, and thus do not create correlate pairs of signal/idler photons. The latter is indeed an intrinsic property of spontaneous FWM, in which only the pump beam is coupled into the waveguide, and signal/idler pairs are generated by the amplification of vacuum fluctuations. This process is of interest for the realization of on chip quantum sources of entangled photons, that was the main motivation for which the straight waveguides were designed and fabricated. The high coupling losses associated to the stage of selective mode excitation prevented the observation of the spontaneous phenomenon. This is the reason why a new class of devices are currently under design and will be tested in the near future. These are essentially the integrated implementation of the two beam experiment described in section 3.3.2, but with highly reduced coupling losses. The main features of such devices are represented by high coupling efficiencies, low modal crosstalk and roboustness against fabrication imperfections.

Chapter 4

Investigation of strain induced $\chi^{(2)}$ nonlinearities in Silicon waveguides through the electro optic effect

In this chapter, the possibility to induce a $\chi^{(2)}$ nonlinearity in Silicon by straining its unit cell is investigated. Within the framework of the project SIQURO, this task has the final aim to propose Silicon as a platform for generating entangled photon pairs through SPDC. Enabling a $\chi^{(2)}$ in Silicon would allow to integrate the $\chi^{(2)}$ quantum sources directly on a chip, removing the constraint to look for bulky external sources like Lithium Niobate or Barium Borate crystals. From a more general point of view, the enabling of the whole class of $\chi^{(2)}$ effects, like SHG, Sum Frequency Generation, Difference Frequency Generation and especially electro optic modulation (Pockels effect), would enormously boost the applications and engineering possibilities of Silicon Photonics. This will constitute an important step towards standardization, in which only one material (Silicon) and only one fabrication process (CMOS) is used to accomplish an increasingly number of functionalities within the same integrated chip.

As already introduced in Chapter 1, crystalline Silicon has a diamond structure, which means that it is intrinsically centrosymmetric. With reference to Fig.4.1(a), showing the Silicon unit cell, this means that the points indicated by the vectors $\mathbf{r}$ and $-\mathbf{r}$ are equivalent, i.e, they share all the symmetry and geometric properties.

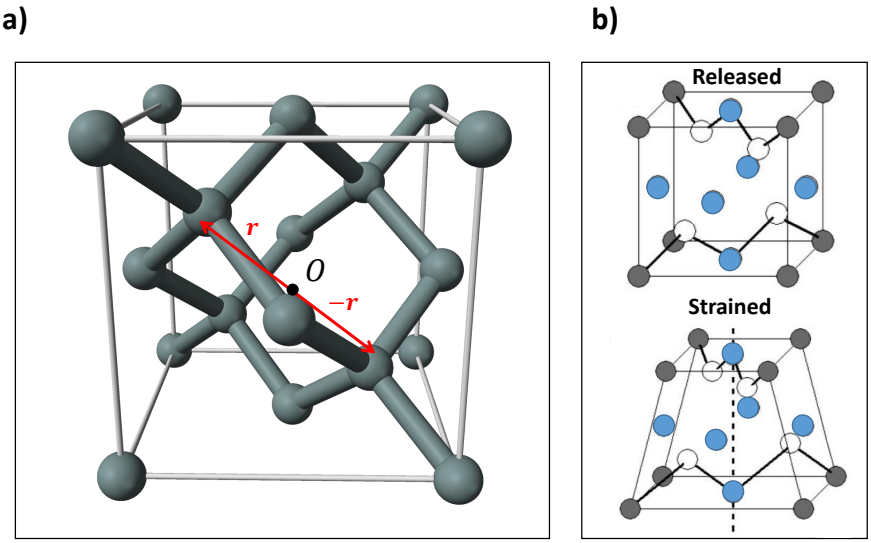

Figure 4.1: (a) Hard ball model of the unit cell of crystalline Silicon. The point O, where opposite vectors $\mathbf{r}$ and $-\mathbf{r}$ originate, is the inversion point. (b) Top panel: unstrained unit cell. Low panel: unit cell with inhomogeneous strain applied and loss of centrosymmetry.

The point O, which is located exactly at the center of the cubic lattice, is called the inversion point. The macroscopic polarization $\mathbf{P}$ should then change sign upon inversion of the direction of an applied static electric field $\mathbf{E}$, in other words:

$$\mathbf{P}(\mathbf{E}) = -\mathbf{P}(-\mathbf{E}) \tag{4.1}$$

By expanding the constitutive relation $\mathbf{P}(\mathbf{E})$ up to the third order in $\mathbf{E}$, we have:

$$\mathbf{P}(\mathbf{E}) \approx \epsilon_0(\chi^{(1)} \cdot \mathbf{E} + \chi^{(2)} \cdot \mathbf{EE} + \chi^{(3)} \cdot \mathbf{EEE}) \tag{4.2}$$

Equations (4.1) and (4.2) are compatible only if the second order susceptibility tensor $\chi^{(2)}$ is equal to zero, that is, crystalline Silicon has no native second order nonlinearities. The only way to enable second order nonlinearities is to break the centrosimmetry of the fundamental unit cell. In the experiments described later, this is accomplished by covering Silicon waveguides with a thin stressing layer of Silicon Nitride.
In this chapter, a method which, in principle, would allow to determine most of the components of the $\chi^{(2)}$ tensor, is presented. The latter makes use of the electro optic effect in titled strained racetrack resonators. In contrast with all the previous works, in which the Pockels effect is monitored using DC signals [139, 140, 141, 138, 142], the probe here is a low frequency (KHz) AC voltage captured by two Lock In Amplifiers. The basic theory and the experimental methods are introduced in section 4.1.1 and 4.1.3, while the results are discussed in section 4.3.1. At this stage, some anomalies have been encountered, which suggested that the observed electro optic modulation does not have a $\chi^{(2)}$ origin but it is rather a consequence of plasma carrier dispersion. To distentagle the two contributions, high frequency (GHz) electro optic measurements have been performed on the same devices, and the results and conclusions are presented in section 4.3.4 and 4.3.5.
The experiments described in section 4.3.1 and in section 4.3.2 have been done with the collaboration of Dr. Mattia Mancinelli (University of Trento). Experiments described in section 4.3.5 have been done with the collaboration of Mr. Saeed Sharif, Dr. Florian Merget and Dr. Jeremy Witzens (RWTH-Aachen University).

4.1 Electro optic effect in titled racetrack resonators: principles and design

4.1.1 Principles of the method

In most of the previous works, the elements of the $\chi^{(2)}$ tensor have been probed by measuring the electro optic effect in an unbalanced integrated Mach Zehnder (MZ) interferometer [139, 138, 142]. Electrodes are placed on the top of one or both arms of the interferometer, and are driven by a DC (or low frequency) voltage. A stressing layer, usually Silicon Nitride, is conformally deposited on the waveguide core to break the centrosymmetry [157, 140]. As a consequence of the applied voltage and of the electro optic effect, the refractive index of the material changes by Δn, and a relative phase shift $\Delta\phi(\Delta n)$ between the two arms is induced. Since interference fringes of the form $\cos(\Phi_0 + \Delta\phi(\Delta n))$ are created at the output of the MZ, this has the effect to shift the whole pattern and form this shift, $\Delta\phi$ can be extracted. Plotting $\Delta\phi$ as a function of the applied voltage V has revealed a linear relationship, which has been considered as the proof of the presence of a $\chi^{(2)}$ electro optic modulation in Silicon. The reason why the shift should be linear in V comes directly from Eq.4.2: if we write the total electric field inside the material as the sum of an optical field $\mathbf{E}(\omega)$ plus a DC field $\mathbf{E}_{DC}$, we obtain a polarization source at frequency ω of the form:

$$\mathbf{P}_{eo}(\omega) = \epsilon_0 \chi^{(2)} \cdot \mathbf{E}_{DC} \mathbf{E}(\omega) \tag{4.3}$$

This polarization factorizes with the linear polarization induced by the valence bond electrons $\mathbf{P}^{(1)}(\omega) = \epsilon_0 \chi^{(1)} \mathbf{E}(\omega)$, to give a total polarization:

$$\mathbf{P}(\omega) = \mathbf{P}^{(1)} + \mathbf{P}_{eo} = \epsilon_0(\chi^{(1)} + \chi^{(2)} \cdot \mathbf{E}_{DC}) \cdot \mathbf{E}(\omega) = \epsilon_0 \epsilon_r \cdot \mathbf{E}(\omega) \tag{4.4}$$

From the relation $\epsilon_r = n^2$, where $n$is the material refractive index, we obtain:

$$\mathbf{n} \approx n_0 + \Delta\mathbf{n} = n_0 \left(1 + \frac{\chi^{(2)}}{2} \cdot \mathbf{E}_{DC}\right) \tag{4.5}$$

which states that a linear relation exists between the induced refractive index change $\Delta\mathbf{n}$ (hence $\Delta\phi$) and the applied static field $\mathbf{E}_{DC}$ (hence V).
Following this approach, only few elements of the $\chi^{(2)}$ tensor have been extracted, and the reason lies in the geometry of the implemented configurations. Fig.4.2(a) shows a typical layout of the MZ device, while the cross section is shown in Fig.4.2(b).

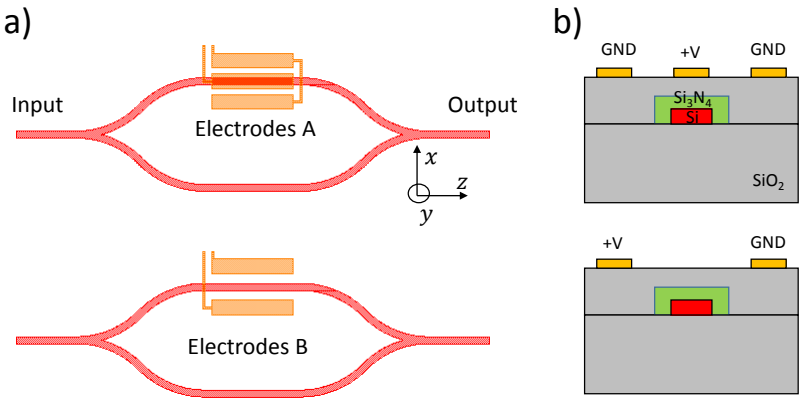

Figure 4.2: (a) A typical layout of the MZ interferometer for testing the electro optic effect. Electrodes in configuration A applies an electric field in the $\hat{y}$ direction. Electrodes in configuration B applies an electric field in the $\hat{x}$ direction. (b) Cross sections of the device (xy plane) associated to the configurations of electrodes A and B. The green layer is the stressing material, usually Silicon Nitride (Si_3N_4). $+V$ indicates a positive voltage, while GND stands for Ground.

The propagation direction is $\hat{z}$, while $(\hat{x}, \hat{y})$ are the transverse directions of modal confinement. Using the set of electrodes indicated as (A), a DC field in the $\hat{y}$ direction can be applied, while using the set (B), the direction is along $\hat{x}$. The optical field can be set either TE ($\hat{x}$) or TM ($\hat{y}$). With these constraints, the four elements of the $\chi^{(2)}$ tensor that can be extracted from an electro optic measurement are reported in Table 4.1.

$\chi^{(2)}_{ijk}$ component	Optical field polarization	DC field polarization
$\chi^{(2)}_{xxx}$	x	x
$\chi^{(2)}_{yyx}$	y	x
$\chi^{(2)}_{xxy}$	x	y
$\chi^{(2)}_{yyy}$	y	y

Table 4.1: Elements of the $\chi^{(2)}$ tensor which can be extracted using the electrodes configuration shown in Fig.4.2.

It is worth to point out that, in principle, by sending a cross polarized field at the input and by monitoring the fringes separately for the TE and TM polarizations, one could also get some informations about the $\chi^{(2)}_{ijk}$ components with $i \neq j$. However, this approach is complicated by the fact the device can not be easily optimized for achieving good performances for both the TE and TM polarizations due to the strong birifrangences of Silicon waveguides.

Probing components which involve the $\hat{z}$ direction is extremely difficult due to the fact that the electric fields of the optical modes are mainly transverse. The component along the propagation direction is typically one order of magnitude lower with respect to the transverse ones, and it decreases as the width of the waveguide increases.

This bottleneck could be removed using tilted devices. The tilting angle is referred to a reference crystallographic axes, and the choice of the latter depends on the SOI wafer cut orientation. In the work described in section 4.3.1, this direction is the [100], which means that devices at 0 degrees have waveguides where [100] correponds the propagation direction. To illustrate the concept, consider the two waveguides shown in Fig.4.3.

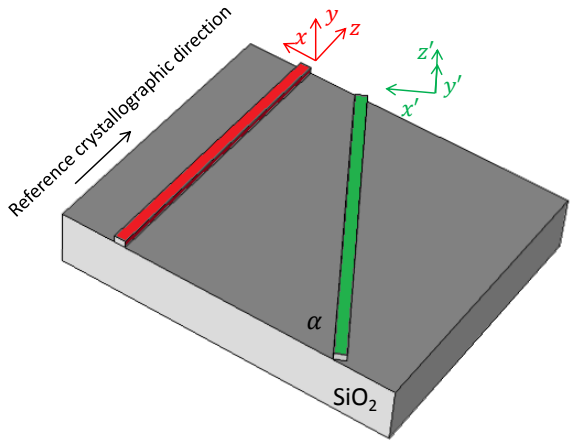

Figure 4.3: Two waveguides rotated by an angle α, together with their reference frames ((x, y, z) for the red one, (x', y', z') for the green one). The red waveguide has the propagation direction aligned with the reference crystallographic axis, shown with a black arrow.

The red one is at 0 degrees, the green one at α degrees. The two reference frames $O(x, y, z)$ and $O'(x', y', z')$ have the $z(z')$ direction aligned with the direction of propagation of light, and are linked together by the rotation matrix $R_{ij}(\alpha)$. If one applies to the Maxwell's equations, written in the O reference frame, the transformation described by the rotation matrix $R_{ij}(\alpha)$, one would obtain the same set of equations in which the new $\chi^{(2)}$ tensor is written as:

$$\chi^{(2)}_{i'j'k'} = \sum_{lmn} R_{il} R_{jm} R_{kn} \chi^{(2)}_{lmn} \tag{4.6}$$

Which states that the $\chi^{(2)}$ tensor in the rotated reference frame can be written as a linear combination of the $\chi^{(2)}$ components in the not rotated one. A 3^{rd} rank tensor has in general $3^3 = 27$ independent elements, but from Maxwell's equations it turns out that only 18 are independent [160]. It would be sufficient to tilt the device in at least five independent orientations, and for each direction measure four components as the ones listed in Table 4.1, to build a set of $5 \times 4 = 20$ equations in 18 unknowns and consequently map the $\chi^{(2)}$ tensor.
However, this is subjected to some assumptions, which have to be validated from the experiment:

- Each set of four measurements, executed at a fixed angle, constitutes a set of four independent equations. Each set of equations is independent from each other.
- The strain distribution does not depend on the direction of the waveguide. This condion is necessary to use Eq.4.6.

4.1.2 Design of racetrack resonators

The MZ structure requires quite long arms (at the order of $1 - 2\,cm$ in Ref.[139]) to be sensitive to small phase shifts $\Delta\phi$, so in order to reduce the footprint and accomodate on a single chip more devices at different tilting angles, racetrack shaped resonators have been designed. The use of high Q cavities allows to detect very small phase shifts, keeping low footprints, by monitoring the wavelength position of the resonances when a voltage is applied at the electrodes. The resonator is arranged in the AD configuration, so it has two output ports, the Drop and the Through one. The coupling length L_c and the resonator perimeter L_{tot} fix, together with the propagation losses, the Q factor of the resonator and, hence, the FWHM of the resonance. In order

to detect the small phase shifts imparted by the electro optic effect, the resonance width has to be sufficiently narrow to resolve such small phase variations. Using a value of $\chi^{(2)} \approx 100\,pmV^{-1}$ [139] and an electric field of the order of $10^6\,Vm^{-1}$ (which corresponds to approximately $100\,V$applied to the electrodes in Ref.[139]), the voltage induced refractive index shift can be predicted using Eq. 4.5 to be $\Delta n \approx 10^{-4}$. The associated resonance shift $\Delta\lambda$ is of the order of $\Delta\lambda = \lambda_0(\Delta n/n_g) \approx 40\,pm$ (the resonance wavelength is assumed to be $1.55\,\mu m$ and the group index $n_g = 4$). The FWHM of the resonator should be then of the order of $40\,pm$ to easily detect the resonance shift. In Fig.4.4 it is shown the FWHM of an Add Drop filter as a function of the perimeter and the coupling coefficient κ^2 at $\lambda = 1.53\,\mu m$, with the propagation loss fixed at $4\,dBcm^{-1}$.

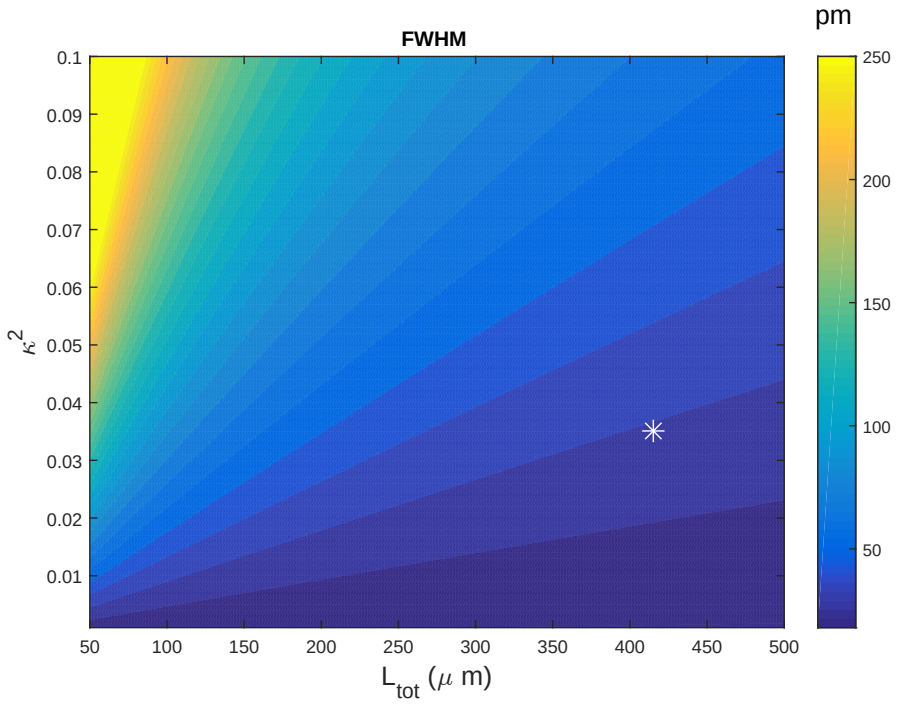

Figure 4.4: The FWHM of an Add-Drop filter as a function of the coupling coefficient κ^2 and of the resonator perimeter, with the losses fixed to $4\,dBcm^{-1}$

The white star in the contour plot indicates the values of κ^2 and L_{tot} that have been chosen for the design. These are $\kappa^2 = 3.5\%$ and $L_{tot} = 415\,\mu m$, corresponding to a FWHM of $\approx 35\,pm$. Four class of devices have been designed, and are referred as CAP140, CAP70, HAT140 and HAT70. These differ from the shape and the thickness of the stressing layer (Silicon Nitride (Si_3N_4)) deposited on the top of the waveguides, as shown in Fig.4.5. The length of L_c and the coupling gap c_g will depend on the polarization and on the type/geometry of the stressing layer deposited on the top of the waveguides. The coupling length L_c is kept fixed and c_g is tuned for achieving $\kappa^2 \leq 3.5\%$ (which means a $FWHM \leq 35\,pm$), as indicated in Table 4.2.

Wafer	**Deposition**	Si_3N_4 **thickness**	L_c	$c_g\,(nm)$	κ^2
CAP140	**Conformal**	$140\,nm$	12.17	$450(TE), 600(TM)$	$3.5\%(TE), 3.5\%(TM)$
CAP70	**Conformal**	$70\,nm$	12.17	$450(TE), 600(TM)$	$2.4\%(TE), 4\%(TM)$
HAT140	**Only on the WG top**	$140\,nm$	12.17	$450(TE), 600(TM)$	$1.4\%(TE), 2.5\%(TM)$
HAT70	**Only on the WG top**	$70\,nm$	12.17	$450(TE), 600(TM)$	$1.4\%(TE), 3.8\%(TM)$

Table 4.2: Design details of the four class of devices dedicated for the study of the electro optic effect in strained Silicon resonators.

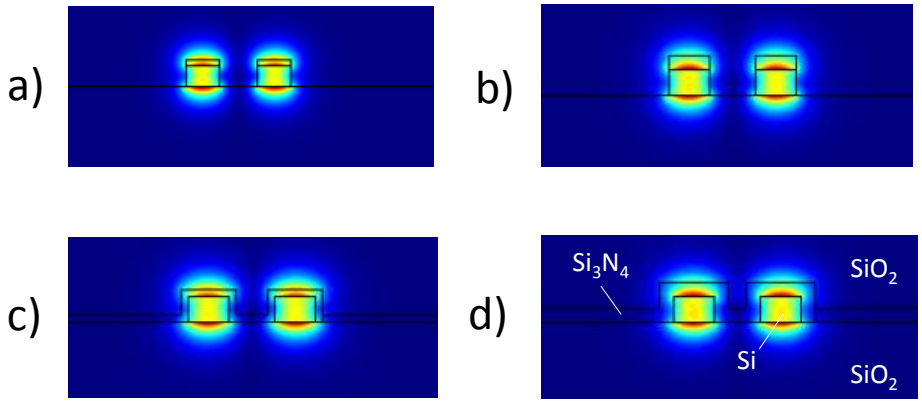

Figure 4.5: FEM simulations of the first TM supermode of the directional coupler used to couple energy from the bus waveguide to the resonator. The colormap refers to the field intensity. (a) HAT70, (b) HAT140, (c) CAP70, (d) CAP140.

To study the connection between the induced $\chi^{(2)}$ tensor and strain, resonators with different waveguide widths have been designed. The waveguide width, which strongly influences the strain distribution, is changed from $400\,nm$ to $4\,\mu m$ with steps of $400\,nm$. The final device geometry is shown in Fig.4.6.

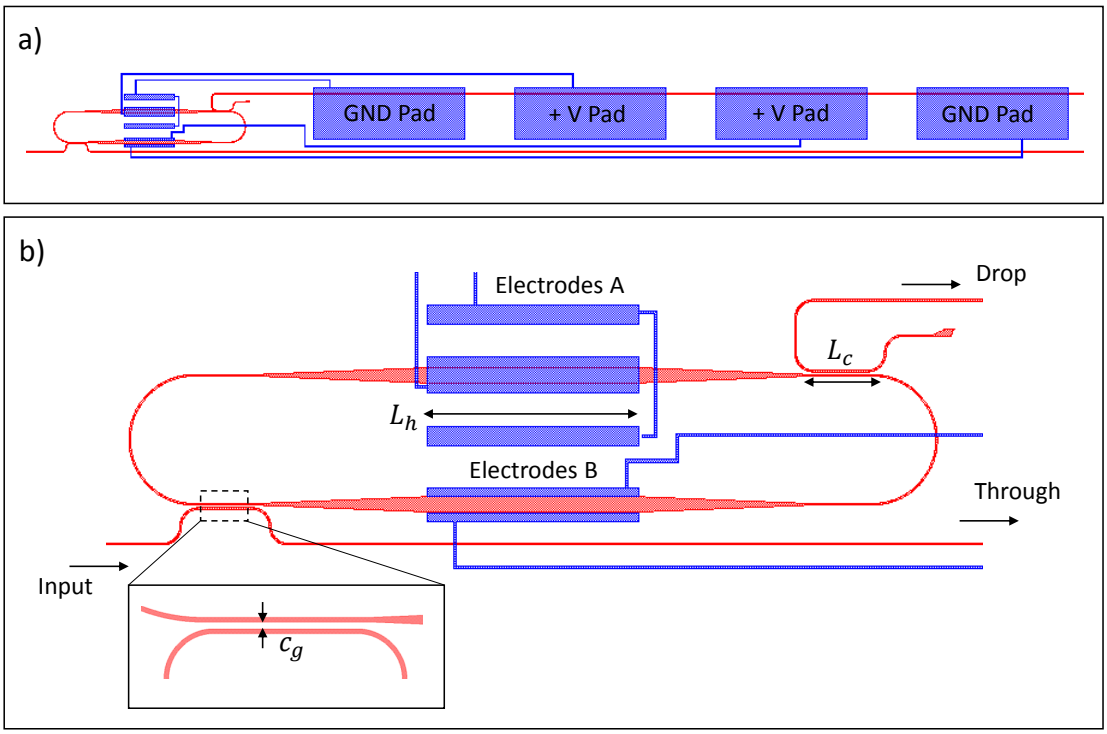

Figure 4.6: (a) Extended layout of the resonator geometry, showing the Aluminium pads connections to the electrodes. (b) Zoom of the device geometry. L_c = coupling length, c_g = coupling gap, L_h = electrode length. In the electrode configuration A, the central electrode has a width of $8.5\,\mu m$ and is separated by the two external electrodes (of $4.5\,\mu m$ width) by $7.75\,\mu m$. The external electrodes are shorted to a common voltage (usually GND). In the configuration B, the electrodes have a width of $2\,\mu m$ and are separated by $4\,\mu m$.

To preserve single mode operation, the resonator waveguide is tapered from $400\,nm$ to the desired width using an adiabatic taper of length $40\,\mu m$. Two set of Alluminium electrodes of length $L_h = 50\,\mu m$, in the same configuration as the ones shown in Fig.4.2, are deposited on the top of the waveguides, and optically isolated using a Silica layer of thickness $900\,nm$. Only one set of electrodes can be activated at the same time. As shown in Fig.4.7, the geometry of the electrodes provides a quite flat electric field profile inside the waveguide. The intensity of such field depends on the direction, the width of the waveguide and the Silicon Nitride thickness/conformation. For example, in Fig.4.7, the average electric field inside a waveguide of $800\,nm$ width in the CAP140 configuration is $\mathbf{E}_{DC} = -0.5{\cdot}10^4 \hat{\mathbf{y}} V m^{-1}$ (Fig.4.7(a)) or $\mathbf{E}_{DC} = 8.2{\cdot}10^4 \hat{\mathbf{x}} V m^{-1}$ (Fig.4.7(b)) at $1\,V$ applied to the set of electrodes A and B respectively. The average electric field increases linearly as a function of the applied voltage, as it is shown in Fig.4.8.

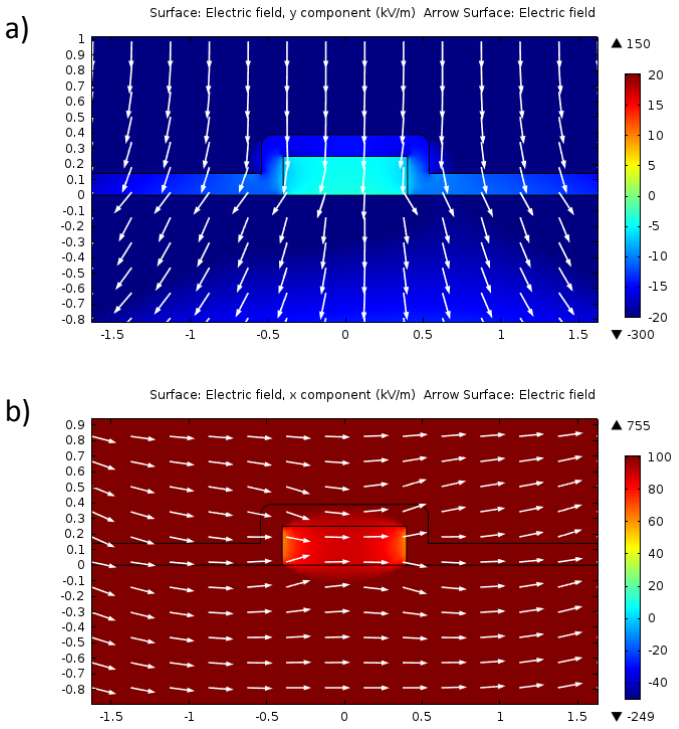

Figure 4.7: (a) Electric field intensity and direction for the electrode configuration indicated as A in Fig.4.6 when a voltage of $1\,V$ is applied. (b) Electric field intensity and direction for the electrode configuration indicated as B in Fig.4.6 when a voltage of $1\,V$ is applied.

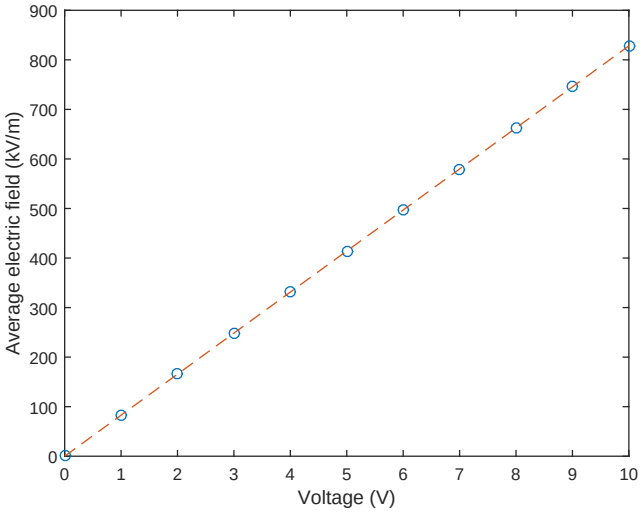

Figure 4.8: Average electric field in the $\hat{x}$ direction as a function of the applied voltage V for a $800\,nm$ waveguide in the CAP140 configuration.

Five tilting angles have been chosen. These are $\alpha = 0, 30, 45, 60, 90$. Angles are referred with respect to the crystallographic direction [100]. Considering all the permutations of waveguide widths (10), polarizations (2), Si_3N_4 thickness/conformation (4), the total number of different devices is $N = 4 \times 2 \times 10 \times 5 = 400$.

4.1.3 AC Electro optic measurements using a Lock In amplifier: theory

The simplest idea for extracting the value of one of the $\chi^{(2)}$ components using the electro optic effect could be the following:

1. Measure one of the resonance wavelengths λ_0 when zero bias voltage is applied between the electrodes.
2. Apply a voltage V, and measure the resonance shift $\Delta\lambda$ due to the voltage induced refractive index shift described in Eq.4.5.
3. Compute the slope of the $\Delta\lambda(V)$ curve. The slope is proportional to the involved $\chi^{(2)}$ component, which can be extracted from the knowledge of the device geometry and the applied electric field.

However, this method does not provide a very high sensitivity. In fact, any temperature fluctuation of the sample at the order of $0.5\,K$ induces a resonance shift of the order of $30\,pm$, which corresponds approximately to the FWHM of the resonance linewidth. What is even worse, strong Fabry Perot (FP) oscillations are always superimposed to the device spectral response, which are due to the reflections of the propagating mode at the input/output facets of the sample. FP oscillations alter the resonance lineshape, making difficult to recognize small resonance shifts $\Delta\lambda$.
To greatly enhance the sensitivity, a homodyne detection which makes use of a Lock In amplifier is used. This is sketched in Fig.4.9.

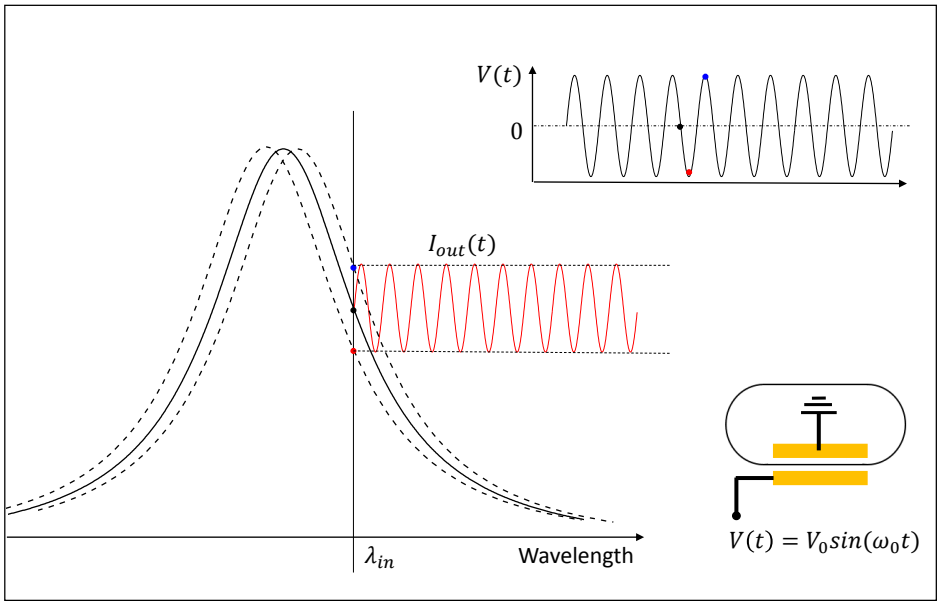

Figure 4.9: A sketch of the modulation system implemented to quantify the resonance shift. A sinusoidal voltage is applied at the resonator electrodes, inducing a periodic shift of the resonance with respect to the zero-bias position (black dot). As a result, the optical signal I_{out} at the output (in this case the Drop port) oscillates between a maximum (blue dot) and a minimum (red dot). The amplitude of these oscillations are proportional to the electro optic induced refractive index shift.

The laser wavelength λ_{in} is tuned near the $-3\,dB$ point of one of the resonances, where the sensitivity to small refractive index variations is maximized. A sinusoidal voltage is applied to the sample electrodes. As a result of the bias modulation, the resonance oscillates back and forth with respect to the laser wavelength, inducing a periodic modulation of the transmitted optical signal I_{out} at the Through/Drop port of the resonator, similar to the operation of a conventional resonant ring modulator (RRM). The modulated signal is sent

to a Lock in Amplifier, which detects the amplitude of the modulation. The use of a Lock In allows to eliminate all the noise sources which can affect the measurement (thermal fluctuations, detector shot noise, laser instabilities, FP oscillations), reaching a signal to noise ratio which is typically $60\,dB - 80\,dB$.
The question now is how to relate the amplitude of the modulation to the $\chi^{(2)}$ component that is inducing them. In what follows, no assumptions on the origin of the modulation mechanism is done. The relation between the applied voltage $V(t)$ and the resonance position λ_{res} is given by a generic function $\lambda_{res}(V)$, which is assumed to be differentiable. In this general treatment, also the amplitude A_{res} of the resonance can be affected by the modulation voltage. At any time t, and when the input wavelength λ_{in} is tuned close to a resonance, the light intensity $I_{out}(t)$ at the output of the Drop port of the resonator can be well approximated by:

$$I_{out}(t) = A_{res}(V(t)) \left(\frac{\gamma^2}{\gamma^2 + (\lambda_{in} - \lambda_{res}(V(t)))^2} \right) \tag{4.7}$$

where 2γ is the FWHM of the lorentzian. The dynamics of $I_{out}(t)$ follows the differential equation:

$$\frac{dI_{out}(t)}{dt} = \left(\frac{\partial I_{out}}{\partial \lambda_{res}} \frac{\partial \lambda_{res}}{\partial V} + \frac{\partial I_{out}}{\partial A_{res}} \frac{\partial A_{res}}{\partial V} \right) \frac{dV}{dt} \tag{4.8}$$

Since λ_{res} and A_{res} are differentiable, they can be expanded in Taylor series around a reference voltage $V = 0$:

$$\frac{\partial \lambda_{res}}{\partial V} = \sum_m \left(\frac{\partial^m \lambda_{res}}{\partial^m V} \right)_0 V^{m-1} \frac{1}{(m-1)!}; \qquad \frac{\partial A_{res}}{\partial V} = \sum_m \left(\frac{\partial^m A_{res}}{\partial^m V} \right)_0 V^{m-1} \frac{1}{(m-1)!} \tag{4.9}$$

By inserting Eq.4.9 into Eq.4.8 and setting $V(t) = V_0 \cos(\omega t)$, the output intensity can be written as:

$$\frac{dI_{out}(t)}{dt} = -V_0 \omega \sin(\omega t) \sum_m \frac{1}{(m-1)!} \left[\frac{\partial I_{out}}{\partial \lambda_{res}} \left(\frac{\partial^m \lambda_{res}}{\partial^m V} \right)_0 V^{m-1} + \frac{\partial I_{out}}{\partial A_{res}} \left(\frac{\partial^m A_{res}}{\partial^m V} \right)_0 V^{m-1} \right] \tag{4.10}$$

Keeping only terms up to the fourth order in V, it is found that $I_{out}(t)$ can be expressed as the sum of terms oscillating at $\omega, 2\omega, 3\omega$ and 4ω. The first and second harmonics amplitudes $I_{out}(\omega)$ and $I_{out}(2\omega)$ are given respectively by:

$$I_{out}(\omega) = \frac{\partial I_{out}}{\partial \lambda_{res}} \left[\left(\frac{\partial \lambda_{res}}{\partial V} \right)_0 V_0 + \frac{1}{4} \left(\frac{\partial^3 \lambda_{res}}{\partial^3 V} \right)_0 V_0^3 \right] + \frac{\partial I_{out}}{\partial A_{res}} \left[\left(\frac{\partial A_{res}}{\partial V} \right)_0 V_0 + \frac{1}{4} \left(\frac{\partial^3 A_{res}}{\partial^3 V} \right)_0 V_0^3 \right] \tag{4.11}$$

$$I_{out}(2\omega) = \frac{\partial I_{out}}{\partial \lambda_{res}} \left[\frac{1}{2} \left(\frac{\partial^2 \lambda_{res}}{\partial^2 V} \right)_0 V_0^2 + \frac{1}{24} \left(\frac{\partial^4 \lambda_{res}}{\partial^4 V} \right)_0 V_0^4 \right] + \frac{\partial I_{out}}{\partial A_{res}} \left[\left(\frac{\partial^2 A_{res}}{\partial^2 V} \right)_0 V_0 + \frac{1}{24} \left(\frac{\partial^4 A_{res}}{\partial^4 V} \right)_0 V_0^4 \right] \tag{4.12}$$

It can be readly seen that the first harmonic amplitude depends only on odd powers of the voltage amplitude V_0, while the second harmonic amplitude only on even powers of the voltage amplitude V_0. The two contributions on the right hand side of Eq.4.11 and Eq.4.12 have opposite parity if considered as a function of the wavelength position λ_{in}. This is shown in Fig.4.10, which plots $\frac{\partial I_{out}}{\partial \lambda_{res}}$ and $\frac{\partial I_{out}}{\partial A_{res}}$ as a function of λ_{in}.

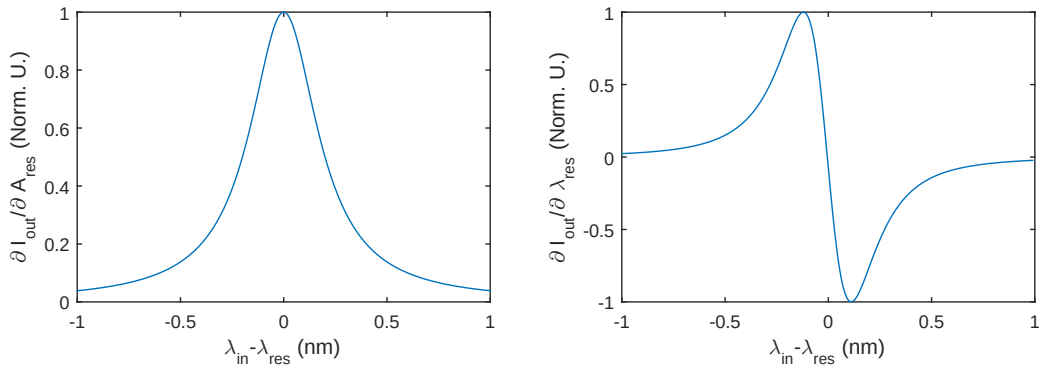

Figure 4.10: The functions $\frac{\partial I_{out}}{\partial \lambda_{res}}$ and $\frac{\partial I_{out}}{\partial A_{res}}$ as a function of $\lambda_{in} - \lambda_{res}$.

It can be seen that $\frac{\partial I_{out}}{\partial \lambda_{res}}$ is an odd function of λ_{in}, while $\frac{\partial I_{out}}{\partial A_{res}}$ is an even function. These opposite behaviour will be of crucial importance for understanding the outcomes of the experiments described in section 4.3.2. If Eq.4.11 and Eq.4.12 are applied to the specific case of $\chi^{(2)}$ electro optic modulation, it comes out that $\frac{\partial I_{out}}{\partial A_{res}} = 0$, since the modulation alters only the resonance wavelength position but not the amplitude (i.e., no losses are introduced). The link between the $\chi^{(2)}$ component and the resonance position λ_{res} can be derived starting from a generalization of Eq.4.5 for guided modes (see Apppendix B):

$$\Delta n_{eff} = \frac{\chi^2_{eff,jjj} E_{DC}}{2n_0^2} n_g \tag{4.13}$$

where Δn_{eff} is the electro optic effective index change, n_g the modal group index, n_0 the core refractive index and the effective $\chi^{(2)}_{eff}$ is defined as:

$$\chi^{(2)}_{eff,jjj} = \frac{\int_{core} \chi^{(2)}_{mat,jjj}(r_T) n^2(r_T) |e_j(r_T)|^2 dr_T}{\int n^2(r_T) |\mathbf{e}(r_T)|^2 dr_T} \tag{4.14}$$

where j could be (x, y, z), $\chi^{(2)}_{mat,jjj}$ is the $\chi^{(2)}_{jjj}$ component in the material, n is the refractive index profile, $e(r_T)$ is electric field profile of the optical mode and $\mathbf{r}_T$ denotes the transverse dimensions of the waveguide. In Eq.4.14 it has been assumed that the optical field is mainly polarized in the j direction, so that off-diagonal tensor elements do not contribute to the integral. The change in the effective index Δn_{eff} results in the resonance shift:

$$\Delta \lambda_{res} = \lambda_{res,0} \frac{\Delta n_{eff}}{n_g} \frac{L_h}{L_{tot}} \tag{4.15}$$

where $\lambda_{res,0}$ is the resonance wavelength at zero bias applied. By inserting Eq.4.13 into Eq.4.15, and by expressing E_{DC} as $E_{DC} = \frac{dE_{DC}}{dV} V$ (the linear relation is an excellent approximation as it can be seen in Fig.4.8), the relation between λ_{res} and V reads:

$$\lambda_{res}(V) = \lambda_{res,0} \left(1 + \frac{L_h \chi^{(2)}_{eff,jjj}}{2 L_{tot} n_0^2} \frac{dE_{DC}}{dV} V \right) \tag{4.16}$$

Using Eq.4.16 to compute $\frac{\partial \lambda_{res}}{\partial V}$ in Eq.4.11 and in Eq.4.12, the first and second harmonic amplitudes in the case of $\chi^{(2)}$ electro optic modulation become:

$$I_{out}(\omega) = \frac{\partial I_{out}}{\partial \lambda_{res}} \frac{\lambda_{res,0} L \chi^{(2)}_{eff,jjj}}{2 L_{tot} n_0^2} \frac{dE_{DC}}{dV} V_0 \tag{4.17}$$

$$I_{out}(2\omega) = 0 \tag{4.18}$$

A linear relation between the applied voltage amplitude V_0 and the first harmonic amplitude $I_{out}(\omega)$ is expected in the case of pure electro optic modulation, while the second harmonic amplitude should vanish. The Lock In amplifier is able to detect both $I_{out}(\omega)$ and $I_{out}(2\omega)$, and from the knowledge of the parameters $\frac{\partial I_{out}}{\partial \lambda_{res}}, \lambda_{res,0}$ (from experiment), L_h, L_{tot} (from the geometry), $\frac{dE_{DC}}{dV}$ (from FEM simulations) it is possible to extract $\chi^{(2)}_{eff}$.

4.2 Device fabrication and passive characterization

The resonators have been fabricated on $6''$ SOI wafer using $293\,nm$ UV lithography by FBK [204]. An optical microscope image is shown in Fig.4.11(b). A Low Pressure Chemical Vapour Deposition Silicon Nitride (Si_3N_4) layer is deposited on the Silicon waveguides. The thickness and the conformation of this layer depend on the type of device. A $3\,\mu m$ thick buried oxide layer (BOX) and a $900\,nm$ thick Plasma Enhanced Chemical Vapour Deposition Silica layer serve as lower and upper cladding materials, respectively. Post fabrication measurements, shown in Fig.4.12 (Ox-Nit column) revealed that the residual stress on the top Silica layer was $-0.19\,GPa$, nearly an order of magnitude lower with respect to the values reported in similar experiments on the electro optic effect in strained Silicon [140, 157]. The reason of this lies in the fact that the upper Silica cladding applies a compressive stress which overcomes the tensile one provided by the Si_3N_4. Such a low stress level could not be suffiient to make $\chi^{(2)}$ effects detectable. For this reason, some of the samples have been fabricated without the top cladding, in which a residual strain of $\approx -1.4\,GPa$ has been recorded (Fig.4.12 (Nit column)). The absence of the top cladding precludes the possibility to position the electrodes in the configuration A of Fig.4.2, because the Nitride thickness is not sufficient to isolate the optical mode from the metallic electrodes.

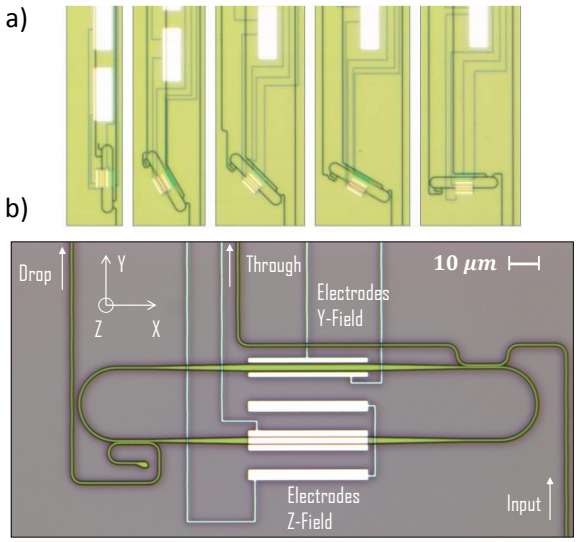

Figure 4.11: (a) An optical microscope image of the fabricated devices, showing the five different tilting angles. (b) A zoomed view of one of the devices. Pictures are at the courtesy of Mr.Martino Bernard from FBK [204].

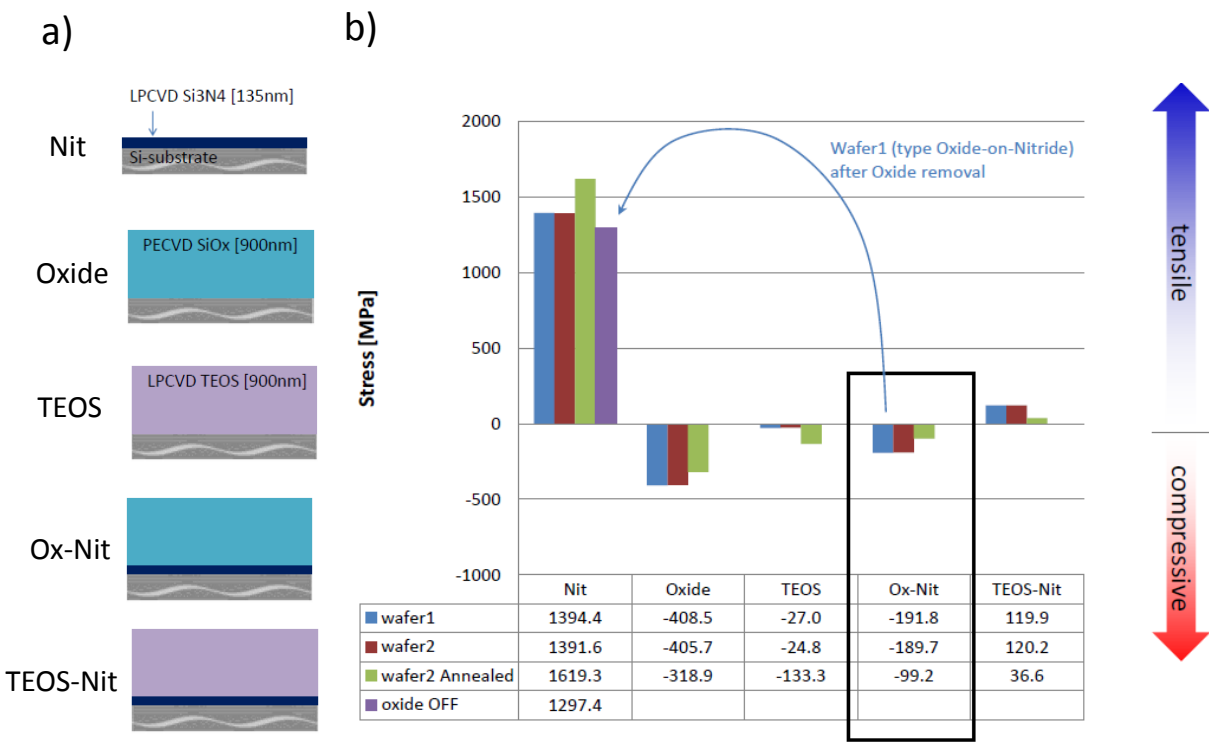

Figure 4.12: (a) Layer configuration and materials. The configuration implemented for the fabrication of the devices is the one indicated as Ox-Nit. (Oxide-Nitride). (b) Stress measurements executed on the layer configurations shown in (a). The stress level is evaluated by measuring the curvature of the wafer surface after the material deposition [208]. Datas are courtesy of Dr.Mher Ghulinyan, from FBK [204].

A first passive characterization is done on the fabricated devices. This is done using the experimental setup shown in Fig.4.13. Light from a tunable C-band laser is edge coupled to the input waveguide using tapered lensed fibers ($2\,\mu m$ spot size, $14\mu m$ working distance) and a XYZ micrometric and nanometric positioning stage. The alignment stage is monitored using an Infra-Red camera placed on the top of the sample which is equipped with a $10\,X$ objective and a variable zoom. The output light from the Drop (Through) waveguide is edge coupled to another lensed fiber and sent to an Infra-Red detector.

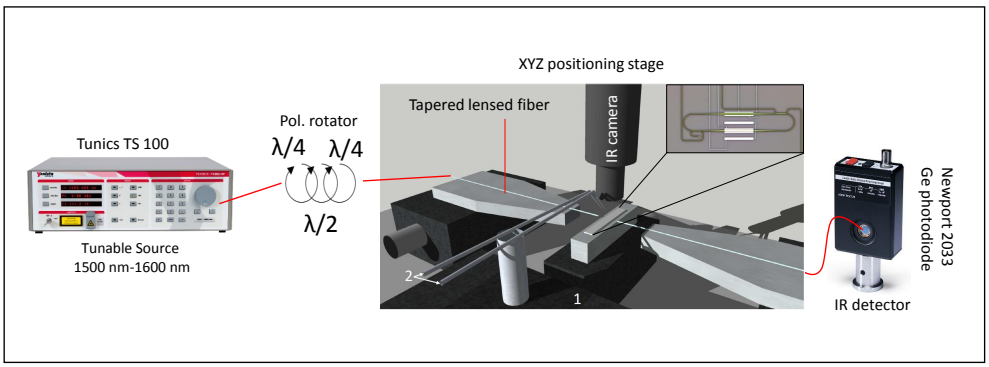

Figure 4.13: The experimental setup used to perform passive characterizations.

The first passive characterization concernes a propagation loss measurement. To achieve that, straight waveguides of various lengths have been designed on the same chip which contains the resonators. These are fabricated along the [100] direction. The ratio between the output signal and the input one is plotted

as a function of the waveguide length. An example is shown in Fig.4.14 for the CAP140 sample at a laser wavelength of $1.550\,\mu m$. From the slope of the curves, the propagation loss values listed in Table 4.3 have been extracted. The highest losses have been observed for HAT samples in TE polarization. This is due to the fact that, in the CAP configuration, the Silicon Nitride layer completely covers the side walls of the waveguide, acting as a passivation mechanism which reduces the surface roughness.

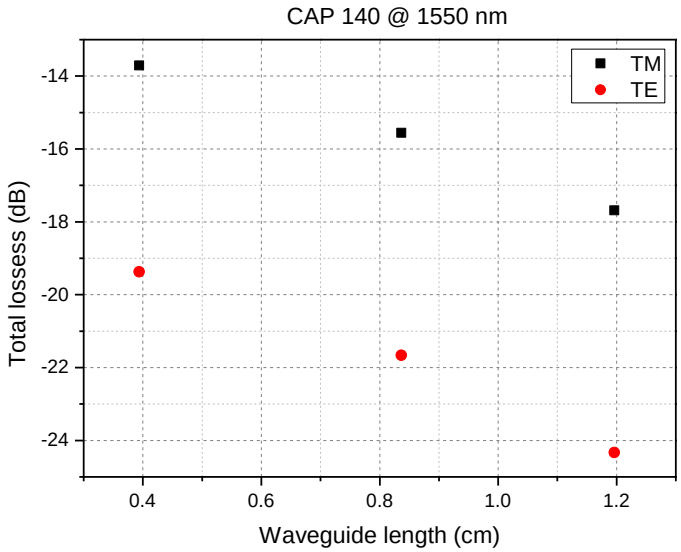

Figure 4.14: Transmittance of waveguides of different lengths and for different polarizations lying on the CAP140 chip.

Sample type	**Propagation loss TM** ($dBcm^{-1}$)	**Propagation loss TE** ($dBcm^{-1}$)
CAP140	4.9 ± 0.5	6.1 ± 0.6
CAP70	4.5 ± 0.1	4.5 ± 0.1
HAT140	11 ± 2	> 15
HAT70	12.0 ± 0.4	> 12

Table 4.3: List of propagation losses measured for the different device configurations.

The second passive characterization concernes the spectral response of the devices. As discussed in Section 4.1.2, resonators have been designed to have a FWHM of $\approx 35\,pm$, corresponding to a quality factor of $Q \approx 44000$. As we can see from Fig.4.15, which shows the spectra recorded in the Through port of a CAP140 device, these requirements well matches with the ones of the experiment. Quality factors ranging from $Q \approx 25000$ up to $Q \approx 55000$ have been measured, depending on the waveguide size and Silicon Nitride layer conformation.

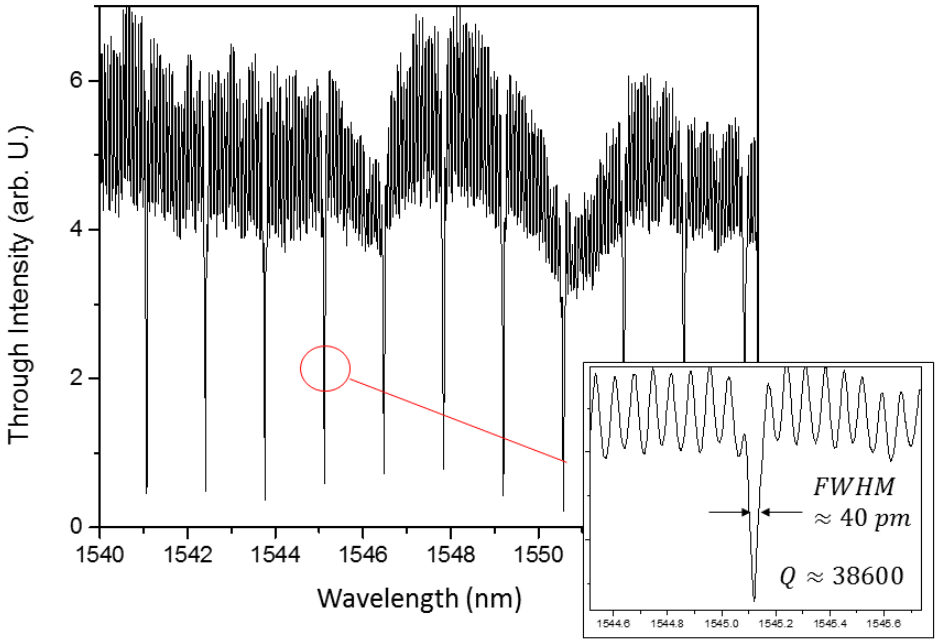

Figure 4.15: Example of one of the Through transmission spectra. The inset shows the details of one resonance order.

4.3 AC electro optic measurements using a Lock In amplifier: experiment

The experimental setup implemented for the Lock In measurements is shown in Fig.4.16. The light coupling stage is the same as the one in Fig.4.13. To provide the electric field across the metallic pads of the device, two Tungsten tips connected to a function generator have been used. This function generator provides the sinusoidal signal at a frequency ω. A static bias can be added to the sinusoidal modulation using a static voltage source connected to the Aluminum sample holder. When the static bias is not applied, the sample holder is kept grounded. The modulated signal which exists from the photodetector is sent to a digital Lock In amplifier to extract the amplitude of the first and second harmonic components $I_{out}(\omega)$ and $I_{out}(2\omega)$ respectively. To measure the local slope of the spectrum $\frac{\partial I_{out}}{\partial \lambda_{res}}$, the laser wavelength is modulated at frequency ω_λ by a second function generator, and the first harmonic component is detected by a second Lock In (not shown in Figure 3 for clearness).

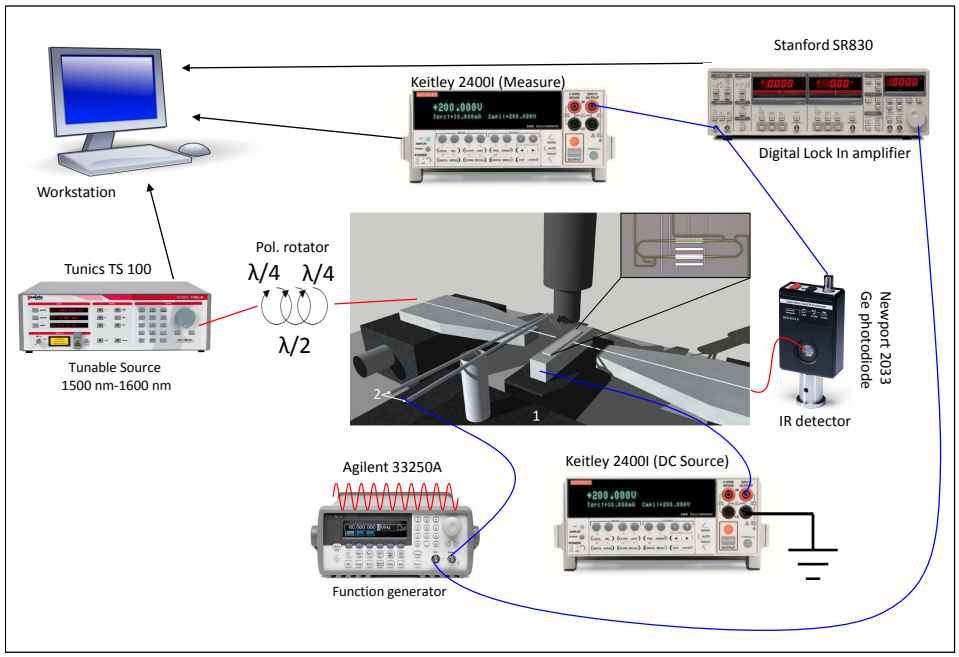

Figure 4.16: The experimental setup used to perform AC electro optic measurements using the Lock In amplifier.

The whole setup is automated by computer routine which:

1. Performs a coarse spectrum ($0.1\,nm$ resolution) in a wavelength interval which covers approximately one FSR.
2. Finds the resonance peak in the interval, performs a fine spectra ($5\,pm$ resolution) around the maximum value and sets the laser wavelength at the point where the slope of the spectrum is maximum.
3. Applies a modulated voltage across the pads, starting from $V_0 = 0.35\,V$ to $V_0 = 7\,V$ with $0.35\,V$ increments, and simultaneously detects the amplitude of the first harmonic component $I_{out}(\omega)$ and the second harmonic one $I_{out}(2\omega)$.
4. Extracts the value of $\chi^{(2)}_{eff}$ using the method discussed in Section 4.1.3.
5. Shifts to the next resonance order and repeats the points from 1 to 5. This is repeated for the desired number of resonance orders (a number of 3 resonances have been chosen).

4.3.1 Normal behaviour

A large number of devices exhibited a "normal behaviour" when probed by AC electro optic measurements. For "normal behaviour" it is meant that the first harmonic amplitude $I_{out}(\omega)$ is linear in the amplitude voltage V_0 and that the second harmonic amplitude is negligible or it has a noisy trend. This behaviour is consistent with an electro optic modulation which has a $\chi^{(2)}$ origin. An example of "normal behaviour" is shown in Fig.4.17 for three different type of devices.

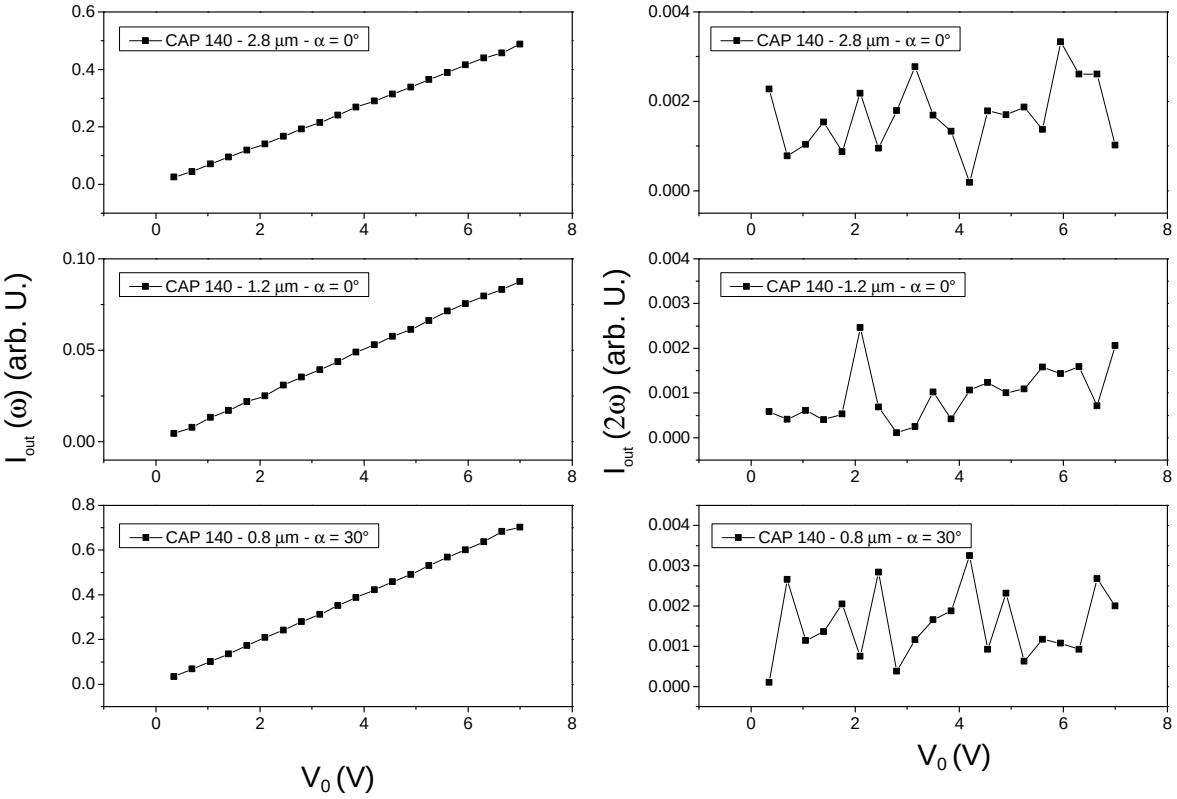

Figure 4.17: Example of first and second harmonic amplitudes as a function of the amplitude voltage V_0 for different devices. All these devices exhibited a "normal" behaviour.

For the same device, slightly different values of the slope of the first harmonic can be found at different resonance orders. This is mainly due to the FP oscillations between the input and output facets of the samples that can distort the shape of the resonance, and consequently the local value of $\frac{\partial I_{out}}{\partial \lambda_{res}}$. The Fabry Perot oscillations constitute the main source of uncertainties in determining of the $\chi^{(2)}_{eff}$ value. Normal behaviour is also observed when $I_{out}(\omega)$ is measured as a function of wavelength, keeping the amplitude voltage V_0 fixed to $V_0 = 5\,V$. This is shown in Fig.4.18.

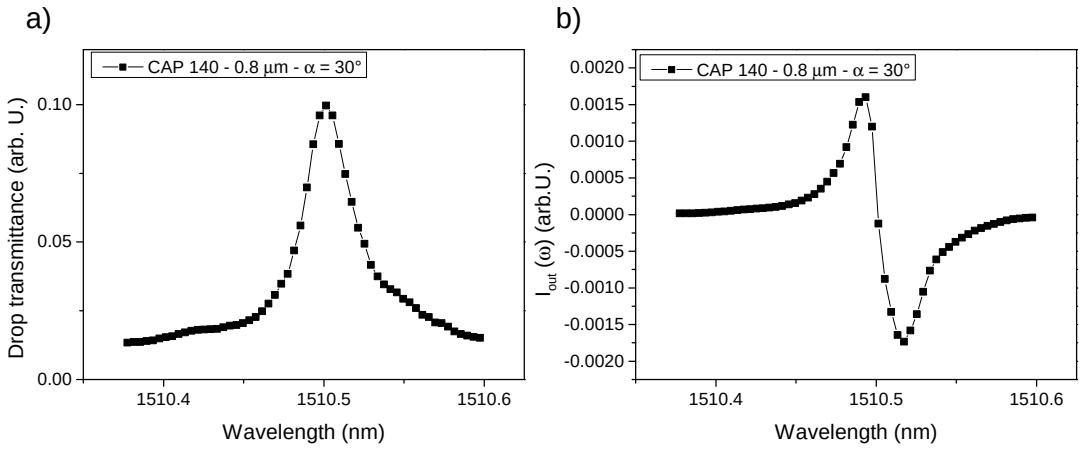

Figure 4.18: (a) Spectral response of the Drop port of a device, showing one resonance order. (b) First harmonic amplitude as a function of the laser wavelength at a fixed amplitude voltage V_0.

The curve has an odd parity, which is expected from the fact that $I_{out}(\omega)$ is proportional to $\frac{\partial I_{out}}{\partial \lambda_{res}}$ (see Eq. 4.17), which is in turn an odd function of $(\lambda_{res} - \lambda_{in})$. Starting from the slopes of $I_{out}(\omega)$, and using Eq.4.17, some of the values of the $\chi^{(2)}_{eff}$ component have been extracted. As an example, in Fig.4.19, the data for all the different angles and for several waveguide widths of the CAP 140 sample (with top cladding) are reported. Assuming the same reference frame shown in Fig.4.11, the measured component of the tensor is the $\chi^{(2)}_{eff,zzz}$, since both the static field and the optical field are polarized in the $\hat{z}$ direction.

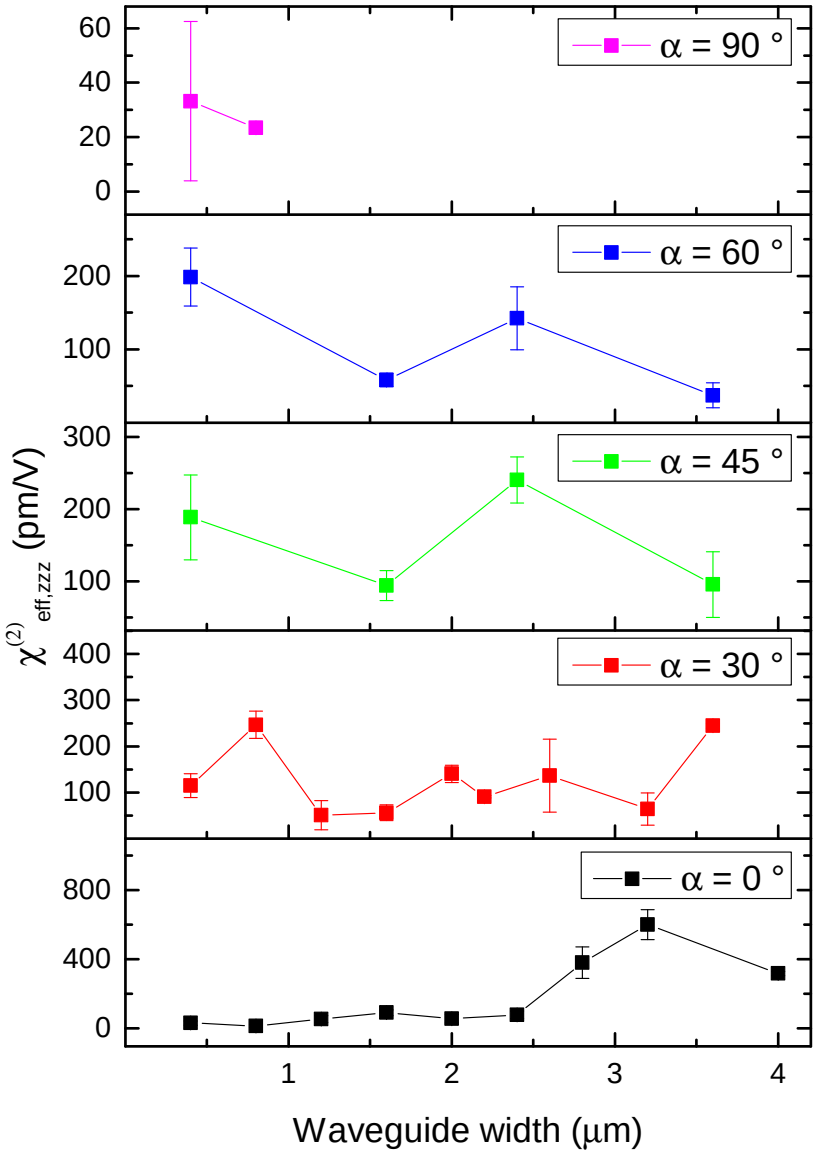

Figure 4.19: The extracted values of $\chi^{(2)}_{eff,zzz}$ for different waveguide widths and different angles for the CAP140 sample. The reported values are the result of an average between three different resonance orders.

A closer look at Fig.4.19 reveals several anomalies in the extracted values of $\chi^{(2)}_{eff,zzz}$. Firstly, there is not a precise trend with the waveguide width, or with the waveguide tilting angle. This is considered as an anomaly since it is expected that the strain distribution should smoothly vary as a function of the waveguide width. From FEM simulations, the average strain and strain gradient is found to decrease as the waveguide width increases, and consequently also the $\chi^{(2)}$ value should decrease. This behaviour has been observed, for example, in Refs [140, 138]. However, it has to be pointed out that their analysis was restricted to the very

small range of waveguide widths between $300\,nm$ and $500\,nm$, in which a different trend might be observed. Secondly, the value can be as high as $600\,pmV^{-1}$, which is much greater than the ones reported in literature for similar geometries ($122\,pmV^{-1}$ in Ref. [139], $188\,pmV^{-1}$ in Ref.[141] or $336\,pmV^{-1}$ in Ref.[138]). What is more, surprisingly these extremely high values have been found with a stress level of $-0.19\,GPa$, which is an order of magnitude lower than the one in the above cited works. Already at this stage it can be claimed that the modulation mechanism is not probably related to the $\chi^{(2)}$ non linearity, even if it shares all the distinctive signs. Values of $\chi^{(2)}_{eff}$ comparable to the ones reported in Fig.4.19 , showing no clear trend, have been also found for CAP70, HAT140 and HAT70 samples. No appreciable differences have been found in samples in which the Silica top cladding has been removed, which constitues another anomalous behaviour since the residual stress is higher by an order of magnitude. In general, samples without the Si_3N_4 layer showed values of $\chi^{(2)}_{eff}$ which are nearly an order of magnitude lower with respect to the samples covered by the stressing layer.

4.3.2 Not normal behaviour

The anomalies encountered in the so called "normal" behaviour are supported by the observation of "not normal" behaviours in many other samples. One of the latter can be seen in Fig.4.20, which compares $I_{out}(\omega)$ with $I_{out}(\omega_\lambda)$ as a function of the laser wavelength λ_{in} in a CAP 140 sample with a waveguide width of $400\,nm$.

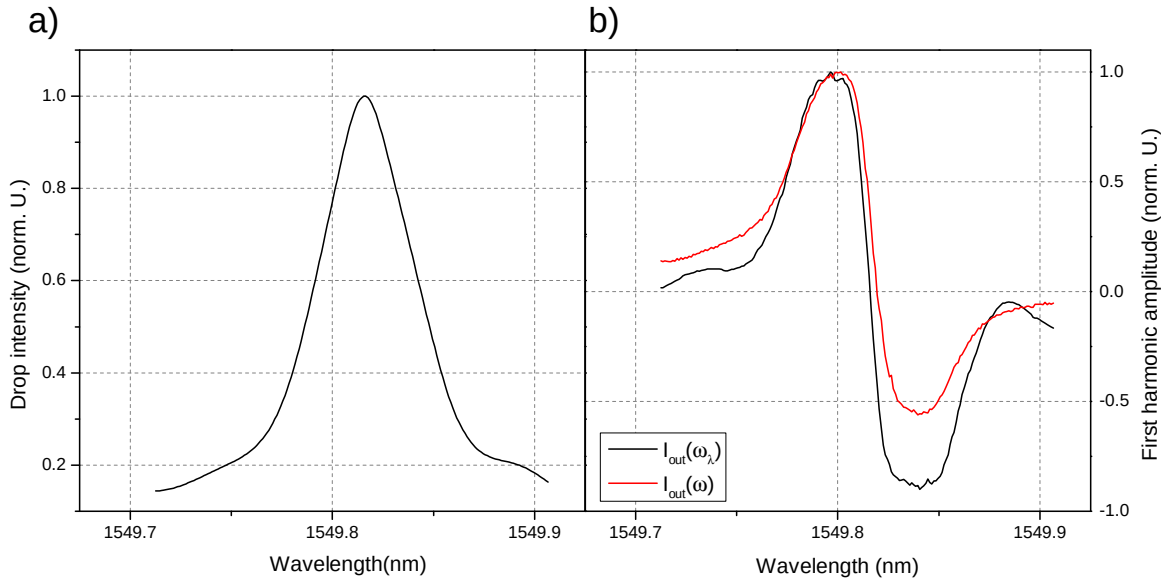

Figure 4.20: (a) Drop spectral response of the resonator centered on the reference resonance. (b) Normalized first harmonic amplitudes recorded by the Lock in locked at ω (red curve, recorded using an amplitude of the voltage modulation of $V_0 = 5\,V$) and by the Lock in locked at ω_λ (black curve).

The two curves should share the same odd parity, since they are both proportional to $\frac{\partial I_{out}}{\partial \lambda_{res}}$. However it can be noticed that while $I_{out}(\omega_\lambda)$ is almost odd, $I_{out}(\omega)$ is of not defined parity. This behaviour is encountered in many samples. In all the cases the asymmetry was recorded in the function $I_{out}(\omega)$, i.e., the one related to the electro optic modulation. As it can be seen in Fig.4.21(c), the degree of asymmetry Γ, defined as:

$$\Gamma = \int I_{out}(\omega, \lambda_{in})\, d\lambda_{in} \tag{4.19}$$

can be tuned if a static voltage bias V_{DC} is added to the sinusoidal modulation.

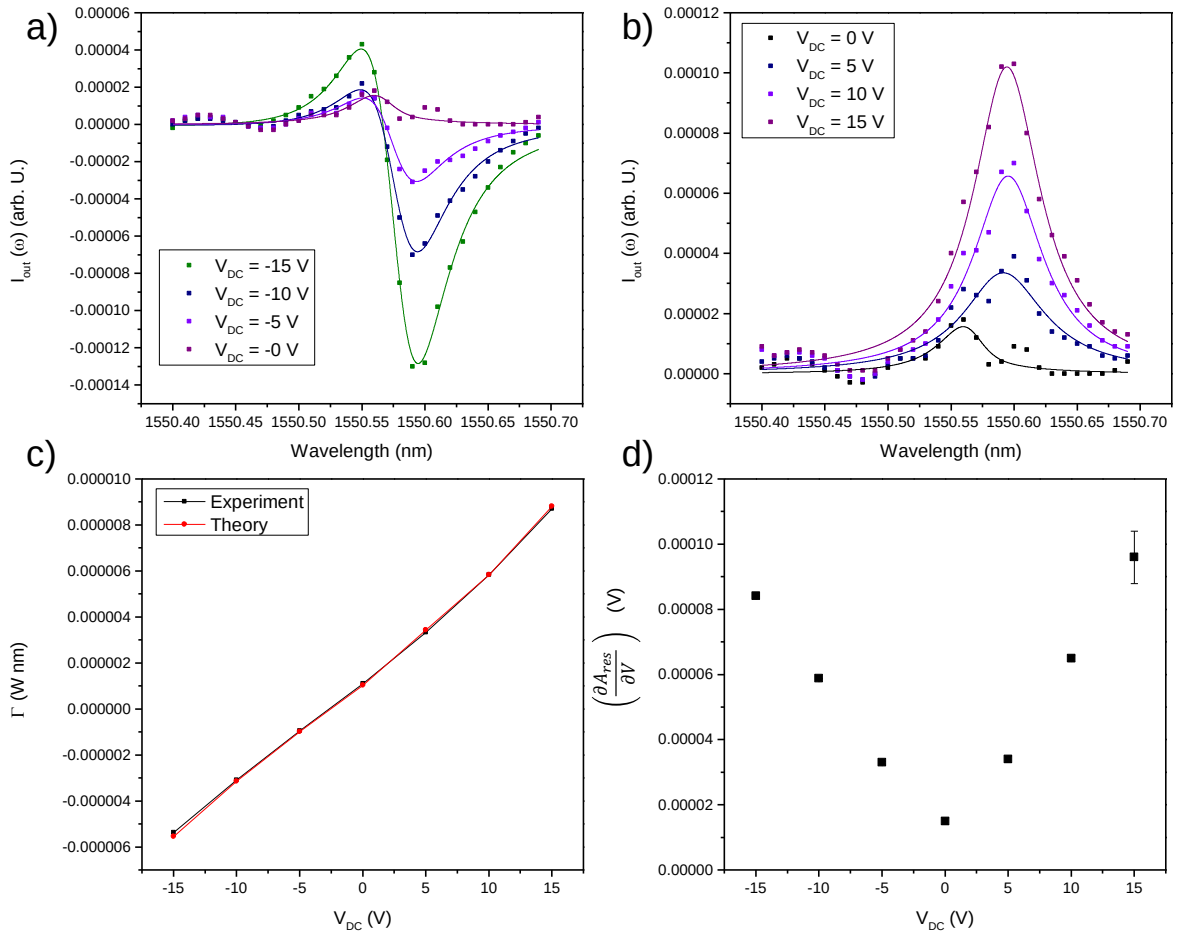

Figure 4.21: (a) First harmonic amplitude $I_{out}(\omega)$ as a function of wavelength for different values of positive applied voltages. Scatter points represent experimental data, while solid lines are obtained using Eq.4.20. (b) First harmonic amplitude $I_{out}(\omega)$ as a function of wavelength for different values of negative applied voltages. (c) Asymmetry coefficient Γ, defined in Eq.4.19, plotted as a function of the bias voltage V_{DC}. The black line is obtained by directly integrating $I_{out}(\omega)$ with respect to λ_{in} on experimental data. The red line is obtained by integrating the solid curves in panels (a,b) with respect to λ_{in}. (d) Values of $\left(\frac{\partial A_{res}}{\partial V}\right)$ for different bias voltages. For simplicity, in computing the value of $\frac{\partial A_{res}}{\partial V}$, the quantity $\frac{\partial I_{out}}{\partial A_{res}}$ has been assumed normalized to one. In all these measurements, the amplitude of the sinusoidal voltage modulation has been fixed to $V_0 = 5\,V$.

The static bias does not influence the behaviour of $I_{out}(\omega_\lambda)$, which remains always of odd parity. Other anomalous behaviours concern the relations between the applied voltage amplitude V_0 and the first and second harmonic amplitudes. As predicted by Eq.4.17 and by Eq.4.18, if the electro optic modulation had a $\chi^{(2)}$ origin, the first harmonic should be linear in V_0 and the second harmonic equal to zero. However, as shown in Fig.4.22, in some of the samples $I_{out}(\omega)$ is found to be cubic in V_0 and $I_{out}(2\omega)$ to be quadratic in V_0.

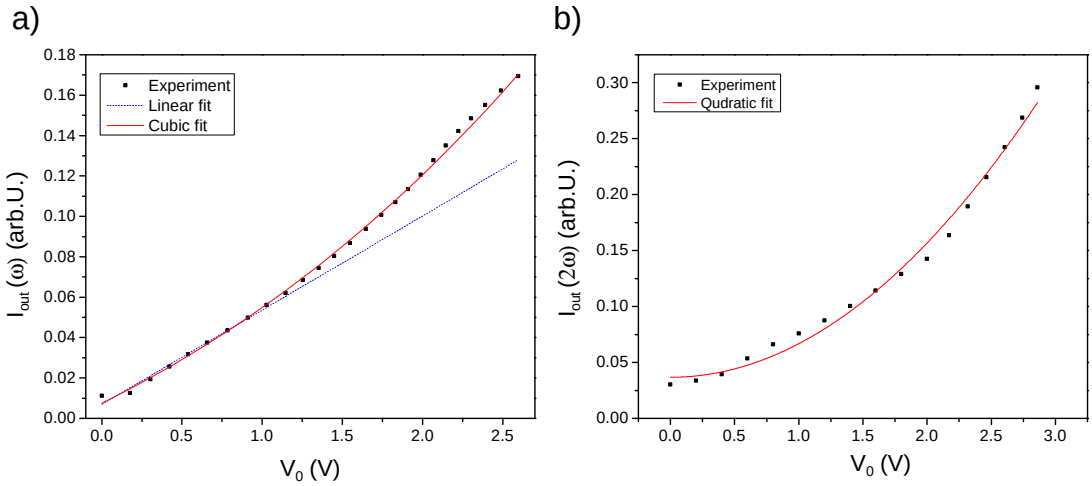

Figure 4.22: (a) First harmonic amplitude as a function of the sinusoidal voltage amplitude V_0. The cubic polynomial is $I_{out}(\omega) = a_0 + a_1 V_0 + a_3 V_0^3$. The linear polinomial is $I_{out}(\omega) = b_0 + b_1 V_0$. (b) Second harmonic amplitude as a function of the sinusoidal voltage amplitude V_0. The second order polinomial is $I_{out}(2\omega) = c_0 + c_2 V_0^2$. Values of the coefficients are listed in Table 4.4.

Coefficient	Value
a_0	$(-0.07 \pm 0.01)\, W$
a_1	$(0.019 \pm 0.007)\, WV^{-1}$
a_3	$(7.6 \pm 0.6) \cdot 10^{-4} WV^{-3}$
b_0	$(-0.133 \pm 0.007)\, W$
b_1	$(0.047 \pm 0.002)\, WV^{-1}$
c_0	$(0.037 \pm 0.003)\, W$
c_2	$(0.030 \pm 0.008)\, WV^{-2}$

Table 4.4: Values of the coefficients of the polynomials used to fit the experimental data shown in Fig.4.22.

All the reported anomalies seem to not have no clear relationship either with the waveguide width, or with the stress distribution, since they have been randomly observed for different widths and in different type of samples. It is worth to note that two nominally identical samples could exhibit respectively a normal and an anomalous behaviour depending on their position on the wafer. From these observations, it is clear that the source of electro optic modulation is not of $\chi^{(2)}$ origin, since it does not follow the theoretical predictions outlined in section 4.1.3.

4.3.3 Interpretation of the anomalous behaviour

In the previous section it has been shown that Eq.4.17 and Eq.4.18 are able to account for the behaviour of only a limited class of samples, the ones which show a normal behaviour. For samples exhibiting an anomalous behaviour, one has necessary to refer to the more general forms of Eq.4.11 and of Eq.4.12. By keeping only the leading terms in Eq.4.11, one obtains:

$$I_{out}(\omega) = \frac{\partial I_{out}}{\partial \lambda_{res}} \left(\frac{\partial \lambda_{res}}{\partial V} \right)_0 V_0 + \frac{\partial I_{out}}{\partial A_{res}} \left(\frac{\partial A_{res}}{\partial V} \right)_0 V_0 \tag{4.20}$$

which differs from Eq.4.17 by the term $\frac{\partial I_{out}}{\partial A_{res}} \left(\frac{\partial A_{res}}{\partial V} \right)_0 V_0$. As already discussed in Section 4.1.3, this term is an even function of λ_{in}. Eq.4.20 is now a function with an undefined parity, and as can be seen in Fig.4.20

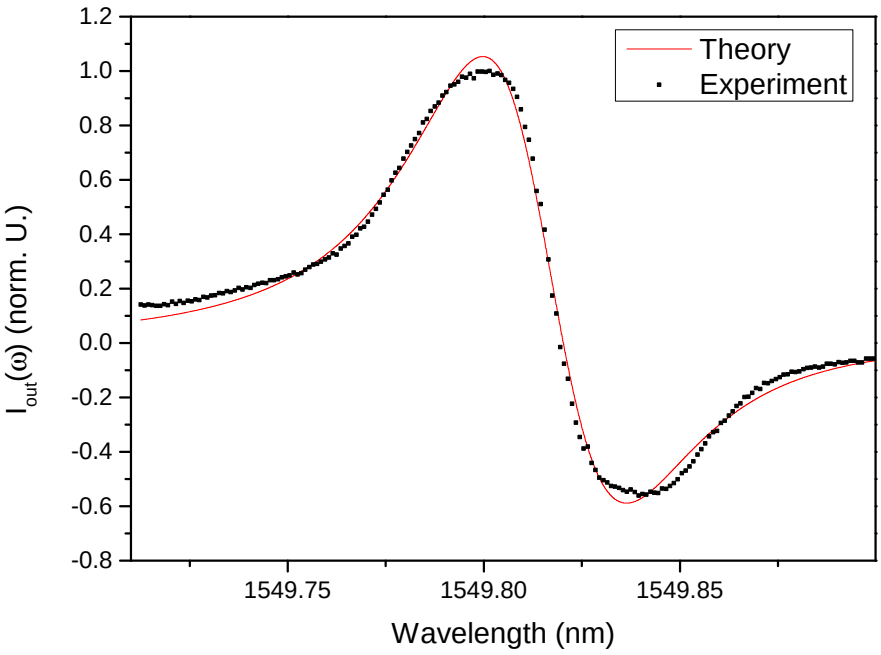

Figure 4.23: The asymmetric first harmonic amplitude shown in Fig.4.20 (black scatters) is fitted using Eq.4.20 (red solid curve).

it makes possible to account for the asymmetry shown in Fig.4.20(b).

By integrating Eq.4.20 with respect to λ_{in}, and by using the fact that $\frac{\partial I_{out}}{\partial \lambda_{res}}$ is an odd function in this variable, the degree of asymmetry of $I_{out}(\omega)$ is found to be:

$$\Gamma = \int \frac{\partial I_{out}}{\partial A_{res}} \left(\frac{\partial A_{res}}{\partial V} \right)_0 V_0 \, d\lambda_{in} \tag{4.21}$$

which is different from zero if $\left(\frac{\partial A_{res}}{\partial V}\right)_0 \neq 0$. Since, as can be seen in Fig.4.21(c), values of $\Gamma \neq 0$ have been found experimentally, it has to be concluded that the modulation voltage affects both the resonance position and the resonance amplitude, i.e., losses are induced. This fact is not compatible with the assumption of a $\chi^{(2)}$ induced electro optic modulation, since the latter only affects the resonance position by changing the refractive index. The variable asymmetry in the first harmonic amplitude $I_{out}(\omega)$ shown in Fig.4.21(a-b) as a function of the bias voltage V_{DC} can be explained by assuming that $\frac{\partial A_{res}}{\partial V}$ is a function of V_{DC}. This means that the amount of losses which are induced by the voltage modulation depends on the bias point. In Fig.4.21(a-b) the experimental data is fitted using Eq.4.20 to find the value $\frac{\partial A_{res}}{\partial V}$ as a function of V_{DC}. During this procedure, the quantities $\frac{\partial I_{out}}{\partial \lambda_{res}}$ and $\frac{\partial I_{out}}{\partial A_{res}}$ have been assumed normalized to one. It is worth to note that this means that the true value of $\frac{\partial A_{res}}{\partial V}$ differs from the one shown in Fig..4.21(d) by a proportionality factor. As it can be seen from Fig.4.21(a-b), a good agreement is found between the experimental data and the curves generated by Eq.4.20.

Evidences of voltage induced absorption have been also found in purely DC measurements , in which V_0 is set to zero and the spectral response of the resonator in the Drop port is recorded as a function of V_{DC}. In this measurement, performed on a HAT 140 resonator with a waveguide width of $1.2\,\mu m$, V_{DC} is swept from $-70\,V$ to $70\,V$, and the recorded spectra are shown in Fig.4.24(a-b). Both the optical field and the static field were polarized in the $\hat{z}$ direction.

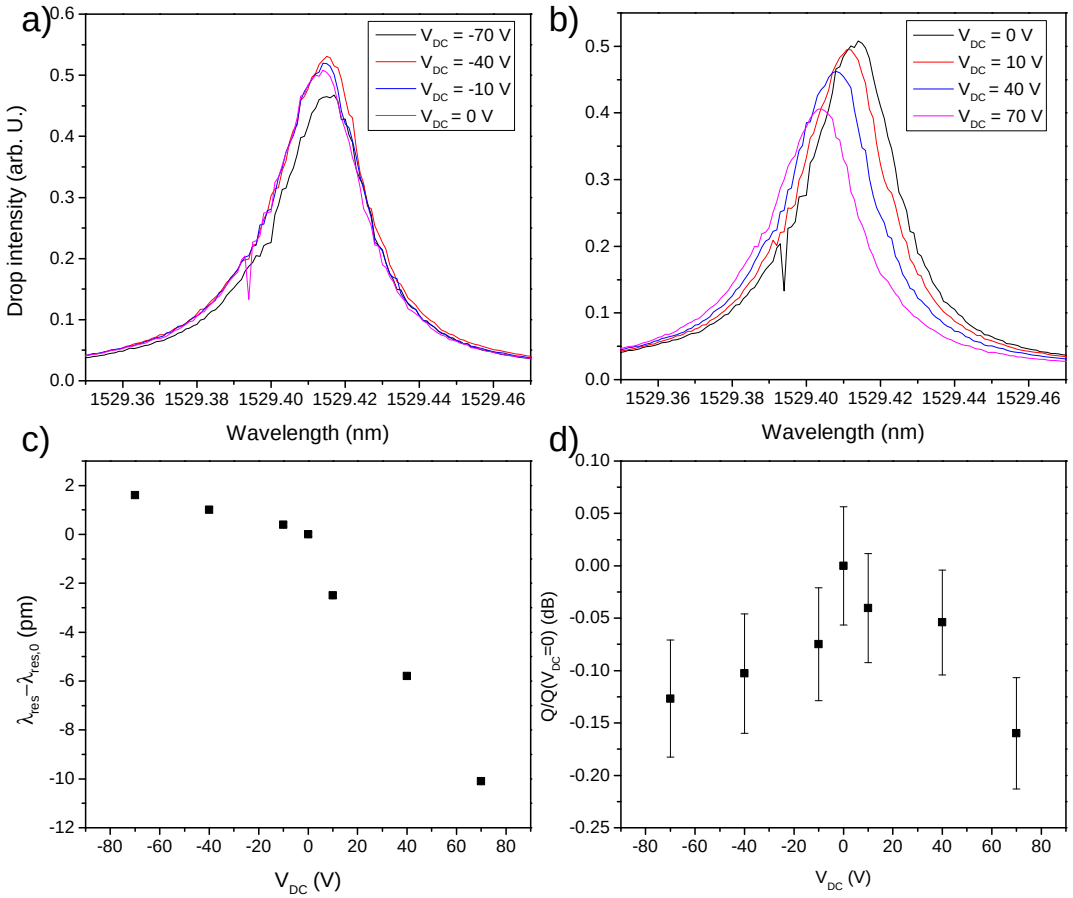

Figure 4.24: (a) Drop spectral response of the resonator at different values of negative bias voltage V_{DC}. (b) Drop spectral response of the resonator at different values of positive bias voltage V_{DC}. (c) Resonance shift with respect to the zero bias ($V_{DC} = 0\,V$) wavelength position at different values of V_{DC} (error bars are smaller than the symbols). (d) Quality factor of the resonance as a function of the bias voltage V_{DC}. Data are normalized with respect to the quality factor value at zero bias.

Two important features emerge from this analysis. The first is that the amplitude and the quality factor of the resonance is affected by the applied voltage. The signal at $70\,V$ is lower then the one at $0\,V$ of about $1\,dB$, while the quality factor decreases of $(0.16 \pm 0.05)\,dB$. This is accompained by a blue shift of the resonance wavelength of $(-10.10 \pm 0.09)\,pm$ with respect to its position at $V_{DC} = 0$ (see Fig.4.24(d) and Fig.4.24(c) respectively). The second important feature is that the losses and the resonance blue shift are not symmetric with respect to the zero bias point at $V_{DC} = 0$. A phenomenological justification of this behaviour will be given in section 4.3.4. The magnitude of the resonance shift and of the induced losses are not independent. It is evident from Fig.4.24(a-b) that higher losses are accompained to higher resonance shifts. This fact suggests that the mechanism which causes the two phenomena has a common origin. A closer look at Fig.4.24(a) reveals that the amplitude of the resonance at $V_{DC} = 0$ is lower with respect to the amplitude at $V_{DC} = -10\,V$ or $V_{DC} = -40\,V$, while in Fig.4.24(d) the Q factors corresponding to these points are lower. These two observations seem to be in contradiction. However this can be probably explained by noting that in Fig.4.6(a), a portion of the Drop waveguide lies under the two pads used to apply voltage to the electrodes, and, thus, it is subjected to an electric field of the same order of magnitude and direction of the resonator waveguide. Voltage induced absorption occurs also in this portion of waveguide, which is not part of the resonator. However, in this part the zero bias point is located at $V_{DC} < 0$, so it is possible to decrease the propagation losses by applying a negative voltage. Further details will be outlined in Section 4.3.4. The

more general forms of Eq.4.11 and of Eq.4.12 are also able to account for the non linear relationship observed between $I_{out}(\omega)$ and V_0 and $I_{out}(2\omega)$ and V_0. The first non linear correction to Eq.4.11 is indeed cubic in V_0, which well fits the behaviour observed in Fig.4.22. The quadratic relation between $I_{out}(2\omega)$ and V_0 is predicted by the lowest order term in Eq.4.12.
It is worth to note that, even though a theory which relies only on $\chi^{(2)}$ effects is not able to account for the observed anomalies, some of them can be predicted by assuming the simultaneous action of a linear electro optic effect mediated by the $\chi^{(2)}$ nonlinearity and a quadratic electro optic effect mediated by the $\chi^{(3)}$ nonlinearity. The terms linear and quadratic refer to the dependence of the refractive index change with respect to the applied DC electric field E_{DC}. Under these conditions Eq.4.13 modifies to (see Appendix B):

$$\Delta n_{eff} \approx \frac{\chi^{(2)}_{eff,jjj} n_g}{2n_0^2} E_{DC} + \frac{9\chi^{(3}_{eff,jjjj} n_g}{16 n_0^2} E_{DC}^2 \tag{4.22}$$

If now the relationship between the applied voltage V and the induced electric field E_{DC} is assumed to be quadratic, in the form:

$$E_{DC} = E_{DC0} + c_1 V + c_2 V^2 \tag{4.23}$$

where c_1 and c_2 are coefficients and E_{DC0} is a frozen electric field which may be present in the material (it could be due to a surface charge distribution at the $Si - Si_3N_4$ interface, or at the $Si - SiO_2$ interface, or to an applied electric bias [159]), the first and second harmonic amplitudes get the following form:

$$I_{out}(\omega) = \left(K_1 c_1 + 2K_2 E_0 c_1\right) V_0 + 12 K_2 c_1 c_2 V_0^3 \tag{4.24}$$

$$I_{out}(2\omega) = \left(2K_2 c_1^2 + 2K_1 c_2 + 4K_2 E_0 c_2\right) V_0^2 \tag{4.25}$$

where the constants K_1 and K_2 are defined as:

$$K_1 = \frac{\lambda_{res,0} L_h \chi^{(2)}_{eff,jjj}}{2n_0^2 L_{tot}} \tag{4.26}$$

$$K_2 = \frac{9\lambda_{res,0} L_h \chi^{(3)}_{eff,jjjj}}{16 n_0^2 L_{tot}} \tag{4.27}$$

and the effective third order non linearity $\chi^{(3)}_{eff,jjjj}$ is written as:

$$\chi^{(3)}_{eff,jjjj} = \frac{\int_{core} \chi^{(3)}_{mat,jjjj}(r_T) n^2(r_T) |e_j(r_T)|^2 dr_T}{\int n^2(r_T) |\mathbf{e}(r_T)|^2 dr_T} \tag{4.28}$$

From Eq.4.23 and Eq.4.24 it can be seen that by including a $\chi^{(3)}$ nonlinearity it is possible to predict a cubic relation between $I_{out}(\omega)$ and V_0, and a quadratic relation between $I_{out}(\omega)$ and V_0. However, the order of magnitude of the $\chi^{(3)}$ contribution can be easily demonstrated to be not sufficient for accounting the observed anomalies reported in Fig.4.22. To prove this, from Eq.4.24 it can be seen that the magnitude of the corrections due to the $\chi^{(3)}$ term is of the order of $\approx V_0^2 K_2 c_2 / K_1$. By assuming the set of parameters listed in Table 4.5, which are meaningful for the experiment described in section 4.3.1 for a CAP 140 resonator of width $1.2\,\mu m$ (both the optical field and the static field are applied in the $\hat{z}$ direction), this correction is of the order of $10^{-8} \ll 1$. This means that the presence of $\chi^{(3)}$ nonlinearites alone can not quantitatively accounts for the cubic relation observed in Fig.4.22, since the measured correction, as shown in Table 4.4, is

Parameter	Value	Source
V_0	$5\,V$	Experiment
$\chi^{(2)}_{eff}$	$10^2\,pmV^{-1}$	[139]
$\chi^{(3)}_{eff}$	$10^{-18}m^2V^{-2}$	[127]
c_2	10^{-1}	FEM simulation

Table 4.5: Values of the parameters used to evaluate the order of magnitude of the cubic correction in Eq.4.24.

of the order of 10^{-2}. What is more interesting, the quadratic electro optic effect alters only the real part of the effective index, thus it does not explain the presence of voltage induced absorption.

4.3.4 Phenomenological interpretation in terms of trap released free carriers

The presence of a voltage induced absorption, which is accompained by a dominant blue shift of the resonance wavelength, indicates that the origin of the electro optic modulation could rely on free carrier effects. Injection of free carriers inside the core of the waveguide has the effect to decrease the real part of the refractive index by a quantity Δn, while at the same time increases the absorption coefficient by a quantity $\Delta\alpha$. This is described by the relations reported in Eqs.1.14-1.15. From these equations, it can be seen that Δn and $\Delta\alpha$ are not independent, since both depends on the same electron and hole concentration. It comes out that the blue shift of the resonance wavelength and the corresponding losses observed in Fig.4.24(a-b) should follow the same trend. In order to translate the changes in the refractive index and in the absorption coefficient into a shift of the resonance wavelength and into a decrease of the quality factor of the resonator, one can use the relations (see Appendix B):

$$\Delta n_{eff} = \frac{\Gamma_c \Delta n}{n_0} n_g \tag{4.29}$$

$$\Delta \alpha_{eff} = \frac{\Gamma_c \Delta \alpha}{2 n_0} n_g \tag{4.30}$$

where Γ_c is the modal confinement factor, together with Eq. 4.15 and the relation (reported in Table 1.1):

$$Q = \frac{\pi n_g L_{tot} \sqrt{1-\kappa^2}\sqrt{\tau}}{(1-(1-\kappa^2)\tau)\lambda_{res,0}} \tag{4.31}$$

where $\tau = \tau_0 e^{-\Delta\alpha_{eff} L_h}$. Here, τ_0 represents the round trip losses when no voltage is applied through the electrodes. Using the set of parameters listed in Table 4.6, which refer to the experimental conditions in which the curves shown in Fig.4.24(a-b) have been recorded, the resonance shift $\Delta\lambda_{res}$ and the quality factor decrease have been computed through Eqs.1.14, 1.15, 4.29, 4.30, 4.31, and plotted in Fig.4.25 as a function of ΔP and ΔN. During this procedure, it has been assumed a unipolar injection mechanism, in which only electrons (holes) are injected in the core of the waveguide.

Parameter	Value	Source
κ^2	0.025	FEM simulation
n_g	4.24	FEM simulation
τ_0	0.9	Experiment
Γ_c	0.705	FEM simulation
$\lambda_{res,0}$	$1.5294\,\mu m$	Experiment
n_0	3.485	[96]

Table 4.6: List of the parameters used to simulate the curves in Fig.4.25.

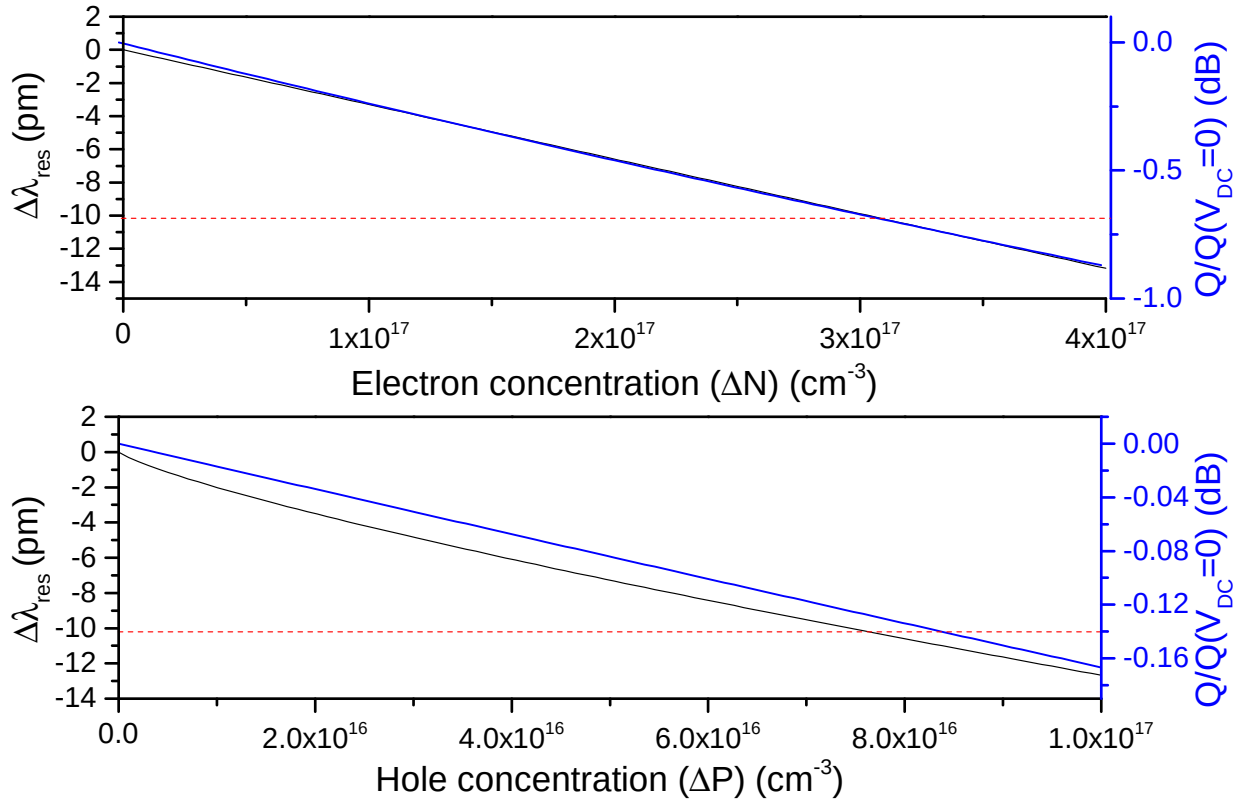

Figure 4.25: Shift of the resonance wavelength (black curve) and corresponding decrease of the quality factor (blue curve) as a function of the holes and electrons concentrations. The red dashed line correspond to the resonance shift shown in Fig.4.24(c) when $V_{DC} = 70\,V$.

From the curves in Fig.4.25 it comes out that, if the injected carriers were holes, a concentration of $(7.67 \pm 0.01) \cdot 10^{16}\,cm^{-3}$ is needed to cause the same resonance shift found in the experiment. At the same time, this causes a decrease of the quality factor with respect to the zero bias condition of $(-0.12 \pm 0.01)\,dB$. On the other hand, if the carriers responsable to the electro optic modulation were electrons, a concentration of $(3.07 \pm 0.01) \cdot 10^{17}\,cm^{-3}$ is needed to cause the same shift, and the resulting decrease in the quality factor is $(-0.68 \pm 0.01)\,dB$. The Q factor decrease measured in the experiment is $(-0.16 \pm 0.05)\,dB$, thus indicating that holes are probably the carriers which are the responsible of the electro optic modulation. This is not surprising, since the Silicon layer of the SOI wafer implemented in the fabrication of the samples is slightly $p-$doped, with an inpurity concentration of $10^{-16}\,cm^{-3}$. The question which now arise is on the type of injection mechanism. The core of the waveguide is surrounded by SiO_2, which is an electrical insulator, so holes can not be injected from the outside. The oxide thickness on the top of the waveguide is $900\,nm$, which also precludes tunneling of carriers through this layer. One can then infer that the change in the absorption and in the refractive index comes from a redistribution of the carriers inside the waveguide as a consequence of the applied electric field. However, as indicated in Fig.4.26, which shows a FEM simulation of a HAT140 waveguide of $1.2\,\mu m$ width under the action of an electric field, holes are depleted from the center of the waveguide and directed towards the upper (or lower, depending on the field direction, which in Fig.4.26(a) is polarized along $-\hat{z}$) interfaces of the oxide. This is expected since, as in metals, carriers tend to shield the applied electric field by redistribution. As a consequence of carrier depletion, their overlap with the optical mode decreases, and this increases the refractive index of the material and at the same time lowers the losses.

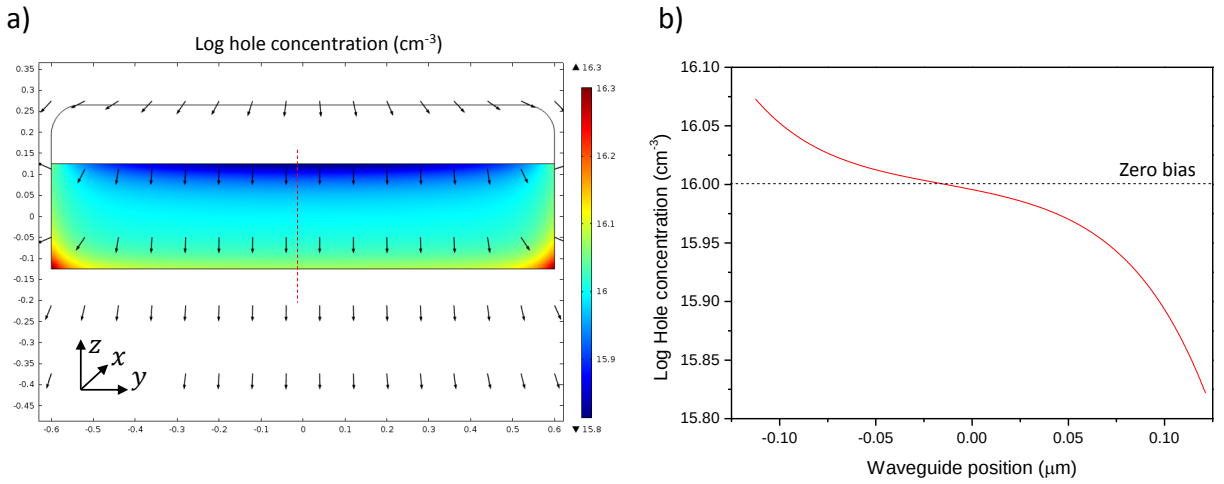

Figure 4.26: (a) Hole concentration inside the waveguide core under an applied voltage of $V_{DC} = 10\,V$. Black arrows represent the direction of the applied electric field. (b) Hole concentration along the vertical red dashed line shown in panel (a). The zero point on the x axis corresponds to the center of the waveguide.

This is in contradiction with the experimental observations. The most plausible explanation on the origin of the carrier injection relies on Surface Transfer Doping (STD) between Silicon and the Si_3N_4 interface (or with the SiO_2 interface) [209, 210]. STD is a mechanism through which electrons and holes of a semiconductor can be exchanged with an insulating interface due to the trap states located at the boundary between the semiconductor and the insulator. These trap states introduce energy levels within the energy gap of the semiconductor, which can be of donor type or acceptor type, depending on the interface in which they are located. For example, in Ref.[211], acceptor sites, located at $0.3\,eV$ from the semiconductor valence band, are introduced as a consequence of the dimer-bond reconstruction which occurs at the interface between Silicon and air. The energy band diagram of the system exhibiting $p-$type STD, which probably corresponds to the case of the $Si - Si_3N_4$ interface, is schematically shown in Fig.4.27.

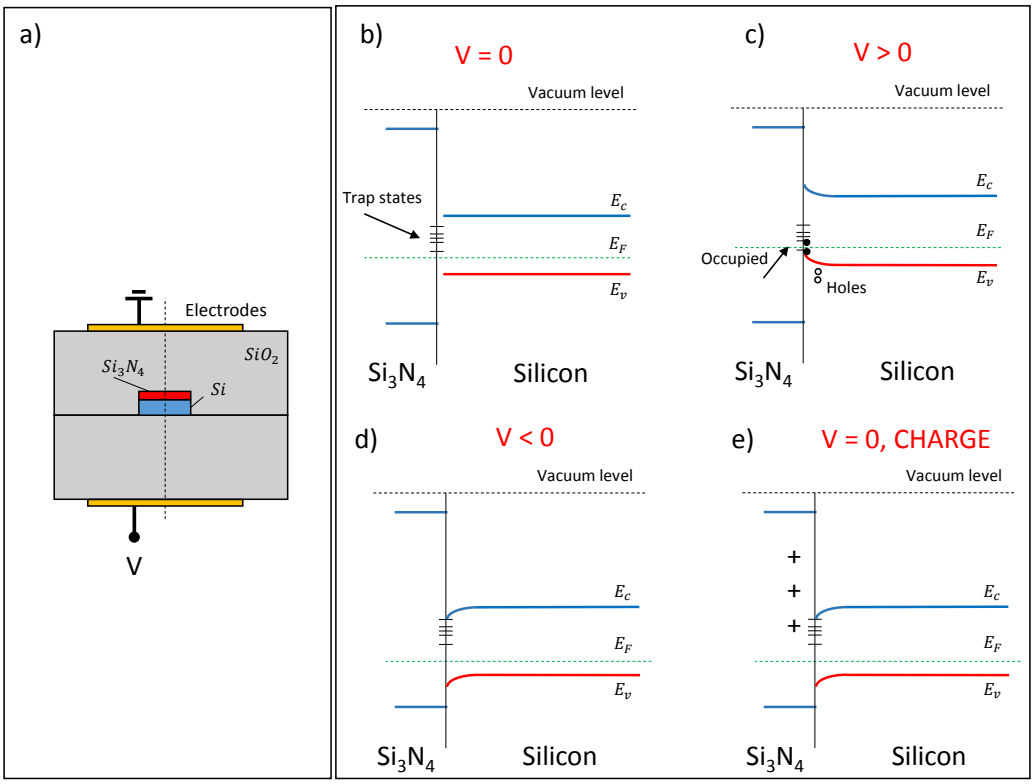

Figure 4.27: (a) Cross section of the waveguide in the resonator, with the different layers and materials. (b) Energy band diagram of the $Si - Si_3N_4$ interface when no voltage is applied. This is the flat band condition. (c) Energy band diagram of the $Si - Si_3N_4$ interface when a positive voltage is applied, showing the release of holes from the trap states. (d) Energy band diagram of the $Si - Si_3N_4$ interface when a negative voltage is applied. (e) Energy band diagram of the $Si - Si_3N_4$ interface when no voltage is applied but a positive charge layer is present at the interface. Panels from (b) to (e) refer to the band diagrams along the vertical black dashed line of panel (a). E_c = conduction band, E_v = valence band, E_F = Fermi level.

The Silicon is slightly $p-$doped, so it has the Fermi level close to the top of the valence band. The energy levels due to interface states within the bandgap are acceptors, i.e, they are empty and can be occupied by electrons from the valence band of Silicon when a positive bias is applied. The occupancy $f_T(E)$ of the interface states follows the usual Fermi distribution [212]:

$$f_T(E) = \frac{1}{1 + g_A e^{\frac{E - E_F}{KT}}} \tag{4.32}$$

where E is the energy of the trap, g_A is the ground state degeneracy, E_F is the Fermi level, K is the Boltzmann constant and T is the temperature. Traps are distribuited within the energy gap with a trap density $D_t(E)$. If a positive voltage is applied, the Fermi level is pushed toward the lowest energy trap states (Fig.4.27(c)), and electrons fill the trap states tunneling from the valence band of the semiconductor, just as for bulk impurity acceptors. As a result, holes will form in Silicon, and negative charge will be localized on the surface acceptors. This is the injection mechanism which creates carriers in the waveguide core. When the applied voltage is negative, the Fermi level is pulled away from the lowest energy trap states (Fig.4.27(c)), so no holes are created in Silicon. This could explain the asymmetric resonance shift observed in Fig.4.24(c) between positive and negative applied voltages. A fixed surface charge can be present at the Si_3N_4 interface, which induces band bending when no voltage is applied (Fig.4.27(c)). In this case the flat band condition is reached if a positive/negative (depending on the surface charge sign) is applied. This is similar to what

happens in a Metal Oxide Semiconductor capacitor in which trapped charges are present within the oxide layer [212]. The presence of a surface charge may be the cause of the shift of the zero bias point, where the propagation losses are lower, which is observed in Fig.4.24(a) and located near $V_{DC} = -40\,V$. The concentration of injected holes as a function of the applied voltage V_{DC} can be estimated using the relation:

$$\Delta P(V) = \int_{E_v}^{E_c} D_t(E) f_T(E, E_F(V))\, dE \tag{4.33}$$

which can be a non linear function of V. The trap density $D_t(E)$ is closely related to the type and quality of the interface, which is not easily controllabe during fabrication. As a result, each device could have its own trap density distribution, and this could explain the random trends observed in the electro optic modulation shown in Fig.4.19. As a further support that the interface type plays a primary role in the experiment, in Section 4.3.1 it has been proved that samples without the Si_3N_4 stressing layer exhibited an electro optic modulation which is an order of magnitude lower with respect to the ones with Si_3N_4. Nevertheless, a more quantitative analysis is needed to confirm the hypotesis of STD.

4.3.5 High frequency electro optic measurements

In case that the trap distribution $D_t(E)$, introduced in section 4.3.4 is generating a linear relation between the injected holes and the applied voltage, the resulting electro optic modulation would show exactly the same behaviour as if it was induced by $\chi^{(2)}$ nonlinearities. This is because the refractive index change is in both cases linear with the applied voltage, and also the orders of magnitude ($\Delta n_{eff} \approx 10^{-5}$) of these changes are comparable. The linearity of the effective index change as a function of the applied voltage necessarily requires the presence of a surface charge at the $Si_3N_4 - Si$ interface, since the zero bias point has to be shifted from $V_{DC} = 0$, as shown in Fig.4.27(d). If this was not the case, and the flat band condition was reached at $V_{DC} = 0$, the negative part of the sinusoidal modulation will not inject holes, while the positive part will do. This will result in an asymmetric refractive index change with respect to the zero bias point, which does not occur in a electro optic modulation of a $\chi^{(2)}$ origin.
A method which allows to distinguish free carriers from second order nonlinearites uses the different timescales on which the two dispersion mechanisms act. The electro optic modulation induced by $\chi^{(2)}$ effects has a response which is instanteneous with respect to voltage variations. This is because the nonlinearity origins from the second order dipole moment of the electrons in the material, which can follow an applied electric field up to optical frequencies (fs timescale). On the other hand, free carriers in a waveguide have a characteristic effective lifetime in the range of $500\,ps - 1\,ns$. This means that they are not able to follow voltage variations if these are sufficiently fast, i.e, in the GHz range. In this sense, a definitive proof of the presence of strain induced second order nonlinearities would rely on high frequency electro optic measurements.
This is accomplished using the experimental setup in Fig.4.28(a).

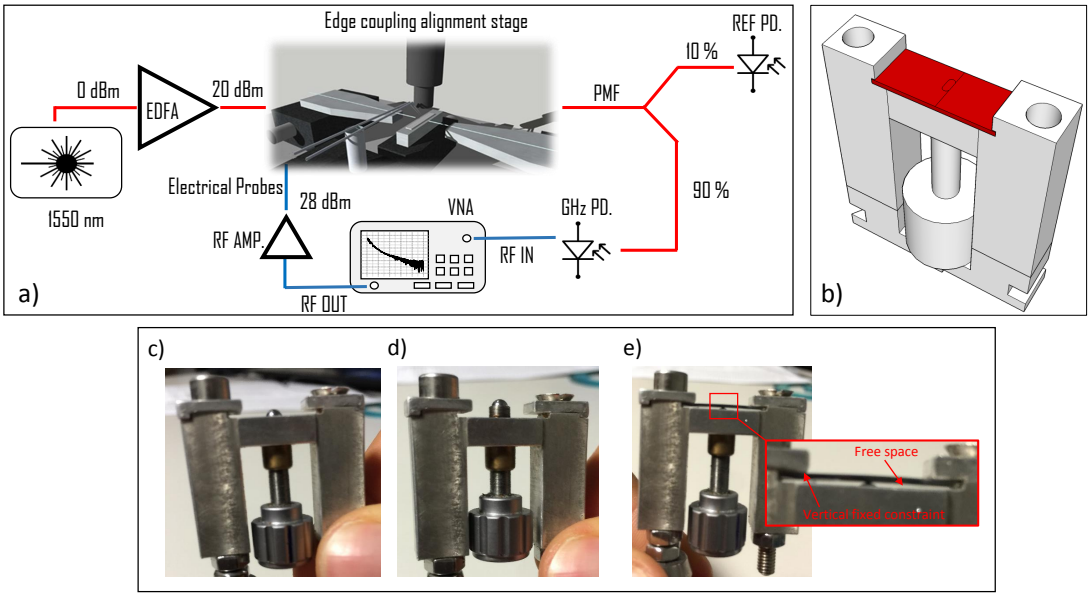

Figure 4.28: (a) Experimental setup used for the electro-optic measurements. PMF = polarization maintaining fibers; PD = photodiodes; VNA = vector network analyzer RF IN(OUT) = Radio frequency IN(OUT). (b) 3D model of the stressing sample holder. The sample is indicated in red. (c-d) Stressing sample holder with the screw set at two different displacements. (c) Stressing sample holder with the Silicon chip mounted on it. The inset shows that the sample is not touching the Alluminium surface. The contact lines between the holder and the sample, which constitute a fixed constraint on the vertical direction, are also indicated.

Light from a C-band Infra-Red laser amplified by an EDFA is edge coupled to the input port of the resonator using a polarization maintaining lensed fiber (PMF). The light polarization is set to TM . A nanometric XYZ positioning stage is used to minimize the coupling losses. The transmitted light from the resonator Through port, which is a CAP140 racetrack with a waveguide width of $1.6\,\mu m$, is split: 10% is sent to a reference photodiode, while 90% feeds a high-bandwidth photoreceiver ($43\,GHz$) connected to a vector network analyzer (VNA). The VNA also provides a $28\,dBm$ (after amplification) sinusoidal voltage modulation to the electrodes, using impedance matched Tungsten tips with $40\,GHz$ bandwidth. For this experiment, the sample is strained by a mechanical deformation through a special sample holder. This is shown in Fig.4.28(b). The device is fixed on a sample holder that can provide a variable stress, adjusted by rotating a $250\,\mu m$ pitch screw. The strain is mechanically induced since the sample ends are fixed to the holder, while the screw pushes the center of the sample. The pressure exercised by the screw bends the sample (see Fig.4.28(c,d,e)). It is possible to displace the screw by approximately its complete pitch before breaking the chip. To avoid microfractures, the screw displacements are kept lower than $150\,\mu m$. The reason why the mechanical sample holder is used is to exhamine the behavior of the electro optic modulation as a function of different stress levels at high frequencies, where free carrier effects should be not present. In this way it is possible to investigate the dependence of the induced $\chi^{(2)}$ tensor components as a function of the applied strain. The relationship between the screw displacement and the stress induced inside the waveguide is computed from FEM computations. The results are shown in Figs.4.29(a) and 4.29(b).

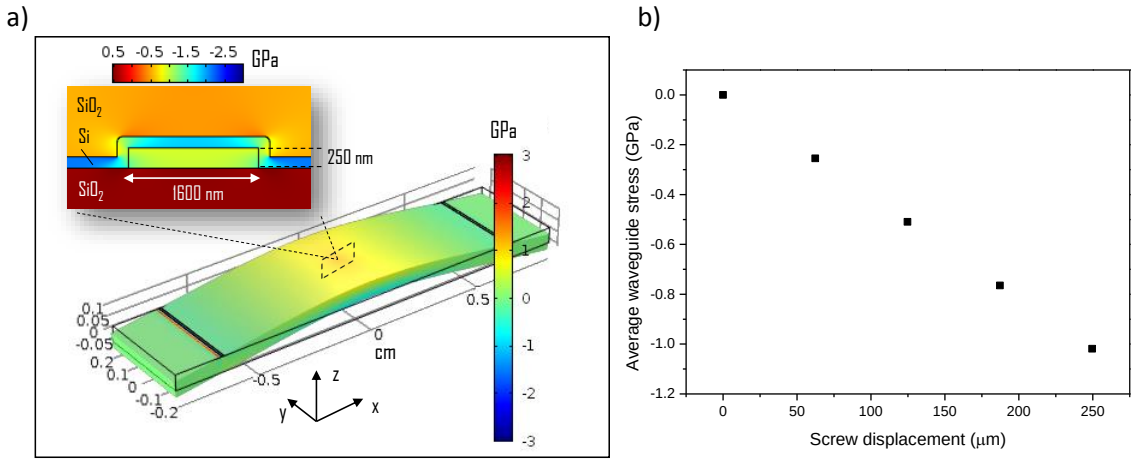

Figure 4.29: (a) Finite element simulation of the stress distribution (σ_{xx} element of the stress tensorσ_{ij}) on the sample subjected to a 62.5 μm screw displacement. The discontinuities near the ends are due to the line contact with the sample holder (see Fig.4.28(c-d)), which lies 2 mm from the end. The inset shows the stress profile along the waveguide cross section. (b) Average stress (σ_{xx}) inside the waveguide as a function of the screw displacement.

Only the σ_{xx} element of the stress tensor σ_{ij} is plotted, since it was found to be one order of magnitude higher than the σ_{yy} component and five orders of magnitude higher than the remaining tensor elements. In the reference frame indicated in Fig.4.29(a), $\hat{x}$ is the direction of light propagation while (x, z) are the transverse dimensions of the waveguide. In the region where the resonator is located (dashed rectangle in Fig.4.29(a)), the overall stress distribution can be approximated as compressive and uniaxial in the $\hat{x}$ direction. In Fig. 4.29(b), it is shown the linear relationship between the screw displacement and the computed average stress in the waveguide. At the working point (displacement $\sim 125\,\mu m$), the stress level is about $-0.48\,GPa$ in the waveguide and $-0.78\,GPa$ in the Si_3N_4 layer. The stress magnitude and direction are comparable to the ones used in other experiments [140, 138]. In the inset of Fig. 4.29(a) it can be noticed that a high stress (hence strain) gradient is present at the upper and lower interface between the Si_3N_4 and the waveguide. This feature is essential since it is theoretically predicted that the induced $\chi^{(2)}$ is proportional to the strain gradient in the material [160]. At first, the screw displacement is set to zero, so no stress (except the residual one due to the Si_3N_4 interface) is applied to the waveguide. By monitoring the output signal at the reference photodiode, the laser wavelength is tuned near the $-3\,dB$ point of one of the resonances (Fig.4.30(a), inset), where the sensitivity to small refractive index variations is maximized. The quality factor of this resonance is ≈ 23200. The sinusoidal modulation is then applied to the sample electrodes using the VNA and a $32\,dB$ electrical amplifier (see Fig.4.28(a)). With reference to Fig.4.29(a), both the optical field and the static electric field lie in the $\hat{z}$ direction. Exactly as discussed for the homodyne detection described in Section 4.1.3, as a result of the bias modulation, the resonance oscillates back and forth with respect to the laser wavelength, inducing a periodic modulation of the transmitted optical signal at the Through port of the resonator. Assuming that this signal modulation is due to the electro optic effect caused by the strain induced second order nonlinearity, the oscillation amplitude I_{out} is given by Eq.4.17. By following the method described in section 4.1.3 and 4.3.1, the effective $\chi^{(2)}_{eff,zzz}$ is measured and plotted in Fig.4.30(a) as a function of the driving bias frequency, swept from $50\,MHz$ to $5\,GHz$.

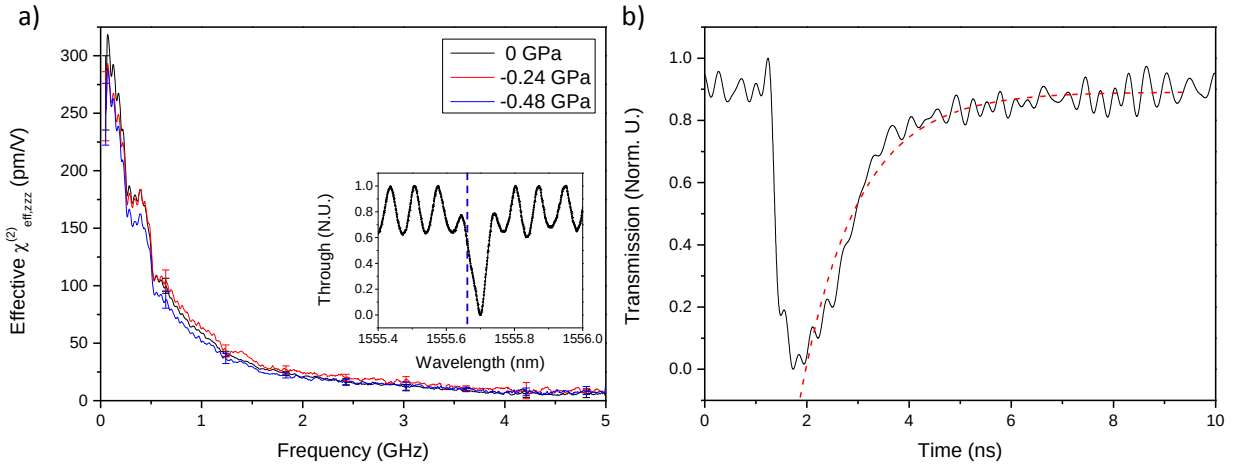

Figure 4.30: (a) Effective $\chi^{(2)}_{eff,zzz}$ as a function of the electrical modulation frequency for three different stress levels in the waveguide. For clarity, the errors are reported only for certain points of the curves. The inset shows the working point of the electro optic measurement. The black line denotes the Through transmission, while the vertical blue dashed line represents the wavelength of the laser. (b) Measurement of the carrier lifetime. The black line is the Drop signal (in normalized units) in time, while the red dotted line is an exponential fit of the rising edge.

As can be seen, the value of $\chi^{(2)}_{eff,zzz}$ is maximum in the low frequency range and decreases as the modulation frequency increases. The extracted value of $\chi^{(2)}_{eff,zzz}$ close to the DC regime is $\approx 270\,pmV^{-1}$, which is comparable to values reported in the literature for static electro-optic measurements using the same electric field and optical polarization directions [141, 138], and is also comparable to the ones found using the Lock In and shown in Fig.4.19. The cutoff frequency, i.e., the frequency at which the $\chi^{(2)}_{eff,zzz}$ halves, is $\nu_c = (0.50 \pm 0.01)\,GHz$, corresponding to a time constant $\tau = \frac{\sqrt{3}}{2\pi}\nu_c = (0.55 \pm 0.01)\,ns$. The minimum value of $\chi^{(2)}_{eff,zzz}$ that can be detected is limited by the electrical noise floors of the VNA and the photoreceiver. This corresponds to an effective $\chi^{(2)}_{eff,zzz}$ of $(8 \pm 3)\,pmV^{-1}$. From Fig.4.30(a), one can see that this value is reached for $\nu \geq 4.5\,GHz$. To exclude the possibility that the bandwidth is limited by the photon lifetime in the cavity, the optical input is modulated and the signal at the Drop port is measured with the laser wavelength tuned on resonance. The cavity response is shown in Fig.4.31.

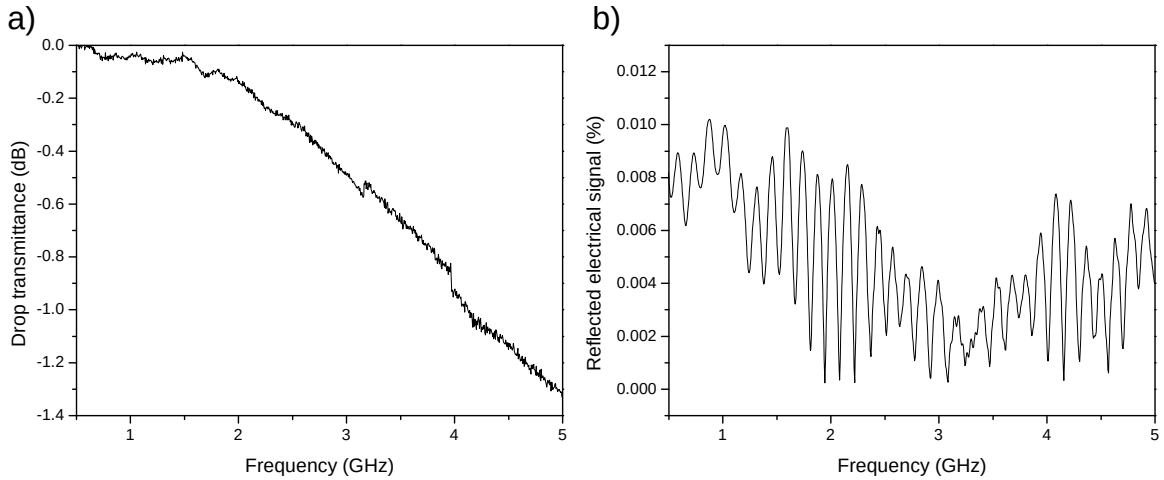

Figure 4.31: (a) Drop transmission as a function of the frequency of the input optical signal. Data are normalized with respect to the response at $0.5\,GHz$. (b) Electrical signal reflected back from the sample electrodes toward the VNA due to impedance mismatch.

The signal drops by $\approx -1.3\,dB$ from $50\,MHz$ to $5\,GHz$, showing that the cavity is far from the optical cutoff. This frequency response has been subtracted from the curves in Fig.4.30(a). To ensure that the voltage which exists from the VNA is effectively applied to the sample electrodes, the electrical signal which is reflected back from the on chip metallic pads towards the VNA is recorded and plotted in Fig.4.31(b). This is found to be $< 0.01\%$, so that almost all the power which exits from the VNA reaches the sample electrodes. As shown in Fig. 4.30(a), the electro-optic measurements are repeated after applying different stress levels to the waveguide of $-0.24\,GPa$ and $-0.48\,GPa$. Very slight differences are observed with respect to the no-stress case. These results clearly show that the modulation cannot be attributed to a strain-induced $\chi^{(2)}$. In fact, if the latter was the cause for the observed effect, one would expect the transmitted signal to follow the voltage variations instantaneously up to optical frequencies. Rather, the signal modulation is related to a slower dispersion mechanism, with a characteristic time in the nanosecond scale. This confirms the results discussed in Section 4.3.4, in which the electro optic modulation has been supposed to be attribuited to free carrier dispersion. As a further demonstration, the effective carrier lifetime in the waveguide is measured to verify its consistency with the cutoff frequency in the electro optic experiments. This is done by using a pump and probe scheme, in which an intense picosecond laser pulse is coupled to the waveguide, and the time-dependent losses of a weaker probe beam are monitored. The short pump pulse generates free carriers due to TPA; these free carriers in turn attenuate the probe signal due to free-carrier absorption. After switching off the pump laser, the probe beam transmission slowly recovers due to free carrier recombination or diffusion away from the spot of the pump laser. The effective free carrier lifetime can then be extracted from the time-resolved measurement of the recovering probe beam transmission. The result is shown in Fig.4.30(b). The sudden signal decrease is due to the pulse arrival and, consequently, to TPA carrier generation. The subsequent slower signal recovery is due to the finite free carrier lifetime. From these data, a carrier life time of $\tau_c = (1.06 \pm 0.01)\,ns$ has been estimated. Being $\tau_c \approx 1/\nu_c$, this constitutes another proof that the observed modulation can be attributed to plasma carrier dispersion.
In the implemented resonator geometry and with $\sim -0.5\,GPa$ of applied stress, the upper limit to the strain induced $\chi^{(2)}_{eff,zzz}$ is $(8 \pm 3)\,pmV^{-1}$. This value is about an order of magnitude lower than those extracted from DC measurements, as reported here and in the literature [139, 138, 141].

4.3.6 Summary and conclusions

In this chapter, the possibility to induce a second order nonlinearity in Silicon waveguides has been investigated. The key for enabling a $\chi^{(2)} \neq 0$ is to break the centrosymmetry of the unit cell of the material, and this has been performed using different types of stressing layer of Silicon Nitride deposited on the top of the waveguide. Strained racetrack shaped optical resonators have been designed and fabricated, with the aim to probe the linear electro optic modulation induced by the second order nonlinearity. In this approach, a portion of the resonator perimeter is subjected to a quasi static (KHz regime) electric field which imparts a variable phase shift to the travelling wave inside the resonator. This phase shift, which should be proportional to the magnitude of the strain induced $\chi^{(2)}$ component, is detected by a Lock In amplifier. From the amplitude of the signal detected by the Lock in, and from the knowledge of the resonator parameters, the value of the $\chi^{(2)}_{eff,zzz}$ tensor component have been extracted for different device geometries and stress distributions. Similar approaches, which exploited the static electro optic effect in integrated Mach Zenhder interferometers (even though no Lock in amplification was used) were already reported in literature, and values of $\chi^{(2)}$ as high as $330\,pmV^{-1}$ were found. Even though the presence of a linear electro optic modulation was found, with values of $\chi^{(2)}$ comparable to the ones reported in literature, a large number of anomalies has been encountered during the measurements. Many of them were incompatible with the assumption that the electro optic modulation had a $\chi^{(2)}$ origin. The most evident one was the presence of losses which are

introduced as a consequence of the applied static electric field. Evidences of voltage induced absorption have been encountered both in Lock in measurements and in purely DC regime. The presence of losses suggested that the mechanism responsable for the observed electro optic modulation was the injection of free carriers in response to an applied electric field. This has been supported by the quantitative relation which exists between the change in the real part of the refractive index and the change in the absorption coefficient. From this analysis, it emerged that the injection is unipolar, and that the type of injected carriers is holes. The most plausible explanation of the observed phenomenon, is $p-$type Surface Transfer Doping between Silicon and Si_3N_4 occurring at their interface. At quasi DC regimes, $\chi^{(2)}$ induced modulation is completely masked by free carrier effects. In order to distinguish the two contributions, high-frequency (GHz) measurements of the optical transmission under an AC electric field variation have been performed. This allowed to separate the contribution arising from $\chi^{(2)}$ non linearities, which are able to follow instantaneously the electric field variations, to the one due to free carriers, whose modulation speed is bandwidth limited to few hundreds of MHz due to the electron-hole recombination time. It has been found that the electro optic modulation vanished as the modulation speed exceeded the free carrier lifetime. No appreciable differences have been found by increasing the stress level in the waveguide core up to $-0.48\,GPa$. A time response in the nanosecond range has been revealed, which consequently rules out potential strain induced $\chi^{(2)}$ as the origin of the modulation. An upper limit of $(8 \pm 3)\,pmV^{-1}$ for the strain induced $\chi^{(2)}_{eff,zzz}$ in Silicon waveguides has been set, which corresponds to the minimum detectable signal of the implemented apparatus. This value is more than one order of magnitude lower than the ones reported in the low frequency regime in the literature.
It has to be remarked that these results do not completely exclude the presence of a strain-induced $\chi^{(2)}$ in Silicon. Indeed, there exist proofs of SHG in strained Silicon that intrinsically cannot have explanations relying purely on free carriers [157, 213]. These experiments revealed a $\chi^{(2)}$ value up to $40\,pmV^{-1}$ for $-1.2\,GPa$ of applied stress [157]. Differences can be due to the fact that the $\chi^{(2)}$ tensor is dispersive, so its value at optical frequencies can be significantly different from the one measured under DC [160]. In addition, it has recently been shown that electrostatic fields at the $Si_3N_4 - Si$ interface can couple with the optical fields through $\chi^{(3)}$ nonlinearities, resulting in an electric field second harmonic contribution (EFISH) [159]. This may have altered and consequently increased the extracted values of the $\chi^{(2)}$ in the optical measurement. Larger stress or different stressing materials than Si_3N_4 are needed to definitely prove the presence of the electro optic effect in strained silicon waveguides.
From the point of view of the project SIQURO, these considerations cast several doubts on the feasibility and on the efficiency of MIR photon pair generation through SPDC.

Chapter 5

Manipulation of SPDC photon pairs in a Mach Zehnder interferometer

In chapters 3 and 4, the possibility to integrate quantum sources of photon pairs based on $\chi^{(3)}$ and $\chi^{(2)}$ nonlinearities in Silicon have been investigated. Multi Modal Four Wave Mixing in straight Silicon waveguides, has been proved to be a powerful tool for achieving efficient wavelength conversion with large spectral translations. Despite this fact, the predicted photon pair generation was too much low for being exploited in a photonic circuit. In parallel, investigations of $\chi^{(2)}$ nonlinearities through the electro optic effect in strained Silicon resonators demonstrated that the value of the strain induced $\chi^{(2)}$ is (probably) lower than $8\,pmV^{-1}$, which casts several doubts on the feasibility of MIR photon sources through SPDC. At the moment of writing this work, the project SIQURO still lacks of integrated quantum sources. Nevertheless, quantum optics experiments have been done, which were preparatory for the next developements of the project. Such experiments have been performed using photon pairs produced by SPDC in a PPLN crystal coupled to a free space Mach Zehnder (MZ) interferometer. Although the whole setup was far from being compact, it allowed to get all the necessary knowledges and skills required for the realization of the same experiment on a chip. In fact, from the point of view of photon pair manipulation and interference, there are no differences between a free space device and an integrated device which shares the same transfer function. In order to shift from one to the other, it is sufficient to replace the refractive index of the medium in which photons are propagating with the effective index of the optical mode of the waveguide.
In this chapter, it will be firstly reviewed the process of SPDC. Then the source will be characterized and the correlated nature of the photons will be revealed by a coincidence measurement of their arrival time in two photon counters. Finally, photon pairs will be used to excite a free space MZ interferometer, and two photon interference will be monitored as a function of the relative phase between the two arms of the interferometer. This work has been done with the collaboration of Mr. Alessandro Trenti, Dr. Mattia Mancinelli and Dr. Hannah Price. Dr. Iacopo Carusotto also gave an important contribution through helpful discussions.

5.1 Spontaneous Parametric Down Conversion

The process of SPDC occurs in any medium which exhibits a second order nonlinearity. The process can be schematically represented as in Fig.5.1(a): a pump photon, of energy $\hbar\omega_p$, interacts with the $\chi^{(2)}$ nonlinearity of the material and is split into two lower energy photons, called signal and idler, at frequencies ω_s and ω_i. During this process, both energy and momentum have to be conserved, which means that:

$$\hbar\omega_p = \hbar\omega_i + \hbar\omega_s \tag{5.1}$$

$$\omega_p n(\omega_p) = \omega_i n(\omega_i) + \omega_s n(\omega_s) \tag{5.2}$$

where $n(\omega)$ is the refractive index of the material evaluated at angular frequency ω. If the frequency of the signal is expressed with respect to half of the frequency of the pump as $\omega_s = \frac{\omega_p}{2} + \Omega$, Eq. 5.1 implies that $\omega_i = \frac{\omega_p}{2} - \Omega$. This means that the signal and the idler frequencies are simmetrically located with respect to half of the frequency of the pump.

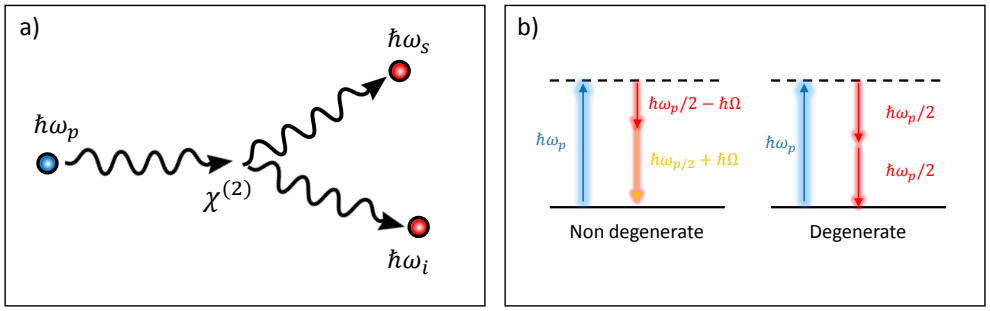

Figure 5.1: (a) Schematic process of SPDC which converts one pump photon at energy $\hbar\omega_p$ into two photons at energies $\hbar\omega_s$ and $\hbar\omega_i$. (b) Energies of the photons involved in the degenerate and non degenerate SPDC process.

When $\Omega = 0$, the process is said to be degenerate, and the signal and the idler photons have the same frequency (see Fig.5.1(b)). It is worth to note that Eq.5.1 does not imply Eq.5.2, since the medium can be dispersive. In free space, Eq.5.1 is always satisfied since there exist a continuum of radiation modes at different frequencies. However, due to the fact that energy and momentum are connected by the refractive index, Eq.5.2 is not in general satisfied. When Eq.5.2 is not fullfilled, the SPDC process is said to be not phase matched. As it will be demonstrated, when a phase mismatch Δk exists in a material of length L, the efficiency of the process scales as:

$$\frac{P_{\Delta k=0}}{P_{\Delta k}} \propto sinc^2\left(\frac{\Delta k L}{2\pi}\right) \tag{5.3}$$

where $P_{\Delta k=0}$ is the generated signal/idler power (if we assume a degenerate process they are equivalent) at perfect phase matching ($\Delta k = 0$), while $P_{\Delta k}$ is the generated signal/idler power when a phase mismatch Δk exists. From Eq.5.3, it is possible to define a characteristic length L_c , called the coherence length, as:

$$L_c = \frac{2\pi}{\Delta k} \tag{5.4}$$

The coherence length is a measure of the maximum length within which the parametric interaction is efficient. Several techniques exist to achieve perfect phase matching. Some of them have been reported in Chapter 3, since they are shared with the FWM process. The particular technique implemented in the following of this chapter is called periodically poling, or quasi phase matching. Here, the material has a $\chi^{(2)}$ value which periodically changes its value along the direction of light propagation, with a period of Λ. When light travels in a medium with a periodic $\chi^{(2)}$ variation, Eq.5.2 modifies to:

$$\omega_p n(\omega_p) = \omega_i n(\omega_i) + \omega_s n(\omega_s) + m\frac{c}{\Lambda} \tag{5.5}$$

in which c is the speed of light in vacuum and m is an integer number. Usually $m = 1$, the reason will be clearified in section 5.1.1. Eq.5.5 tells that momentum is conserved up to a multiple of the reciprocal vector of the unidimensional lattice defined by the $\chi^{(2)}$ periodicity. This phenomenon has analogues in photonic crystals [88], as well in the study of the electronic structure and transport in matter [214].
By tuning Λ, it is possible to obtain quasi phase matching in a very high range of wavelengths. In principle, the tuning is limited by the fabrication tolerances of the poling. The crystal used in the experiment described in section 5.2.2 has a poling which is realized by periodically inverting the sign of the $\chi^{(2)}$ nonlinearity. This has been achieved by lithographically exposing the crystal (which is ferroelectric) to a periodic strong electric field which reverses the direction of the permanent dipole moment [215].
Depending on the relative polarization directions between the generated signal and idler photons, the process of SPDC is said to be of Type I or Type II. In the first case, both photons share the same polarization while in the second case their polarizations are ortogonal.

5.1.1 A brief theory of SPDC

The process of SPDC has no classical analogue. To see this, one can assume that the total electric field inside the material is given by $E = (E_p + E_s + E_i) + c.c$, where E_p is the pump field, E_s the signal field and E_i the idler field. By inserting this expression into Eq.4.2, the polarization source which generates the signal (idler) is:

$$P_{s(i)} = \epsilon_0 \chi^{(2)} E_p E^*_{s(i)} \tag{5.6}$$

If the initial field amplitude at the input of the crystal $E_{s(i)}$ is zero, which corresponds to a classical assumption, also the polarization source in Eq.5.6 vanishes. This means that no field at frequency $\omega_{s(i)}$ will be built inside the material as the pump propagates. In order to generate down converted photons, an input seed is needed. As already discussed in section 3.1, this is provided by the vacuum fluctuations of the quantized electric field.
In order to derive more precisely the expressions for the photon rates of the down converted radiation, the work of M.Fioretino et. al. will be followed [165] . In this work, they derive an expression for the generated signal power in a Periodically Poled Potassium Titanyl Phosphate (PPKTP) waveguide. This geometry is quite dissimilar to the one implemented in the experiment described in section 5.2.2, since it refers to a guiding geometry rather than to a poled bulk crystal. However, it allows to cover all the principal physical results without the need of using the more general (and complex) theory of non collinear phase matching in bulk crystals [216]. The signal and idler fields are written inside the single mode waveguide as:

$$E_{s,i}(r,t) = \frac{1}{2}\left(c_{s,i}\frac{u_{s,i}(x,y)}{\sqrt{L}}e^{i(\beta_{s,i}z-\omega_{s,i}t)} + c.c\right) \tag{5.7}$$

in which $u(x,y)$ is the normalized transverse field profile, $\beta = \frac{\omega}{c}n(\omega)$ the propagation constant and L the length of the waveguide. The direction of light propagation is assumed to be $\hat{z}$. The quantized form of the fields in Eq.5.7 are:

$$\hat{E}_{s,i}(r,t) = \frac{i}{2}\left(\frac{2\hbar\omega_{s,i}}{n^2(\omega_{s,i})\epsilon_0}\right)^{\frac{1}{2}}\frac{1}{\sqrt{L}}u_{s,i}(x,y)e^{i(\beta_{s,i}z-\omega_{s,i}t)}a_{s,i} + c.c \tag{5.8}$$

where $a_{s,i}$ is the operator which annihilates a photon at the signal (idler) frequency. The pump field is assumed to be in the classical form:

$$E_p = \frac{1}{2}\left(\sqrt{\frac{2P_p}{cn_p\epsilon_0}}u_p(x,y)e^{i(\beta_p z-\omega_p t)} + c.c\right) \tag{5.9}$$

where P_p is the pump power. The field is not quantized since it is much more intense than the signal/idler ones. The fields in Eqs.5.7, 5.8, 5.9 are not coupled and evolve freely if the electromagnetic field hamiltonian is the one in Eq.3.21. If a second order nonlinear polarization $\mathbf{P}^{NL} = \epsilon_0\chi^{(2)}\mathbf{E}^2$ is added as a perturbation in the material, the displacement field modifies to $\mathbf{D} = \mathbf{D}_0 + \epsilon_0\chi^{(2)}\mathbf{E}^2$. By inserting the expression for $\mathbf{D}$ into Eq.3.21, and by expressing the field $\mathbf{E}$ as the sum of the pump, the signal and the idler fields given in Eqs.5.8-5.9, one obtains:

$$H = H_0 + H^{NL} \tag{5.10}$$

in which the nonlinear hamiltonian H^{NL} is given by:

$$H^{NL} = -\frac{\epsilon_0}{2}\int_{wg}\chi^{(2)}(x,y,z)\left(E_p\hat{E_i^\dagger}\hat{E_s^\dagger} + c.c\right)d\mathbf{r} \tag{5.11}$$

Due to the waveguide poling, the non linear susceptibility is periodic in the propagation direction with period Λ, and has the form of a square wave. It is then possible to expand $\chi^{(2)}$ in Fourier series as:

$$\chi^{(2)}(x,y,z) = \sum_m d_m(x,y)e^{im\frac{2\pi}{\Lambda}z} \tag{5.12}$$

The perturbation hamiltonian H^{NL} in Eq.5.10 can induce a transition between the vacuum state $|0_s0_i\rangle$, in which there are no signal/idler photons, into the two photon state $|1_s1_i\rangle$ by means of the annihilation of a pump photon. The generated power per unit frequency can be evaluated using the Fermi's Golden rule as:

$$P_{s,i} = \hbar\omega_{s,i} \times \frac{2\pi}{\hbar}\rho_{s,i}\left|\langle 1_s1_i|\, H_{int}\,|0_s0_i\rangle\right|^2 \tag{5.13}$$

in which $\rho_{s,i}$ is the number of signal (idler) states in a frequency interval $d\omega_{s,i}$ allowed insed the waveguide, which is given by [165]:

$$\rho_{s,i} = \frac{L^2 n(\omega_s)n(\omega_i)}{\hbar c^2}d\omega_{s,i} \tag{5.14}$$

It is worth to note that the density of states in Eq.5.14 differs from the one of a bulk medium since in the latter case light is not confined in the transverse direction [165]. This has important consequences on the dependence of the final output power as a function of the crystal length L, even though these are not important for the results discussed in section 5.2.2. In deriving Eq.5.13, the energy conservation relation in Eq.5.1 has been assumed. By inserting Eqs.5.11, 5.12, 5.14 into Eq.5.13, one obtains:

$$P_{s,i} = \frac{\hbar\omega_{s(i)}^2\omega_{i(s)}L^2P_p}{\pi c^3\epsilon_0 n(\omega_s)n(\omega_i)n(\omega_p)A_{eff}}\sum_m d_m sinc^2\left(\frac{\Delta k_m L}{2}\right)d\omega_{s,i} \tag{5.15}$$

where the effective area is defined as:

$$A_{eff} = \left(\int_{wg}u_p(x,y)u_s^*(x,y)u_i^*(x,y)\,dxdy\right)^{-2} \tag{5.16}$$

and the phase mismatch Δk_m is given by the expression in Eq.5.5. For a $\chi^{(2)}$ periodically changing its sign as a square wave between the values d_0 and $-d_0$, $d_m = \frac{2}{m\pi}d_0$ for m odd ($d_m = 0$ if m is even). It is clear that maximum efficiency is reached if the poling period Λ is chosen such as the quasi phase matching condition

is satisfied with $m = 1$. In this case, it is possible to neglect the contribution arising from the higher order periods, and Eq.5.15 becomes:

$$P_{s,i} = \frac{4d_0^2\hbar\omega_{s(i)}^2\omega_{i(s)}L^2P_p}{\pi^3c^3\epsilon_0 n(\omega_s)n(\omega_i)n(\omega_p)A_{eff}} sinc^2\left(\frac{\Delta k_1 L}{2\pi}\right) d\omega_{s,i} \tag{5.17}$$

If one had performed the whole calculations for a poled bulk crystal, in which a continuum of plane wave modes are able to satisfy the phase matching condition at different angles, one would have obtained a more complex dependence of the generated power as a function of the angle of emission and of the signal (idler) frequency [216]. The bulk and waveguide dependencies of the generated power on frequency become similar in the limit of collinear emission (signal, idler and pump beams propagates in the same direction) and with a pump beam which is spatially large enough to carry negligible transverse momentum with respect to the longitudinal one [165]. In addition, the power per unit frequency would scale as L instead of L^2 [165]. However, it can be demonstrated that by integrating Eq.5.17 to get all the generated signal (idler) power, the integrated power scales as L exactly as it happens in a bulk medium. The result shown in Eq.5.17 tells that the generated signal/idler power scales linearly with the pump power P_p, and due to the *sinc* term, the process of down conversion is efficient only near phase matching.
Even though the approach based on Fermi's Golden rule is able to predict the generated power, it does not tell anything about the quantum state which is generated upon down conversion. The knowledge of this state is essential for the manipulation of SPDC photons in external interferometric structures, and for predicting the outcomes of two photon interference experiments. A common approach which allows to evaluate the state produced during the process SPDC relies on considering the evolution of the initial vacuum state $|\Psi(t=0)\rangle = |\Psi_{in}\rangle = |0\rangle$, under the action of the perturbation hamiltonian in Eq.5.11, written in the interaction picture:

$$|\Psi(t)\rangle = exp\left[-\frac{i}{\hbar}\int_0^t H^{NL}(t')dt'\right]|0\rangle \tag{5.18}$$

By skipping all the calculations, and keeping only the first order terms in H^{NL} (which means that only one pump photon is annihilated at a time, so no multi photon pair emission occurs), the down converted state is:

$$|\Psi(t\to\infty\rangle = |\Psi_{SPDC}\rangle = |0\rangle + \int \Phi(\omega_s,\omega_i)\,|1_{\omega_s}1_{\omega_i}\rangle\, d\omega_s d\omega_i \tag{5.19}$$

in which $\Phi(\omega_s,\omega_i)$ is a function of the signal and idler frequencies ω_s and ω_i and it is commonly called the biphoton wavefunction. The modulus square of the latter gives the probability that a signal photon with energy $\hbar\omega_s$ and an idler photon with energy $\hbar\omega_i$ are generated in the SPDC process. The function has to be normalized in order that $\int |\Phi(\omega_s,\omega_i)|^2 d\omega_s d\omega_i = 1$. A example of gaussian biphoton wavefunction is shown in Fig.5.2.

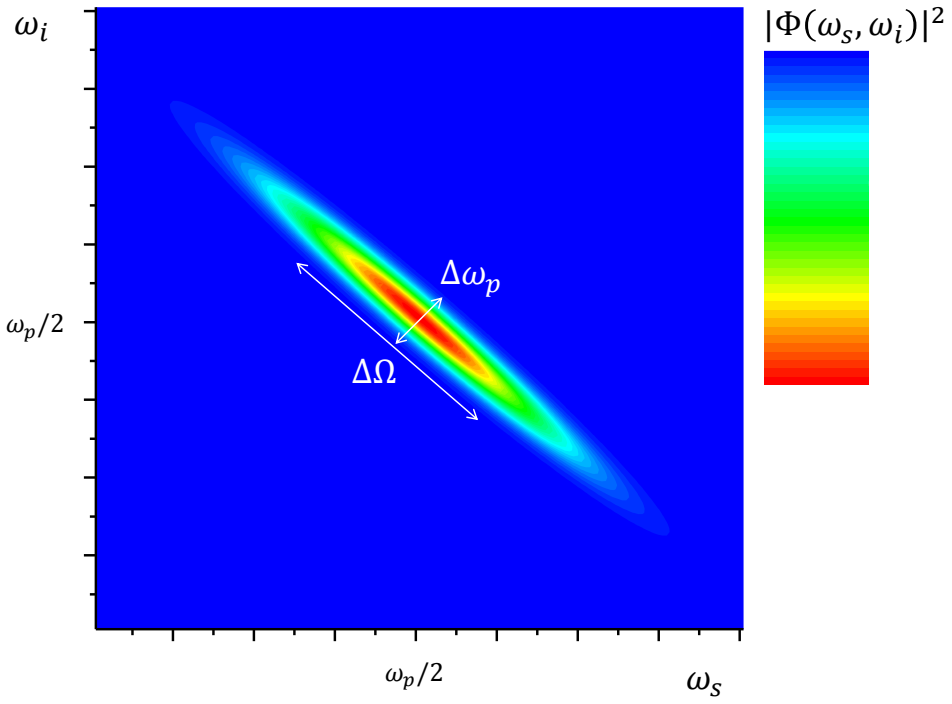

Figure 5.2: The modulus square of the biphoton wavefunction $\Phi(\omega_s, \omega_i)$ is plotted as a function of the signal and idler frequencies ω_s and ω_i. The quantity $\Delta\Omega$ indicates the average spectral bandwidth of the down converted photons. The quantity $\Delta\omega_p$ is the bandwidth of the pump photons.

The function can be viewed as the product of two gaussian distributions, one with a FWHM of $\Delta\Omega$ and the other with a FWHM of $\Delta\omega_p$, tilted by 45° with respect to the ω_i axis. The quantity $\Delta\Omega$ represent the average bandwidth of the generated photons, with mean frequency $\omega_p/2$, i.e, half of the frequency of the pump. Since energy conservation implies that $\omega_p = \omega_s + \omega_i$, the signal and idler frequencies are perfectly anti-correlated. This is reflected in the fact that $|\Phi(\omega_s, \omega_i)|^2$ is titled by 45° degrees. The perfect anti-correlation of the signal and idler frequencies makes the biphoton wavefunction to be not separable, which means that $\Phi(\omega_s, \omega_i)$ can not be expressed as the product of two independent distributions $\Phi(\omega_s)$ and $\Phi(\omega_i)$ which depends only on the frequency of one of the two photons of the pair. This is why the SPDC photon pair is said to be energy or colour entangled. The biphoton wavefunction in Fig.5.2 has also a finite extension $\Delta\omega_p$ along the direction which is transverse with respect to the spectral bandwidth. This seems to violate energy conservation. However, any pump field has always a finite coherence time, which corresponds to a spectral linewidth of $\Delta\omega_p$. This uncertaintly in the energy of the pump reflects in the spectral properties of the down converted radiation. In particular, the effect is to broaden the signal/idler spectral distribution.
Another peculiar property of SPDC process is that the two photons are created simultaneously, i.e., they are time entangled. As shown in Fig.5.3(a), if the pair is firstly separated by a beamsplitter, and then each photon is directed toward single photon detectors, one would measure coincidences in the photodetections. The coincidence measurement is often used to evaluate the degree of entanglement of the down converted radiation [217, 154]. Time and energy entanglement can be exploited in photon heralding, that is, the detection of one of the two photons of the pair heralds the presence of the other and vice versa.

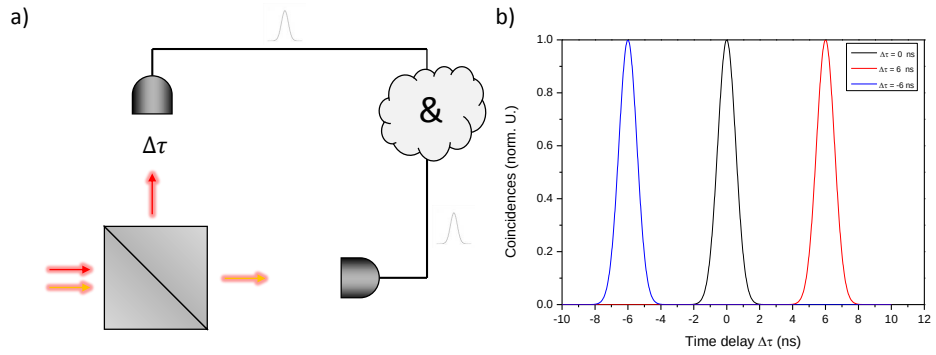

Figure 5.3: (a) A typical coincidence experiment. Signal and idler photons (red and orange arrows) are split by a beamsplitter and directed toward two photodetectors. (b) Coincidences in the photodetections are evaluated as a function of the time delay between the two time traces generated by the detectors. If a time delay $\Delta\tau$ is introduced between the arrival times of the two photons at the photodetectors, then the coincidence peak accordingly shifts from $\Delta\tau = 0$. In this case, the series of pulses registered by one detector is a copy of the time trace of the other detector but shifted by $\Delta\tau$ in time.

5.2 Generation of photon pairs in a periodically poled Lithium Niobate crystal

As introduced at the beginning of this chapter, the lack of integrated quantum sources has been overcome by the use of photon pairs produced by a PPLN crystal. This has been achieved using the experimental apparatus shown in Fig.5.4.

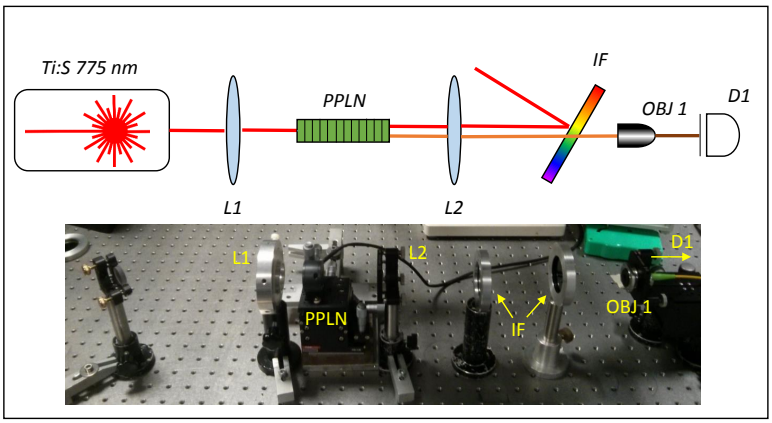

Figure 5.4: (a) Generation stage setup. Ti:S = Titanium Sapphire laser, L1 = Input lens, PPLN = Periodically Poled Lithium Niobate crystal, L2 = Output lens, IF = interference filters (two long wave pass filters with cut-off wavelength 1.5 μm), OBJ = Collection objective for collimation in fiber.

The pump source is a 775 nm Titanium Sapphire laser equipped with an acousto optic modulator that can switch the laser operation from quasi-continuos wave (not mode locked) to mode locked. The laser operates in the first configuration during the experiment. The output beam, of approximately 440 μm waist, has an average power of 1 W and can be regulated using a variable optical attenuator (not shown in Fig.5.4). Two gold mirrors direct the beam into the input converging lens (L1), which has a focal length of 5 cm. The PPLN crystal is placed in the focal plane of the lens, where the beam waist is minimum and equal to $\approx 12\,\mu m$. The

laser intensity at the input facet of the sample is $\approx 0.26\,MW/cm^2$. The PPLN crystal, shown in Fig.5.5(a), is sandwiched between a metal holder and an ITO coated glass.

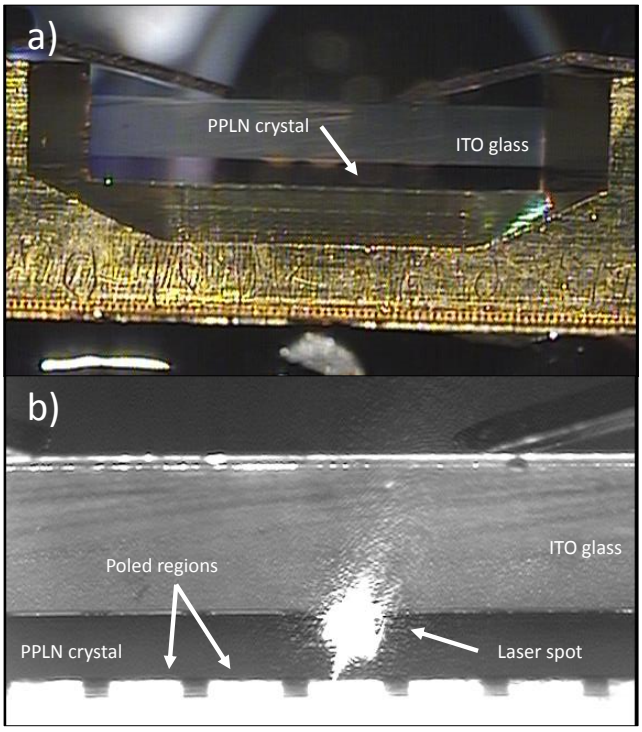

Figure 5.5: (a) Side view of the PPLN crystal. The crystal is completely transparent and is sandwiched between the ITO glass and the metal holder. (b) Enlarged side view of the PPLN crystal, showing the locations of the poled regions (actually a reflection on the metal holder) and the pump laser beam spot.

The crystal contains 9 different poled regions of cross section $500\,\mu m \times 500\,\mu m$ and of length $1\,mm$, some of them are shown in Fig.5.5(b). Each region has a different poling period, which guarantees quasi phase matching in the $760\,nm - 820\,nm$ range of input wavelength. The fine tuning of the phase matching is performed by changing the temperature of the sample with an oven. This is accomplished using a temperature controller (TEC). Temperature slightly changes the refractive index of the material by different amounts at the frequency of the pump and at the frequency of the down converted photons. In this way, Eq.5.5 can be satisfied at different pump wavelengths using the same poling period. The SPDC photons (coming from a type I process, i.e, signal and idler are copolarized) and the $775\,nm$ pump are collected and collimated by a lens of $8.5\,cm$ focal length. Two long wavelength pass filters ($1.35\,\mu m$ of cutoff wavelength) allows to filter out the pump from the Infra-Red light, providing an isolation higher than $100\,dB$. The Infra-Red beam is then coupled into a Single Mode (SM) fiber using a collimator. The latter is connected to a photon counting module (ID Quantique id201). To maximize the coupling efficiency, the collimator can be tilted and translated in all the directions using a micrometric alignment stage. A total loss of $7.8\,dB$ from the output facet of the sample to the SM fiber has been measured.

5.2.1 Source characterization

At first, the PPLN source has been characterized in terms of generation efficiency. Following the guidelines provided by the crystal manufacturier (Covesion Ltd. [215]), it has been verified that the maximum rate of generated photons is found at particular temperatures as reported on the datasheet. Fig.5.6 reports the phase

matching curves as a function of temperature for the 9 different poling periods reported by the manufacturier.

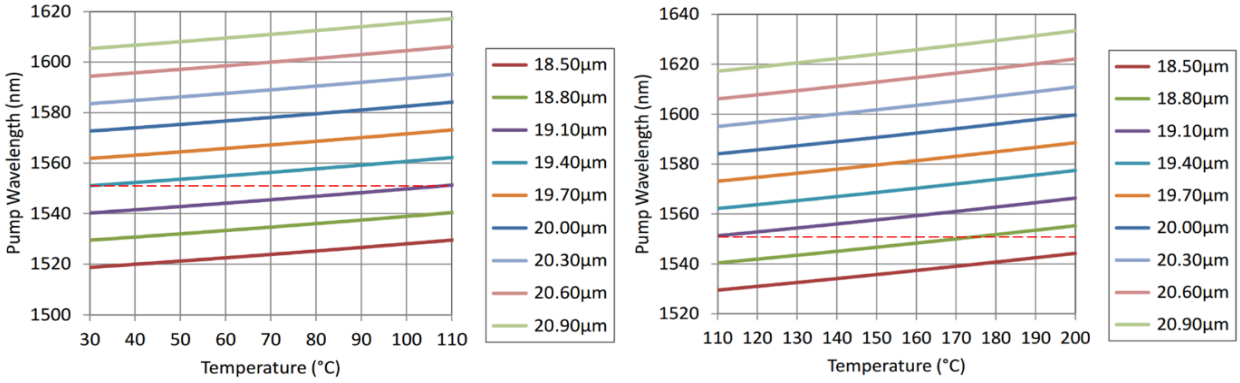

Figure 5.6: Phase matching wavelength as a function of temperature for the 9 different poling periods. The red dashed line indicates the studied wavelength ($1550\,nm$).

For the $775\,nm$ pump, the generation lies at $1550\,nm$, and the maximum efficiency temperatures are listed in Table 5.1. Fig.5.7 shows the measured generation rate as a function of the crystal temperature for 3 poling periods.

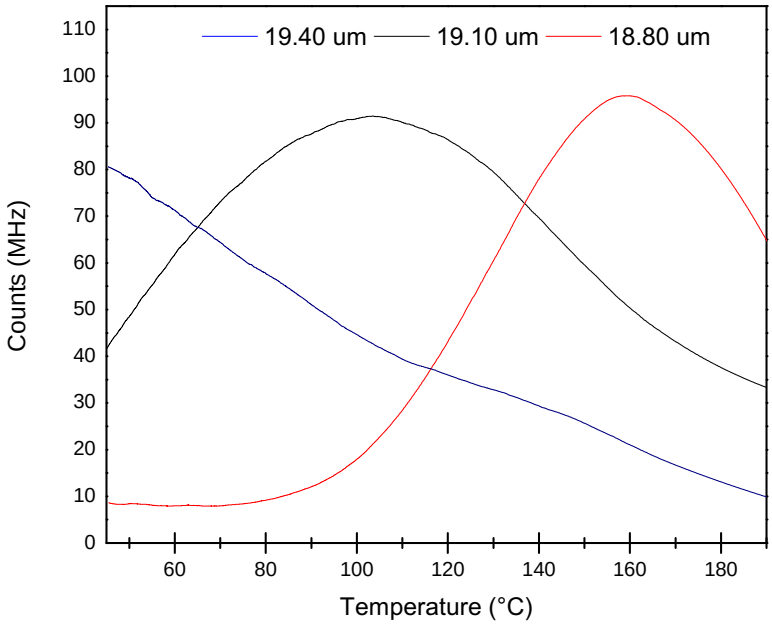

Figure 5.7: Measured generation rate as a function of the crystal temperature for several poling periods: $18.8\,\mu m$, (red) $19.1\,\mu m$ (black) and $19.4\,\mu m$ (blue).

Poling period (μm)	$T_{MAX}^{(th)}$	$T_{MAX}^{(exp)}$
18.8	175	175 ± 1
19.1	105	108 ± 1
19.4	30	< 30

Table 5.1: Temperatures of maximum efficiency for different poling periods. $T_{MAX}^{(th)}$ are the temperatures predicted by the curves in Fig.5.6, $T_{MAX}^{(exp)}$ are the temperatures found in the experiment.

The temperatures of maximum efficiency extracted from the experimental data are very close to the ones reported in the datasheet. The conversion efficiency can be estimated by knowing the pump power, the losses from the output of the sample ($\eta = 7.8\,dB$) toward the photodetector, its detection efficiency (20%) and the measured SPDC photon flux. The pump power has been measured through a thermopile. The generated power has been estimated using the ID Quantique detector. Since the photon counter operates in gated mode at a frequecy of $10\,KHz$ with $100\,ns$ of gate width and no dead time, the measured flux has to be multiplied by a factor 10^3 to take into account the photons which arrive when the detector is blind. Fig.5.8 reports the measured generated power (integrated over all the wavelengths) as a function of pump power.

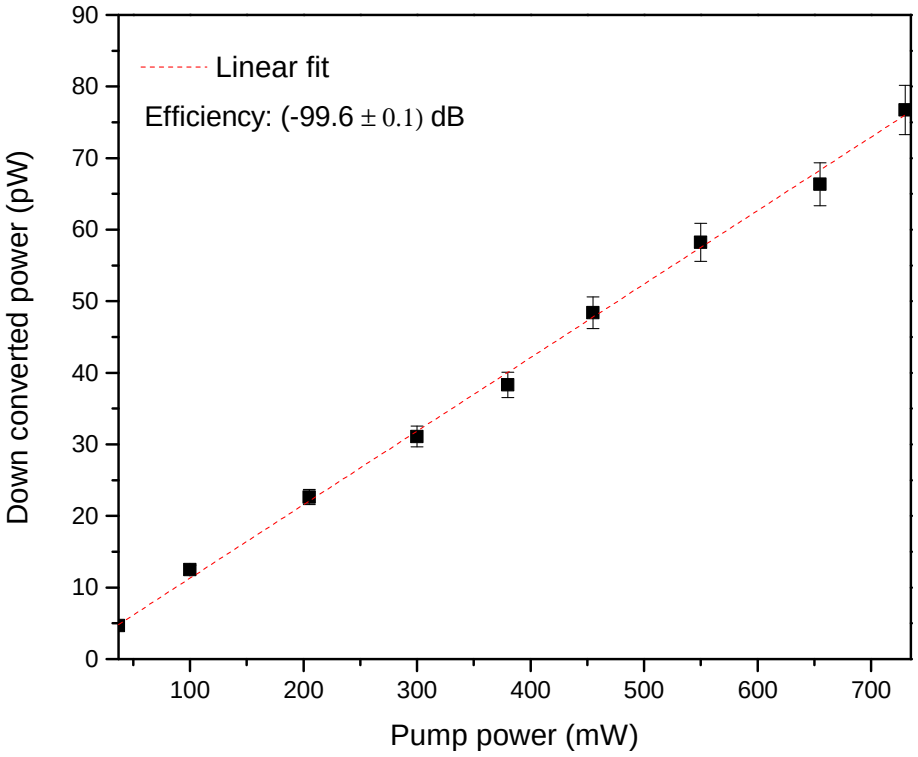

Figure 5.8: Power of the generated SPDC radiation as a function of the input pump power. The slope of the linear fit gives the efficiency of the process.

A linear dependence is found, which agrees with the theoretical predictions of Eq.5.17. A conversion efficiency of $(-99.8 \pm 0.1)\,dB$ is estimated from the slope of the linear fit. In terms of photon flux, the maximum generation rate is $600\,MHz$. Commercial PPLN crystals under similar input conditions predict a SPDC generation efficiency up to $-70\,dB$ [218], which is $30\,dB$ higher then what it has been measured. A possible explanation of such a low generation rate could rely on the very poor quality of the poling of the crystal. Indeed, the microscope image shown in Fig.5.9 reveals that the poling is not perfectly periodic and suffers from several fabrication imperfections (see Fig.5.9(b)). The effect of random imperfections is to lower the amplitudes of the spatial frequencies in the Fourier series in Eq.5.12, and at the same time to add a background of new spatial frequencies (some of them can be phase matched with the input radiation, with the consequence that the spectral width of the generated radiation increases). This effect is known as inhomogeneous broadening [51]). Since the generated power is proportional to the amplitude of these spatial frequencies (see Eq.5.17), the overall efficiency of the process decreases.

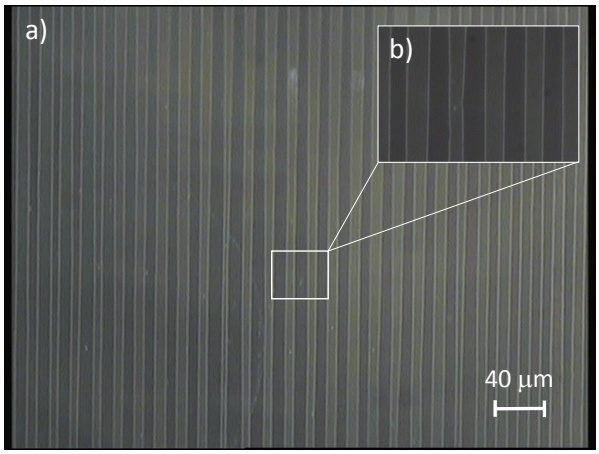

Figure 5.9: a) A microscope image of the 19.4 μm poling period in our sample. b) Details of the poling, revealing fabrication imperfections.

5.2.2 Coincidence measurements

The temperature dependence of the efficiency of the process and the linear relation between the generated power with the input pump indicate that the detected radiation is almost certainly coming from an SPDC process. However, as discussed in Section 5.1.1, in order to have a definitive proof one has to perform a coincidence measurement. This experiment reveals the time entanglement of the pair, which is a distinctive sign of the down converted radiation. To perform the experiment, the setup shown in Fig.5.10 has been implemented.

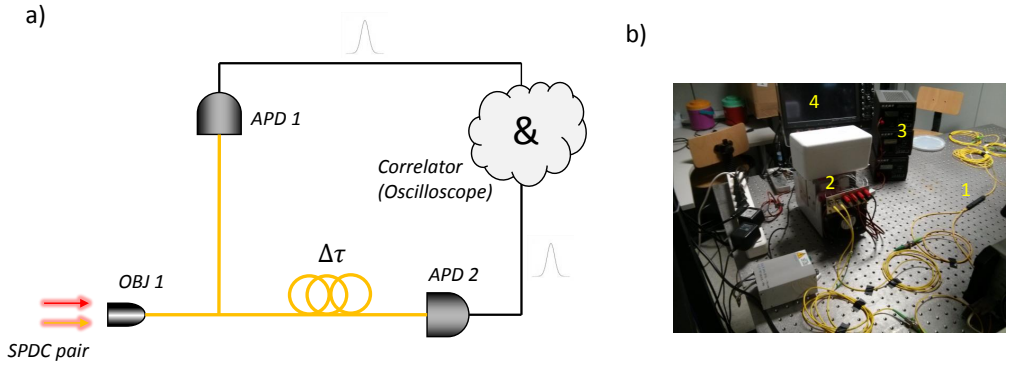

Figure 5.10: a) Schematic of the coincidence measurement setup. (b) A picture of the implemented setup. (1) Fiber beam splitter (2) APD modules (3) Peltier cells current sources (4) Oscilloscope.

The fiber which exits from the collimator OBJ1 in Fig.5.4(a) has been connected to a 3 dB beam splitter. In one of the two outgoing arms has been placed a variable delay line consisting of coils of optical fiber of different lengths. The coil has the effect to delay the arrival time of one photon of the pair with respect to the other. The two outputs were connected to two $InGaAs$ Single Photon Avalance Photodiodes (SPADs) with active home made quenching electronics. The APDs were cooled down to their optimal operating temperature ($-70°C$) using three Peltier cells and liquid nitrogen. The maximum efficiency has been measured to be $\gamma = 5\%$ with 5 MHz of dark counts. The output voltage from the two APDs was sent to a digital oscilloscope.
The post processing functions of the oscilloscope were used for:

1. Squaring the input signal. Each time that a photon was detected, a voltage pulse of about $3\,ns$ duration was generated from the APD. Voltage values going above a fixed threshold were interpreted as ones and voltages below the threshold were interpreted as zeros. At the end of the squaring process, the output consisted of a sequence of square pulses with amplitude one and average width σ.

2. Calculating the cross correlation R_{xy} on the two squared sequences x and y (of $2\,ms$ duration) using the following formula: $R_{xy}(m) = \sum_n^{N-m-1} x_{n+m}y_n$. Here, N is the number of points in a sequence, which is 10^7. The acquisition rate was set to $R = 5\,GS/s$. The calculated cross correlation, divided by σ, gave the number of coincidence events that have been recorded in $2\,ms$ when the two sequences are delayed by m points. The time delay corresponding to m points is m/R.

In order to increase the signal to noise ratio, a number of 500 sequences have been recorded in the same experimental conditions. The presence of spurious periodic correlations due to the gating technique and due to the pump laser oscillations were filtered through a digital filter.
Fig.5.11 shows the coincidence measurement for coil lengths of $L_0 = 0\,m$ (no coil), $L_1 = 6\,m$ and $L_2 = 12\,m$. The associated time delays, calculated as $\Delta\tau_i = \frac{L_i n_g}{c}$ ($n_g \approx 1.45$ for a single mode Silica fiber), are $\Delta\tau_0 = 0\,ns$, $\Delta\tau_1 = 28.8\,ns$ and $\Delta\tau_2 = 57.7\,ns$.

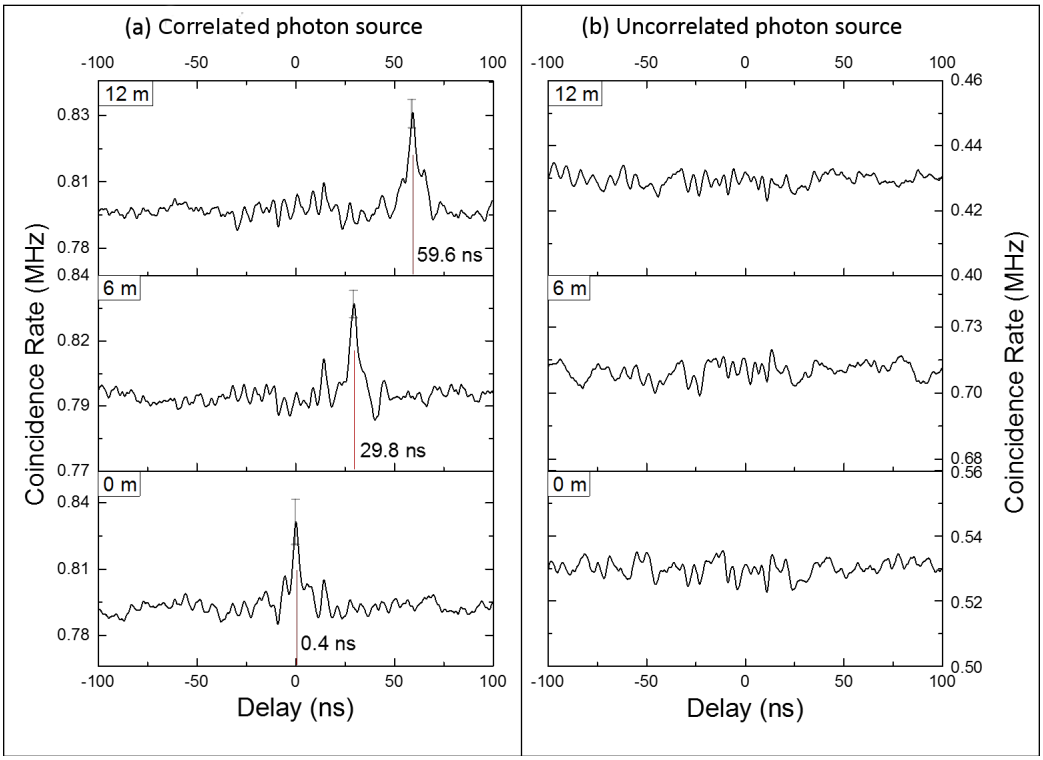

Figure 5.11: Cross correlation curves for several delay line lengths, $0\,m$,$6\,m$, $12\,m$ and 2 different sources: (a) SPDC photons source, (b) Uncorrelated photon source. The grey bar are the error on the maximum. The vertical red dashed lines represent the theoretical delays calculated from the coil lengths L_i and the group index n_g of the fiber.

When no optical delay is inserted between the two APDs (Fig.5.11(a), $0\,m$ panel), the cross correlation curve is found peaked at $0.4\,ns$. This is not zero because of the electronic delay that comes from small differences in the circuitry. If an optical delay is added, the peak shifts to a delay of $29.8\,ns$ and $59.6\,ns$ for the $6\,m$ coil and for the $12\,m$ coil respectively. These values are very close to the theoretical ones calculated starting from the coil length and the fiber group velocity. The width of the coincidence peak is about $\approx 3\,ns$, which is limited

by the time response of the APDs. This means that two photons with arrival times which differ by less than $3\,ns$ are considered as coincident. The coindicence peaks which emerge from the noisy background have an heigth of approximately $(0.04 \pm 0.01)\,MHz$. To check the consistency with the theoretical predictions, one has to find the probability that each photon of the pair reaches the APDs after that the pair splits by the beamsplitter. By denotining with η the losses from the output of the crysytal to the APDs and with γ the APDs efficiencies, this probabability is $P = 0.25 \times (\eta\gamma)^2$, which is the square of the probability that one photon of the pair reaches the APD by travelling in one specific output branch of the beamsplitter. Since the arrival times of photon pairs constitutes a poissonian process, the average coincidence flux is $\Phi_{coinc} = \Phi_{tot}P$, where Φ_{tot} is the flux of photon pairs at the output of the crystal. The curves shown in Fig.5.11 have been recorded with $\Phi_{tot} = 600\,MHz$, thus giving $\Phi_{coinc} = 0.01\,MHz$, which is comparable to the measured flux. Fig.5.11(b) reports the cross correlation curves for an uncorrelated photon source generated from an Amplified Spontaneous Emission (ASE) source with a center wavelength of $1.53\,\mu m$. The photon flux has been regulated to keep the conditions as close as possible to the SPDC case. Also the post processing routine was equal to the one applied to the data shown in Fig.5.11(a). The fact that the cross correlation curves of Fig.5.11(b) did not show any trend ensures that the peaks in Fig.5.11(a) are caused by the time entanglement of the SPDC radiation.

5.2.3 Spectral properties of the generated radation

A common feature of interferometric structures which are based on amplitude division (Mach Zehnder interferometer, Michelson interferometer) is that the input radation E_{in} is, first, split into two beams αE_{in} and βE_{in}, which are then recombined at the output of the device with a time delay $\Delta\tau$. The amplitude of the disturbance E_{out} at the output is $E_{out}(t) = \alpha E_{in}(t) + \beta E_{in}(t + \Delta\tau)$ (the disturbance is assumed to be normalized in such a way that $|E_{in}|^2$ represents the light intensity). Since the photodetectors only respond to a time average of the intensity, the photocurrent J is proportional to:

$$J \propto \left\langle |E_{out}(t)|^2 \right\rangle \propto I_\alpha + I_\beta + 2Re\left[\alpha\beta^* \left\langle E_{in}(t)E_{in}(t+\Delta\tau)^* \right\rangle\right] \tag{5.20}$$

in which $\langle\rangle$ denotes the time averaging operation and $I_{\alpha,\beta} = \left\langle |E_{\alpha,\beta}|^2 \right\rangle$ are the intensities of the two beams. The time averaging process has to be interpreted as:

$$\langle E \rangle = \frac{1}{T} \int_{-T/2}^{T/2} E(t)dt \tag{5.21}$$

in which T is a time window much larger than the time scales over which the optical field fluctuates. It comes out from Eq.5.20 that the ability to create interference fringes as a function of the time delay $\Delta\tau$ is related to the term $2Re\left[\alpha\beta^* \left\langle E_{in}(t)E_{in}(t+\Delta\tau)^* \right\rangle\right]$. One can define the first order correlation function $G^{(1)}(\Delta\tau)$ as:

$$G^{(1)}(\Delta\tau) = \langle E(t)E(t+\Delta\tau)^* \rangle \tag{5.22}$$

In writing Eq.5.22 it has been tacitly assumed that $E(t)$ is a stationary ergodic process, so that $G^{(1)}$ is a function only of the time delay $\Delta\tau$ and the ensemble averages can be replaced by time averages as in Eq.5.21 [219]. From a comparison between Eq.5.20 and Eq.5.22, it can be seen that the range of $\Delta\tau$ in which the function $G^{(1)}$ is appreciabily different from zero coindices with the range in which interference effects can be observed. This range can be defined more precisely as $|\Delta\tau| < \tau_c$, in which τ_c is called the coherence time of the radiation and is defined as:

$$\tau_c = \frac{1}{|G^{(1)}(0)|^2} \int_{-\infty}^{+\infty} |G^{(1)}(\Delta\tau)|^2 d(\Delta\tau) \tag{5.23}$$

It is clear that the knowledge of the coherence time of the radiation is essential for properly designing any interferometric structure. From reasons that will be clear in section 5.3.1, the design of an interferometer which is capable of spanning a time delay greately exceeding τ_c allows to reveal interference effects which have no classical analogue. The magnitude of τ_c can be extracted from the knowledge of the spectra of the radiation. The spectra $S(\omega)$ is defined as:

$$S(\omega) = \frac{1}{T} \lim_{T\to\infty} \left\langle |V_T(\omega)|^2 \right\rangle \tag{5.24}$$

where V_T is the truncated Fourier transform of the electric field $E(t)$:

$$V_T(\omega) = \frac{1}{T} \int_{-T/2}^{T/2} E(t) e^{-i\omega t}\, dt \tag{5.25}$$

A relation exists between $S(\omega)$ and $G^{(1)}(\Delta\tau)$, and is given by the Wiener-Khinchin theorem [219]:

$$S(\omega) = \int_{-\infty}^{\infty} G^{(1)}(\Delta\tau) e^{-i\omega\Delta\tau}\, d(\Delta\tau) \tag{5.26}$$

By inserting Eq.5.26 into Eq.5.23 and by integrating with respect to $\Delta\tau$, one obtains:

$$\tau_c = \frac{1}{|G(0)|^2} \int_{-\infty}^{\infty} |S(\omega)|^2\, d\omega \tag{5.27}$$

By defining the spectral width of the radiation as:

$$\Delta\nu = \frac{|G(0)|^2}{\int_{-\infty}^{\infty} |S(\omega)|^2\, d\omega} \tag{5.28}$$

one obtain the final relation:

$$\tau_c = \frac{1}{\Delta\nu} \tag{5.29}$$

Eq.5.29 tells that by measuring the spectral width of the radiation, one can extract the related coherence time. The measure of the spectral width can be done by using an OSA. However, this task can not be easily accomplished because the noise level of commercial OSA are of the order of $-90\,dBm$ ($1\,pW$), which is very close to the power of the generated radiation (see Fig.5.8). No signal has been detected by the OSA with the pump power set to its maximum value ($1\,W$), which means that the nearly $100\,pW$ of generated power shown in Fig.5.8 is spread in wavelength (so as the resulting spectral density, which is the quantity that actually measures the OSA, is lower than the noise limit). To overcome this limitation, the experimental setup shown in Fig.5.12 has been implemented.

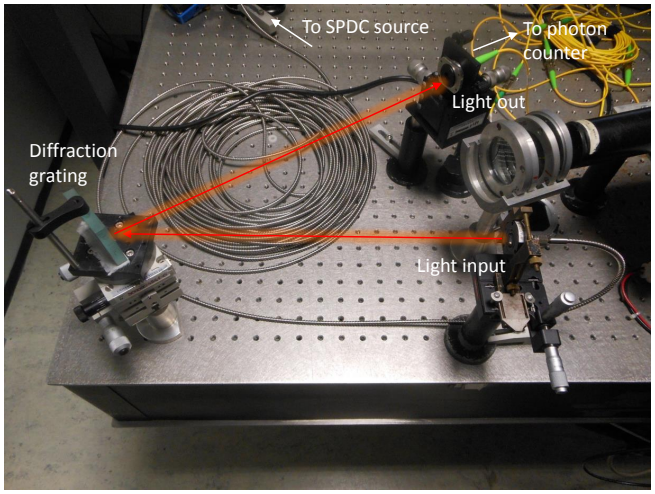

Figure 5.12: The setup implemented for measuring the spectra of the down converted radiation.

The SPDC radiation which exits out from the multimode fiber is collimated using a microlens objective and then sent to a blazed diffraction grating. The latter can rotate by means of micrometric screws. The dispersed light is then coupled to a fixed fiber collimator, interfaced with a photon counting module. The use of a photon counter allows to detect signals as small as $-120\,dBm$. By rotating the screw, the spectrum of the radiation can be recorded. The system has been calibrated using a tunable infrared laser. In Fig.5.13 the spectra of the radiation is reported for two different poling periods ($\Lambda = 19.4\,\mu m$ and $\Lambda = 19.1\,\mu m$) and various temperatures. The variable detection efficiency of the photon counter as a function of the wavelength has been taken into account for correcting the recorded photon flux.

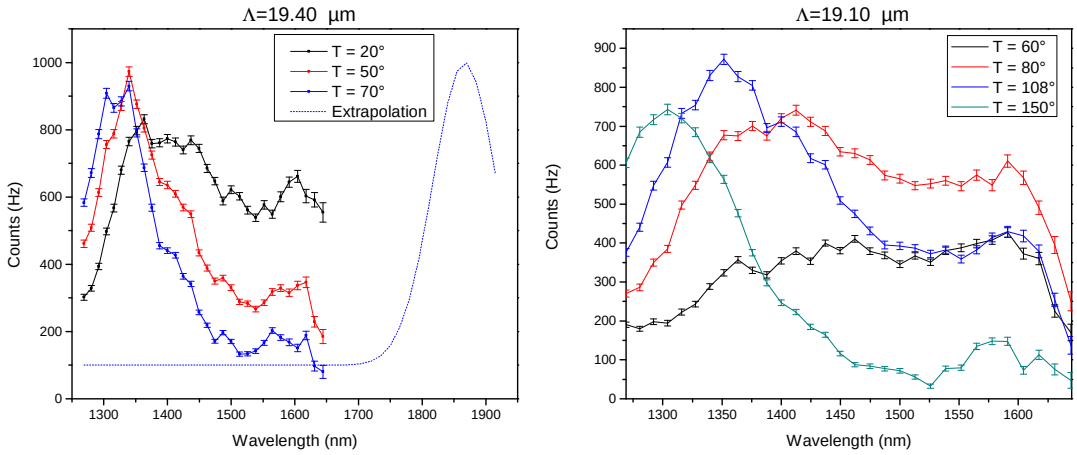

Figure 5.13: Spectra of the SPDC photons for two different poling periods and for different temperatures. The dashed blue line in the spectra relative to the $19.4\,\mu m$ poling period indicates the position of the idler peak, which lies in a wavelength interval that can not be detected by the photon counter.

It is evident that the spectra are quite broad, especially for the $19.1\,\mu m$ poling of at low temperatures. In this case, the average power integrated over $1\,nm$ of bandwidth (which is the minimum resolution that can be set in the OSA of the laboratory) is $-100\,dBm$, far below the noise lovel of the instrument. This justifies the fact that it was not possible to detect any signal by sending directly the SPDC radiation to the OSA. The $19.4\,\mu m$ poling generates a down converted radiation which is strongly not degenerate. A band, placed on the blue side of the $1.55\,\mu m$ degenerate wavelength, has been recorded. The band is approximately peaked at

$1325\,nm$, and corresponds to the signal photons. A wavelength of $1867\,nm$ for the idler peak can be evaluated by Eq.5.1. The idler peak lies in a wavelength interval which can not be detected by the photon counter, since its detection efficiency has a cut off at $1600\,nm$. For the $19.1\,\mu m$ poling period, the raise in temperature has the effect to shift the SPDC signal from a nearly degenerate emission ($T = 60°C$) to a non degenerate one. A signal band is observed as the temperature increases. It may be pointed out that the spectra which are relative to the $19.1\,\mu m$ poling are not symmetric with respect to the degenerate wavelength. In particular, it seems that some power is lacking on the red side. This is probably due to the fact that it has not been possible to measure the detection efficiency of the photon counter at wavelengths above $1600\,nm$, which has been then extrapolated from the instrument datasheet. This procedure probably overestimated the detection efficiency, so the spectral power relative to this wavelength range is probably higher than the one reported in Fig.5.13. In the experiment described in Section 5.3, SPDC photons are emitted from the crystal region with a poling period of $19.1\,\mu m$ when the operating temperature was set to $T = 80°C$. In order to have a rough estimation of the coherence time of the radiation, the spectra has been approximated by a box function of approximately $\Delta\lambda = 300\,nm$ width and centered at $\lambda_c = 1.475\,\mu m$, which gives $\tau_c = \Delta\nu^{-1} = \frac{\lambda_c^2}{c\Delta\lambda} \approx 24\,fs$. The box-like approximation is justified from the fact that the spectrum is bandwidth limited by the high frequency cut-off provided by interference filters in Fig.5.4 at $1.35\,\mu m$, and by the low frequency cut-off provided by the detection efficiency of the photon counters at $1.6\,\mu m$. As it will be shown in Section 5.3, this approximation gives a coherence time which is very close to the one measured through an interferogram.

5.3 One and two photon interference in a free space Mach Zenhder Interferometer

The interferometric structure which allowed to perform the first quantum optics experiment of the project SIQURO is the Mach Zenhder Interferometer The choice has been dictated from the fact that, despite the simplicity of the geometry, the MZI is a versatile and effective tool for the manipulation of entangled states of light. The setup has been entirely realized in free space, but the same theory and experimental results are expected in an integrated MZI. In this sense, the experiment has been preparatory for the next developements of the SIQURO project, for which on chip quantum interference has to be demonstrated. In this section, the theory of the device operation is firstly presented and the probability of recording a coincidence detection of SPDC photons is derived in terms of the parameters of the MZI. The novelties with respect to previously reported experiments in the literature are highlighted [220, 221, 222, 223]. The experimental setup and the results are discussed at the end of the section.

5.3.1 Theory of the MZI excited by SPDC photons

The sketch of the MZI is shown in Fig.5.14.

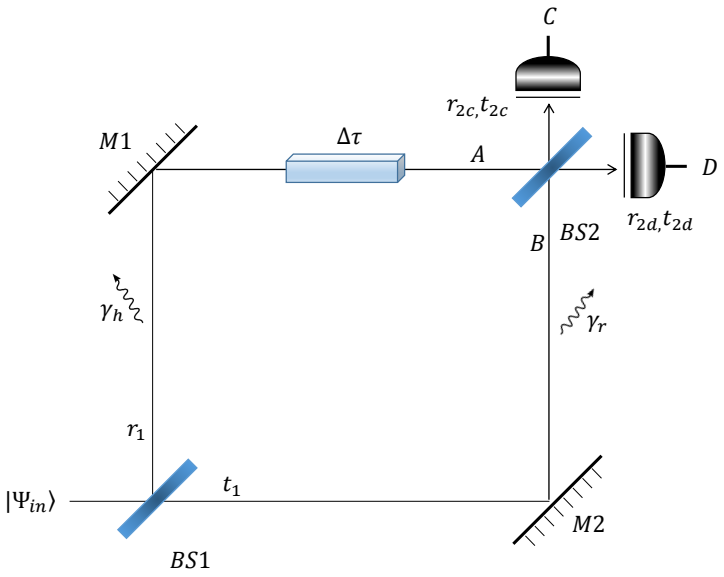

Figure 5.14: A sketch of the MZ device.

The input radiation state $|\Psi_{in}\rangle$ is sent into a single input port of the first beamsplitter ($BS1$). By using only one input port, it is possible to probe a wider range of interference effects than if both input ports are used, as discussed below. The asymmetric excitation constitutes one of the main differences with respect to previously reported experiments, in which both the input ports were excited [220, 221, 222, 223]. After exiting BS1, the light propagates along the MZ arms. The latter have different optical paths, which reduces to a time delay$\Delta\tau$, and different propagation loss γ_h and γ_r. The subscripts r and h stand for Reference and Heater respectively. This is because in the experimental implementation of the device, discussed in section 5.3.2, the time delay $\Delta\tau$ is changed using an electrical heater. Light is then recombined at the second beamsplitter ($BS2$) before being collected by photodetectors C and D. The beasmplitters transform the input fields to the output fields according to [222]:

$$BS1 \rightarrow \begin{pmatrix} r_1 e^{-i\delta} & t_1 \\ t_1 & r_1 e^{-i\delta} \end{pmatrix}, \qquad BS2 \rightarrow \begin{pmatrix} r_{2c} e^{-i\delta} & t_{2c} \\ t_{2d} & r_{2d} e^{-i\delta} \end{pmatrix} \tag{5.30}$$

where the coefficients r_i and t_i are real, and represent the amplitude reflectivity and transmittivity of the BS respectively. For simplicity, it has been assumed that r_i and t_i do not depend on frequency. The operation of $BS1$ is taken to be symmetric, while that of $BS2$ may be different for the light collected by detector C or D, as indicated by the second subscript c, d. In this way, the reflectivity from A to C (r_{2c}) can be different with respect to the reflectivity from B to D (r_{2d}). It is worth to note that, in the modeled experiment, such asymmetry is not attributed to an intrinsic unbalance of the $BS2$ transmittance/reflectance, but rather to controlled misalignments of the detectors C and D with respect to the transmitted/reflected beams from $BS2$. As it will be showed, these coefficients control the amplitude of various photon interference effects and so this controlled asymmetry can be used to tune between different regimes. In the beamsplitter relation of Eq.5.30, a relative phase between the reflection and transmission coefficients exists. For an ideal lossless beamsplitter, the relative phase must be equal to $\pi/2$, as required by energy conservation [224]. However, as derived by Barnett et. al. [225], this stringent phase condition may be relaxed when a beamsplitter is intrinsically lossy. This will be discussed in further detail in section 5.3.1.2. For simplicity, it has been assumed that the relative phase is identical and symmetric for both beamsplitters; this is reasonable for this experiment, as the controlled asymmetry for $BS2$ introduced above affects the amplitude but not the phase

of the light collected. To study photon interference, the coincidence rate of photons arriving at the two photodetectors is calculated. The photodetectors operate with a time resolution T_R. The probability of a joint photodetection at time t and $t+\tau$ is described by the second-order correlation function [222]:

$$g^{(2)}(t,\tau) = K\left\langle E_d^-(t)E_c^-(t+\tau)E_c^+(t+\tau)E_d^+(t)\right\rangle \tag{5.31}$$

where $E_c^+(E_c^-)$ and $E_d^+(E_d^-)$ are the positive(negative) frequency parts of the electric field operator at the output of $BS2$ at the C and D detectors respectively. Here K is a constant that has to be tailored on the experiment. The expectation value is evaluated with respect to the input radiation state $|\Psi_{in}\rangle$. Eq.5.31 is the quantum mechanical generalization of the classical intensity correlation function $g_{cl}^{(2)}(t,\tau) = \langle I(t)I(t+\tau)\rangle$, where $I(t)$ denotes the light intensity at time t and the operator $\langle\rangle$ denotes the time averaging operation of Eq.5.23. Combining Eq.5.31 with the beamsplitter relations in Eq.5.30, it is possible to write the electric fields E_c^- and E_d^- as:

$$\begin{aligned} E_c^-(t) &= r_1\gamma_h r_{2c}e^{-i2\delta}E_{in}^-(t-\Delta\tau) + t_1\gamma_r t_{2c}E_{in}^-(t) \\ E_d^-(t) &= t_1\gamma_r r_{2d}e^{-i\delta}E_{in}^-(t) + r_1\gamma_h t_{2d}e^{-i\delta}E_{in}^-(t-\Delta\tau) \end{aligned} \tag{5.32}$$

where E_{in}^- is the negative frequency part of the input electric field operator at $BS1$. From these expressions, it is possible to calculate the second order correlation function $g^{(2)}(t,\tau)$, and hence the photon coincidence rate, provided that the input radiation state is specified. For SPDC photons, the expression is given by Eq.5.19. In what follows, the pump will be assumed to be monochromatic, since its linewidth $\Delta\omega_p$ is much narrower than the one of the generated radiation. The biphoton wavefunction in Fig.5.2 becomes then a straight line. In this way, it is possible to exploit the energy conservation relation of Eq.5.1 to express the frequency of one photon as ω and the frequency of the twin photon as $\tilde{\omega}-\omega$, where $\tilde{\omega}$ is the frequency of the pump. Using this property, the input radiation field can be written as:

$$|\Psi_{in}\rangle = \int \Phi(\omega)a_{\tilde{\omega}-\omega}^\dagger a_\omega^\dagger |0\rangle\, d\omega \tag{5.33}$$

where $a_\omega^\dagger$ denotes the creation operator of a photon at frequency ω at the input port of $BS1$ and $\Phi(\omega)$ is the biphoton wavefunction. The latter is assumed to be of Gaussian-like distribution:

$$\phi(\omega) = Ne^{-\frac{(\omega-\tilde{\omega}/2)^2}{2\sigma^2}} \tag{5.34}$$

centred at the degenerate frequency $\tilde{\omega}/2$ with bandwidth $\sigma = \frac{1}{\tau_c}$, where τ_c represent the coherence time of each photon. Here, N is a normalization constant which can be determined by using the fact that $\int |\Phi(\omega)|^2\, d\omega = 1$. By inserting a completeness relation between $E_c^+(t)$ and $E_c^+(t+\tau)$ in Eq.5.31, and by using Eq.5.32, one gets:

$$\begin{aligned} g^{(2)} = K\Big|&\gamma_{hc}\gamma_{rd}e^{-i3\delta}\left\langle E_{in}^-(t)E_{in}^-(t+\tau-\Delta\tau)\right\rangle + \\ &+ \gamma_{rd}\gamma_{rc}e^{-i\delta}\left\langle E_{in}^-(t)E_{in}^-(t+\tau)\right\rangle \\ &+ \gamma_{hc}\gamma_{hd}e^{-i3\delta}\left\langle E_{in}^-(t-\Delta\tau)E_{in}^-(t+\tau-\Delta\tau)\right\rangle \\ &+ \gamma_{hd}\gamma_{rc}e^{-i\delta}\left\langle E_{in}^-(t-\Delta\tau)E_{in}^-(t+\tau)\right\rangle\Big|^2 \end{aligned} \tag{5.35}$$

where the expectation values are now evaluated between the initial state $|\Psi_{in}\rangle$ and the vacuum state $|0\rangle$, i.e, $\langle E_{in}^-(t)E_{in}^-(t')\rangle = \langle\Psi_{in}|\, E_{in}^-(t)E_{in}^-(t')\,|0\rangle$. In Eq.5.35 the following parameters have been introduced:

$$\begin{aligned} \gamma_{hc} &= r_1\gamma_h\, r_{2c} \quad & \gamma_{hd} &= r_1\gamma_h\, t_{2d} \\ \gamma_{rc} &= t_1\gamma_r\, t_{2c} \quad & \gamma_{rd} &= t_1\gamma_r\, r_{2d} \end{aligned} \tag{5.36}$$

where the subscript h, r refers to the path along the upper or lower arm of the interferometer respectively, while subscript c, d denotes whether the photon arrives at detector C or D. The expectation values in Eq.5.35 can be evaluated by using the Fourier representation of the negative frequency part of the input electric field:

$$E_{in}^{-}(t) = \int a_{\omega}^{\dagger} e^{i\omega t} d\omega \tag{5.37}$$

and hence that:

$$\langle E_{in}^{-}(t) E_{in}^{-}(t')\rangle = 2\phi(t-t')e^{i\bar{\omega}t'} \tag{5.38}$$

where $\phi(t)$ is the Fourier transform of $\phi(\omega)$. Substituting Eq.5.38 into Eq.5.35, it is obtained that $g^{(2)} = K|p_{h,h} + p_{r,r} + p_{h,r}^{(R)} + p_{h,r}^{(T)}|^2$, where:

$$p_{h,h} = 2N^2\gamma_{hc}\gamma_{hd}\, \exp\left[-i\left(\bar{\omega}\Delta\tau + 3\delta\right)\right] \exp\left(-\frac{\sigma^2\tau^2}{2}\right) \tag{5.39}$$

$$p_{r,r} = 2N^2\gamma_{rc}\gamma_{rd}\, \exp\left(-i\delta\right) \exp\left(-\frac{\sigma^2\tau^2}{2}\right) \tag{5.40}$$

$$p_{r,h}^{(R)} = 2N^2\gamma_{hc}\gamma_{rd}\, \exp\left[-i\left(\frac{\bar{\omega}\Delta\tau}{2} + 3\delta\right)\right] \exp\left(-\frac{\sigma^2(\tau-\Delta\tau)^2}{2}\right) \tag{5.41}$$

$$p_{r,h}^{(T)} = 2N^2\gamma_{hd}\gamma_{rc}\, \exp\left[-i\left(\frac{\bar{\omega}\Delta\tau}{2} + \delta\right)\right] \exp\left(-\frac{\sigma^2(\tau+\Delta\tau)^2}{2}\right) \tag{5.42}$$

Eqs. 5.39-5.42 are the transition amplitudes associated with the indistinguishable paths through which the photon pair can propagate from the input of *BS1* to the photodetectors, as sketched schematically in the grey shaded region of Fig.5.15.

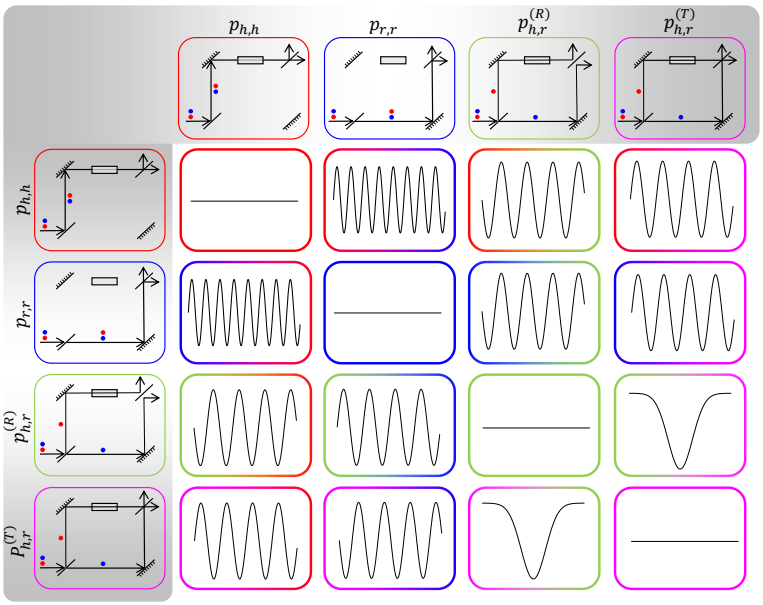

Figure 5.15: A summary of the interference terms between all the possible paths leading to a coincidence photodetection. The paths are sketched in the panels with a gray shaded background. From left to right, in the uppermost row, these are: $(p_{h,h})$ both photons are reflected in the upper arm, $(p_{r,r})$ both photons are transmitted in the lower arm, $(p_{h,r}^{(R)})$ photons are split by *BS1* and reach the detectors by two reflections at *BS2*, $(p_{h,r}^{(T)})$ photons are split by *BS1* and reach the detectors by two transmission at *BS2*. The transition amplitudes associated with the paths are given in Eq.5.39-5.42. The main entries of the table sketch the resulting contribution to the correlation function from the interference of these paths as a function of $\Delta\tau$, where the integration in τ has been performed as described in the main text. By proceeding from left to right, for example, the panels in the second row represent contributions from $|p_{h,h}|^2$, $p_{h,h}^* p_{r,r}$, $p_{h,h}^* p_{h,r}^{(R)}$ and $p_{h,h}^* p_{h,r}^{(T)}$.

As it can be seen, the amplitudes $p_{h,h}$ and $p_{r,r}$ refer to bunching, when both photons are either reflected or transmitted by *BS1*. On the other hand, the amplitudes $p_{h,r}^{(R)}$ and $p_{h,r}^{(T)}$ describe anti-bunching, when the photon pair is split at *BS1*. In these cases, the superscript R, T denotes respectively the cases in which the photons are both either reflected or transmitted at *BS2*. It is important to emphasise that the antibunching paths $(p_{h,r}^{(T,R)})$ are not generally allowed when both input ports of *BS1* are excited, due to the Hong Ou Mandel (HOM) effect at the first beamsplitter [226]. The HOM manifests when two indistinguishable photons simultaneously enter at both the input ports of a BS. The amplitude probabilities associated with the cases in which both photons are reflected or both photons are transmitted, which would crate an antibunchin state, undergoes completely destructive interference due to photon indistinguishability. The result is that the pair is never split, and both photons exit together from one of the two output ports, with equal probability. By exciting the input BS from a single input port, it is therefore possible to explore a richer interplay of interference effects where the photon pair can travel along both antibunching and bunching paths. To calculate the correlation function $g^{(2)}$, one has to square the sum of all the transition amplitudes in Eqs.5.39-5.42, and integrate τ over the coincidence resolving time of the photodetectors T_R. As can be seen from the expressions above, each amplitude vanishes when τ is much greater than the photon coherence time $\tau_c = 1/\sigma$, while for all practical experiments $T_R \gg \tau_c$. Hence, the integration over τ can be effectively extended from $-\infty$ to ∞, to finally obtain:

$$g^{(2)}(\Delta\tau) = K'(C_1 + C_2 + C_3) \tag{5.43}$$

where K' includes all the constants. The three terms on the right hand side are defined as follows:

$$C_1 = \gamma_{hc}^2\gamma_{rd}^2 + \gamma_{hd}^2\gamma_{rc}^2 + 2A_{\tilde{\omega}}\, e^{-\sigma^2\Delta\tau^2}\cos(2\delta) \tag{5.44}$$

$$C_2 = \gamma_{hc}^2\gamma_{hd}^2 + \gamma_{rc}^2\gamma_{rd}^2 + 2A_{\tilde{\omega}}\cos(\tilde{\omega}\Delta\tau - 2\delta) \tag{5.45}$$

$$C_3 = 2e^{-\frac{\sigma^2\Delta\tau^2}{4}}\left(A^{(1)}_{\tilde{\omega}/2}\cos\Big(\frac{\tilde{\omega}\Delta\tau}{2} + 2\delta\Big) + A^{(2)}_{\tilde{\omega}/2}\cos\Big(\frac{\tilde{\omega}\Delta\tau}{2}\Big)\right) \tag{5.46}$$

where the following parameters have been introduced:

$$A_{\tilde{\omega}} = \gamma_{rc}\gamma_{rd}\gamma_{hc}\gamma_{hd} \tag{5.47}$$

$$A^{(1)}_{\tilde{\omega}/2} = \gamma_{hc}\gamma_{rc}(\gamma_{rd}^2 + \gamma_{hd}^2) \tag{5.48}$$

$$A^{(2)}_{\tilde{\omega}/2} = \gamma_{hd}\gamma_{rd}(\gamma_{hc}^2 + \gamma_{rc}^2) \tag{5.49}$$

It will also be convenient to introduce the power-amplitude coefficient $A_{\tilde{\omega}/2}$ associated with the frequency component at $\tilde{\omega}/2$:

$$A^2_{\tilde{\omega}/2} = \Big(A^{(1)}_{\tilde{\omega}/2}\Big)^2 + \Big(A^{(2)}_{\tilde{\omega}/2}\Big)^2 + 2A^{(1)}_{\tilde{\omega}/2}A^{(2)}_{\tilde{\omega}/2}\cos(2\delta) \tag{5.50}$$

In Eqs.5.44-5.46, it has been grouped into $C_{1,2,3}$ those terms which arise respectively from the interplay of antibunching with antibunching paths; of bunching with bunching paths; and of antibunching with bunching paths. These various combinations are illustrated schematically in the table of Fig.5.15, where the photon paths are shown in the first gray-shaded row and column, and the resulting terms in $g^{(2)}(\Delta\tau)$ are sketched in the main entries of the table. For example, all terms on the diagonal of this table represent the interference of a two-photon path with itself and hence are independent of the delay $\Delta\tau$ and are depicted as a constant contribution. As illustrated in the four bottom-right entries of Fig.5.15, the interplay of antibunching with antibunching terms in Eq.5.44 includes the characteristic Hong Ou Mandel dip in the coincidence due to the destructive interference of the two different antibunching paths at the second beamsplitter. This reduction in the coincidence is largest when the time delay between the two arms of the MZ is equal to zero, i.e when it is reached the optical contact of the interferometer. Note that here the term $\cos(2\delta)$ is assumed to be negative, which is appropriate both for a lossless beamsplitter and for the lossy beamsplitters in the experiment discussed later. As it can be seen in the four top-left main panels of Fig.5.15, the interaction between the two different bunching paths leads to fringes at a frequency which is doubled with respect to the average frequency $\tilde{\omega}/2$ of the two photons. By looking at Eq.(5.45), it comes out that these oscillations persist even when the time delay $\Delta\tau$ exceeds the single-photon coherence time τ_c. As discussed in Section 5.2.3, classical interference is expected to vanish at time delays exceeding the coherence time of the radiation. These therefore are two-photon interference effects arising from the colour-entanglement of the SPDC radiation, which is a purely quantum mechanical effect. Finally, in the top-right and bottom-left entries of Fig.5.15, the interplay between the antibunching and bunching paths leads to terms which oscillate at the photon average frequency $\tilde{\omega}/2$. As can be seen from Eq.5.46, these terms are damped out as $\Delta\tau$ increases beyond τ_c, and can be assimilated to single photon interference effects. The equivalence comes from the fact that the phase difference between the bunching and the antibunching cases is always $(\tilde{\omega}/2)\Delta\tau$. In fact, from the comparison of the paths $p_{r,r}$ (or $p_{h,h}$) with the paths $p^T_{h,r}$ (or $p^R_{h,r}$) in Fig.5.15, one can notice that there is always one arm of the interferometer which carries one more photon with respect to the other. The same happens when a single photon enters at the input of *BS1*: it can take either the lower arm or the upper one, giving a

relative phase of $(\tilde{\omega}/2)\Delta\tau$ between the two paths. The combination of all of these terms into Eq.(5.43) leads to a complicated coincidence pattern which will, in general, contain features from both the two-photon and single-photon interference. The strength of the different oscillating terms is respectively measured by the terms $A_{\tilde{\omega}}$ and $A_{\tilde{\omega}/2}$ in Eqs.5.47-5.50. Their ratio

$$\xi = \frac{A_{\tilde{\omega}/2}}{A_{\tilde{\omega}}} \tag{5.51}$$

will be called the *unbalancing parameter*, and it will be used in the following to quantify the relative magnitude of these effects.

5.3.1.1 SPDC Light in a MZ Interferometer with Lossless Beamsplitters

To understand the different physical regimes, let's consider the simplest case of ideal lossless beamsplitters. Then the relative phase of the reflection and transmission coefficients in the beamsplitters is set by energy conservation as $\delta = \pi/2$ [225, 224]. Consequently, the unbalancing parameter simplifies to:

$$\xi = \frac{A_{\tilde{\omega}/2}}{A_{\tilde{\omega}}} = \frac{(\gamma_{hc}\gamma_{rd} - \gamma_{rc}\gamma_{hd})(\gamma_{hc}\gamma_{hd} - \gamma_{rc}\gamma_{rd})}{\gamma_{rc}\gamma_{rd}\gamma_{hc}\gamma_{hd}} \tag{5.52}$$

and the two limits of $\xi = 0$ and $\xi \to \infty$ can be straightforwardly considered. In the limit when $\xi = 0$, antibunching-bunching interactions undergo complete destructive interference, and the single-particle-like features disappear from the coincidence pattern. This happens if some symmetries are imposed on the lossess of the MZ arms or on the beamsplitter coefficients. The simplest example is when both the beamsplitters are $50:50$ devices and the two arms have identical loss rates, which implies $\gamma_{hc} = \gamma_{hd} = \gamma_{rc} = \gamma_{rd}$ and $A_{\tilde{\omega}/2} = 0$. Thus, only one frequency is observed when the device is ideal and symmetric, which is consistent with what was found in previous works [220, 221]. Other three configurations exist for which $\xi = 0$:

1. If *BS2* is balanced, so that $\gamma_{hc} = \gamma_{hd}$ and $\gamma_{rd} = \gamma_{rc}$.
2. If *BS1* is balanced while the γ_r and γ_h lossess are also equal, so that $\gamma_{hc} = \gamma_{rc}$ and $\gamma_{rd} = \gamma_{hd}$.
3. If the transmittance from the input to port C along the upper arm is equal to the transmittance to port D along the lower arm (i.e. $\gamma_{rd} = \gamma_{hc}$) or vice-versa ($\gamma_{hd} = \gamma_{rc}$).

In the opposite limit of $\xi \to \infty$, the $g^{(2)}$ function will show no features of two-photon correlations. This happens when one of the four factors in Eq.5.36 is equal to zero. To see this it is possible to consider, for example, $\gamma_{hc} = 0$; then a photon collected at detector C can only have come from the lower MZ arm, providing *which-way* information and destroying any two-photon interference. Values of the unbalancing parameter ξ between $[0, \infty]$ occur when no particular symmetries are imposed. This leads to coincidence patterns where the hallmarks of both one-photon and two-photon interference are present.

5.3.1.2 SPDC Light in a MZ Interferometer with Lossy Beamsplitters

As introduced above, the $g^{(2)}$ function in Eq.5.43 contains the sum of three oscillating terms, each having a different dependence on δ. Consequently, the qualitative appearance of the coincidence pattern can be remarkably sensitive to the value of this phase. For a lossy beamsplitter, Barnett et. al. [225] showed that in general the complex transmittance t and reflectance r satisfy:

$$|t|^2 + |r|^2 \quad \leq \quad 1 \tag{5.53}$$

where the equality holds for a lossless device. Considering incoming classical or coherent fields of equal or opposite amplitude, he showed that [225]:

$$|tr^* + t^* r| \quad \leq \quad 1 - |r|^2 - |t|^2 \tag{5.54}$$

By assuming for simplicity $t^* = t = \sqrt{\frac{\chi}{2}}$ and $r = te^{-i\delta}$ to describe a balanced *BS* where the photon has an intrinsic survival probability χ, the constraint on the relative phase between the reflection and transmission coefficients is:

$$|\cos\delta| \leq (1/\chi - 1) \tag{5.55}$$

When $\chi = 1$ (i.e. for a lossless beamsplitter), this sets $\delta = \pm\pi/2$, as used in Section 5.3.1.1. When $\chi < 1$, the phase δ can also be larger or smaller than $\pi/2$, with important consequences. First, from Eq.(5.44) it follows that if $\delta \neq \pi/2$, the magnitude of the HOM dip is smaller as the antibunching paths acquire different phases upon exiting *BS2* and no longer interfere completely destructively. This is the reduction in the visibility of the Hong Ou Mandel effect for a lossy beamsplitter with non-orthogonal reflection and transmission coefficients predicted in [225]. Furthermore, from the above discussion, it can be seen that while the condition for $\xi \to \infty$ is not affected by the beamsplitter phase, the limit of $\xi = 0$ is. This can be understood directly from Eq.5.50, by nothing that if $\delta \neq \pi/2$, there will never be a complete cancellation of the antibunching-bunching term.

5.3.1.3 Examples of SPDC Coincidence Patterns for Lossless and Lossy Beamsplitters

To give concrete examples of the coincidence patterns discussed above, Eq.5.43 is plotted in Fig.5.16(a) for three different values of the unbalance parameter ξ. In these cases the phase δ is set to $\pi/2$.

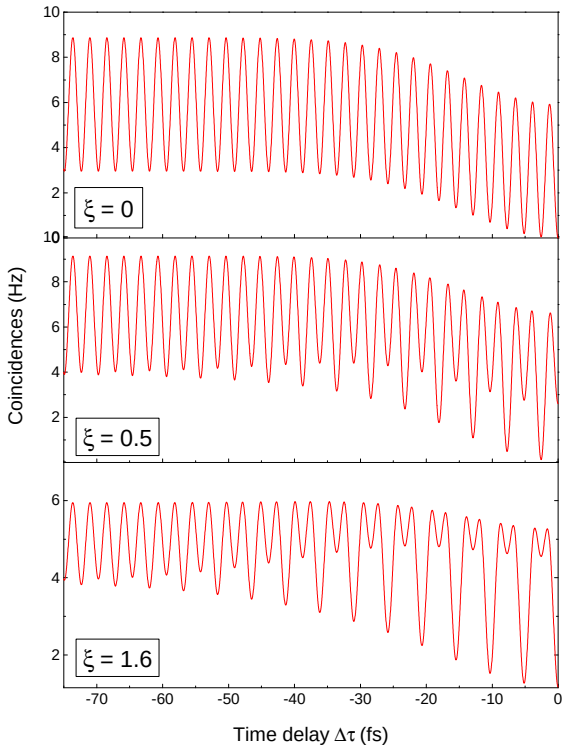

Figure 5.16: The coincidence rate is plotted against the interferometer time delay $\Delta\tau$ for different values of the unbalance parameter ξ. For simplicity, the phase δ has been fixed to $\pi/2$. The parameters used for the simulation are indicated in Table 5.2. The parameters used are meaningful for the experiment as it is discussed in section 5.3.2.

Parameter	$\xi = 0$	$\xi = 0.5$	$\xi = 1.6$
K	3.5		
$\sigma^{-1}\,[fs]$	24.1		
δ	$\frac{\pi}{2}$		
$\tilde{\omega}\,[fs^{-1}]$	2.43		
γ_{hd}	0.4	0.45	0.45
γ_{hc}	0.4	0.5	0.55
γ_{rd}	0.4	0.4	0.12
γ_{rc}	0.4	0.25	0.3

Table 5.2: Values of the parameters used for simulating the curves in Fig.5.16.

For realizing the balanced case $\xi = 0$ in Fig.5.16(a), it has been set $\gamma_{hc} = \gamma_{rd} = \gamma_{hd} = \gamma_{rc}$. As a consequence of the perfect balancing, the $g^{(2)}$ function oscillates at a single frequency $\tilde{\omega}$ both within and outside τ_c. This is a clear manifestation of the correlated or entangled nature of the two photon state created in the down conversion process [222]. As already discussed in Section 5.3.1, it is possible to interpret the single frequency oscillation as a suppression of the antibunching-bunching interference, and the observed pattern as due purely to two photon correlations. The decrease in the average value of the coincidence events as the optical contact is approached is due to the HOM effect. As ξ is increased, the pattern changes significantly with respect to the balanced situation. When $\xi = 0.5$, a new component at frequency $\tilde{\omega}/2$ appears within the coherence time. This is interpreted as follows: outside the coherence time, the antibunching paths in Fig.5.15 have vanishing probability, so the interference fringes at $\tilde{\omega}$ are due to two-photon correlation effects. Within the coherence time of the photon wave packet instead, the bunching paths can interfere together with the antibunching

ones, creating a mixed pattern in which single-particle interference at $\tilde{\omega}/2$ and two-particle interference at $\tilde{\omega}$ coexist. In general the higher the unbalancing between the arms, the higher the visibility of the component at $\tilde{\omega}/2$. We see from Fig.5.16 that it is sufficient to consider a value of $\xi = 1.6$ to practically cancel out the oscillation at $\tilde{\omega}$ within the coherence time. Next, the losses in the beamsplitters are explicitly considered, allowing the value of the intrinsic survival probability χ to be smaller than one. For example, as shown in Fig.5.17, the average value of the losses (for S polarization) of the BS implemented in the experiment described in section 5.3.2 is $(22.0 \pm 0.4)\,\%$, which corresponds to a value of $\chi = (0.78 \pm 0.4)$.

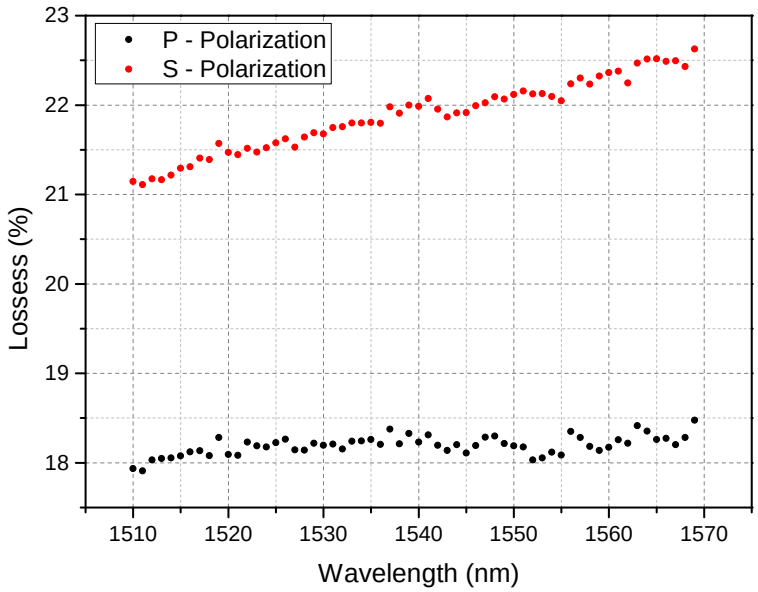

Figure 5.17: Losses of the two BS implemented in the experiment described in section 5.3.2 as a function of wavelength for P and S polarizations.

Then, assuming that the beamsplitter is balanced (i.e. $|r| = |t|$), the range of δ becomes:

$$0.82\,\frac{\pi}{2} \lesssim |\delta| \lesssim 1.12\,\frac{\pi}{2} \tag{5.56}$$

While this may at first seem a small difference from $\delta = \pi/2$, it is enough to dramatically affect the appearance of the coincidence pattern, as can be appreciated in Fig.5.18.

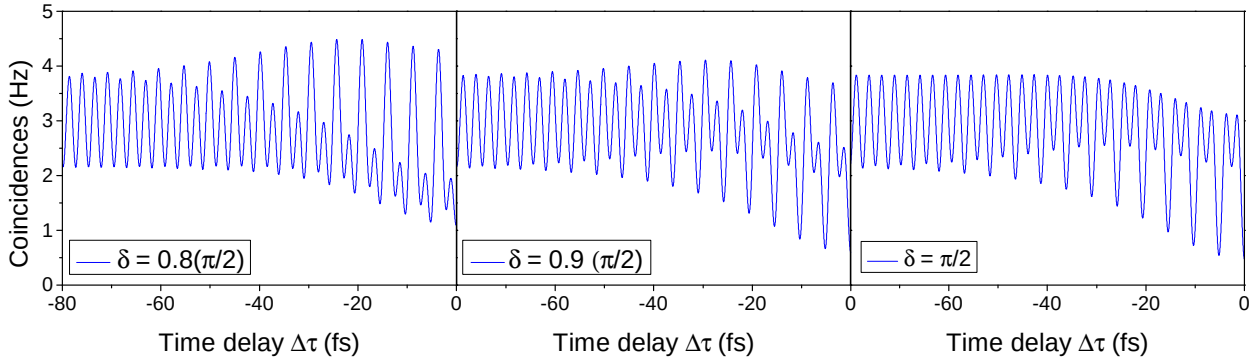

Figure 5.18: The theoretical coincidence rate in Eq.(5.35) is plotted against the interferometer time delay $\Delta\tau$ for different values of the beamsplitter phase δ. The parameters of the simulation are the same used for the solid red curve in Fig.5.21 for $\xi = 1.34$, and are listed in Table 5.3.

Here, patterns have been simulated using the parameters listed in Table 5.3 (panel $\xi = 1.34$), and changing only the value of δ. With a 20% deviation of δ from $\frac{\pi}{2}$, the fringe pattern gets mirrored-like with respect to the lossless case. This high sensitivity comes from the fact that the BS phase δ enters in the three path interactions terms in Eqs.5.44, 5.45, 5.46 with different combinations, so that even small variations can significantly alter the $g^{(2)}$ correlation function.

5.3.2 Experimental results

The practical realization of the free space MZI is shown in Fig.5.19(a). Standard $50:50$ BS cubes and gold mirrors are used to split and guide light through the device respectively. In order to introduce a variable time delay between the two arms of the interferometer, a cylinder of Borosilicate Crown glass (NbK7) was placed in both MZ arms, and, in one arm, the NbK7 was connected to an electric heater. This is shown in Fig.5.19(b).

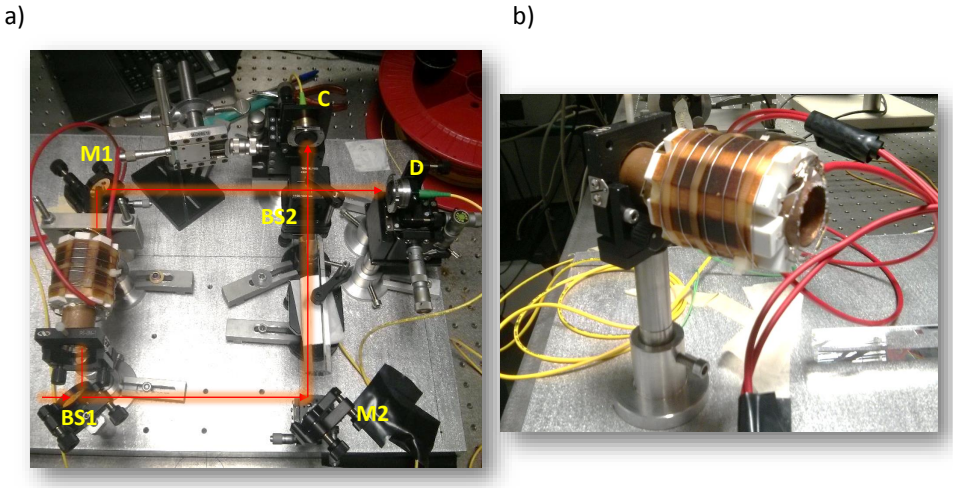

Figure 5.19: (a) The realization of the free space MZI. The symbols indicates the same optical components sketched in Fig.5.14. The heater is inserted in the upper arm. (b) Detail of the electrical heater, which is constituted by a hollow cylinder of copper surrounded by $10\,\Omega$ resistors connected in parallell.

The thermo-optic coefficient of the NbK7 was then exploited to smoothly vary its refractive index as the temperature is changed. The maximum achievable time delay between the arms was $150\,fs$, which was sufficient to span the whole coherence time of the radiation. The latter has been estimated from the spectral response of Fig.5.13 to be approximately $\tau_c = 24\,fs$. The detection stage and the coincidence electronics implemented in this experiment have been greatly improved with respect to the ones used to perform the coincidence measurements described in Section 5.2.2. The photons at the output ports of the interferometer were fiber coupled using two lenses onto two $InGaAs$ single photon counting detectors (ID Quantique Id210 and ID Quantique Id201) with 20% efficiency. One detector was used in free running mode ($40\,\mu s$ of deadtime, $5\,KHz$ of dark counts) to detect one photon of the pair. When the other detector, operating in gated mode ($10\,KHz$ of gating frequency, $100\,Hz$ of dark counts) was triggered, it was enabled for a gate width of $100\,ns$. The outputs of the photon counters were then fed into a Field Programmable Gate Array digital correlator that provided the coincidence rate over a coincidence window of $5\,ns$. This is all performed in real time, which allows to greatly enhance the averaging time and consequently improve the signal to noise ratio. As introduced above, the parameters in Eq.5.36 are tuned by inducing losses in the BS by by purposely misaligning the lenses in front of the photon counters.

First, the single port (in this case, port D) count rate P_d is measured as a function of the time delay $\Delta\tau$. Results are shown in Fig. 5.20. Since the curve is symmetric with respect to the optical contact, only the measured values for negative time delays have been reported.

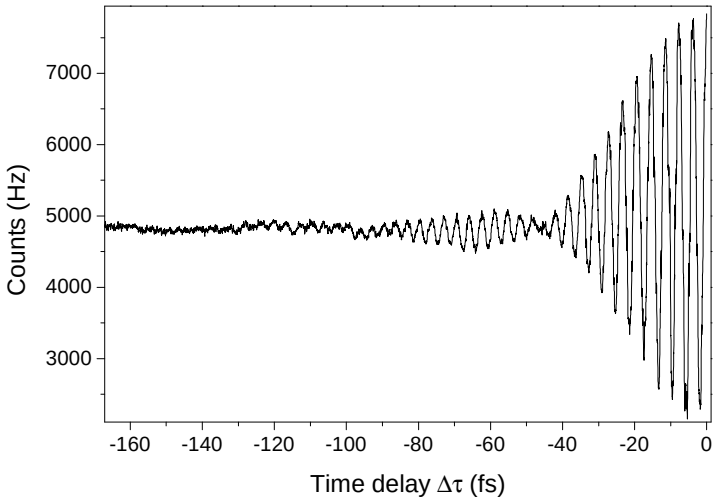

Figure 5.20: The single port count rate of port D in Fig.5.19 is plotted as a function of the time delay $\Delta\tau$. The optical contact, where the two arms have no time delay, is placed at $\Delta\tau = 0$.

In order to interpret the behaviour of this curve, which is proportional to $\left\langle E_d^-(t)E_d^+(t)\right\rangle$ evaluated on the SPDC state in Eq.5.33, one can follow a similar approach as the one described in Section 5.3.1 , which would give:

$$P_d(\Delta\tau) \propto \left\langle E_d^-(t)E_d^+(t)\right\rangle \propto \gamma_{hd}^2 + \gamma_{rd}^2 + 2\gamma_{hd}\gamma_{rd}e^{-\frac{\Delta\tau^2\sigma^2}{4}}\cos\left(\frac{\tilde{\omega}\Delta\tau}{2}\right) \tag{5.57}$$

From the curve displayed in Fig.5.20, a lot of informations can be extracted. As predicted by Eq.5.57, the single port count rate exhibits oscillations with a period equal to $\frac{2\pi}{\tilde{\omega}/2}$, since it comes from single particle interference. These oscillations are modulated by a slowly varying envelope due to the finite coherence time of the photons, through which it can be estimated a value of $\tau_c = (24.1 \pm 0.7)\, fs$. This value is very close to the one extracted from the spectra of the radiation, indicating that the approximations that were done in Section 5.2.3 were reasonable. The oscillations do not damp immediately to zero for $\Delta\tau \gg \tau_c$, but exhibits some ripple. This is due to the box-like distribution of the photons entering in the MZ shown in Fig.5.13, whose Fourier transfrm is a *sinc* function. However, the gaussian distribution in Eq.5.34 will be kept during the rest of this section since it provides an excellent approximation. Second, the full MZ was operated. The results of the two photon interference experiment are displayed in Fig.5.21. Experimental data are shown in black while fits with Eq.(5.43) are shown in red. The fit was done with a Differential Evolution genetic algorithm [227].

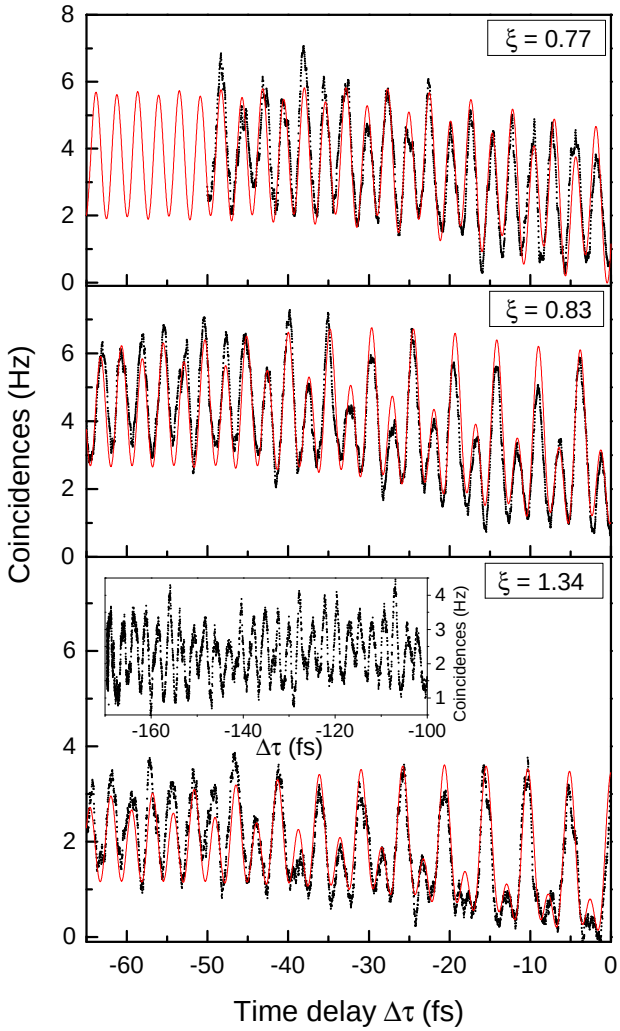

Figure 5.21: Measured coincidence rates for different values of the unbalance parameter ξ for SPDC light. The solid red curves are fits from Eq. (5.43), while black scatter points are experimental data. The reported value of ξ is taken from the fit. Values of the other fit parameters are reported in Table 5.3.

The latter minimizes the cost function $f(\mathbf{x})$ represented by:

$$f(\mathbf{x}) = \frac{1}{T_{tot}} \int_0^{T_{tot}} |g^{(2)}_{exp}(\Delta\tau) - g^{(2)}_{th}(\mathbf{x}, \Delta\tau)|^2 \, d(\Delta\tau) \tag{5.58}$$

where T_{tot} is the range of $\Delta\tau$ over which the experimental $g^{(2)}_{exp}$ (curves in Fig.5.21) has been recorded, $g^{(2)}_{th}$ is the theoretical second order correlation function of Eq.5.31 and $\mathbf{x}$ is the vector of free parameters to be fitted. These are $\mathbf{x} = (\gamma_{hd}, \gamma_{hc}, \gamma_{rd}, \gamma_{rc}, \sigma, \delta, K)$. The frequency $\tilde{\omega}$ has been fixed to $\tilde{\omega} = 2.448\, fs^{-1}$,which corresponds to an average wavelength of $\tilde{\lambda} = 775\, nm$.

The algorithm was runned for 15 times in order to improve the accuracy of the parameters. Each run has been stopped after a fixed number of iterations (600). Further iterations were seen to not significantly improve the goodness of the fit (fit quality increases only by 0.001% by doubling the number of iterations). The list of the fitted parameters is indicated in Table 5.3.

Parameter	$\xi = 0.77$ **(Upper panel)**	$\xi = 0.83$ **(Middle panel)**	$\xi = 1.34$ **(Lower panel)**
$K[fs^{-1}]$	1.8 ± 0.1	3.6 ± 0.4	12 ± 1
$1/\sigma[fs]$	24.1 ± 0.7		
$\delta[rad]$	1.37 ± 0.04		
γ_{hd}	0.47 ± 0.01	0.300 ± 0.001	0.124 ± 0.005
γ_{hc}	0.65 ± 0.02	0.66 ± 0.04	0.55 ± 0.02
γ_{rd}	0.64 ± 0.02	0.500 ± 0.001	0.36 ± 0.01
γ_{rc}	0.65 ± 0.02	0.66 ± 0.03	0.35 ± 0.01
$A_{\tilde{\omega}/2}$	$(9.7 \pm 0.7) \cdot 10^{-2}$	$(5.41 \pm 0.3) \cdot 10^{-2}$	$(1.14 \pm 0.04) \cdot 10^{-2}$
$A_{\tilde{\omega}}$	(0.125 ± 0.002)	$(6.5 \pm 0.2) \cdot 10^{-2}$	$(8 \pm 1) \cdot 10^{-3}$
ξ	0.77 ± 0.05	0.83 ± 0.04	1.34 ± 0.05

Table 5.3: List of the coefficients minimizing the discrepancy between the experimental data and the curve generated by Eq.5.43

This fitting procedure was used to determine the unbalance parameter ξ which is reported each graph; the fitted parameters found in this way were consistent with the controlled losses introduced in the experiment. The measured propagation losses from the input port of the MZ to the two detectors were $\approx 7\,dB$; a value comparable to the one found using the model in Eq.5.36, which gives $9\,dB$. Importantly, the experimental data could not be fitted with a phase of $\delta = \pi/2$, corresponding to lossless beamsplitters. This can be seen at a glance by comparing Fig.5.17 with Fig.5.21, and noting the key qualitative differences between the theoretical pattern obtained for $\delta = \pi/2$ and the experimental results. Allowing then the phase to be a free parameter, the value of δ is found to be $\delta = (1.37 \pm 0.04)\,rad$, where the uncertainly reflected the spread in the phase obtained from independent runs of the fitting algorithm. This value is compatible with the measured beamsplitter losses in Eq.5.56. For all three values of the unbalancing parameter in Fig.5.21, a very good agreement between the experimental results and the theoretical model is observed. For $\xi = 0.77$, the antibunching-bunching interference is suppressed as expected, although there are still some residual oscillations at $\tilde{\omega}/2$ due to the beam-splitter losses as discussed in section 5.3.1.2. To clearly show that the oscillation at frequency $\tilde{\omega}$ is due to purely second order interference effects, the inset of Fig.5.21 (panel $\xi = 1.34$) shows the coincidence rate for time delays greatly exceeding the single photon coherence time ($\Delta\tau > 100fs$). As it can be seen from Fig.5.20, for such time delays any possible contribution arising from first order interference to the coincidence pattern vanishes. Even if not reported in Fig.5.21, the very same oscillations outside τ_c are observed regardless of the value of ξ.
As ξ is increased, the pattern changes significantly; for example, at $\xi = 1.34$ the oscillation at $\tilde{\omega}$ is highly suppressed within the coherence time, while in the intermediate case ($\xi = 0.83$), it is possible to observe feature of single-photon, two-photon and HOM-like interference effects in the same coincidence pattern as expected. The theoretical model is therefore able to predict all the main features of the coincidence rate.

5.3.3 Comparison with other input radiation states

In this section the response of the MZI to input radiation states different from SPDC one are considered. This is done in order compare the two photon interference fringes generated by SPDC, to the ones created by photons which posses weaker correlations, as in the case of thermal light, and to the ones of completely uncorrelated photons. The direct comparison of the interference patterns hallmarks the unique features arising from colour entanglement, which is an intrinsic property of the radiation generated by SPDC. In the first part, a simple model is developed to explore the possibility that the coincidence patterns shown in Fig 5.16 could be reproduced by a fully classical treatment. Then, the case of indipendent photons is considered. At the end, weakly correlated thermal light is examined both from a theoretical and from an experimental point of view.

5.3.3.1 Classical light

A natural question to be explored is if the coincidence patterns shown in Fig 5.16 can be reproduced from a simple classical model. Following the reasoning of Kwiat et al. [228], it is possible to develop a classical-field model in which the rate of coincidence detection can be described by ensemble averages in a *stochastic classical field theory*. In this theory, a signal and an idler beam of frequencies ω_s and ω_i enters at the same port of the MZ. Both frequencies are treated as random variables subjected to the constraint $\omega_s + \omega_i = \tilde{\omega}$, where $\tilde{\omega}$ is fixed and set by the frequency of the pump. Considering the input-output MZ relation in Eq.5.32 as well as the loss factor in Eq.5.36, one can show that the classical electric fields E_c^{cl} and E_d^{cl}, as a function of the signal and idler amplitudes E_{ks} and E_{ki}, are:

$$\begin{aligned} E_c^{cl} &= i\gamma_{rd}\big(E_{ki} + E_{ks}\big) + i\gamma_{hd}\big(E_{ki}e^{-i\omega_i\Delta\tau} + E_{ks}e^{-i\omega_s\Delta\tau}\big) \\ E_d^{cl} &= -\gamma_{hc}\big(E_{ki} + E_{ks}\big) + i\gamma_{rc}\big(E_{ki}e^{-i\omega_i\Delta\tau} + E_{ks}e^{-i\omega_s\Delta\tau}\big) \end{aligned} \tag{5.59}$$

where, for simplicity, it is considered a lossless beamsplitter.
By calculating the cross correlation between the intensities $I_c = |E_c|^2$ and $I_d = |E_d|^2$, and by performing a statistical average on the frequency distribution, one finds:

$$\langle I_c I_d \rangle = g^{(2)}(\Delta\tau) = I_1 + I_2\cos(\tilde{\omega}\Delta\tau) \tag{5.60}$$

where I_1 and I_2 are two constants defined as:

$$\begin{aligned} I_1 = {} & \gamma_{rd}^2\gamma_{rc}^2\big(E_{ki} + E_{ks}\big)^4 + \gamma_{hd}^2\gamma_{hc}^2\big(E_{ki}^2 + E_{ks}^2\big)^2 \\ & + \gamma_{rd}^2\gamma_{hc}^2\big(E_{ki} + E_{ks}\big)^2\big(E_{ki}^2 + E_{ks}^2\big) \\ & + \gamma_{hd}^2\gamma_{rc}^2\big(E_{ki} + E_{ks}\big)^2\big(E_{ki}^2 + E_{ks}^2\big) \\ I_2 = {} & -4\gamma_{rd}\gamma_{hd}\gamma_{rc}\gamma_{hc}E_{ki}E_{ks}\big(E_{ki} + E_{ks}\big)^2 \end{aligned} \tag{5.61}$$

where it has been used that $\langle\cos(\omega_{s,i})\Delta\tau)\rangle = 0$ and $\langle\cos((2\omega_{i,s} - \omega_{s,i})\Delta\tau)\rangle = 0$ [228]. As it can be seen from Eq. 5.60, this classical treatment does not lead to any terms of frequency $\tilde{\omega}/2$ in the mutual intensity correlation function, although these are predicted by the above quantum approach (Eq.5.67). Furthermore, if the case of a perfectly balanced interferometer is considered, one can see from Eq.5.45 that the visibility can reach the 100% outside the single photon coherence time, while from Eq.5.60, the maximum allowed visibility is 50%. This simple classical model does not therefore reproduce the full behaviour predicted above for SPDC light. It is worth to note that, in principle, one can construct a more general model in which frequency, amplitude, and phase of the classical waves are all considered as random variables [228]; however this goes beyond the aim of this current work. In this sense, the arguments presented here do not exclude that a classical model can predict the interferograms of Fig.5.16, at least within the coherence time of the radiation.

5.3.3.2 Independent Photons

The interference effects presented in Section 5.3.1.3 are a manifestation of the correlated nature of the photon pairs produced via SPDC. Indeed, if the two photons entering at *BS1* are treated as being *independent*, i.e, completely not correlated, the probability of observing a coincidence between the output ports C and D factorizes into the product of the two probabilities $P_{in\to C}$ and $P_{in\to D}$ for each photon to reach port C and port D, respectively. Both probabilities describe single photon interference patterns, which can be written

explicitly as:

$$\begin{aligned} P_{in\to C} &= \langle E_c^+ E_c^- \rangle \\ &= \gamma_{hc}^2 + \gamma_{rc}^2 - 2\gamma_{hc}\gamma_{rc} e^{-\frac{\Delta\tau^2\sigma^2}{4}} \cos\Big(\frac{\tilde{\omega}\Delta\tau}{2}\Big) \end{aligned} \tag{5.62}$$

$$\begin{aligned} P_{in\to D} &= \langle E_d^+ E_d^- \rangle \\ &= \gamma_{hd}^2 + \gamma_{rd}^2 + 2\gamma_{hd}\gamma_{rd} e^{-\frac{\Delta\tau^2\sigma^2}{4}} \cos\Big(\frac{\tilde{\omega}\Delta\tau}{2}\Big) \end{aligned} \tag{5.63}$$

where the expectation values are evaluated with respect to the input radiation state $|\Psi_{in}\rangle$ defined in Eq.5.33. Consequently, the product $P_{in\to C}P_{in\to D}$, which is plotted in Fig.5.22 for different values of the unbalancing parameter ξ, contains terms oscillating both as $\cos(\frac{\tilde{\omega}}{2}\Delta\tau)$ and $\cos(\tilde{\omega}\Delta\tau)$. As discussed in section 5.3.1.3, the same frequencies are present for the case of the SPDC light. However, it is still possible to clearly distinguish between SPDC photons and independent particles from several features:

1. The absence of the HOM dip near the optical contact at $\Delta\tau = 0$.
2. The absence of interference fringes outside the coherence time of the radiation.
3. The fact that the component at frequency $\tilde{\omega}$ increases in amplitude as the optical contact is approached.

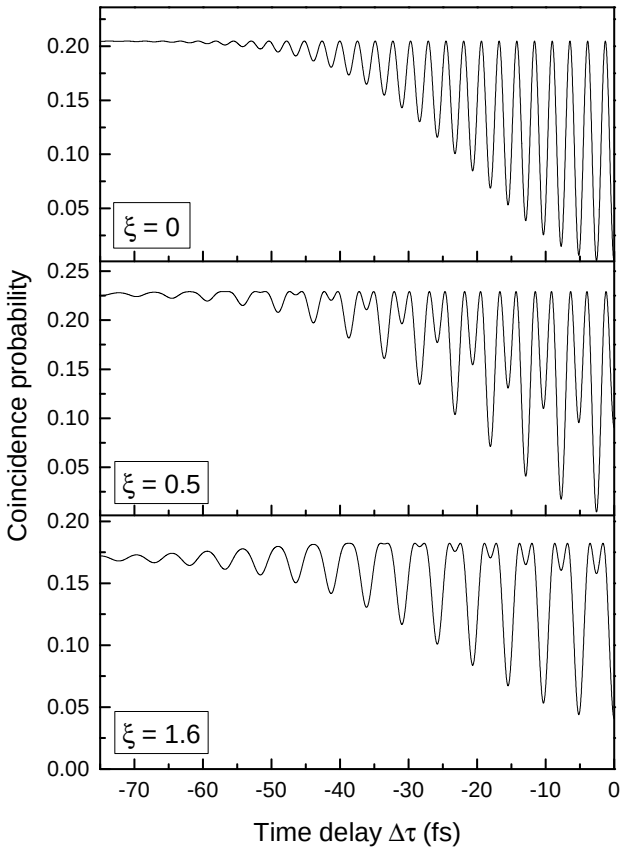

Figure 5.22: The theoretical coincidence probability is plotted against the interferometer time delay $\Delta\tau$ for different values of the unbalance parameter ξ for two photons entering in the same input port of the MZ, treated as *independent* particles. The simulation parameters are the same used in Fig.5.16and listed in Table 5.2.

5.3.3.3 Thermal Light

After having investigated the interference properties of uncorrelated photons in section 5.3.3.2, the case of weakly-correlated thermal photons is considered. An input thermal light is considered as the sum over many independent modes thermally occupied, as described by the following density matrix [229]

$$\hat{\rho} = \frac{1}{Z} \exp\left(\sum_i \frac{\hbar\omega_i}{k_B T} a^\dagger_{\omega_i} a_{\omega_i} \right) \tag{5.64}$$

where Z is the partition function of the grand canonical ensemble of the photon gas at temperature T and k_B is the Boltzmann constant. To calculate the second order correlation function in Eq. (5.31), the Wick's theorem [229] is used as follows:

$$\begin{aligned} g^{(2)}(t,\tau) &= K \mathrm{Tr}(E_d^-(t) E_c^-(t+\tau) E_c^+(t+\tau) E_d^+(t)) \\ &= K(|\langle E_d^-(t) E_c^+(t+\tau)\rangle|^2 + \\ &+ \langle E_d^-(t) E_d^+(t)\rangle \langle E_c^-(t+\tau) E_c^+(t+\tau)\rangle) \\ &= \eta_{corr}(t,\tau) + \eta_d(\tau)\eta_c(\tau) \end{aligned} \tag{5.65}$$

where the expectation values must be calculated on the thermal state defined in Eq.5.64. In Eq.5.65 the term η_{corr} describes two photon correlations between the output ports C and D, while the term $\eta_d(\tau)\eta_c(\tau)$ is simply the product of first order correlation functions, describing single photon interference. By inserting the input-output relations in Eq.5.32 into Eq.5.65, and by using the fact that for a thermal state [229]

$$\langle a^\dagger_\omega a_{\omega'} \rangle = \frac{\delta(\omega - \omega')}{e^{\frac{\hbar\omega}{k_B T}} - 1} \tag{5.66}$$

after integrating in τ as described in section 5.3.1, it is found that the $g^{(2)}$ function is:

$$g^{(2)}(\Delta\tau) = \eta_{corr}(\Delta\tau) + \eta_d(\Delta\tau)\eta_c(\Delta\tau) \tag{5.67}$$

where $\eta_{corr}(\Delta\tau)$ and $\eta_d(\Delta\tau)\eta_c(\Delta\tau)$ are given by:

$$\begin{aligned} \eta_{corr}(\Delta\tau) = KG(0)\Big\{ &\gamma_{hc}^2\gamma_{rd}^2 + \gamma_{rc}^2\gamma_{hd}^2 + \gamma_{hc}^2\gamma_{hd}^2 \\ &+ \gamma_{rc}^2\gamma_{rd}^2 + 2A_{\tilde{\omega}}\cos(2\delta)\, g(2\Delta\tau) + 2A_{\tilde{\omega}}\cos(2\delta) \\ &+ 2\big[A^{(1)}_{\tilde{\omega}/2}\cos(2\delta) + A^{(2)}_{\tilde{\omega}/2}\big]\, g(\Delta\tau)\Big\} \end{aligned} \tag{5.68}$$

and

$$\begin{aligned} \eta_d(\Delta\tau)\,\eta_c(\Delta\tau) = KT_R\Big\{ &(\gamma_{rd}^2 + \gamma_{hd}^2)(\gamma_{hc}^2 + \gamma_{rc}^2)\bar{n}^2(0) \\ &+4A_{\tilde{\omega}}\cos(2\delta)\mathrm{Re}\big[\bar{n}(\Delta\tau)\big]^2 + 2\big[A^{(1)}_{\tilde{\omega}/2}\cos(2\delta) \\ &+A^{(2)}_{\tilde{\omega}/2}\big] \times \bar{n}(0)\mathrm{Re}\big[\bar{n}(\Delta\tau)\big]\Big\} \end{aligned} \tag{5.69}$$

Here the normalized first order correlation function $g(\Delta\tau) = G(\Delta\tau)/G(0)$ is introduced, with:

$$G(\Delta\tau) = \int \mathrm{Re}\big\{\bar{n}(\tau - \Delta\tau)\bar{n}^*(\tau)\big\} d\tau. \tag{5.70}$$

The quantity $\bar{n}(\tau)$ is the Fourier transform of the average number of photons:

$$\bar{n}(\tau) = \int \frac{\phi(\omega)}{e^{\frac{\hbar\omega}{k_B T}} - 1} e^{i\omega\tau} d\omega \tag{5.71}$$

where the function $\phi(\omega)$ defines the bandwidth of the thermal radiation. The integral can be calculated analytically, provided that it is possible to make the approximation $(e^{\frac{\hbar\omega}{k_B T}} - 1)^{-1} \simeq e^{-\frac{\hbar\omega}{k_B T}}$; which will be justified in the experiment described later. Using this approximation, it is found that:

$$\bar{n}(\tau) \simeq N\sqrt{2\pi}\sigma \exp\left(\frac{-\sigma^2\tau^2}{2}\right) \exp\left[i\left(\frac{\tilde{\omega}}{2} - \frac{\sigma^2\hbar}{k_B T}\right)\tau\right] \exp\left(\frac{\hbar\tilde{\omega}}{2k_B T} + \frac{\sigma^2\hbar^2}{2k_B^2 T^2}\right) \tag{5.72}$$

Eq.5.72 can be recognized as a thermally frequency-shifted Gaussian, weighted by an exponential factor that takes into account the thermal distribution. From Eq.5.68, it can be shown that for thermal light, there are oscillating terms in the coincidence pattern both at frequency $\tilde{\omega}/2$ and $\tilde{\omega}$. Consequently, the arguments concerning the effect of the MZ unbalance parameter ξ that have been previously discussed for SPDC light, can again be applied here. The major difference between these two cases is that, for thermal light, the two-photon correlation function η_{corr} is several orders of magnitude lower than the product $\eta_d\eta_c$, as $\eta_{corr}/\eta_d\eta_c \approx 1[fs]/T_R[fs]$ where $T_R \approx 1\,ns$ for typical coincidence electronics [154]. Thus, thermal photons behave more like independent particles, and show negligible second-order interference. This can be seen in Fig.5.23, where the coincidence patterns as a function of ξ are shown for thermal light. These patterns more closely resemble those in Fig.5.22 for independent photons than those in Fig.5.16 for SPDC light. In particular, the oscillations at frequency $\tilde{\omega}$ are always present outside the single-photon coherence time $\tau_c = 1/\sigma$ for SPDC radiation, while they damp out for thermal light due to the negligible two-photon correlations. Finally, the coincidence rate for thermal light is two order of magnitude lower than that for SPDC radiation, reflecting that SPDC photons always enter into the MZ in pairs.

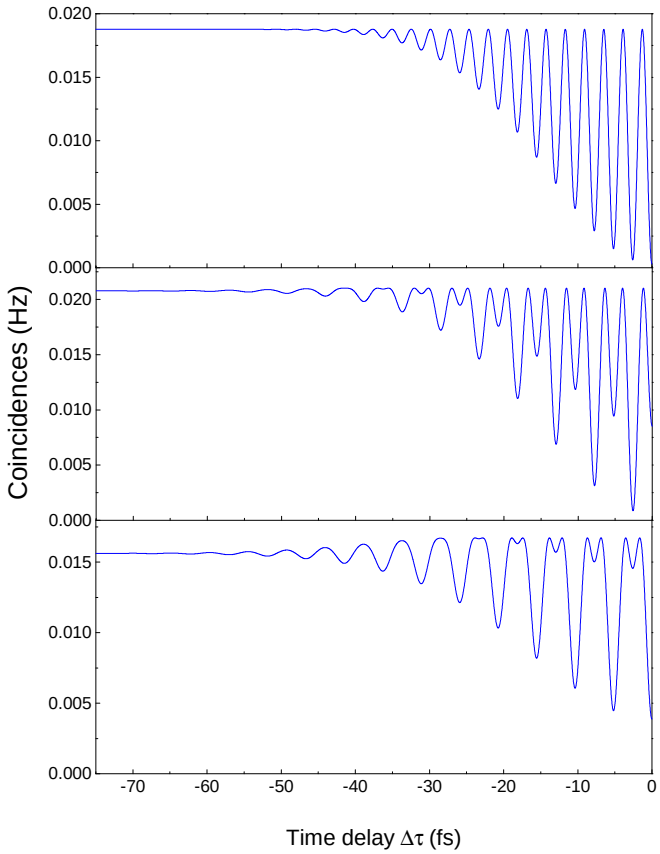

Figure 5.23: Theoretical coincidence rates as a function of the time delay $\Delta\tau$ for thermal photons at the input of the MZ. These are plotted for different values of the unbalance parameter ξ. The parameters used to simulate the curves are the same of the SPDC simulation shown in Fig.5.16 and listed in Table 5.3. The temperature of the source is set to $T = 3000\,K$.

An attempt to realize the coincidence experiment with a thermal light source has been done. For this purpose, a Tungsten Halogen lamp at a temperature of $T = 3000$ K has been used. This has been placed before the interference filters IF of Fig.5.4, while the rest of the setup has not been changed. Within the bandwidth spanned by the interference filters and the detectors, the factor $\hbar\omega/k_BT$ has a value of ≈ 3.15, so that the approximation in Eq.(5.72) holds. The light intensity is regulated in order to have the same average number of photons entering the MZ as in the case of SPDC light. Unfortunately, the result, reported in Fig.5.24 for $\xi = 0.83$ (blue scatter points), shows only noise fluctuations. This is because the coincidence signal probably lies below the noise level of the measuring apparatus. Indeed, the latter is about 1 Hz while the expected coincidence rate, as shown in Fig.5.23, is ≈ 0.02 Hz. While this experiment was therefore not able to test all details of the model for thermal light, it did confirm the overall difference in magnitude between SPDC light and thermal light oscillations, while also providing an additional feedback of the goodness of the measuring setup.

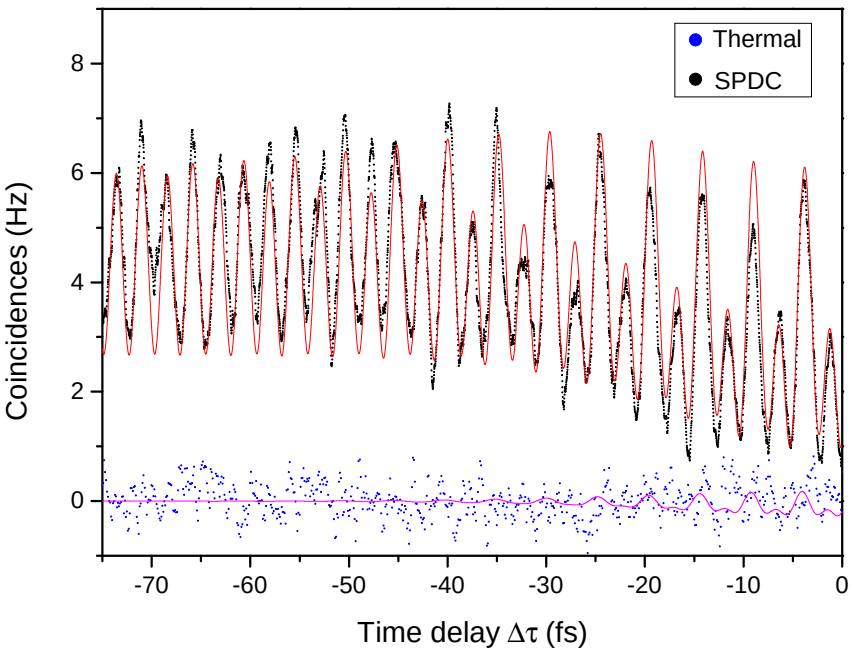

Figure 5.24: Comparison between the coincidence experiment performed with an SPDC state at the input (black scatters) and a thermal state (blue scatters). The solid curves are obtained using Eq.5.43 for the SPDC state and using Eq.5.65 for the thermal state. In both cases, the unbalance parameter ξ has been tuned to $\xi = 0.83$, which is the same condition reported in Fig.5.21.

5.4 Summary and conclusions

In this chapter, it is reported an experiment in which pairs of colour entangled photons produced by SPDC in a PPLN crystal excites a free space MZI. The source has been previously characterized both in frequency and in time domain by respectively implementing a dispersive stage coupled to a photon counter and by performing a coincidence experiment. The particular asymmetrical excitation of the device allowed observing new interference effects which have never been reported in previous works. This is because previous works were often performed using type II degenerate SPDC, for which the pair is firstly separated on the basis of their orthogonal polarizations and then sent to both ports of the input beamsplitter. The Hong Ou Mandel effect occuring after the first beamsplitter impeds the creation of antibunching paths, thus limiting the number of interference channels leading to a coincidence event. On the other hand, if both photons are sent to the same input port, as it is the case of the experiment described in this chapter, after the first beamsplitter there is the coexistence between bunching and antibunching paths, leading to a richer interplay of the interfering channels. The amplitude probabilities of these are seen to be easily manipulated by inducing controlled losses on the two arms of the interferometer, which allowed to shift from a pure two photon interference pattern to a mixture between two photon and single photon interference. This configuration has revealed to be extremely sensitive to the phase imparted by the beamsplitter, which can slightly differ from $\pi/2$ in case of intrinsic losses. In this sense, the asymmetrically excited MZ can be used as a tool for detecting this phase shift. The whole theoretical work developed for predicting the probabilities of observing a coincidence event can be straightforwadly applied to an integrated MZ device. It would be sufficient to replace the thermo optic coefficient of the NbK7 glass with the one of the material employed for fabricating the waveguides. Furthermore, the asymmetric excitation comes natural for an integrated quantum source, since the correlated photons are usually created in the same spatial mode, i.e., they travel collinearly in the same waveguide. This is why the theoretical knowledges and the skills acquired in this work will be of

great help for the future developements of the SIQURO project, in which the MZ will constitute part of the interference schemes which will be proposed on the Silicon chip.

Chapter 6

On chip integrated circuits for the manipulation of quantum states of light

As already introduced in section 1.3 , the field of integrated quantum photonics is rapidly growing, and many examples of on chip generation and manipulation of quantum states of light have been demonstrated. Such experiments share some fundamentals building blocks. One of these is the quantum source. In general, experiments performed on the Silicon platform make use of the $\chi^{(3)}$ non linearity of the material to produce photon pairs through sFWM. This requires the use of a bright pump which has to be filtered out from the generated radiation. This stage is usually accomplished off chip by the use of interference filters, Arrayed Waveguide Gratings (AWG) or Fiber Bragg Gratings (FBG) (see e.g., Ref.[180]). The filter itself constitutes another building block of the experiment. Next, the generated radiation is manipulated in interferometric structures which allow to create well defined quantum states to be eventually fed off chip for further manipulation. These includes the use of delay lines, beamsplitters, AWGs etc. Up to now, a network which integrates all these functionalities on a chip has not been yet demonstrated. Functions that can not be easily integrated, such as the delay lines or filters, have been supplied by external optical components. In this chapter, the design and the simulation of most of the main building blocks for integrated quantum networks is reported. The goal is to produce the first network in which all the functionalities are integrated, and the only external components required to perform the experiment are the pump laser and the photon counters. In the first section the sources are discussed. These are based on sFWM in racetrack resonators or in straight waveguides. The pump filtering stage and its roboustness to fabrication defects is discussed later. Interferometers, AWGs and delay lines are covered at the end of the chapter. In this chapter, the design of the integrated quantum photonic chip is presented. Its fabrication is underway.
The designs and simulations shown in this chapter have been done in collaboration with Mr.Stefano Signorini and Mr.Claudio Castellan.

6.1 Quantum sources based on racetrack resonators

The input pump power required to obtain a bright source of correlated photons can be dramatically decreased by the use of resonators. This is because the resonating structure enhances the power which is circulating inside the cavity with respect to the one that is used to excite the device. In this section, the use of racetrack shaped resonators realized on the SOI platform is investigated as a tool for generating photon pairs through sFWM. The racetrack is organized in the AD filter configuration. In order to estimate the efficiency of the process, one can in principle follow an approach similar to the one derived in Section 5.1.1 to predict the

generation rate of signal/idler pairs. This would require to quantize the field in the resonator geometry, to derive an expression for the $\chi^{(3)}$ perturbation hamiltonian and to use it in the Fermi's golden rule to derive the transition probability to annihilate two pump photons and simultaneously create a signal and an idler pair. Instead of using this approach, it was preferred to use the classical wave equations for stimulated FWM derived in Appendix A integrated with an input "quantum seed" to stimulate the process. This approach has been already used in section 3.4 to predict the efficiency of the sFWM process in straight Silicon waveguides. Following the derivation in Appendix A, the classical coupled wave equations for stimulated FWM in a resonating geometry are:

$$\frac{du_p(t)}{dt} = i\left(\bar{\omega_p}(1-\Delta_p(t)) - \omega_p\right)u_p(t) - \frac{1}{\tau_{tot,p}(t)}u_p(t) + 2i\gamma_{pisp}u_i(t)u_s(t)u_p^*(t) + i\sqrt{\frac{2}{\tau_{ext,p}}P_p} \tag{6.1}$$

$$\frac{du_s(t)}{dt} = i\left(\bar{\omega_s}(1-\Delta_s(t)) - \omega_s\right)u_s(t) - \frac{1}{\tau_{tot,s}(t)}u_s(t) + 2i\gamma_{sppi}u_p^2(t)u_i^*(t) + i\sqrt{\frac{2}{\tau_{ext,s}}P_s} \tag{6.2}$$

$$\frac{du_i(t)}{dt} = i\left(\bar{\omega_i}(1-\Delta_i(t)) - \omega_i\right)u_i(t) - \frac{1}{\tau_{tot,i}(t)}u_i(t) + 2i\gamma_{ipps}u_p^2(t)u_s^*(t) \tag{6.3}$$

where:

- $u_{p,s,i}$ are the slowly varying time envelopes of the pump, signal and idler modes within the resonator, normalized in such a way that $|u_{p,s,i}|^2$ represent the energy.
- $\bar{\omega}_{p,s,i}$ are the eigenfrequencies of the pump, signal and idler modes when the resonator is "cold", that is when no optical power is circulating inside the resonator. When some power is circulating, these frequencies are perturbed from their initial values by a quantity $\Delta_{p,s,i}$ due to power dependent refractive index changes. The ones considered in this model are: the thermo optic effect, the free carrier dispersion effect, the self phase modulation and the cross phase modulation. Since the thermo optic effect and the free carrier dispersion effect requires the knowledge of the temperature of the resonator and of the free carrier concentration, two additional equations, describing their dynamics, are added to the model and detailed in Appendix A.
- ω_p and ω_s are the frequencies of the input pump laser and of the input signal, respectively, while ω_i is determined by energy conservation as $\omega_i = 2\omega_p - \omega_s$.
- $\tau_{tot,psi}$ and $\tau_{ext,ps}$ are respectively the photon lifetime (for pump, signal and idler) in the cavity and the inverse of the energy decay rate into the exciting waveguide. The first is given by the sum of various contributions, which are: linear losses, two photon absorption, cross photon absorption and free carrier absorption.
- γ is the nonlinear FWM coefficient, which is inversely proportional to the effective modal volume and proportional to the magnitude of the $\chi^{(3)}$ in the material.
- $P_{p,s}$ are the pump and signal power in the exciting waveguide.

The definition of the parameters and their link with the resonator geometry is indicated in Appendix A. According to Ref.[200], the "quantum seed" used as the input signal power is given by:

$$P_s = \frac{\hbar\omega_s v_g}{2L|F_0|^2} \tag{6.4}$$

where $v_{g,s}$ is the group velocity of the signal, L is the length of the resonator and F_0 is the field enhancement factor. From the analysis of Eq.6.1-6.3 it comes out that the efficiency of the process is maximized when:

$$\bar{\omega_s}(1+\Delta_s(t))-\omega_s=0; \qquad \bar{\omega_p}(1+\Delta_p(t))-\omega_p=0; \qquad \bar{\omega_i}(1+\Delta_i(t))-\omega_i=0 \tag{6.5}$$

which can be interpreted as the energy conservation relations of the FWM process applied to resonators. As a first approximation, the corrections $\Delta_{p,s,i}$ can be neglected and the above set of equations can be cast in the equivalent form:

$$(\bar{\omega_s}+\bar{\omega_i}-2\bar{\omega_p})+(2\omega_p-\omega_s-\omega_i)=0 \tag{6.6}$$

Energy conservation implies that $2\omega_p-\omega_s-\omega_i=0$, so that Eq.6.6 reduces to an energy conservation relation between the resonator eigenfrequencies:

$$\bar{\omega_s}+\bar{\omega_i}-2\bar{\omega_p}=0 \tag{6.7}$$

Eq.6.7 can be satisfied if the signal and the idler eigenfrequencies are symmetrically shifted with respect to the pump frequency by a quantity Ω, in this way $\bar{\omega_s}=\bar{\omega_p}+\Omega$, $\bar{\omega_p}-\Omega$ and $\bar{\omega_s}+\bar{\omega_i}=2\bar{\omega_p}$. According to Eq.1.10, the resonance frequencies ω_m of a resonator of perimeter L and effective index $n_{eff}(\omega)$ are $\omega_m=(2m\pi c)/(n_{eff}(\omega)L)$. Eq.6.7 can then be satisfied provided that the effective index does not depend on frequency. This condition clearly does not apply to the case of the guided modes of a nanophotonic wire, in which the geometric dispersion is high due to modal confinement. This reflects in a not equidistant mode spacing which is mathematically described by a free spectral range that is frequency dependent. It can be demonstrated [183] that the spread in the FSR $\Delta(FSR)$ due to the dispersion of the effective index is related to the group velocity dispersion β_2 through:

$$\Delta(FSR)=2\pi L\times(FSR)^3\times\beta_2 \tag{6.8}$$

To obtain a mode spacing which is as constant as possible, it is therefore possible to engineer the waveguide geometry in order to achieve zero GVD. This constitues the starting point for choosing the waveguide width of the resonator. The waveguide height is fixed to $250\,nm$ since this value corresponds to the thickness of the Silicon layer implemented in the fabrication. In order to keep a small mode volume, and hence a higher nonlinear FWM coefficient, light is chosen to propagate with TE polarization and in the fundamental mode of the waveguide. The group velocity dispersion is then computed using FEM simulations in the interval of wavelengths which goes from $1.4\,\mu m$ to $1.7\mu m$ and for different waveguide widths. The range of investigated waveguide widths spans from $400\,nm$ to $860\,nm$, with increments of $20\,nm$. The plot in Fig.6.1 shows the computed β_2 for only some of these widths.

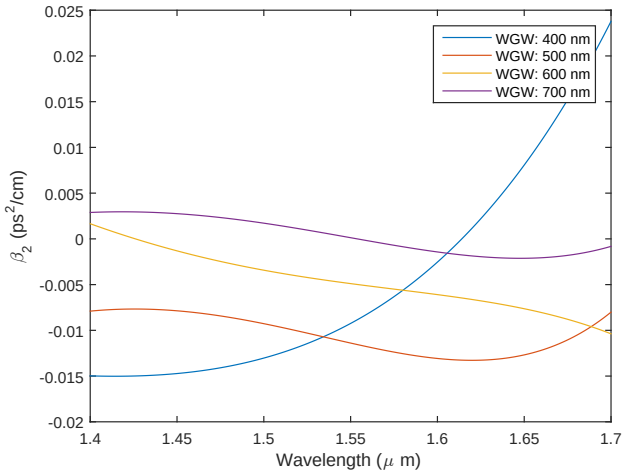

Figure 6.1: Group velocity dispersion of Silicon waveguides of 250 nm height and different widths.

From the results shown in Fig.6.1, two widths have been selected for designing the resonators: 400 nm and 700 nm. At 1.55μm, where the pump wavelength is placed, the 400 nm waveguide has a high value of β_2, which indicates that the efficiency of the FWM process will be limited to a narrow bandwidth around the degenerate wavelength. For this reason, this design will be called the "narrowband" one. On the other hand, the 700 nm waveguide has a group velocity dispersion which is flat and close to zero in all the investigated wavelength interval. This will be called the "broadband" design. The performances of the two designs will be now compared. The resonator parameters which have not been set yet are the coupling coefficient and the perimeter. For this purpose, the generation rate of the signal/idler photons are computed using Eq.6.1-6.3 for different combinations of the coupling coefficient and of the resonator perimeter. This is done by setting the propagation losses to 5 $dBcm^{-1}$ (which corresponds to a realistic value for the fabrication process involved, as shown in Table 4.3), the pump power to $-10\,dBm$ and the waveguide width to 700 nm. The result is shown in Fig.6.2.

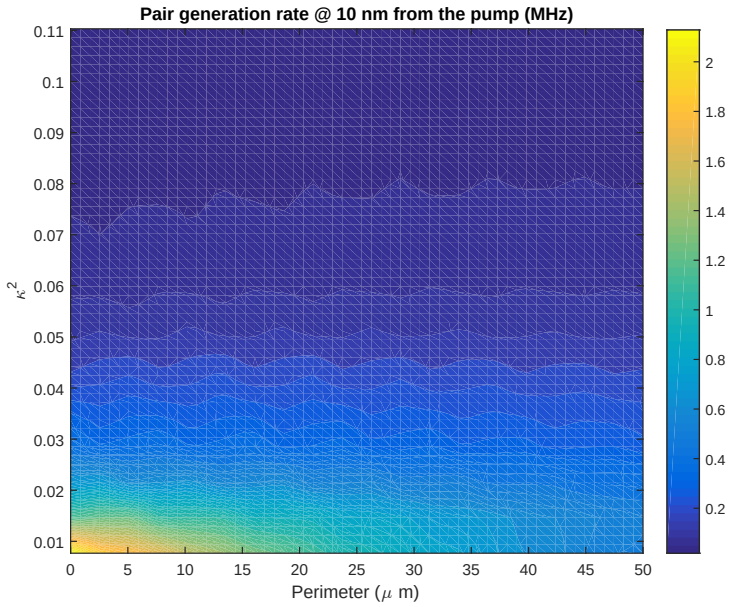

Figure 6.2: Pair generation rate at the resonance orders m_p+1 (for the signal) and m_p-1 (for the idler) (m_p is the resonance order of the pump) as a function of the coupling coefficient κ^2 and the resonator perimeter.

As expected, the highest generation rates are found at low coupling coefficients and at small perimeters. A low coupling coefficient implies a high power enhancement of the circulating power within the resonator. Small perimeters ensure tiny mode volumes and higher nonlinear FWM coefficients. Of course there exists some practical limitations to the smallest perimeter that can be achieved. The bending radius of the resonator can not be arbitrarily decreased if one wants to avoid significative energy leakage into the cladding. It is worth to note that the waveguide bending affects the group velocity dispersion of the waveguide, the amount of which is inversersely proportional to the bending radius. At the same time, a section of the resonator waveguide has to be coupled to the exciting waveguide. The finalized geometry is shown in Fig.6.3. For the narrow band design, the (inner) radius of curvature is $R = 5\,\mu m$, while the coupling with the waveguide is achieved using a directional coupler of length $6\,\mu m$. The coupling gap is lower limited by the fabrication resolution, which in this case corresponds to $400\,nm$. The coupling coefficient is then $\approx 2\%$ at $1.55\,\mu m$ and the corresponding $Q \approx 30000$. For the broadband design, the curved sections are of $700\,nm$ width and the bending radius equal to $R = 5\,\mu m$. The waveguide size is then reduced to $400\,nm$ using a tapering section of $600\,nm$ before entering in the directional coupler stage. The length of the coupler is $7.57\,\mu m$, which yelds a coupling coefficient of $\approx 3\%$ and $Q \approx 20000$.

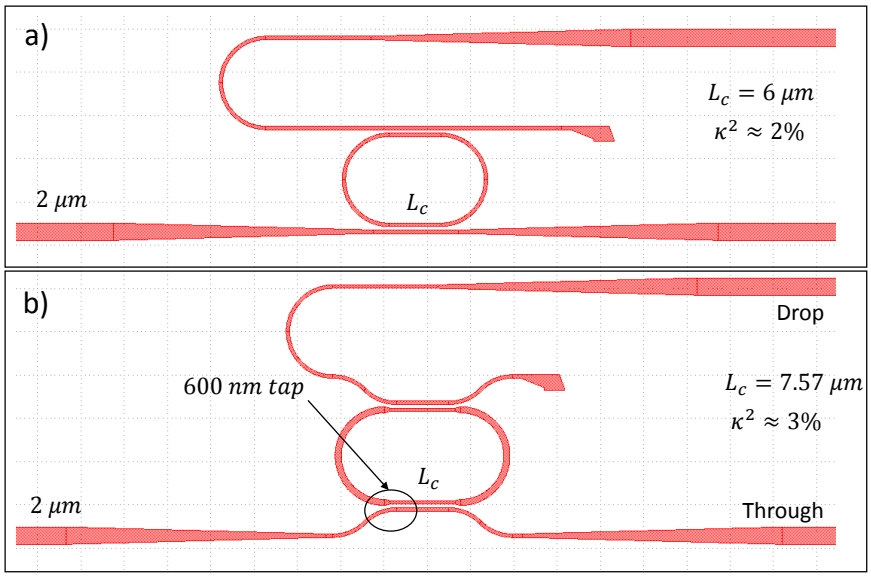

Figure 6.3: (a) Resonator geometry for the narrow band design, in which all the waveguide sections of the resonator are made with waveguides of $400\,nm$ width. (b) Resonator geometry for the broad band design, in which the curved sections are of $700\,nm$ width and the straight ones of $400\,nm$ width.

Once the geometry is finalized, the generation efficiency of both the broad band and the narrow band design are simulated and compared. The pump power used to excite the waveguide is $0\,dBm$. Fig.6.4 summarizes the results.

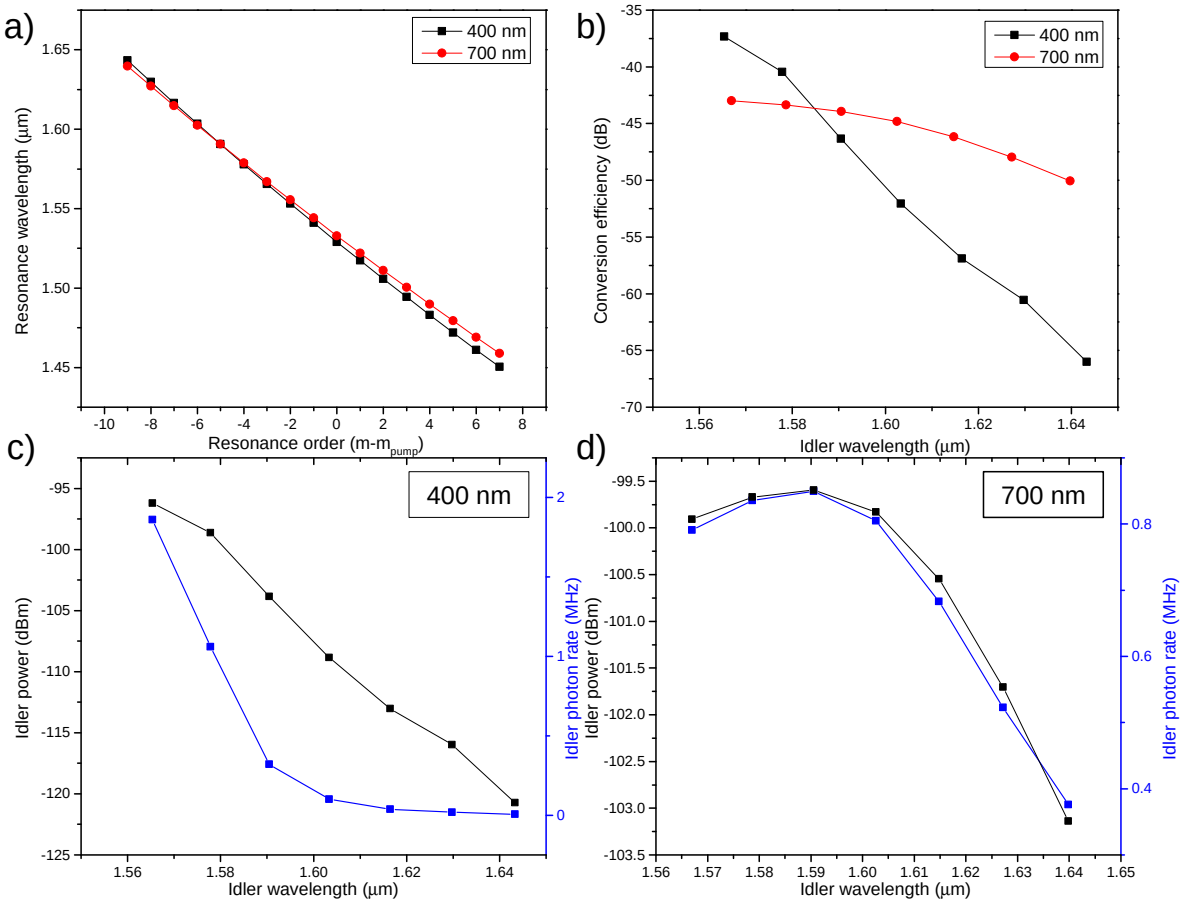

Figure 6.4: (a) Resonance wavelengths on the red and blue side of the pump (resonance order $m_{pump} = 0$) for the racetracks of $400\,nm$ width and $700\,nm$ width. (b) Conversion efficiency of the idler photons. (c-d) Idler photon rate as a function of wavelength, expressed both in terms of power and in terms of numbers of photon per second.

From Fig.6.4(a), it can be noticed that the FSR of the two designs are similar, with a value of $FSR \approx 13\,nm$ at $1.55\,\mu m$. As a result, the number of resonances at the red and blue side of the pump (centered at $1.55\,\mu m$ for the $400\,nm$ design and at $1.553\,\mu m$ for the $700\,nm$ design) are almost the same. The effect of the different group velocity dispersion can be appreciated in Fig.6.4(b), where the conversion efficiencies are reported. It is evident that the $700\,nm$ design has a much higher bandwidth ($\approx 43\,nm$ of $3\,dB$ bandwidth) with respect to the $400\,nm$ one ($\approx 18\,nm$). The generated power, for the signal photons, is in both cases at the order of $\approx -100\,dBm$, which corresponds to a photon pair generation rate of $\approx 1\,MHz$. Since this flux has been obtained with a pump power of $0\,dBm$, it comes out that a filtering stage which realizes a pump suppression higher than $100\,dB$ is needed to isolate the correlared pairs. Furthermore, especially for the broad band design, each photon pair has to be separated from the others which form the comb before applying any further manipulation. This is necessary since the energy entaglement exists between signal and idler photons of the same pair, but not for photons of different pairs. As discussed in section 6.5, this filtering stage will be implemented using integrated AWGs.

6.2 Quantum sources based on degenerate FWM in multimode waveguides

The quantum source based on racetrack resonators described in the previous section generates signal/idler pairs of different colour. It is also desirable to have a source which is capable to produce photons which are degenerate in wavelength. This would allow to perform quantum optics experiment without the use of interference filters for separating the signal from the idler photon before their detection [180, 230]. Typically, degenerate FWM is achieved using a dual pump scheme, as described for example in Ref. [198]. In this work, two pump photons, one at frequency $\omega_p + \Omega$ and one at $\omega_p - \Omega$ are annihilated to produce two entangled photons at frequency ω_p. This experiment can be viewed as the time reversal of the FWM process which converts two pump photons at ω_p into a signal and an idler photon whose frequencies are symmetrically located with respect to ω_p. A way to realize degenerate FWM using a single pump beam relies on the MMFWM process described in Chapter 3. The frequencies of the pump, the signal and the idler photons are all the same and equal to ω_{deg}, but the pump travels in a waveguide mode that is different from the one of the signal/idler pair. In this way, it is possible to distinguish the pump photons from the ones of the correlated pair by labelling them with a different modal index. An example of modal combination which achieves this goal is the $(1, 1, 4, 4)$ in a Silicon waveguide of cross section $1.6\,\mu m \times 0.25\,\mu m$, where the same notation of Section 3.4 has been used to label the modal combination. The pump propagates in TM polarization, while the signal and the idler in TE polarization. Fig.6.5 shows the phase mismatch Δk introduced in Eq.3.19 as a function of the idler wavelength. In this simulation, the wavelengths of all the fields involved in the FWM process are the same. At the degenerate wavelength of $\lambda_{deg} = 1549.96\,nm$, the curve cross the zero, i.e., phase matching occurs.

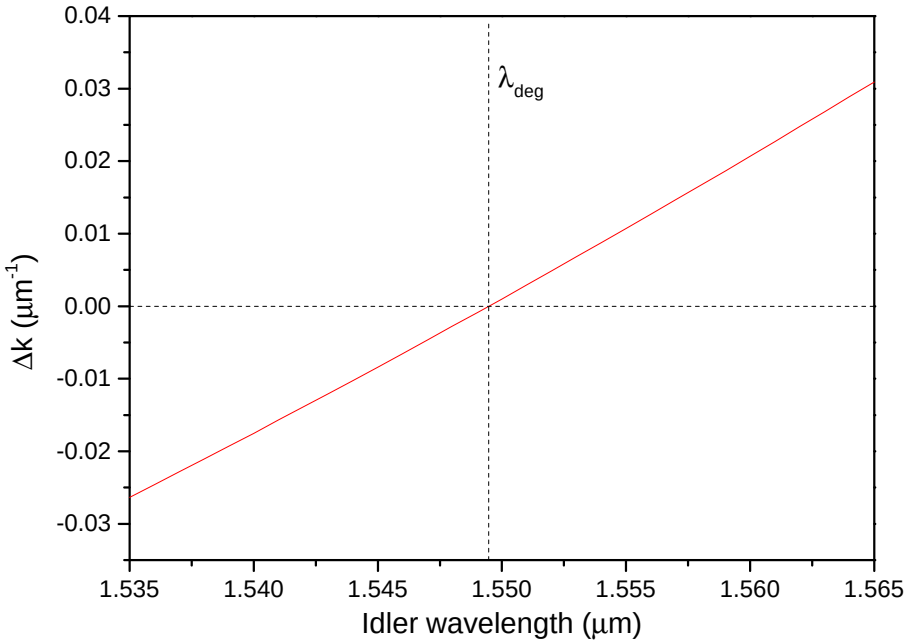

Figure 6.5: Phase mismatch Δk as a function of the idler wavelength. The phase matching point, where $\Delta k = 0$, is found at $\lambda_{deg} = 1549.96\,nm$, and it is the wavelength of all the waves involved in the FWM process.

By using the same semiclassical approach adopted in Section 3.4, it is possible to get an estimation of the generated power starting from the bandwidth of the process B and from the classical efficiency η_{FWM}. Fig.6.6

shows the conversion efficiency as a function of the pump wavelength, with the pump power set to $0\,dBm$.

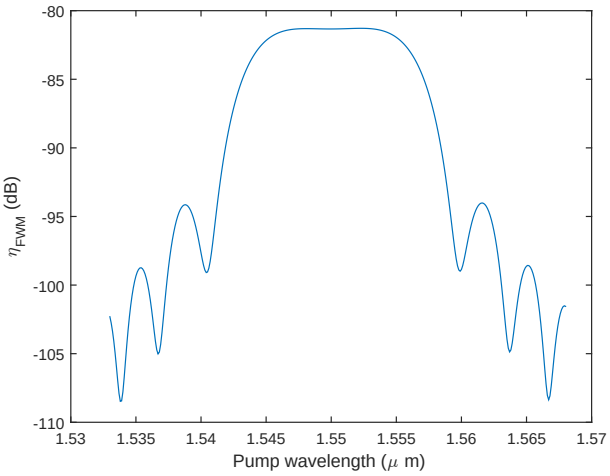

Figure 6.6: Conversion efficiency η_{FWM} as a function of the pump wavelength for degenerate MMFWM in a $1.6\,\mu m$ waveguide.

The peak efficiency is about $-81\,dB$ for a waveguide length of $1.75\,cm$ with $2\,dBcm^{-1}$ of propagation loss. A wide bandwith, $B = 2500\,GHz$ ($\sim 20\,nm$), is achieved by the virtue of the fact that the process is degenerate. By performing the calculations as in section 3.4, the estimated signal/idler power is $\sim -115\,dBm$. This value is comparable to the ones achieved using the resonant structures described in Section 6.2. At this point, a way to separate the generated pairs from the pump in necessary. The lower confinement factor of the TM pump mode with respect to the TE mode where the signal/idler photons are propagating can be exploited to introduce a selective loss. As shown in Fig.6.7, a Titanium Nitride (TiN) metal stripe, of width $450\,nm$, is placed at $250\,nm$ from the top of the waveguide, separated by a thin Silica layer.

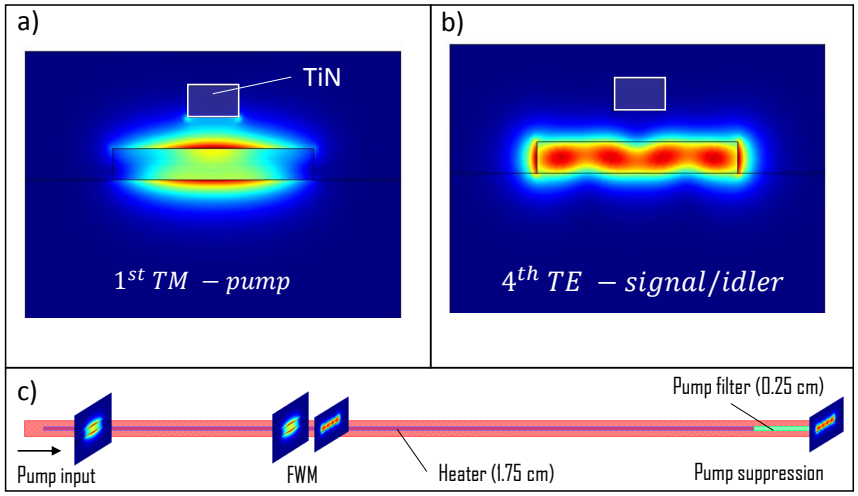

Figure 6.7: (a) Pump mode profile with the TiN metal stripe placed at $250\,nm$ from the top of the waveguide. (b) The same as (a), but showing the signal/idler mode profile. (c) How pump suppression is realized. The pump is coupled into the first TM mode, then FWM occurs during the propagation in the $1.75\,cm$ waveguide (in red), generating signal/idler pairs in TE polarization. The pump is suppressed at the end of the waveguide using a $0.25\,cm$ long TiN metal stripe (in green). A TiN heater (in blue) is placed along the direction of light propagation to tune the phase matching point as shown in Fig.6.8.

The TM mode is highly delocalized along the vertical direction, and couples to the metallic stripe, leading to energy dissipation through the Joule effect (Fig.6.7(a)). The TE mode is instead mostly delocalized in the horizontal direction, and does not efficiently overlap with the TiN (Fig.6.7(b)). The associated propagation losses have been computed through FEM simulations and are $570\,dBcm^{-1}$ for the pump mode and $33\,dBcm^{-1}$ for the signal/idler mode. If the length of the stripe is $2.5\,mm$, the pump gets attenuated by $-142.5\,dB$ while the signal/idler by $-8.25\,dB$. Such value of pump suppression is sufficiently high to achieve a good isolation from the generated photon pair. As discussed in detail in Section 3.4, the phase matching point for combinations involving TE modes is highly sensitive to small changes in the waveguide width. These unavoidably occur during the fabrication process, so a tuning mechanism to restore the perfect phase matching is necessary. This can be provided by changing the temperature of the waveguide or by changing the input laser wavelength, as shown in Fig.6.7(c). If the dimension of the fabricated waveguide is lower than $1.6\,\mu m$, phase matching can be recovered by heating the material (Fig.6.7(a)). On average, a temperature increase of $100\,K$ allows to correct a mismatch of $1.5\,nm$ on the fabricated waveguide dimension with respect to the nominal value. Temperature variations are realized by placing a TiN heater on the top of the waveguide, as shown in Fig.6.8(c). The heater is separated from the optical mode by $900\,nm$ of Silica cladding, so that the energy of the pump and signal/idler modes does not couple to the metal. If the wavguide is larger than the nominal dimension, phase matching is restored by increasing the wavelength of the input laser (Fig.6.8(b)). In this case, a mismatch of $3\,nm$ on the width can be corrected by changing the laser wavelength by $10\,nm$.

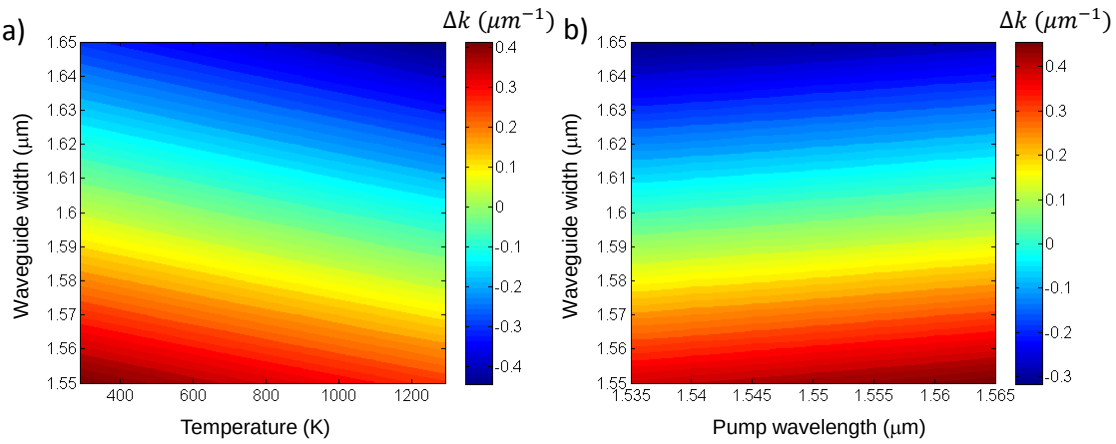

Figure 6.8: (a) Phase mismatch Δk as a function of the waveguide width and temperature. (b) Phase mismatch Δk as a function of the waveguide width and the pump wavelength.

6.3 Pump filter

It is clear from Fig.6.4 that, in order to isolate the photon pairs from the bright pump, a filtering stage which operates a pump suppression higher than $100\,dB$ is needed after the racetrack resonator. For this purporse, the different colours of the pump photons with respect to the ones of the signal/idler pairs are used. The idea is to use a MZI as an interleaver, in which the pump exists from one port of the interferometer and the signal/idler are directed to other ports. This can be achieved by choosing the FSR of the MZI to be equal to twice the FSR of the resonator. In this way, the signal and idler wavelengths are both transmitted in the same port of the MZ, while the pump wavelength, which lies exactly at the half of the FSR of the interferometer, is transmitted to the other port. The design of the MZ is shown in Fig.6.9(a).

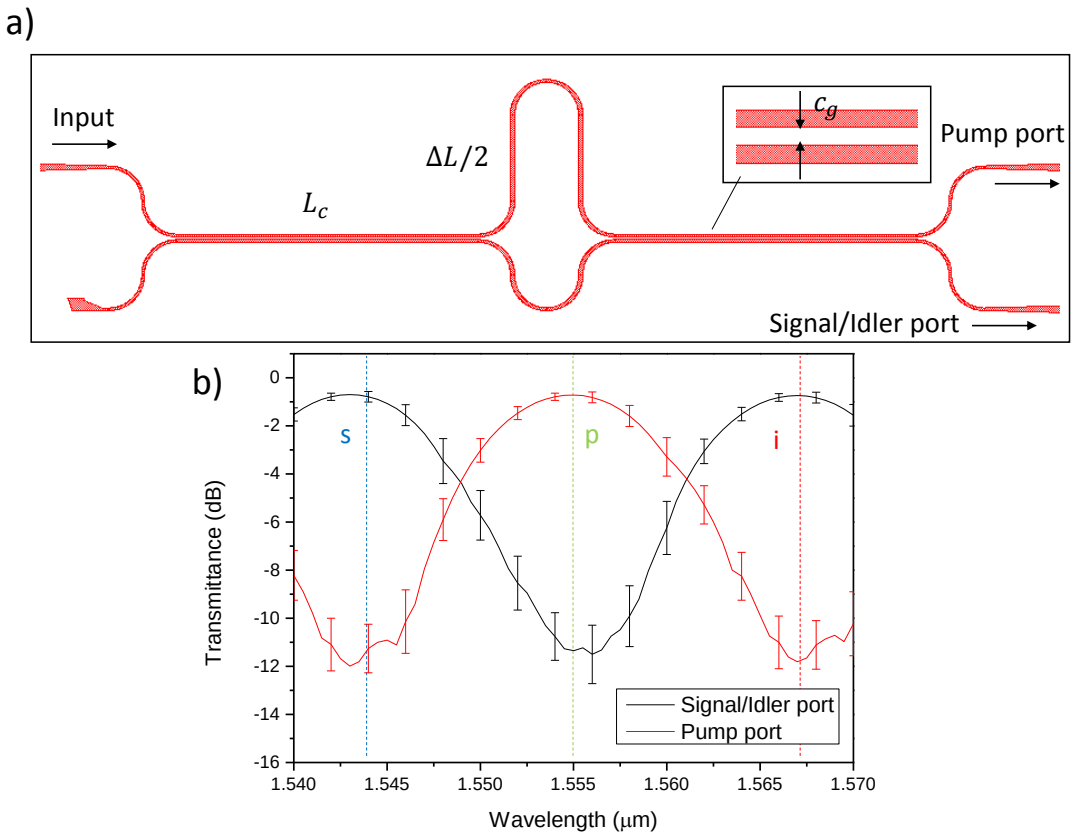

Figure 6.9: (a) Design of the MZI. The couplers have length L_c and coupling gap c_g. The upper arm is longer than the lower one by a quantity ΔL. The pump is directed toward the pump port, while the signal/idler wavelengths are directed toward the signal/idler port. (b) Spectral response of the MZ with the effect of fabrication defects included. The reported spectra is the result of an averaging over 30 independent spectra. The arrows indicate where the pump, signal and idler wavelengths are located.

The MZ is composed by two directional couplers operating as $50:50$ BS at $1.55\mu m$ and by two arms which differ in length by a quantity ΔL. This is chosen to give a $FSR = 26\,nm$. Table 6.1 summarizes all the principal geometrical details. The spectral response of the port in which signal and idler pairs exit is shown in Fig.6.9(b). This takes into account the fabrication detects of the structure, among which:

- Errors in the couplers and consequent deviation from a $50:50$ operation. The width of the waveguides which compose the coupling region are let to deviate from their nominal dimension by a random quantity Δw. The latter is a normally distribuited variable with zero mean value and variance $3\sigma = 50\,nm$. The change in the waveguide width is assumed to be the same for both waveguides. As a consequence, the coupling gap changes by a quantity $-\Delta w$.

- Errors in the width of the waveguide of the longer arm. The error is treated as a perturbation of the nominal width by a quantity Δw_2. The latter is a normally distribuited variable with zero mean value and variance $3\sigma = 50\,nm$.

The magnitude of the errors have been previously estimated from Scanning Electron Microscopy images of grating couplers with similar waveguide widths and gaps.
From the analysis of Fig.6.9, it comes out that the presence of fabrication defects induces a cross talk of $(-11 \pm 1)\,dB$ between the output ports of the interferometer. Such a cross talk is too high for completely

Parameter	Value
L_c	$44.245\,\mu m$
c_g	$400\,nm$
ΔL	$25.315\,\mu m$
Average bending radius	$5\,\mu m$
Waveguide width bending	from $400\,nm$ to $700\,nm$ (lin.tapered)
Waveguide width couplers	$400\,nm$
Waveguide width of ΔL	$700\,nm$

Table 6.1: List of the main geometrical parameters used for the design of the MZ based pump filter. Symbols are indicated in Fig.6.9.

isolating the pump. In order to reduce the cross talk under the $-100\,dB$ level, several MZI are connected in series. The signal/idler port in Fig.6.9(a), where the generated photons are directed, is connected to the input port of the following stage, while the pump port is suppressed using an attenuator which also kills the back reflections. A number of 10 MZ have been used to build the final pump filter. The spectral response is shown in Fig.6.10.

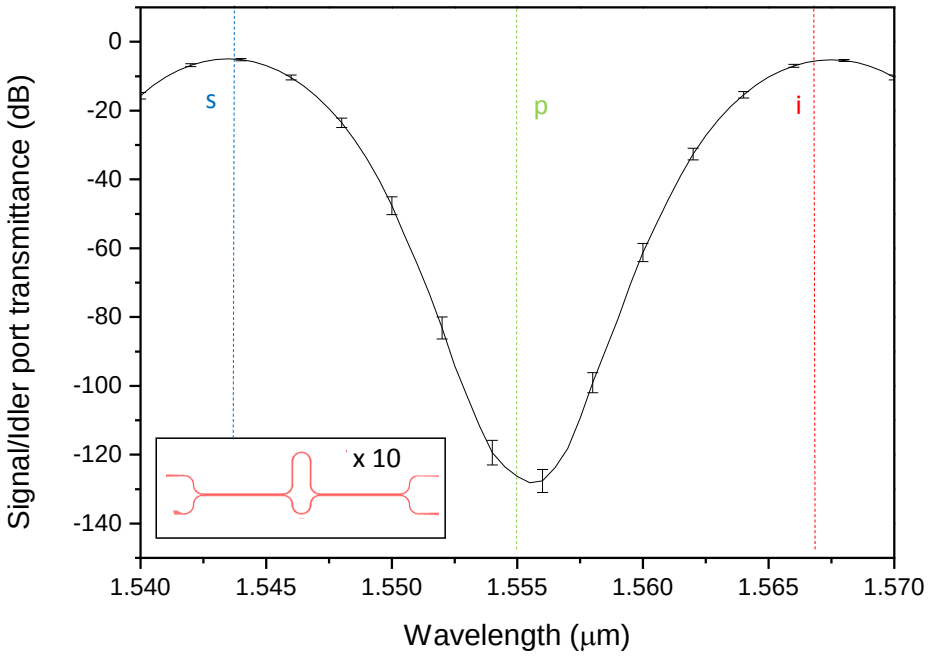

Figure 6.10: Spectral response of the pump port as a function of wavelength for a chain of 10 MZ. Each individual stage has the signal/idler port connected to the input of the following stage. The pump port signal is suppressed using an attenuator which also kills back reflections.

Now, the crosstalk at the pump wavelength is $(-128\pm3)\,dB$, which is an acceptable value to completely isolate the pump from the generated radiation. The transmittance at the signal/idler wavelength is $(-5.2\pm0.3)\,dB$, which represents the insertion loss of the filter.
In conclusion, the advantages of the filter are the simple operating principle and the ability to achieve $\approx -130\,dB$ pump suppression at the expense of only $-5\,dB$ of insertion loss. The major drawback is that the filter operates as an interleaver, so half of the pairs, whose spectral distance contains an even number of FSR of the MZI, are lost because directed into the pump port. Furthermore, the more is the spectral distance between the pairs, the more is difficult to separate them from the pump due to the wavelength dependence of both the FSR of the MZI and of the resonator. As a consequence, the maximum transmittance of the

filter will depart from the spectral position of the signal/idler resonances as their wavelength distance from the pump increases.

6.4 Phase shifters and delay line

In many quantum optics experiment, it is necessary to delay one photon of the pair with respect to the other to manipulate their relative phase or to alter the overlap of their wavepackets in time. Depending on the magnitude $\Delta\tau$ of the time delay, two different approaches can be used. In case of small delays, for which $\omega\Delta\tau < 2\pi$, it is easy to induce small phase shifts by simply placing an electrical heater on the top of a waveguide, and by using the thermo optic effect to change the phase velocity of light. When, a current flows in the heater, a change in temperature ΔT is induced in the waveguide. The effective index of mode changes by a quantity $\Delta n_{eff} \approx n_g \frac{\Gamma_e}{n_0}\frac{dn}{dT}\Delta T$. The phase velocity accordingly changes by a quantity $\Delta v_f = -\frac{c}{n_{eff}^2}\Delta n_{eff}$, and a phase shift of $\Delta\phi = -\frac{\omega}{v_f^2}\Delta v_f L = \omega\Delta\tau(\omega)$ is introduced during the propagation in a section of waveguide of length L. This expression holds for each frequency contained in the spectra $E_{in}(\omega)$ of the input electric field $E_{in}(t)$. If the spectra is centered at ω_0 and it is narrowband (i.e., the bandwidth $\Delta\omega$ satisfies $\Delta\omega \ll \omega_0$), as applies for signal/idler photons, the field $E_{in}(t)$ can be written as $E_{in}(t) = E_0(t)e^{i\omega_0 t}$, where $E_0(t)$ is a slowly varying envelope. The field $E_{out}(t)$ at the end of the waveguide section is then:

$$E_{out}(t) = \int E_0(\omega+\omega_0)e^{i\omega(t+\Delta\tau(\omega))}\,d\omega \tag{6.9}$$

which yelds $E_{out}(t) \approx E_{in}(t+\Delta\tau) = E_0(t+\Delta\tau(\omega_0))e^{i\omega_0(t+\Delta\tau(\omega_0)}$ provided that the phase perturbation $\omega(\Delta\tau(\omega)-\Delta\tau(\omega_0))$ is much smaller than 2π in the frequency range where $E_0(\omega+\omega_0)$ is appreciably different from zero. Since the latter condition is met when $\omega < \Delta\omega$, the above approximation is well justified when $\Delta\omega(\Delta\tau(\omega)-\Delta\tau(\omega_0)) \ll 2\pi$. Using the fact that, from Eq.5.29, $\Delta\omega = 2\pi/\tau_c$, the inequality can be rewritten as $(\Delta\tau(\omega) - \Delta\tau(\omega_0)) \ll \tau_c$. In other words, the delay imparted by the electrical heater can be considered to be the same for all the frequencies of the input spectrum, and equal to $\Delta\tau(\omega_0)$, if the deviation $\Delta\tau(\omega)-\Delta\tau(\omega_0)$ from the average delay $\Delta\tau(\omega_0)$ is less than the coherence time of the radiation. This approximation has been used, as instance, for expressing the fields at the output ports of the MZ as a function of the input ones in Eq.5.32. As example of a phase shifter for which Eq.6.9 applies, the simulations of the electrical heaters described in Section 6.1 are reported. The geometry of the heater is shown in Fig.6.11(a-b), while a cross section of the temperature distribution is shown in Fig.6.11(c).

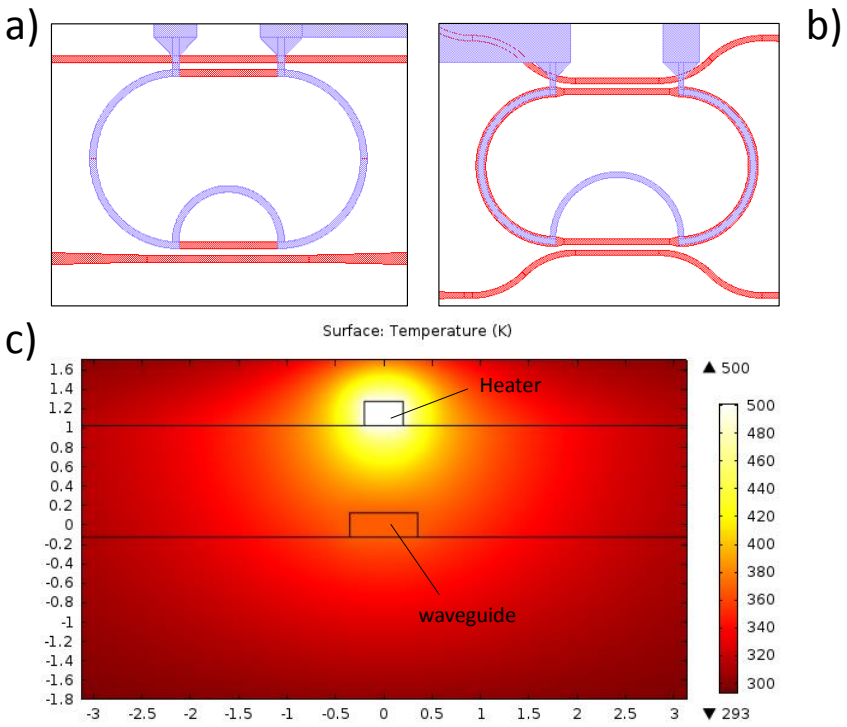

Figure 6.11: (a) Geometry of the heater for the resonator with the 400 nm wide waveguide. (b) Geometry of the heater for the resonator with the with the 700 nm wide waveguide. In both (a) and (b), the blue layer represent TiN while the red one Silicon. The metal stripe has a cross section of 450 $nm \times 250\,nm$. (c) FEM simulation of the temperature distribution across the waveguide section when the heater is at 500 K.

Heaters are separated from the top of the waveguides by an oxide thickness of 900 nm and are realized in TiN. This thickness ensures a good temperature tuning and at the same time it keeps the losses induced by the coupling of the optical energy to the metal stripe negligible. The resonance shift associated to a thermo optic change of the effective index Δn_{eff} is given by Eq.4.15. This relation is used to calculate the resonance shift as a function of the heater temperature, which is shown in Fig.6.12.

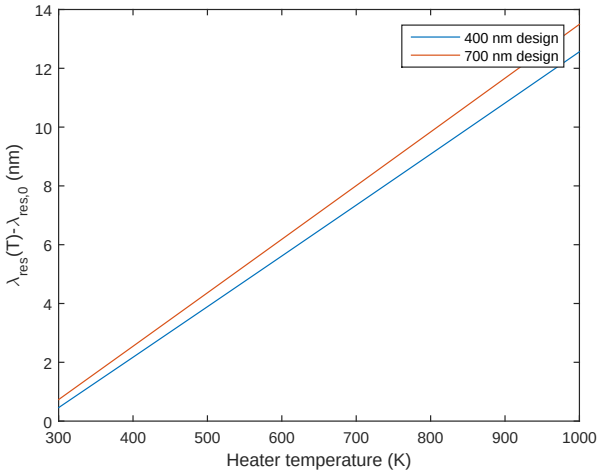

Figure 6.12: Temperature dependence of the wavelength position of the resonance peak $\lambda_{res}(T)$. Data have been subtracted from its value at $T = 273.15\,K$ (room temperature) $\lambda_{res,0} = 1.55\mu m$ to obtain a relative wavelength shift.

It can be seen that by heating the TiN stripe at a temperature of $\approx 950\,K$, the resonance wavelength shifts of an amount which correspond to the resonator FSR ($FSR \approx 13\,nm$ at $1.55\,\mu m$, as described in Section 6.1). This corresponds to a phase shift inside the resonator of 2π (or, equivalently, to a time delay of $\sim 5.2\,fs$). The thermal tuning of the resonance wavelength is essential for:

- Aligning the signal/idler wavelengths exactly on the maximum of the transmittance of the pump filter described in Section 6.3.
- Aligning the signal/idler wavelengths of two independent quantum sources for the creation of N00N and split quantum states, as discussed in section 6.6.1.

When the required time delay is high, and the inequality $\omega\Delta\tau \gg 2\pi$ holds, a different solution is needed. For example, if one wants to use the signal/idler pairs generated by the racetrack resonators for Hong Ou Mandel interference, one has to be able to induce time delays of the order of the coherence time of the generated radiation [226]. To get an estimate of the amount of the required delay, one can consider that the resonators implemented in the so called "broad band" design have a quality factor of $Q \approx 30000$, corresponding to a linewidth of $\Delta\nu_{FWHM} = \frac{\nu}{Q} \approx 6.45\,GHz$. For a lorentzian lineshape, the quantity $\Delta\nu_{FWHM}$ is connected to the spectral width $\Delta\nu$ by the relation $\Delta\nu = \pi\Delta\nu_{FWHM}$ [51], which yields a coherence time of $\tau_c \approx 33\,ps$. It can be easily proved that in order to induce a similar time delay using the thermo optic tuning of the phase velocity, tens of centimeters of waveguide are required. By assuming the realistic value of $5\,dBcm^{-1}$ of propagation loss, this means more than $50\,dB$ of loss. From this analysis, it is clear that different approaches are needed.
The limitation can be overcome by using slow light structures. The simplest one, which will be studied in the following, is to use a chain of resonators in the AP configuration. To understand the working principle, let's consider what happens when narrowband light travels a single resonator. This is described by the transfer function $H_{AP}(\omega) = |H_{AP}(\omega)|e^{i\delta(\omega)}$ reported in section 1.1.4, where $\delta(\omega)$ is the frequency dependent phase shift. According to Eq.6.9, the output field is given by:

$$E_{out}(t) = e^{i\omega_0 t}\int |H_{AP}(\omega+\omega_0)|E_0(\omega)e^{i\omega t}e^{i\delta(\omega+\omega_0)}\,d\omega \tag{6.10}$$

This time the approximation that $(\delta(\omega) - \delta(\omega_0))/\omega \ll \tau_c$ does not hold, and one has to expand the phase according to $\delta(\omega+\omega_0) \approx \delta(\omega_0) + \tau_g(\omega_0)\omega$, where $\tau_g(\omega_0) = \left(\frac{d\delta}{d\omega}\right)_{\omega_0}$ represents the group delay. With this linear approximation, Eq.6.10 gives:

$$E_{out}(t) = E_0^{'}(t+\tau_g)e^{i\omega_0 t}e^{i\delta(\omega_0)} \tag{6.11}$$

where $E_0' = \int E_0(\omega)|H_{AP}(\omega+\omega_0)|\,d\omega$. If $|H_{AP}(\omega)|$ is smoothly varying over the spectral width of $E_0(\omega)$, it can be approximated by the constant value $|H_{AP}(\omega_0)|$, with the result that the output field is proportional to the input field shifted by a time delay equal to $\tau_g(\omega_0)$. By combining N filters in series, one has to multiply $H_{AP}(\omega)$ by itself for N times to produce the final transfer function, with the result that the group delay is increased to $\tau_g^N = N\tau_g$. Fig.6.13 reports the group delay τ_g^N as a function of wavelength for two different chains of $N = 10$ all pass filters. One chain is used as a delay line for the idler photon generated by the $700\,nm$ resonator at wavelength $\lambda_{idler} = 1.567\,\mu m$. The other chain works similarly but for the idler photon generated by the $400\,nm$ resonator at $\lambda_{idler} = 1.565\,\mu m$. The design of the full delay line is shown in Fig.6.14, while the main geometrical parameters are indicated in Table 6.2.

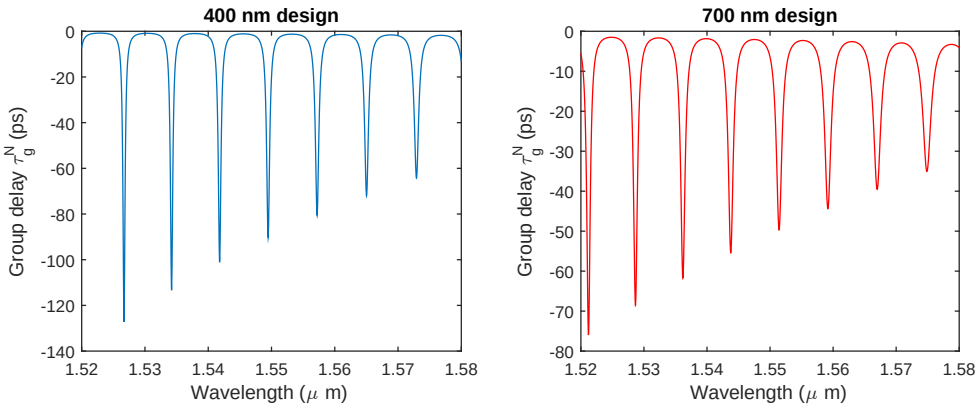

Figure 6.13: Group delay as a function of the wavelength for both the broadbad 700 nm design (red) and for the narrowband 400 nm design (blue).

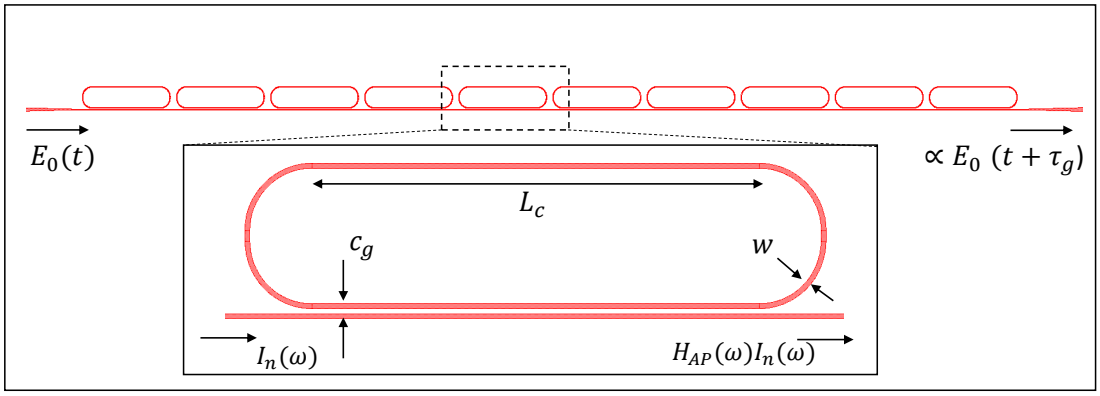

Figure 6.14: Design of the optical delay line, showing the main geometrical parameters. These are the coupling gap c_g, the waveguide width w and the coupling length L_c. The inset contains a zoom of the geometry of one of the AP filters which compose the chain. An input spectrum $I_n(\omega)$ is converted to an output one given by $H_{AP}(\omega)I_n(\omega)$, where $H_{AP}(\omega)$ is the transfer function of the filter.

Parameter	**For broadband design**	**For narrow band design**
N	10	10
Waveguide width (w)	400 nm	400 nm
Coupling gap (c_g)	400 nm	400 nm
Coupling length (L_c)	50 μm	36 μm
Coupling coeff.	58%	33%
Perimeter	133.54 μm	105.12 μm
Losses	5 $dBcm^{-1}$	5 $dBcm^{-1}$
Insertion loss	1.25 dB	2.21 dB

Table 6.2: List of the parameters used for designing the delay lines for both the broadband geometry and for the narrowband one.

For example, if one concentrates on the operation of the delay line implemented in the 700 nm design (red curve in Fig.6.13), it can be seen that the group delay at the ider wavelength is $\tau_g^N \approx 40\,ps$, which is sufficient to exceed the coherence time of the photon wavepacket. Note that this delay line has been designed in such a way that the resonance is exactly centered at the idler wavelength. Probably, this will not hold also for the fabricated device, but thermal trimming will allow to compensate for small resonance misalignments. For

this purpose, a series of electrical heaters will be placed on each all pass filter to uniformly shift the spectral response of the delay line without distortion. The use of heaters allows to perform a continuos tuning of the group delay. As can be seen from Fig.6.13, if the idler wavelength is tuned outside the filter resonance, then $\tau_g^N \approx 0$. On the contrary, if the idler wavelegth is thermally tuned toward the filter resonance, the group delay will monotonically increase and it will reach the maximum value when the two resonances wavelengths will exactly overlap. This is shown in Fig.6.15, in which a time domain simulation of th propagation of a photon pulse has been performed. In this simulation, the complex photon wavepacket is described in the frequency domain by a lorentzian function $\phi(\omega) = \gamma^2/(\gamma^2 + (\omega - \omega_0)^2)$ of central frequency ω_0 and linewidth $\gamma = \frac{1}{\tau_c}$. This constitues an approximation to the true biphoton wavefunction introduced in Eq. 5.19. In Fig.6.15, the quantity $\Delta\lambda$ indicates the mismatch between the photon central wavelength and the resonance of the AP filter.

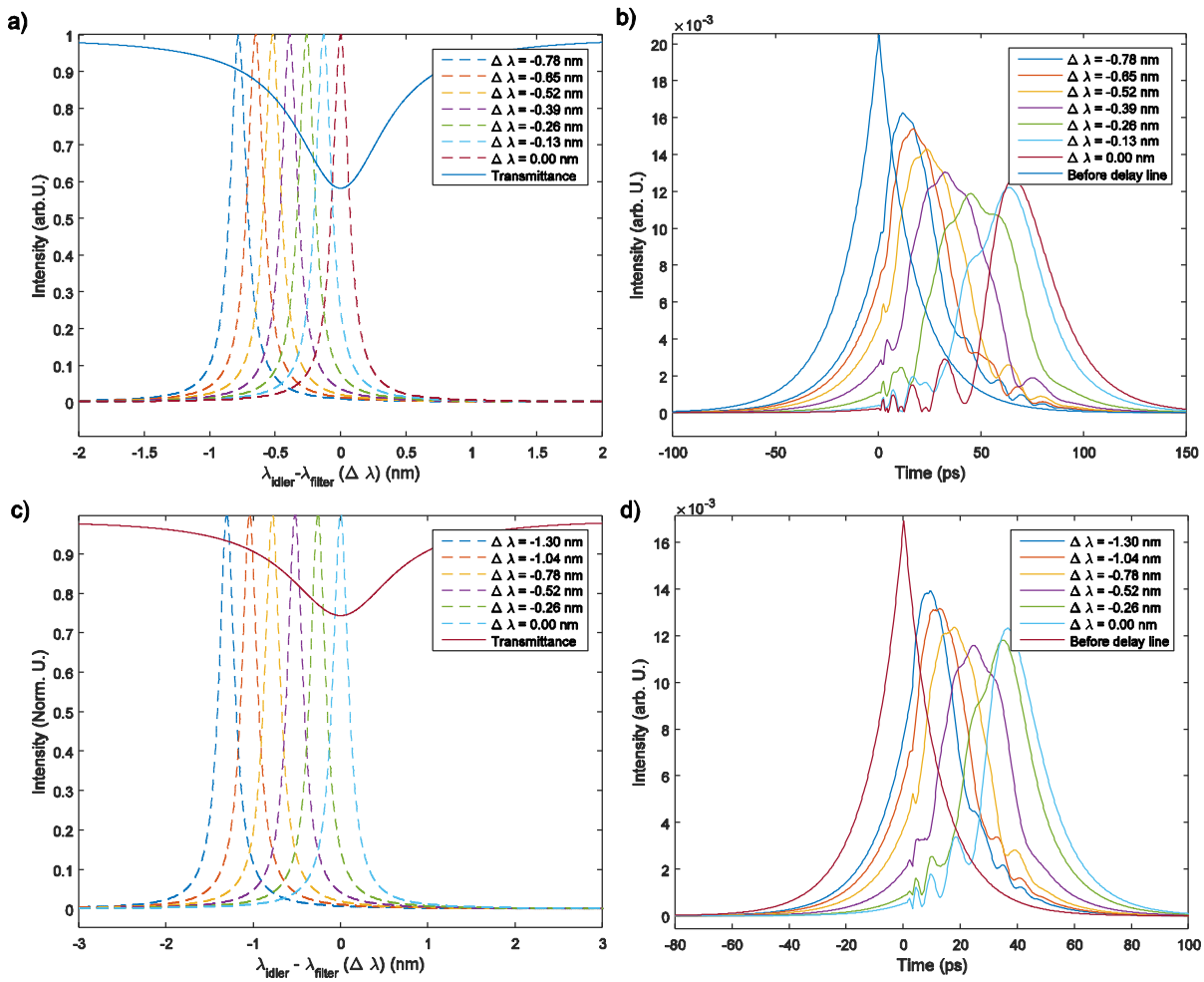

Figure 6.15: (a) Spectrum of the idler photon plotted together with the transmittance of the delay line for different wavelength mismatch $\Delta\lambda$. (b) Time domain simulation of the modulus square of the envelope of the photon wavepacket for different values of wavelength mismatch $\Delta\lambda$. Paneles (a) and (b) refer to the delay line designed for operating with idler photons generated by the $400\,nm$ design. Panels (c) and (d) refer to the delay line designed to operate with idler photons coming from the $700\,nm$ design.

The increasing group delay imparted by the delay line to the wavepacket as the the wavelength mismatch $\Delta\lambda$ decreases is shown in Fig.6.15(b) and Fig.6.15(d) as a shift of the main wavepacket peak towards higher delays. Since the twin signal photons will have a similar coherence time, the delay line can be effectively used

in a HOM experiment. What emerges from Fig.6.15(b) and from Fig.6.15(d) is that the wavepacket is not simply delayed, but it is also distorted. This is due to the fact that the transfer function of the filter can not be considered as perfectly constant over the linewidth of the input radiation, with the consequence that the shape of the initial envelope $E_0(t)$ is no more proportional to the the final $E_0'(t)$. This is the reason why the FWHM of the all pass filter can not be arbitrarily decreased to enhance the group delay. In the design of the delay line, a trade off between the magnitude of the group delay and the amount of wavepacket distortion has been considered. Furthermore, one sees from Fig.6.15(b,d) that the intensity of the delayed field decreases as $\Delta\lambda$ approaches to zero. This comes out from the fact that the on resonance filter transmittance is lower than its value out of resonance.

6.5 Arrayed Waveguide Gratings

The quantum source described in Section 6.1 has the property that it emits a comb of entangled photon pairs. For the narrowband design, only the pairs which are generared close to the pump wavelength have sufficiently high efficiency to be used for further manipulation. On the other hand, for the broadband design, many pairs are generated with similar efficiency even at large spectral distances from the pump. If one considers a signal photon at energy $\hbar\omega_s = \hbar(\omega_p + \Omega)$, then the corresponding entangled idler has energy $\hbar(\omega_p - \Omega)$. All the other idler photons of the comb which do not satisfy this energy relation are not entangled with the considered signal, so in principle they constitute accidental counts in coincidence measurements. Furthermore, if an interferometer is designed for the manipulation of a pair, it will not work for another pair of a different colour. This is because the phase shifters, the splitters/combiners, the delay lines and all the other components which compose the integrated network are strongly wavelength sensitive. From these considerations, it comes out that to simplify the design of the network and to perform a clean interferometric experiment it is necessary to separate the generated pairs on the basis of their different color. The structure implemented for achieving this is the AWG. The device operates as a wavelength demultiplexer. A set of different wavelengths which travels collinearly in the AWG input waveguide is chromatically dispersed, and each wavelength is directed into a different output channel waveguide. Although it is not the aim of this work to cover in detail the physics of the AWG, the basic parameters are now reviewed. The AWG is made by three main components, as shown in Fig.6.16(a).

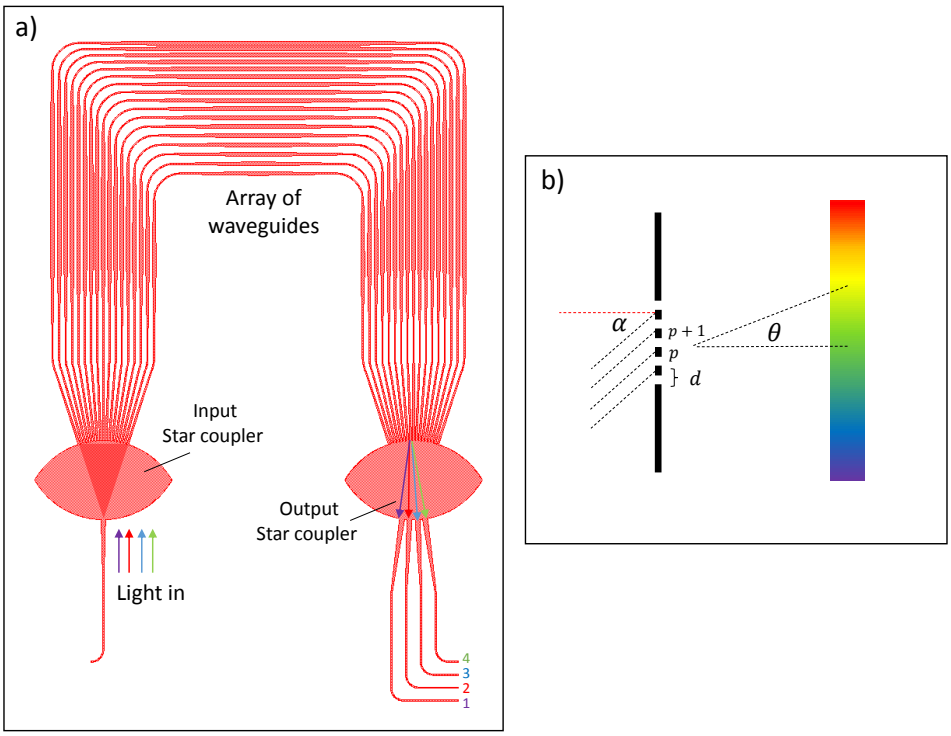

Figure 6.16: (a) Geometry of an AWG, with indicated the main components. (b) Schematic of a transmittive diffraction grating with period d. Here, α is the angle of incidence of the input beam, and θ the angle of observation of the diffracted field. Each element of the grating is labeled with an increasing index p. The output channels are numbered from 1 to 4.

The first is the input star coupler, in which the light carried by the input waveguide is let to freely diffract. The end of the star coupler is of circular shape, with a radius of curvature of R, and has a number of N_{in} waveguides which collect the diffracted light. The circular shape ensures that the phase profile of the diffracted light is constant over all the waveguides. The n^{th} waveguide has a length L_n which is given by $L_n = L_{n\pm1} \pm \Delta L$. All the waveguides, whose center to center separation is given by d, shine light into the ouput star coupler. As a consequence of the different length of the waveguides, the phase profile at the input of the second star coupler linearly changes with the curved abscissa. The diffracted light in the second star coupler is collected by a number of N_{out} output waveguides spread by a quantity D. The way light is chromatically dispersed and focalized into different waveguides can be intuitively explained by making the analogy with a free space transmissive diffraction grating shown in Fig.6.16(b). When white light is normally incident on the grating, the transmitted maximum power is localized into the 0^{th} diffraction order, which lies in the same position for all the wavelengths ($\theta = 0^\circ$ in Fig.6.16(b)). The higher order diffraction peaks satisfies the grating's equation [203]:

$$d\sin(\theta) = m\lambda_m \tag{6.12}$$

where d is the grating periodicity, θ is the observation angle and m an integer number.
If the input beam is titled by an angle α, Eq.6.12 modifies to:

$$d(\sin(\theta) - \sin(\alpha)) = m\lambda_m \tag{6.13}$$

which states that the position of the 0^{th} diffraction order is shifted from $\theta = 0$, and what is most important,

the shift depends on the wavelength. In this way it is possible to separate the different colours on the basis of the different angles at which the 0^{th} diffraction order is created. This principle is applied to chromatically dispersed light in the AWG as well. The phase of the titled beam at the p^{th} element of periodicity of the transmittive grating is given by $\phi_p = p\Delta\phi$, where $\Delta\phi = d\sin(\alpha)$, and thus is linearly increasing with the number of the element. The same happens in the AWG, where the phase of the field at the input of the second star coupler is given by $\phi_{n,wg} = n\Delta\phi_{wg}$, where $\Delta\phi_{wg} = n_{eff}\Delta L$ and n is the number of the waveguide. In the AWG, the output waveguides are placed where the 0^{th} diffraction orders of the different wavelengths are located. The AWG design starts from the knowledge of the spectral position of the input wavelengths, which must be equally spaced by a quantity $\Delta\lambda$, and from the number of desired output channels. The first is given by the resonance wavelengths of the resonators constituting the quantum sources. The second depends on the number of pairs which one wants to filter from the comb. Once that these parameters are fixed, the practical design rules for finding the geometrical parameters of the AWG are given by [231]:

$$\Delta\lambda = \frac{n_g R\Delta L}{n_{eff}^{sc} d\lambda_0} \tag{6.14}$$

$$N_{max} = \frac{R\lambda}{n_{eff}^{sc} dD} \tag{6.15}$$

where n_{eff}^{sc} is the effective index of the star coupler and λ_0 is the wavelength collected in the central output channel indicated with the label 2 in Fig.6.16(a). λ_0 is determined by the equation:

$$n_{eff}(\lambda_0)\Delta L = q\lambda_0 \tag{6.16}$$

with q an integer number. The number N_{in} of waveguides at the output of the first star coupler determines the losses of the device and the wavelength resolution of the output spectrum, i.e, the cross talk between the output waveguides. It is of considerable interest to have a number of input waveguides which is as high as possible, compatibly with the fabrication resolution and with the cross talk issues that arises when the waveguide spacing d decreases. This is because as N_{in} increases, the portion of the diffracted wavefront which is coupled to the waveguide array accordingly increases, and losses are consequently lowered. The number of waveguides of the array plays the same role of the number of grooves which are illuminated in a free space diffraction grating. The higher is this number, the narrow is the linewidth of the diffraction peaks [203]. However, for most of the routing applications, one is interested in having a device with insertion loss which are as low as possible, and a common design rule which fulfills this requirement is:

$$N_{in} = \frac{0.666\, R}{d} \tag{6.17}$$

which fixes the relation between d, N_{in} and R in such a way that 90% of the diffracted energy in the input star coupler is coupled to the array of waveguides. By following the design rules given by Eq.6.14 through Eq.6.17, two AWGs have been simulated and designed for the demultiplexing of a photon pair generated in the $700\,nm$ resonator and in the $400\,nm$ resonator. Each AWG has three output channels: one is centered at the pump wavelength and the two adjacent ones are centered at the signal and idler wavelength respectively. In this way, only the photon pair which is closest to the pump wavelength is collected. The geometrical details of the design are given in Table 6.3. The simulated spectral response of each channel is shown in Fig.6.17. The simulation is the result of the averaging of 30 different spectral responses, in which the width of the waveguides of the array (which constitute the most sensible element) are let to deviate from their nominal value by a quantity Δw. This is a normally distribuited variable with zero mean value and standard deviation $3\sigma = 15\,nm$.

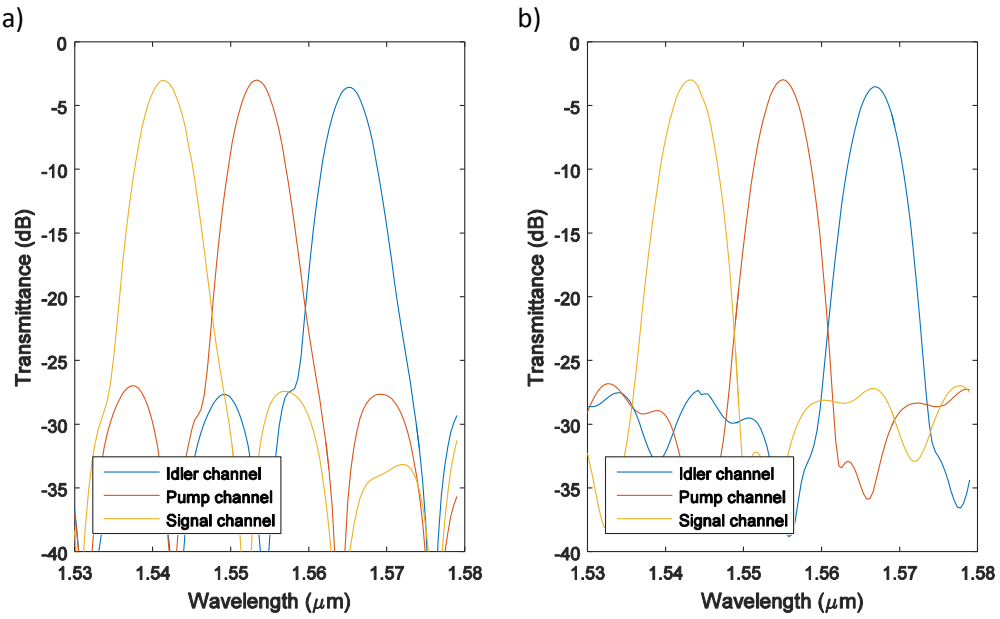

Figure 6.17: (a) Spectral response of each output channel of the AWG for the resonator of $400\,nm$ width. (b) Spectral response of each output channel of the AWG for the resonator of $700\,nm$ width.

Parameter	**Value ($400\,nm$ design)**	**Value ($700\,nm$ design)**
R	$30.63\,\mu m$	$30.63\,\mu m$
N_{in}	16	16
N_{out}	3	3
ΔL	$11.224\,\mu m$	$11.24\,\mu m$
d	$0.4\,\mu m$	$0.4\,\mu m$
D	$0.9\,\mu m$	$0.9\,\mu m$
λ_0	$1.553\,\mu m$	$1.55\,\mu m$
w_{in}	$0.8\,\mu m$	$0.8\,\mu m$
w_{out}	$1.99\,\mu m$	$1.99\,\mu m$

Table 6.3: List of the key parameters used to design the AWGs.

From Fig.6.17, it can be seen that for both designs the channel cross talk is below $-25\,dB$, and that the insertion loss at the signal/idler wavelength are at the order of $-3.5\,dB$.

6.6 Examples of integrated quantum circuits

In the previous sections, the main builnding blocks which compose a quantum circuit have been designed and simulated. Here, two examples of the complete networks are reported to show the full system. The first example is an integrated implementation of the experiment described by J.Silverstone et. al. [180], where a reconfigurable circuit capable of manipulating entangled states produced by spontaneous FWM in spiral waveguides is demonstrated. In the following circuit, the spiral waveguides will be replaced by racetrack resonators. The pump filter and the delay line, which in Ref.[180] were implemented off-chip, will be integrated and thermally tuned directly on the chip. The second example is the realization of Hong Ou Mandel interference using degenerate photon pairs produced by Multi Modal spontaneous FWM in straight silicon waveguides.

6.6.1 Reconfigurable network for the creation and manipulation of N00N and antibunching states

The schematic of this network is shown in Fig.6.18.

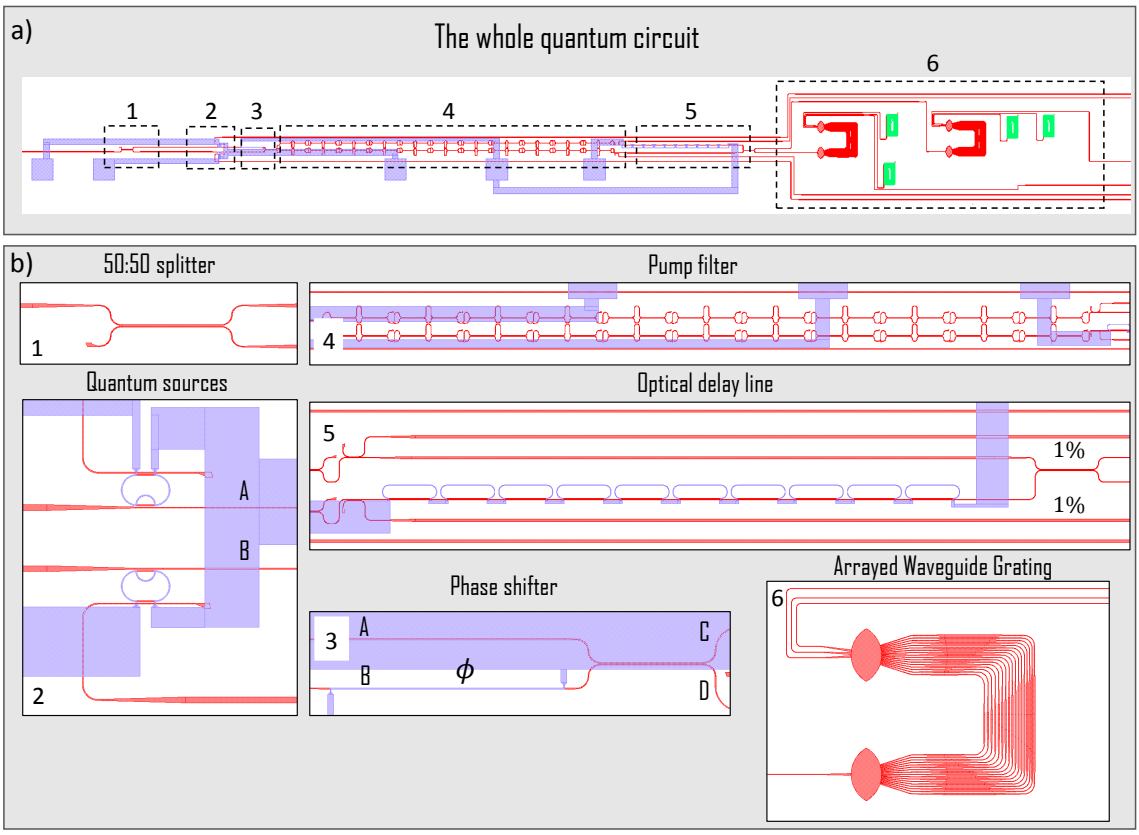

Figure 6.18: (a) The whole integrated quantum network. Sections labeled with numbers from 1 to 5 indicate different building blocks, which are shown in detail in the lower panel. The network has three different layers: the waveguide layer (red), the metal layer used for the heaters (blue), and the metal layer used to absorb the undesired energy from the waveguide (green layer, see section 6.2). (b) Zoomed view of the main building blocks which constitute the network.

This implements racetrack resonators of $400\,nm$ width for a narrow band comb generation of photon pairs. The network is organized in three different layers. The main layer is the one where waveguides are fabricated (indicated in red in Fig.6.18(a)). The second one (indicated in green in Fig.6.18(a)) is a TiN metal layer, which is separated by $100\,nm$ of oxide from the top of the waveguides. This layer is used to absorb light from the lower waveguides, and it is implemented to cancell reflections. The metal layer (indicated in blue in Fig.6.18) is realized in TiN and is placed $900\,nm$ above the waveguide layer. This is used to realize the electrical heaters. By moving from left to right in Fig.6.18(a), a bright pump laser at $1.55\,\mu m$ is coupled into the input waveguide and it is split by a $3\,dB$ directional coupler (1). The two outgoing arms excite the quantum sources (2), which will generate photon pairs through sFWM. In the weak pump approximation, the probability that both sources generate a pair is negligible, so pair generation will occur in one of the two resonators, with equal probability. Since only one pair of the comb will be post selected by the AWG filters, it is sufficient to consider the evolution of the quantum state associated to a single pair. The state $|\Psi_{in}\rangle$ of the selected pair of signal and idler photons after the sources can be written as:

$$|\Psi_{in}\rangle = \frac{1}{\sqrt{2}}\left(\left|1^A_{\omega s}1^A_{\omega i}\right\rangle - \left|1^B_{\omega s}1^B_{\omega i}\right\rangle\right) \tag{6.18}$$

where A and B labels the spatial mode where the photon is generated (A = waveguide A, B = waveguide B), while $\omega_{s,i}$ designates the frequencies of the signal/idler photon. The state of Eq.6.18 is called a N00N state (in this case, $N = 2$) [179], and is an equal superposition of two photons in spatial mode A and two photons in spatial mode B. This corresponds to a bunching state, because the probability to register a coincidence photodetection event from waveguide A and B is zero. The state in Eq.6.18 can be manipulated using the phase shifter (3) placed on a section of the waveguide A. The phase shifter is an electrical heater as the ones described in Section 6.4, which operates in the regime where the imparted phase ϕ is $\phi \leq 2\pi$. After the phase shifter, the state $|\Psi_{in}\rangle$ becomes:

$$|\Psi_{in}\rangle = \frac{1}{\sqrt{2}}\left(\left|1^A_{\omega s}1^A_{\omega i}\right\rangle - e^{i2\phi}\left|1^B_{\omega s}1^B_{\omega i}\right\rangle\right) \tag{6.19}$$

where the factor 2 comes from the fact that two photons travels in the same spatial mode A. Note that an equivalent phase shift will be acquired by a single photon of doubled energy. The state in Eq.6.19 is then sent to a $3\,dB$ beamsplitter, again realized using a directional coupler. The output state then becomes:

$$|\Psi_{out}\rangle = \sin\phi\,|\Psi_{split}\rangle + \cos\phi\,|\Psi_{N00N}\rangle \tag{6.20}$$

with:

$$|\Psi_{split}\rangle = \frac{i}{\sqrt{2}}\left(\left|1^C_{\omega_s}1^D_{\omega_i}\right\rangle + \left|1^C_{\omega_s}1^D_{\omega_i}\right\rangle\right) \tag{6.21}$$

$$|\Psi_{N00N}\rangle = \frac{1}{\sqrt{2}}\left(\left|1^C_{\omega s}1^C_{\omega i}\right\rangle - \left|1^D_{\omega s}1^D_{\omega i}\right\rangle\right) \tag{6.22}$$

The state $|\Psi_{split}\rangle$ describes a situation in which there is one photon in mode C and one photon in mode D, with equal probability. There is a complete indetermination on the colour of the photon occupying each mode. One sees from Eq.6.20 that, by tuning the phase ϕ, one can shift from $|\Psi_{split}\rangle$, when $\phi = \frac{\pi}{2}$, to $|\Psi_{N00N}\rangle$,when $\phi = 0$. This constitues an example of deterministic preparation of a quantum state of light. Next, the bright pump is filtered from both the waveguides C and D using the cascated of MZ (4) described in Section 6.3. At this point, 1% of the signal is picked from each waveguide and monitored. An off-chip coincidence experiment can be performed to find the value of current to be applied to the electrical heater in order to set the quantum state $|\Psi_{out}\rangle$ to the desired one. The observation of a minimum in the coincidence rate between channels C and D would correspond to the quantum state $|\Psi_{N00N}\rangle$, while a maximum would correspond to the state $|\Psi_{split}\rangle$. Once that the state is prepared, it can be further manipulated. In the case of the network shown in Fig.6.18, an HOM interference with non degenerate photons is performed. This is achieved by configuring the output state $|\Psi_{out}\rangle$ to $|\Psi_{out}\rangle = |\Psi_{split}\rangle$, and then by placing an optical delay line (5) at the end of waveguides C or D. The working principle of the latter is the same described in Section 6.4, but a little care has to be paid to modify the geometry in such a way that the FSR of the delay line coincides with the one of the resonator constituting the quantum source. This is because the colour of the photon which enters into the delay line is not know in advance (see Eq.6.21), but the latter has to impart a similar delay independently on the colour. For example, if the FSR are not matched, the signal wavelength can be on resonance with the ones of the delay line, while the idler wavelength can lie completely off resonance. As a consequence, the device will work as a delay line only for signal photons. At the end of the delay line, the selected pair is separated from the other using two AWGs (6), which work as the interference filters of

the HOM experiment described in Ref.[180]. The two outputs of the AWGs are then collected off chip using lensed fibers and sent to two photon counters coupled to a coincidence electronics. The use of thermal heaters is essential for the outcome of the experiment. They are used to:

1. Align the resonances of one source with the resonances of the other source. This is needed since the pair generated by one source has to be indistinguishable from the pair produced by the other source on the basis of the signal/idler color.

2. Apply the phase ϕ required for tuning the output state between $|\Psi_{split}\rangle$ and $|\Psi_{N00N}\rangle$.

3. Apply a tunable group delay.

It is worth to note that the wires which connect the heaters to the metal pads in Fig.6.18 are characterized by a very large cross section to decrease their resistivity. This allows to reduce the dissipated electrical power in the circuit regions where the meaterial temperature has not to be changed. The magnitude of the coincidence rate expected from the HOM interference can be estimated by knowing the insertion loss of each stage. These are summarized in Table 6.4 and give a total insertion loss of $\approx -17.75\,dB$. This value has to be considered twice since a coincidence event is registered only when both photons of the pair survive from the source to the detectors. By considering $0\,dBm$ of input pump power, the expected generation rate is, from Fig.6.4(c-d), of the order of $1\,MHz$. The coincidence rate will be reduced by a factor $-35.5\,dB$, which gives $\approx 300\,Hz$. This value can be easily detected using the coincidence electronics described in the experiment in Section 5.3.2.

Network block	**Insertion loss** (dB)
Pump filter	5
Delay line	1.25
AWG	3.5
Off chip light coupling	8

Table 6.4: A summary of the approximate insertion loss of the different blocks which compose the quantum network.

6.6.2 On chip Hong Ou Mandel interference with degenerate photon pairs

The main difference between the circuit described in this section and the one in Fig.6.18(a) lies in the type of quantum sources that is implemented. Here the racetrack resonators are replaced with straight waveguides, and the pair generation occurs through MMFWM. The waveguides are engineered in such a way that the FWM process is degenerate, i.e., signal and idler have the same wavelength. As described in Section 6.2, the pump field has TM polarization and it propagates in the fundamental mode of the waveguide, while signal/idler fields have TE polarization and are generated in the fourth order mode. The schematic of this circuit is shown in Fig.6.19.

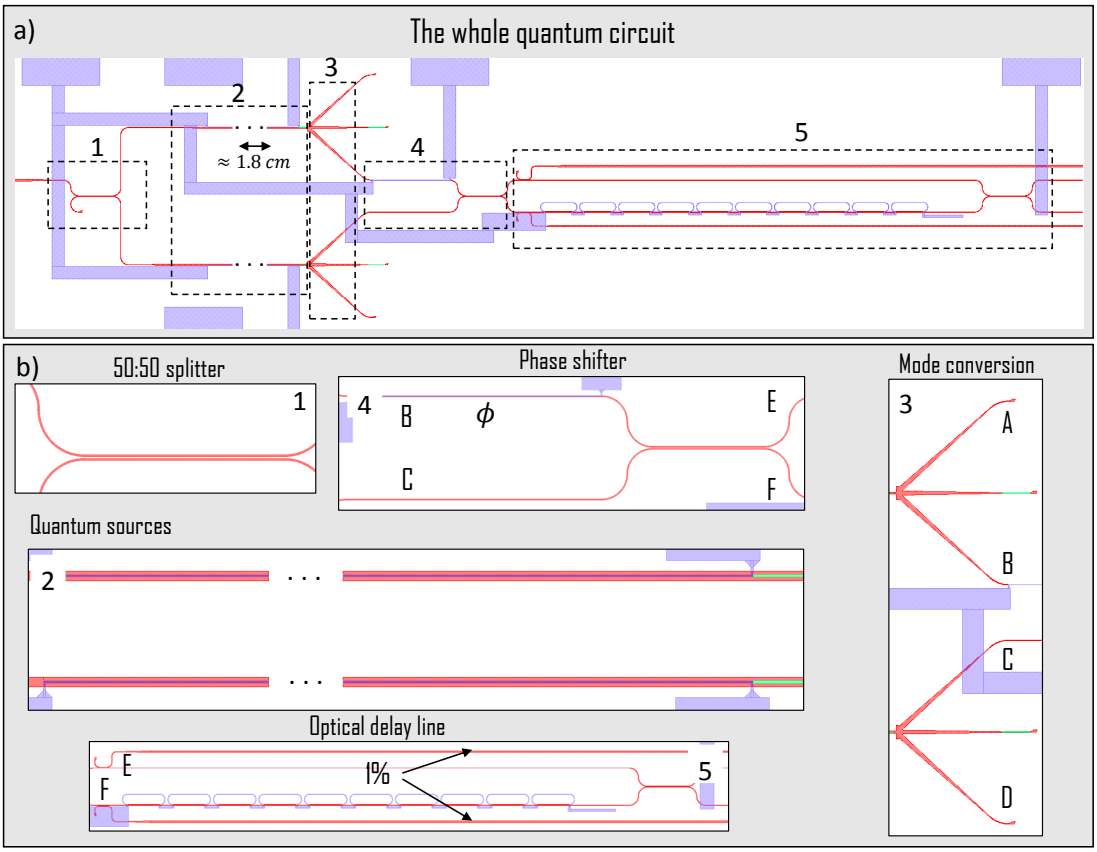

Figure 6.19: (a) The whole integrated quantum circuit. Sections labeled with numbers from 1 to 5 indicate different building blocks, which are shown in detail in the lower panel. The circuit has three different layers, whose function and color are the same as in Fig.6.18(a). (b) Zoomed view of the main building blocks which constitute the circuit.

Similarly to the circuit of Fig.6.18(a), the whole structure is realized in three layers. The type of material, the thickness and the position (except for the green layer, which lies $250\,nm$ from the top of the waveguides) of these layer are the same as the ones described in Section 6.6.1 and shown in Fig.6.18(a), reason why the same colors are used in Fig.6.19. By moving from left to right, the bright pump is split by a $3\,dB$ directional coupler to obtain two coherent beams. In the two outgoing waveguides, of $2\,cm$ length, photon pairs are generated through MMFWM. After $1.75\,cm$ of propagation, a metal stripe of $0.25\,mm$ is positioned at the center of the waveguide to suppress the pump. As detailed in Section 6.2, the lower confinement factor of the pump with respect to the signal/idler beams and its different modal field profile is used to induce selective loss on the pump beam. The result is that the pump is attenuated by the metal stripe by approximately $-142.5\,dB$, while the signal/idler fields are attenuated by only $\approx -8.25\,dB$. In order to manage more easily the generated pair, it is desirable to convert the fourth order mode in which entangled photons are propagating into the fundamental mode. For this purpose, the interferometer described in Section 3.6 is used. Two waveguides, forming a relative angle θ, input light into a FPR. The power is carried by the fundamental mode of each waveguide. The diffracted field is coupled into the m^{th} mode order of a multimode waveguide. If the direction of light propagation is reversed, light will be coupled from the m^{th} mode order into the fundamental mode of the two waveguides at the input of the FPR. This property is used to convert the fourth order mode of the signal/idler pair into a fundamental mode. Each interferometer has two output waveguides (A-B and C-D respectively) in which the pair can be split or bunched. By post selecting only the case in which both photons are directed into one of the two waveguides (waveguide B and C in Fig.6.19(b), panel 3), the state

at the output of the two interferometers can be written as:

$$|\Psi_{N00N}\rangle = \frac{1}{\sqrt{2}}\left(\left|2^B_{\omega_p}0^C_{\omega_p}\right\rangle - \left|0^B_{\omega_p}2^C_{\omega_p}\right\rangle\right) \tag{6.23}$$

whis is a N00N state with $N = 2$. Post selection can be done by placing an attenuator at the end of waveguides A and D, which scatters the incoming photons into radiative modes. Next, the state described by Eq.6.23 is manipulated to create the degenerate split state $|\Psi_{split}\rangle = i\left|1^E_{\omega_p}1^F_{\omega_p}\right\rangle$. This is done by using the same procedure discussed in Section 6.6.1. The state can be monitored by taking 1% of the intensity from waveguide E and F and by performing a coincidence measurement. To realize the HOM interference, one of the two photons is sent into a delay line, of the same kind described in Section 6.4. Signal and idler photons are then collected using two lensed fibers and sent to two photon counters coupled to a coincidence electronics. The total loss experienced by a photon which travels from the source to the detectors is given by the sum of the insertion loss of each stage, which are listed in Table 6.5. This sum gives $\approx -22.5\,dB$. Again, the loss factor has to be counted twice in order to account for the joint probability that both photons of the pair reach the detectors, which yelds $\approx -45\,dB$. With the pump power set to $10\,dBm$, the expected coincidence rate should be of the order of $10\,Hz$.

Network block	**Insertion loss (dB)**
Interferometer (with post selection)	5
Delay line	1.25
Pump filter (metal stripe)	8.25
Off chip light coupling	8

Table 6.5: A summary of the approximate insertion loss of the different blocks which compose the quantum network.

6.7 Summary and conclusions

In this chapter it is reported the design and simulation of the main building blocks which form an integrated circuit used for generating and manipulating quantum states of light. Signal and idler entangled photon pairs are produced using non degenerate spontaneous FWM in racetrack resonators. Two different resonator designs have been investigated. In the first, a broadband comb of photon pairs is generated by exploiting the low group velocity dipersion of the resonator waveguide. In the second, the waveguide width has been chosen to achieve high group velocity dispersion at the pump wavelength, with the result that the generated comb is narrow band. The efficiency of the process and the expected photon flux is computed by a semi classical approach, in which the dynamics of the fields inside the resonator is treated as classical, while the input seed which stimulates the FWM process comes from a quantum mechanical analysis. The geometry of the resonators are then optimized to achieve the highest efficiency, compatibly with the resolution limits imposed by the photolithographic process. A filter constituted by a chain of 10 Mach Zenhder interferometers working as interleaver for the pump, the signal and the idler wavelengths is presented. This achieves $-130\,dB$ of pump rejection, thus isolating the photon pairs from the bright pump. Some tools for photon manipulation are then presented. One is the phase shifter. This allows to impart a variable phase to the propagating light, and is implemented by using electrical heaters on the waveguides to change the effective index of the material through the thermo optic effect. The variable phase is used to prepare the quantum state at the output of the circuit. In the proposed examples, this can be either a split (or antibunching) state, in which the signal and idler photon travel in different spatial modes, or a N00N (or bunching) state, where both photons are bunched into the same spatial mode. Other tools are used for photon manipulation after that the state is prepated. These include optical delay lines and AWGs. The firsts are used to delay the arrival time of a photon with

respect to the other by a quantity which is of the order of the single photon coherence time. Such delays can be obtained in slow light structures like chains of AP resonators. AWGs are implemented for demultiplexing the pair. They direct the signal photon into one channel and the idler photon into another one. In principle, they can be also used for demultiplexing the whole comb of signal/idler pairs generated by the resonators. Two quantum circuit examples are presented at the end of the chapter. These integrate several functionalities for performing a complete quantum optics experiment on a chip. The experiment includes photon pair generation, bright pump suppression, quantum state preparation, and HOM two photon interferometry. The total insertion loss of each circuit has been analyzed in order to predict the expected coincidence rate of the HOM experiment. The major limitation comes from the quite high insertion loss encountered during the input and output coupling of light from the chip. The insertion losses of the integrated photonic components are comparable to the ones of the off-the-shelf optical components implemented in free space experiments. The only functionalities which are not integrated in the circuit, are the pump laser and the photon detectors. As discussed in section 0, the on chip integration of the pump laser and of the photodetectors will be the next steps of the project SIQURO, and will be performed after that the circuit operation will be experimentally validated. The designs discussed in this chapter are at the present being fabbricated.

Conclusions

This thesis work has been largely carried out within the framework of the project SIQURO, which is focused on the study of integrated devices for quantum optics applications. Different milestones of the project were covered in the different chapters. Chapter 3 theoretically studied and experimentally demonstrated, MMFWM in integrated straight Silicon waveguides. This chapter was devoted to investigate the possibility of using MMFWM as a tool for the generation of entangled photon pairs through Spontaneous FWM. High fiber to chip coupling losses prevented the observation of the spontaneous process, but nevertheless the proof of concept has been validated by Stimulated FWM. Novel approaches for selective mode excitation have been proposed, which led to the design of innovative integrated devices which exploit two beam interference for maximixing the coupling to specific mode orders by shaping of the electric field. These new devices should minimize the coupling losses while attaining excellent mode selectivity, thus enabling the observation of photon pairs. The research toward innovative quantum sources then moved to chapter 4, in which it is investigated the $\chi^{(2)}$ tensor of strained Silicon resonators. This chapter was focused to the measurement of the different $\chi^{(2)}$ tensor componens of strained Silicon, in order to prove the efficiency and, thus, the feasibility of on chip quantum sources based on $\chi^{(2)}$-mediated SPDC. The presence of second order nonlinearities has been proven through the dynamical electro optic effect using homodyne detection. This approach differs from the other works reported in literature, which are all based on the static electro optic effect. The technique offered enhanced sensitivity, immunity to noise sources and was able to reveal novel physical features which were hidden in static measurements. Thanks to this approach, it has been possible to detect plasma carrier dispersion as the main mechanism involved in the electro optic modulation, which then masks truly $\chi^{(2)}$ effects. A method to distinguish the two contributions has been implemented, which relies on time resolved measurements of the electro optic modulation. The results of these measurements confirmed the hypotesis of an electro optic modulation of free carrier origin, and set an upper limit to the magnitude of the $\chi^{(2)}$ tensor components. This work furnished the evidence that previously reported values for the $\chi^{(2)}$ components were overestimated because of the free carrier contribution. By virtue of the very weak (if present) induced second order nonlinearity, a doubt can be cast on the feasibility of integrated SPDC sources.
The preliminar results on the efficiencies of photon pair generation of both $\chi^{(2)}$ and $\chi^{(3)}$ sources were not satisfactory, so in chapter 5 it is discussed about a free space quantum optics experiment which implements photon pairs produced by SPDC in an external PPLN crystal. Such experiment can be viewed as the free space implementation of an integrated Mach Zenhder interferometer, which will be one of the interferometric structures for photon manipulation to be realized in the next developements of the SIQURO project. A theory has been enstablished to interpret the two photon interference patterns which emerged from coincidence measurements of the outputs. Such a theory can be straightforwardly applied to the integrated version of the device. A novel experimental technique which allows to smoothly change the phase of one arm of the interferometer, enabled to obtain very low noise interference patterns even with few coincidence events. As a consequence of the particular asymmetric excitation of the device, new interference effects have been reported. These arise from the superposition of bunching and antibunching states which coherently interfere

at the output of the interferometer. Future perspectives of the project have been given in chapter 6, where the steps toward the integration of a complete quantum circuit on a chip are discussed. All the main bulding blocks have been designed and their performance evaluated through numerical simulations. Quantum sources will be realized using either resonators or straight waveguides through Spontanoeous FWM, pump filters using cascaded Mach Zenhder interferometers, optical delay lines using slow light in sequences of resonators and interference filters using arrayed waveguide gratings. Two examples of circuits, in which the quantum state can be deterministically prepared and entanglement tested by Hong Ou Mandel interference, have been designed. This work will pave the way toward the realization, on a Silicon chip of few mm^2, of a complete, compact and reconfigurable quantum circuit, which incorporates all the functionalities which are now bolted on bulky optical tables. The designs are on the way to be fabbricated.
A separate treatement is deserved for chapter 2. The latter does not strictly belong to the project SIQURO, but focuses on a different aspect of the same nonlinearity which governs FWM, that is the $\chi^{(3)}$ nonlinearity. In particular, the phenomenologies discussed throughout the whole chapter are induced by Two Photon Absorption, which is linked to the imaginary part of the $\chi^{(3)}$ tensor. It is shown that TPA can induce dynamical free carriers and temperature variations inside single and coupled resonators, which convert a CW input beam into a pulsed one. While the pulse sequences are always periodic in a single resonator, they can turn to chaotic when many cavities are coupled together in the SCISSOR geometry. A first attempt to engineer a simple three cavity system to produce "chaos on demand" has been done. Using a simple post processing algorithm applied to the chaotic waveforms, random sequences of bit have been generated which passed all the required statistical tests. The work carried out in this chapter explore a new range of applications of sequence of resonators. Up to now, only the linear behaviour of the SCISSOR was exploited for wavelength routing or slow light propagation. The nonlinear chaotic dynamics opens brand new possibilities. One is the realization of an all optical, all passive and CMOS compatible random number generator. Another could be the implementation of the SCISSOR as the fundamental block of photonic neural networks.
In conclusion, this thesis constitutes a step forward to the realization of integrated quantum circuits on Silicon Photonics. The final aim has been to extend the capabilities of the quantum circuits demonstrated so far by providing additional functionalities. This work could pave the way to the realization of self subsistent devices for quantum enhanced measurement, quantum computation or quantum crypthography.

List of publications

M.Mancinelli, M.Borghi, P.Bettotti, J.M. Fedeli and L.Pavesi, "*An All Optical Method for Fabrication Error Measurements in Integrated Photonic Circuits*", Journal of Lightwave Technology, Vol. 31, pp. 2340-2346, (2013).

M.Mancinelli, M.Borghi, F.Ramiro Manzano, J.M. Fedeli and L.Pavesi, "*Chaotic dynamics in coupled resonator sequences*", Opt. Express, Vol.22, pp.14505-14516, (2014).

M.Borghi, M.Mancinelli, F.Merget, J.Witzens, M.Bernard, M.Ghulinyan, G.Pucker and L.Pavesi, "*High-frequency electro-optic measurement of strained silicon racetrack resonators*", Opt. Letters, Vol. 40, pp.5287-5290, (2015).

M. Borghi, D. Gandolfi, M. Ghulinyan, R. Guider, M. Mancinelli, G. Pucker, F. Ramiro Manzano, F. Turri, L. Pavesi, "*Silicon microresonators: how to give a new twist to silicon photonics*", book chapter in Plenary Lectures on Nanoscience and Engineering, ISBN: 9781628417951, (2015).

Appendix A: Nonlinear coupled wave theory for optical resonators

This section derives the coupled wave equations for the energy amplitudes of the eigenmodes of the resonator, subjected to linear and nonlinear perturbations of the polarization. In what follows, a ring resonator of cylindrical symmetry will be considered, since it is implemented in chapter 2 and in chapter 6. The geometry is shown in Fig.6.20.

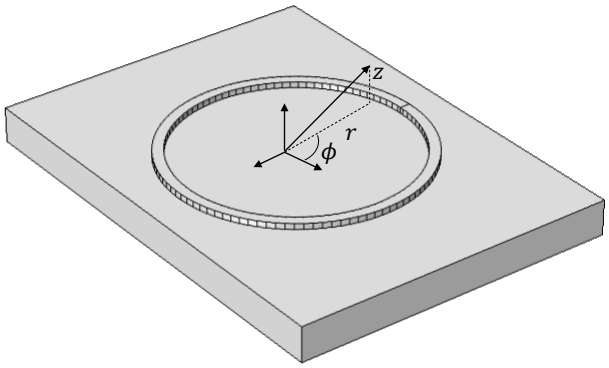

Figure 6.20: Sktech of the resonator geometry under consideration. A cylindrical coordinate system has been adopted, in which each point of space is indicated by its radial distance r, the height z and the azimuthal angle ϕ.

The origin is placed at the center of the resonator. The radial coordinate is designated as r, the height with z and the azimuthal angle with ϕ. The resonator possess eigenmodes u_{mj} which are solution of the Helmoltz equation:

$$\left(\nabla^2 + \frac{\bar{\omega}_{mj}^2 n^2(\mathbf{r})}{c^2}\right)\tilde{u}_{mj} = 0 \tag{6.24}$$

The resonance frequencies associated to eigenmodes $\tilde{u}_{mj}$ are indicated as $\bar{\omega}_{mj}$. The subscript m labels the radial mode number, while j labels the azimuthal mode number. The waveguide which forms the resonator is assumed to be single mode in the z direction, so no label will be used to indicate the vertical mode order. This is implicitally assumed to be the fundamental one. To simplify the treatement, the eigenmodes are assumed to be scalar quantities. The total electric field E_{mj} can be written as:

$$E_{mj}(r,t) = \frac{1}{2}A_{mj}\tilde{u}_{mj}(r,z)e^{-im\phi}e^{i\bar{\omega}_{mj}t} + c.c \tag{6.25}$$

where A_{mj} is a constant amplitude. It can be demonstrated [232] that two different eigenmodes $\tilde{u}_{mj}$ and $\tilde{u}_{m'j'}$ satisfies the orthogonality condition:

$$\int n^2(\mathbf{r})\tilde{u}_{mj}(\mathbf{r}) \cdot \tilde{u}_{m'j'}(\mathbf{r})\, d\mathbf{r} = \delta_{mm'}\delta_{jj'}K_{mj} \tag{6.26}$$

where δ_{ik} is the Kronecker delta, and the normalization constant K_{mj} is defined as:

$$K_{mj} = 2\pi \int n^2(r,z)|\tilde{u}_{mj}(r,z)|^2 r dr dz \tag{6.27}$$

From Eqs.6.26-6.27, it is possible to define the normalized fields u_{mj}:

$$u_{mj} = \frac{\tilde{u}_{mj}}{\left(2\pi \int n^2(r,z)|\tilde{u}_{mj}|^2 r dr dz\right)^{1/2}} \tag{6.28}$$

which satisfies:

$$\int n^2(\mathbf{r})u_{mj}(\mathbf{r}) \cdot u(\mathbf{r})\, d\mathbf{r} = \delta_{mm'}\delta_{jj'} \tag{6.29}$$

The different eigenmodes are not coupled beacuse they are orthogonal. However, if some perturbation acts on the medium, this is no longer holds. Here, only $\chi^{(3)}$, thermal and free carrier perturbations are considered to act at the same time. The $\chi^{(3)}$ tensor, being of the fourth rank, couples four waves. As reported in Eq.2.1, thermal and free carrier are instead perturbations of the linear susceptibility $\chi^{(1)}$, so they are described by a second rank tensor, and thus couple only two waves. It is then sufficient to write the total electric field E as the sum of four waves E_m for deriving the coupled amplitude equations. These waves will be labelled by the subscripts $m = 1, 2, 3, 4$. In principle, each of these subscripts can be associated to a different combination of radial and azimuthal mode numbers m and j. The perturbation δP to the polarization can be written as the sum of two contributions, one arising from thermal and free carrier effects, indicated as δP^L, and one due to the $\chi^{(3)}$ nonlinearity, indicated as δP^{NL}. These are given by:

$$\delta P^L = 2\epsilon_0 n(\Delta n_{th} + \Delta n_{fc}) \sum_m (E_m + c.c) \tag{6.30}$$

$$\delta P^{NL} = 3\epsilon_0 \chi^{(3)} \sum_{mnl} (E_m E_n^* E_l + c.c) \tag{6.31}$$

where Δn_{th} and Δn_{fc} represent the refractive index perturbations induced by thermal and free carrier effects, whose expressions are given by Eq.2.1. Each of the subscripts m, n, l spans from 1 to 4. In writing Eq.6.31, the term $\epsilon_0\chi^{(3)}\sum_{mnl} E_m E_n E_l$ has been neglected because it is usually off resonance with any of the eigenfrequecies of the resonator, so it does couple to any of the travelling waves, neither generates new frequencies. Furthermore, the value of the $\chi^{(3)}$ considered in Eq.6.31 is an average of the projected tensor components along the radial direction (TE modes are considered). The field E satisfies the nonlinear wave equation:

$$\left(\nabla^2 - \frac{n(r)}{c^2}\frac{\partial^2}{\partial^2 t}\right) E(r,t) = \mu_0 \frac{\partial^2(\delta P^L + \delta P^{NL})}{\partial^2 t} \tag{6.32}$$

Due to this fact, the waves E_m can not be written as in Eq.6.25, since they are not solution of Eq.6.24. However, if the perturbation δP is small, it is possible to assume that only the amplitudes A_m are altered, and replace them with slowly varying envelopes $A_m(t)$. These have the property that $\frac{d^2 A_m(t)}{dt^2} \ll \bar{\omega}_m^2 A_m$.
By multiplicating both sides of Eq.6.32 by $u_q^* e^{-i\bar{\omega}_q t}$, by integrating over all the volume, and by using the

orthogonality relation in Eq.6.29, one finds:

$$\frac{dA_q(t)}{dt} = \frac{i\mu_0 c^2}{\bar{\omega}_q} e^{-i\bar{\omega}_q t} \frac{\partial^2}{\partial^2 t} \int u_q^*(\mathbf{r}) \left(\delta P^L + \delta P^{NL}\right) d\mathbf{r} \tag{6.33}$$

The next step is to insert the expressions for the linear and nonlinear perturbations δP^L and δP^{NL}, given by Eq.6.30 and Eq.6.31, into Eq.6.33, which results in the equation of motion:

$$\frac{dA_q(t)}{dt} = -i\frac{\bar{\omega}_q A_q}{n_0}\left(\Delta\bar{n}_{fc,q} + \bar{\Delta n}_{th,q}\right) - i\frac{3\chi^{(3)}}{8n_0^4\omega_q}\sum_{mnl}\frac{(\bar{\omega}_m - \bar{\omega}_n + \bar{\omega}_l)^2}{V_{qmnl}} A_m A_n^* A_l e^{i\Delta\omega_{qmnl}t} \tag{6.34}$$

where n_0 is the refractive index of the core. In Eq.6.34, the following definitions have been used:

$$\Delta\bar{n}_{fc,q} = \frac{\int_{wg} n^2(r,z)\Delta n_{fc}(r,z)|u_q(r,z)|^2\, drdz}{\int n^2(r,z)|u_q(r,z)|^2\, drdz} \tag{6.35}$$

$$\Delta\bar{n}_{th,q} = \frac{\int_{wg} n^2(r,z)\Delta n_{th}(r,z)|u_q(r,z)|^2\, drdz}{\int n^2(r,z)|u_q(r,z)|^2\, drdz} \tag{6.36}$$

$$\frac{1}{V_{qmnl}} = \frac{\int_{wg} n^2(r,z)u_q^*(r,z)u_m(r,z)u_n^*(r,z)u_l(r,z)\, drdz}{L_{tot}\left[\left(\int n^2(r,z)|u_q(r,z)|^2\, drdz\right)\left(\int n^2(r,z)|u_m(r,z)|^2\, drdz\right)\left(\int n^2(r,z)|u_n(r,z)|^2\, drdz\right)\left(\int n^2(r,z)|u_l(r,z)|^2\, drdz\right)\right]^{1/2}} \tag{6.37}$$

$$\Delta\omega_{qmnl} = \bar{\omega}_m - \bar{\omega}_n + \bar{\omega}_l - \bar{\omega}_q \tag{6.38}$$

where L_{tot} is the resonator perimeter. In deriving Eqs.6.35, 6.36, 6.37, the perturbation is assumed to be localized within the core of the waveguide, and the approximation $\int f(r,z)\, rdrd\phi dz \approx L_{tot}\int f(r,z)\, drz$ (here $f(r,z)$ is an arbitrary function of the coordinates r and z) has been used. The quantity in Eq.6.37 is called the effective modal volume of FWM. Eq.6.34 can be cast in an equivalent form in which the amplitudes A_q are replaced by the energy amplitudes U_q. These are defined in such a way that their modulus square give the total electromagnetic energy stored inside the resonator. The relationship between A_q and U_q can be derived by considering that the energy density ρ_q is given by [203] $\rho_q = \frac{1}{2}\epsilon_0 n^2|E_q|^2$, so the total energy stored inside the resonator is $|U_q|^2 = \int \rho_q d\mathbf{r}$. By inserting into this expression the one for E_q , given by Eq.6.25, one gets:

$$|U_q|^2 = \frac{1}{2}\epsilon_0|A_q|^2\int n^2(\mathbf{r})|u_q(\mathbf{r})|^2 dr = \frac{1}{2}\epsilon_0|A_q|^2 \tag{6.39}$$

where the ortogonality relation in Eq.6.29 has been used. From Eq.6.39 it comes out that the quantities A_q and U_q are related by:

$$A_q = \sqrt{\frac{2}{\epsilon_0}}U_q \tag{6.40}$$

Expressed as a function of the energy amplitude U_q, Eq.6.34 has the form:

$$\frac{dU_q}{dt} = -i\frac{\bar{\omega}_q U_q}{n_0}\left(\Delta\bar{n}_{fc,q} + \bar{\Delta n}_{th,q}\right) - i\left(\frac{cn_2}{n_0^2\bar{\omega}_q} + i\frac{\beta_{TPA}c^2}{2n_0\bar{\omega}_q^2}\right)\sum_{mnl}\frac{(\bar{\omega}_m - \bar{\omega}_n + \bar{\omega}_l)^2 U_m U_n^* U_l e^{i\Delta\omega_{qmnl}t}}{V_{qmnl}} \tag{6.41}$$

in which the real and the imaginary part of the $\chi^{(3)}$ tensor have been expressed in terms of the nonlinear coefficient n_2 and the TPA coefficient β_{TPA} using the relation in Eq.1.19. Up to now, the resonator has been considered an isolated system. In order to excite the optical modes, one has to couple the resonator to an

external source. This can be accomplished, for example, by placing a straight waveguide in close proximity to the waveguide of the resonator. At the same time, the energy of the resonator can leak into the waveguide with a characteristic decay constant τ_{ext}. It can be demonstrated that the rate η with which energy is coupled from the waveguide into the resonator is related to τ_{ext} by $\eta = \sqrt{\frac{2}{\tau_{ext}}}$ [233, 101]. If the exciting field is written as $P_{inc} = P_q e^{i\omega_q t}$, where ω_q is the laser frequency and $|P_q|^2$ is the incoming optical power in the bus waveguide, the right hand side of Eq.6.41 gets one more term, written as $\eta_q P_q e^{i(\omega_q - \bar{\omega}_q)t}$ (the difference $\omega_q - \bar{\omega}_q$ at the exponential comes from the multiplication by the factor $u_q^* e^{-i\bar{\omega}_q t}$, which has been done to shift from Eq.6.32 to Eq.6.33). This term forces U_q to oscillate at the frequency $\omega_q - \bar{\omega}_q$. In this way, one can write the internal energy as $U_q = \tilde{U}_q(t) e^{i(\omega_q - \bar{\omega}_q)t}$, in which $\tilde{U}_q(t)$ is a slowly varying envelope. In chapter 6, two laser fields, placed in proximity of two different resonance orders, are used to excite the resonator. The first is called the pump laser, it has a frequency ω_p and it carries a power $|P_p|^2$. The second is the idler laser, it has a frequency ω_i and it carries a power $|P_i|^2 \ll |P_p|^2$. By virtue of the FWM term on the right hand side of Eq.6.41, new frequencies are generated inside the resonator. The FWM process of interest is the partially degenerate one in which two pump photons annihilates to create a signal and an idler photon. Therefore, two of the four coupled waves represent the pump, one indicates the signal and one the idler. The source term for the signal is proportional to $U_p^2 U_i^* e^{i\Delta\omega_{ipsp} t}$, which then oscillates as $e^{i(2\omega_p - \omega_i - \bar{\omega}_s)t}$ (the fact that $U_{p(i)}$ evolves in time as $\tilde{U}_{p(s)} e^{i(\omega_{p(s)} - \bar{\omega}_{p(s)})t}$ has been used). The signal is generated at $\omega_s = 2\omega_p - \omega_i$. The final set of equations for the pump, the signal, and the idler energy amplitudes are:

$$\frac{d\tilde{U}_p(t)}{dt} = i\left(\bar{\omega_p}(1 - \Delta_p(t)) - \omega_p\right)\tilde{U}_p(t) - \frac{1}{\tau_{tot,p}(t)}\tilde{U}_p(t) - 2i\gamma^R_{pips}\tilde{U}_i(t)\tilde{U}_s(t)\tilde{U}_p^*(t) + i\sqrt{\frac{2}{\tau_{ext,p}}P_p} \tag{6.42}$$

$$\frac{d\tilde{U}_s(t)}{dt} = i\left(\bar{\omega_s}(1 - \Delta_s(t)) - \omega_s\right)\tilde{U}_s(t) - \frac{1}{\tau_{tot,s}(t)}\tilde{U}_s(t) - 2i\gamma^R_{spip}\tilde{U}_p^2(t)\tilde{U}_i^*(t) + i\sqrt{\frac{2}{\tau_{ext,s}}P_s} \tag{6.43}$$

$$\frac{d\tilde{U}_i(t)}{dt} = i\left(\bar{\omega_i}(1 - \Delta_i(t)) - \omega_i\right)\tilde{U}_i(t) - \frac{1}{\tau_{tot,i}(t)}\tilde{U}_i(t) - 2i\gamma^R_{ipsp}\tilde{U}_p^2(t)\tilde{U}_s^*(t) \tag{6.44}$$

The following definitions have been adopted:

$$\Delta_k = \frac{\sigma_{FCD}}{n_0}\bar{\Delta N}_k + \frac{1}{n_0}\frac{dn}{dT}\bar{\Delta T}_k + \gamma^R_{kkkk}|\tilde{U}_k|^2 + 2\gamma^R_{kkjj}|\tilde{U}_j|^2 + 2\gamma^R_{kkll}|\tilde{U}_l|^2 \tag{6.45}$$

$$\frac{1}{\tau_{tot,k}(t)} = \frac{1}{\tau_{TPA,k}(t)} + \frac{1}{\tau_{FCA,k}(t)} + \frac{2}{\tau_{ext,k}} + \frac{1}{\tau_{0,k}} \tag{6.46}$$

where the indexes $k \neq l \neq j$ can indicate the pump, the signal or the idler. In Eqs.6.45-6.46, the following quantities have been defined:

$$\bar{\Delta N}_k = \frac{\int_{wg} n(r,z)^2 |u_k(r,z)|^2 \Delta N(r,z)\, drdz}{\int n(r,z)^2 |u_k(r,z)|^2\, drdz}; \qquad \bar{\Delta T}_k = \frac{\int_{wg} n(r,z)^2 |u_k(r,z)|^2 \Delta T(r,z)\, drdz}{\int n(r,z)^2 |u_k(r,z)|^2\, drdz} \tag{6.47}$$

$$\frac{1}{\tau_{TPA,k}} = \gamma^I_{kkkk}|\tilde{U}_k|^2 + 2\gamma^I_{kkjj}|\tilde{U}_j|^2 + 2\gamma^I_{kkll}|\tilde{U}_l|^2; \quad \frac{1}{\tau_{FCA,k}} = \frac{\sigma_{FCA} c}{2n_0}\bar{\Delta N}_k; \quad \frac{1}{\tau_{0,p}} = \alpha_k v_{g,k} \tag{6.48}$$

$$\gamma^R_{jklr} = \frac{cn_2}{n_0^2 V_{jklr}}; \qquad \gamma^I_{jklr} = \frac{\beta_{TPA} c^2}{2n_0^2 V_{jklr}} \tag{6.49}$$

Losses associated with scattering of radiation from the sidewalls roughness have been taken into account by the inclusion of the decay time τ_0, which is inversely proportional to the linear attenuation coefficient α_k and to the group velocity $v_{g,k}$ [117].

Rate equation for temperature

The resonator heats as a consequence of the absorbed optical power P_{abs}. The latter can be computed as the decay rate of the internal energy $\frac{d|\tilde{U}|^2}{dt}$. Since $|\tilde{U}|^2 = \tilde{U}\tilde{U}^*$, the decay rate is given by $\frac{d\tilde{U}}{dt}\tilde{U}^* + \frac{d\tilde{U}^*}{dt}\tilde{U}$, which can be computed starting from one of the Eqs.6.42, 6.43, 6.44. This gives:

$$\frac{d|\tilde{U}_k|^2}{dt} = -|\tilde{U}_k|^2 \frac{2}{\tau_{tot,k}(t)} \tag{6.50}$$

where k can label the pump, the signal or the idler. The total absorbed power P_{abs} is the sum of the decay rates of the pump, the signal and the idler waves:

$$P_{abs}(t) = |\tilde{U}_p|^2 \frac{2}{\tau_{tot,p}(t)} + |\tilde{U}_s|^2 \frac{2}{\tau_{tot,s}(t)} + |\tilde{U}_i|^2 \frac{2}{\tau_{tot,i}(t)} \tag{6.51}$$

The resonator can also exchange heat with the external environement by conduction through the Silica cladding. This occurs with a characteristic decay time τ_{th}. Due to the quite high thermal conductivity of Silicon, the temperature distribution inside the resonator is approximately uniform. This is used to write the modal average temperature $\bar{\Delta T}$ as $\bar{\Delta T}_k = \Gamma_k \Delta T$, in which Γ_k is the modal confinement factor defined in Eq.1.2. In this way, it is sufficient to track the evolution of the quantity ΔT to express the thermo optic frequency shift in Eq.6.45. The equation of motion for the temperature is then:

$$\frac{d\Delta T}{dt} = -\frac{\Delta T}{\tau_{th}} + \frac{P_{abs}(t)}{M_{res} c_p} \tag{6.52}$$

where the mass of the resonator M_{res} and the specific heat at constant pressure c_p have been introduced.

Rate equations for free carriers

Free carriers are generated inside the resonator as a consequence of Two Photon Absorption and Cross Photon Absorption (XPA). The plasma carrier frequency shift in Eq.6.45 is related to the local free carrier concentration $\Delta N(\mathbf{r})$. Then, one has to derive a relation between the local TPA and XPA absorbed power and $\Delta N(\mathbf{r})$. By looking at Eq.6.50, one can notice that the TPA and XPA decay rates can be rewritten as:

$$\frac{d|\tilde{U}_k|^2}{dt} = \int \left(P_{TPA,k}(\mathbf{r}) + P_{XPA,k}(\mathbf{r})\right) d\mathbf{r} \tag{6.53}$$

where the local TPA and XPA absorbed powers $P_{TPA,k}(\mathbf{r})$ and $P_{XPA,k}(\mathbf{r})$ are given by:

$$P_{TPA,k}(\mathbf{r}) = |\tilde{U}_k|^4 \frac{\beta_{TPA} c^2 n^2(\mathbf{r}) |u_k(\mathbf{r})|^4}{L_{tot}^2 \left(\int n^2 |u_k(r,z)|^2 \, dr dz\right)^2} \tag{6.54}$$

$$P_{XPA,k}(\mathbf{r}) = c^2\beta_{TPA}n^2(\mathbf{r})\left(|\tilde{U}_k|^2|\tilde{U}_j|^2\frac{|u_k(r)|^2|u_j(r)|^2}{L_{tot}^2\left(\int n^2|u_k(r,z)|^2\,drdz\right)\left(\int n^2|u_j(r,z)|^2\,drdz\right)}+\right.$$
$$\left. = +2|\tilde{U}_k|^2|\tilde{U}_i|^2\frac{|u_k(r)|^2|u_l(r)|^2}{L_{tot}^2\left(\int n^2|u_k(r,z)|^2\,drdz\right)\left(\int n^2|u_l(r,z)|^2\,drdz\right)}\right) \tag{6.55}$$

where the subscripts $k \neq j \neq l$ can designate the pump, the signal or the idler. When a concentration ΔN of free carriers enstablishes above equilibrium, electron-hole recombination occurs to restore the initial concentration. The recombination rate is described by a characteristic free carrier lifetime τ_{fc}. The local free carrier concentration $\Delta N(\mathbf{r})$ is a balance between generation and recombination:

$$\frac{d\Delta N_k(\mathbf{r},t)}{dt} = -\frac{\Delta N_k(\mathbf{r},t)}{\tau_{fc}} + \frac{P_{TPA,k}(\mathbf{r})}{2\hbar\omega_k} + \frac{P_{XPA,kj}(\mathbf{r})}{\hbar(\omega_k+\omega_j)} + \frac{P_{XPA,kl}(\mathbf{r})}{\hbar(\omega_k+\omega_l)} \tag{6.56}$$

where $P_{XPA,kj}$ and $P_{XPA,kl}$ indicate, respectively, the first and the second term on the right hand side of Eq.6.55. By performing a modal averaging on ΔN_k, the following equations of motions are obtained:

$$\frac{d\bar{\Delta N}_p}{dt} = -\frac{\bar{\Delta N}_p}{\tau_{fc}}+\frac{c^2\beta_{TPA}}{2n_0^2\hbar}\left(\frac{\Gamma_{ppp}|\tilde{U}_p|^4}{\omega_p V_{ppp}^2}+\frac{\Gamma_{ssp}|\tilde{U}_s|^4}{\omega_s V_{ssp}^2}+\frac{\Gamma_{iip}|\tilde{U}_i|^4}{\omega_i V_{iip}^2}+\frac{2\Gamma_{psp}|\tilde{U}_p|^2|\tilde{U}_s|^2}{(\omega_p+\omega_s)V_{psp}^2}+\frac{2\Gamma_{ppp}|\tilde{U}_p|^2|\tilde{U}_i|^2}{(\omega_p+\omega_i)V_{pip}^2}+\frac{2\Gamma_{sip}|\tilde{U}_s|^2|\tilde{U}_i|^2}{(\omega_s+\omega_i)V_{sip}^2}\right) \tag{6.57}$$

$$\frac{d\bar{\Delta N}_s}{dt} = -\frac{\bar{\Delta N}_s}{\tau_{fc}}+\frac{c^2\beta_{TPA}}{2n_0^2\hbar}\left(\frac{\Gamma_{pps}|\tilde{U}_p|^4}{\omega_p V_{pps}^2}+\frac{\Gamma_{sss}|\tilde{U}_s|^4}{\omega_s V_{sss}^2}+\frac{\Gamma_{iis}|\tilde{U}_i|^4}{\omega_i V_{iis}^2}+\frac{2\Gamma_{pss}|\tilde{U}_p|^2|\tilde{U}_s|^2}{(\omega_p+\omega_s)V_{pss}^2}+\frac{2\Gamma_{pis}|\tilde{U}_p|^2|\tilde{U}_i|^2}{(\omega_p+\omega_i)V_{pis}^2}+\frac{2\Gamma_{sis}|\tilde{U}_s|^2|\tilde{U}_i|^2}{(\omega_s+\omega_i)V_{sis}^2}\right) \tag{6.58}$$

$$\frac{d\bar{\Delta N}_i}{dt} = -\frac{\bar{\Delta N}_i}{\tau_{fc}}+\frac{c^2\beta_{TPA}}{2n_0^2\hbar}\left(\frac{\Gamma_{ppi}|\tilde{U}_p|^4}{\omega_p V_{ppi}^2}+\frac{\Gamma_{ssi}|\tilde{U}_s|^4}{\omega_s V_{ssi}^2}+\frac{\Gamma_{iii}|\tilde{U}_i|^4}{\omega_i V_{iii}^2}+\frac{2\Gamma_{psi}|\tilde{U}_p|^2|\tilde{U}_s|^2}{(\omega_p+\omega_s)V_{psi}^2}+\frac{2\Gamma_{pii}|\tilde{U}_p|^2|\tilde{U}_i|^2}{(\omega_p+\omega_i)V_{pii}^2}+\frac{2\Gamma_{sii}|\tilde{U}_s|^2|\tilde{U}_i|^2}{(\omega_s+\omega_i)V_{sii}^2}\right) \tag{6.59}$$

with the definitions:

$$\Gamma_{jkl} = \frac{\int_{wg} n^6(r,z)|u_j|^2|u_k|^2|u_l|^2\,drdz}{\int n^6(r,z)|u_j|^2|u_k|^2|u_l|^2\,drdz} \tag{6.60}$$

$$\frac{1}{V_{jkl}^2} = \frac{\int n^6(r,z)|u_j|^2|u_k|^2|u_l|^2\,drdz}{\left(\int n^2(r,z)|u_j|^2\,drdz\right)\left(\int n^2(r,z)|u_k|^2\,drdz\right)\left(\int n^2(r,z)|u_l|^2\,drdz\right)} \tag{6.61}$$

Appendix B: Linear and nonlinear refractive index changes in straight nanophotonic waveguides

This appendix quantifies the relation between a change in the refractive index Δn in the material, and a change Δn_{eff} of the effective index in the waveguide. The straight waveguide shown in Fig.1.12 has modal solutions which can be expressed as:

$$\mathbf{E}_{0j}(x,y,z,t) = \sqrt{\frac{Z_0 P_0}{A_0}}\mathbf{e}_{0j}(x,y)e^{i(\beta_{0j}z-\omega t)} + c.c \tag{6.62}$$

$$\mathbf{H}_{0j}(x,y,z,t) = \sqrt{\frac{P_0}{Z_0 A_0}}\mathbf{h}_{0j}(x,y)e^{i(\beta_{0j}z-\omega t)} + c.c \tag{6.63}$$

where $\mathbf{E}_{0j}$ is the electric field, $\mathbf{e}_{0j}$ its transverse profile (the same holds for $\mathbf{H}_{0j}$ and $\mathbf{h}_{0j}$, which refer to the magnetic displacement), Z_0 the vacuum impedance, P_0 the power carried by the mode and A_0 the area of the core. The fields in Eq.6.62-6.63 are normalized in such a way that:

$$\frac{1}{4A_0}\int \left(\mathbf{e}_{0j}\times\mathbf{h}^*_{0j} + \mathbf{e}^*_{0j}\times\mathbf{h}_{0j}\right)\cdot\hat{\mathbf{z}}\,dxdy = 1 \tag{6.64}$$

which implies that the flux of the Poyinting vector $\mathbf{S} = \frac{1}{2}Re(\mathbf{E}_{0j}\times\mathbf{H}_{0j})$ on the xy plane (i.e., the power) gives:

$$\frac{1}{2}\int Re(\mathbf{E}_{0j}\times\mathbf{H}^*_{0j})\cdot\hat{\mathbf{z}} = P_0 \tag{6.65}$$

When a perturbation $\delta\mathbf{P}$ to the polarization $\mathbf{P}$ occurs, and this depends only on the transverse coordinates, the modal solutions are expressed as:

$$\mathbf{E}_j(x,y,z,t) = \sqrt{\frac{Z_0 P_0}{A_0}}\mathbf{e}_{j0}(x,y)u_j(z)e^{i(\beta_j z-\omega t)} + c.c \tag{6.66}$$

$$\mathbf{H}_j(x,y,z,t) = \sqrt{\frac{Z_0 P_0}{A_0}}\mathbf{h}_{j0}(x,y)u_j(z)e^{i(\beta_j z-\omega t)} + c.c \tag{6.67}$$

where the slowly varying envelope $u_j(z)$ has been introduced. This satisfies $\frac{d^2u_j(z)}{d^2z} \ll \beta^2_{0j}u_j$. In what follows, the waveguide will be assumed to support only the fundamental mode, so the subcript j will be dropped. The set of solutions $(\mathbf{E}_0, \mathbf{H}_0)$ and $(\mathbf{E}, \mathbf{H})$ can be demonstrated to satisfy [53]:

Origin	$\Delta\mathbf{n}$
Thermo optic	$\frac{dn}{dT}\Delta T(x,y)$
Free carrier dispersion	$\left(\sigma_{FCD} + i\frac{c}{2\omega}\sigma_{FCA}\right)\Delta N(x,y)$
Linear electro optic	$\frac{\chi^{(2)}\cdot\mathbf{E}_{DC}}{2n_0}$
Qudratic electro optic	$\frac{9\chi^{(3)}\cdot\mathbf{E}_{DC}\mathbf{E}_{DC}}{16n_0}$

Table 6.6: Bulk refractive index changes associated to different physical quantities.

$$\frac{d}{dz}\int (\mathbf{E}_0^* \times \mathbf{H} + \mathbf{E} \times \mathbf{H}_0^*)\cdot\hat{\mathbf{z}}\, dxdy = i\omega \int \delta\mathbf{P}\cdot\mathbf{E}_0^* dxdy \tag{6.68}$$

By inserting the expressions for $\mathbf{E}_0, \mathbf{H}_0, \mathbf{E}$ and $\mathbf{H}$ into Eq.6.68, and by using the orthogonality relation in Eq.6.64, one finds:

$$\frac{du(z)}{dz} + i(\beta - \beta_0)u(z) = \frac{i\omega}{4P_0}\int \delta\mathbf{P}\cdot\mathbf{E}_0^*\, dxdy \tag{6.69}$$

The expression for $\delta\mathbf{P}$ depends on the physical mechanisms which are inducing the refractive index change.

- *Thermo optic shift.* If the change in polarization $\delta\mathbf{P}$ is induced by a temperature variation $\Delta T(x,y)$, one has $\delta\mathbf{P}(x,y) = 2\epsilon_0 n_0 \Delta n(x,y)\mathbf{E} = 2\epsilon_0 n_0 \frac{dn}{dT}\Delta T(x,y)\mathbf{E}$.
- *Free carrier dispersion.* If the change in polarization $\delta\mathbf{P}$ is induced by a variation $\Delta N(x,y)$ of the free carrrier concentration (assumed electrons, for simplicity), one has: $\delta\mathbf{P}(x,y) = 2\epsilon_0 n_0 \Delta n(x,y)\mathbf{E} = 2\epsilon_0 n_0 \left(\sigma_{FCD} + i\frac{c}{2\omega}\sigma_{FCA}\right)\Delta N(x,y)\mathbf{E}$.
- *Linear electro optic effect.* In this case, the change in polarization $\delta\mathbf{P}$ is given by $\delta\mathbf{P} = \epsilon_0\chi^{(2)}\cdot\mathbf{EE}$. The electric field is the sum of an optical field $\mathbf{E}_\omega$ and of a static field $\mathbf{E}_{DC}$. By inserting the expression (6.66) for the electric field $\mathbf{E}_\omega$, and by keeping only the terms which evolve in time as $e^{-i\omega t}$, one gets $\delta\mathbf{P} = \epsilon_0\chi^{(2)}\cdot\mathbf{E}_\omega\mathbf{E}_{DC}$.
- *Quadratic electro optic effect.* In this case, the change in polarization $\delta\mathbf{P}$ is given by $\delta\mathbf{P} = \epsilon_0\chi^{(3)}\cdot\mathbf{EEE}$. The electric field is the sum of an optical field $\mathbf{E}_\omega$ and of a static field $\mathbf{E}_{DC}$. By inserting the expression (6.66) for the electric field $\mathbf{E}_\omega$, and by keeping only the terms which evolve in time as $e^{-i\omega t}$, one gets $\delta\mathbf{P} = \frac{9}{8}\epsilon_0\chi^{(3)}\cdot\mathbf{E}_\omega\mathbf{E}_{DC}\mathbf{E}_{DC}$.

In all the cases described above, the perturbation $\delta\mathbf{P}$ can be written in the form $\delta\mathbf{P} = 2\epsilon_0 n_0 \Delta\mathbf{n}\cdot\mathbf{E}$, in which the refractive index change $\Delta\mathbf{n}$ (generally a second second rank tensor) can assume the different expressions indicated in Table 6.6.

By inserting the expression for $\delta\mathbf{P}$ into Eq.6.69, and by using the relation [53]:

$$\frac{Z_0}{A_0} = \frac{2n_g}{c\epsilon_0\int n^2(x,y)|\mathbf{e}(x,y)|^2\, dxdy} \tag{6.70}$$

one finds:

$$\frac{du(z)}{dz} = i\left(\beta - \beta_0 + \frac{\omega n_g}{c}\xi\right)u(z) \tag{6.71}$$

where the parameter ξ is defined as:

$$\xi = \frac{n_0\int \Delta\mathbf{n}(x,y)\cdot\mathbf{e}(x,y)\mathbf{e}^*(x,y)\, dxdy}{\int n^2(x,y)|\mathbf{e}(x,y)|^2\, dxdy} \tag{6.72}$$

Origin	Refractive index shift	Effective index shift
Thermo optic	$\frac{dn}{dT}\Delta T(x,y)$	$\frac{n_g}{n_0}\frac{dn}{dT}\frac{\int_{wg} n^2(x,y)\Delta T(x,y)\lvert\mathbf{e}(x,y)\rvert^2\,dxdy}{\int n^2(x,y)\lvert\mathbf{e}(x,y)\rvert^2\,dxdy}$
Free carrier dispersion	$\left(\sigma_{FCD}+i\frac{c}{2\omega}\sigma_{FCA}\right)\Delta N(x,y)$	$\frac{n_g}{n_0}\sigma_{FC}\frac{\int_{wg} n^2(x,y)\Delta N(x,y)\lvert\mathbf{e}(x,y)\rvert^2\,dxdy}{\int n^2(x,y)\lvert\mathbf{e}(x,y)\rvert^2\,dxdy}$
Linear electro optic	$\frac{\chi^{(2)}\cdot\mathbf{E}_{DC}}{2n_0}$	$\frac{n_g}{2n_0^2}\frac{\int_{wg} n^2(x,y)\chi^{(2)}\cdot\mathbf{E}_{DC}\mathbf{e}(x,y)\mathbf{e}(x,y)\,dxdy}{\int n^2(x,y)\lvert\mathbf{e}(x,y)\rvert^2\,dxdy}$
Quadratic electro optic	$\frac{9\chi\cdot\mathbf{E}_{DC}\mathbf{E}_{DC}}{16n_0}$	$\frac{9n_g}{16n_0^2}\frac{\int_{wg} n^2(x,y)\chi^{(3)}\cdot\mathbf{E}_{DC}\mathbf{E}_{DC}e(x,y)e(x,y)\,dxdy}{\int n^2(x,y)\lvert\mathbf{e}(x,y)\rvert^2\,dxdy}$

Table 6.7: Summary of the relations between the bulk refractive index changes and the associated effective index variations. The quantity $\sigma_{FC}=\sigma_{FCD}+i\frac{c}{2\omega}\sigma_{FCA}$ has been introduced to compact the notation.

The solution of Eq.6.71 is $u(z)=u_0e^{i\beta' z}$, with $\beta'=\beta-\beta_0+\frac{\omega n_g}{2c}\xi$, which, if inserted into Eq.6.66, gives:

$$\mathbf{E}_j(x,y,z,t)=\sqrt{\frac{Z_0P_0}{A_0}}\mathbf{e}_{j0}(x,y)u_0e^{i((\beta_0+\Delta\beta)z-\omega t)}+c.c \tag{6.73}$$

where $\Delta\beta=\frac{\omega n_g}{c}\xi$. Eq.6.73 states that if the bulk refractive index is perturbed by a quantity $\Delta n(x,y)$, whose expression is given in Table 6.6, the propagation constant of the mode changes by a quantity $\Delta\beta$. Since the latter is related to the effective index through $\Delta\beta=\frac{\omega}{c}\Delta n_{eff}$, it is possible to conclude that $\Delta n_{eff}=n_g\xi$. Table 6.7 summarizes the different expressions for Δn_{eff} for the cases of thermo optic shift, free carrier dispersion, linear electro optic effect and quadratic electro optic effect.

In deriving the expressions reported in Table 6.7, the refractive index perturbation $\Delta\mathbf{n}(x,y)$ has been assumed localized within the core of the waveguide.

Aknowledgements

- *Ringraziamenti tecnici:* la stesura di questo lavoro non sarebbe stata possibile senza l'aiuto dei miei colleghi di NL. Ringrazio il Dr. Mattia Mancinelli per i contributi fondamentali a tutti gli esperimenti descritti nei capitoli 2,3,4,5. Alessandro Trenti per le attività descritte nel capitolo 5. Stefano Signorini per gli esperimenti e le simulazioni del capitolo 3 e 6. Claudio Castellan per le simulazioni del capitolo 6. Fernando Ramiro Manzano per il contributo importante al capitolo 2, e per tutte le ruotine LabView che mi hanno permesso di risparmiare ore e ore di lavoro. Ringrazio poi il Dr.Mher Ghulynian, Martino Bernard e il Dr.Georg Pucker per le fotografie al microscopio ottico del capitolo 4 e per le analisi al SEM.

- Ringrazio il prof. Lorenzo Pavesi per avermi concesso l'opportunità di lavorare all'interno del laboratorio di NanoScienze. Lo ringrazio per il lavoro di supervisione svolto durante questi tre anni, e per aver contribuito, grazie ai suoi consigli, commenti e accorgimenti, alla mia crescita professionale.

- Ringrazio il Dr.Mher Ghulynian, Martino Bernard e il Dr.Georg Pucker della Fondazione Bruno Kessler per la continua collaborazione che abbiamo avuto durante la fabbricazione dei campioni. E' stato una grande opportunità, di certo non scontata, quella di poter seguire passo passo il processo produttivo. Il vostro supporto e i vostri feedback sono stati fondamentali per il design di tutte le strutture.

- Ringrazio tutta la mia famiglia per il supporto che mi ha sempre dato. In tutti i momenti che ho passato, belli e brutti che siano, voi siete sempre stati presenti. Siete la forza che mi permette di non smettere mai di sognare.

- *Un po di miele*: ringrazio tutti i membri del laboratorio di NL per aver sempre creato un ambiente stimolante e piacevole di lavoro. Una menzione particolare va (in ordine di citazione casuale) a Mattia Mancinelli, Alessandro Trenti e Stefano Tondini. Mattia, ti ringrazio perchè sei stato tu ad iniziarmi a questo "duro" lavoro, e con te ho condiviso gran parte delle gioie e dei dolori di questi tre anni di intensa ricerca. Sei stato un maestro esemplare, mi ha insegnato tantissimo, e nei tuoi confronti avrò sempre gran rispetto e profonda ammirazione. Perchè non bisogna mai dimenticare da dove si è iniziato. Alessandro, prima di essere un collega, sei un grande amico. Abbiamo sempre lavorato bene insieme e in grande sintonia... non vedo l'ora di ricominciare a imprecare sul tavolo ottico con te come ai tempi del buon vecchio scatolone! Ho sempre ammirato il tuo atteggiamento positivo e ottimista, mi hai rallegrato molte giornate e mi hai spinto a non mollare mai in tutte le cose che ho fatto. Stefano, purtroppo con te non ho quasi mai avuto l'occasione di lavorare, ma sei sempre stato una spalla dentro e fuori dalle mure universitarie. Ti ringrazio per tutte le uscite, le corse, le camminate, e per l' immensa disponibilità che mi hai sempre dimostrato ogni qual volta che ho avuto bisogno di te. Sei una persona di cui ho grande stima, e spero un giorno di poter avere anche una decima parte del tuo carisma quando col tuo "Siiiiiii Tondini per 20" prenoti un tavolo all'Orostube.

Bibliography

[1] http://events.unitn.it/en/siquro.

[2] G. P. Agrawal, *Nonlinear fiber optics*. Academic press, 2007.

[3] Y. Ding, J. Xu, H. Ou, and C. Peucheret, "Mode-selective wavelength conversion based on four-wave mixing in a multimode silicon waveguide," *Optics express*, vol. 22, no. 1, pp. 127–135, 2014.

[4] J. Chen, Y. Gong, M. Fiorani, and S. Aleksic, "Optical interconnects at the top of the rack for energy-efficient data centers," *IEEE Communications Magazine*, vol. 53, no. 8, pp. 140–148, 2015.

[5] C. Kachris, K. Kanonakis, and I. Tomkos, "Optical interconnection networks in data centers: recent trends and future challenges," *IEEE Communications Magazine*, vol. 51, no. 9, pp. 39–45, 2013.

[6] L. Pavesi and G. Guillot, "Optical interconnects," *Springer series in optical sciences*, vol. 119, 2006.

[7] R.-J. Essiambre and R. W. Tkach, "Capacity trends and limits of optical communication networks," *Proceedings of the IEEE*, vol. 100, no. 5, pp. 1035–1055, 2012.

[8] C. Kachris and I. Tomkos, "A survey on optical interconnects for data centers," *Communications Surveys & Tutorials*, vol. 14, no. 4, pp. 1021–1036, 2012.

[9] C. DeCusatis, *Handbook of fiber optic data communication: a practical guide to optical networking*. Academic Press, 2013.

[10] S. Miller, *Optical fiber telecommunications*. Elsevier, 2012.

[11] Z. Li, I. Shubin, and X. Zhou, "Optical interconnects: recent advances and future challenges," *Optics express*, vol. 23, no. 3, pp. 3717–3720, 2015.

[12] C. A. Brackett, "Dense wavelength division multiplexing networks: Principles and applications," *IEEE Journal on Selected Areas in Communications*, vol. 8, no. 6, pp. 948–964, 1990.

[13] I. Present, "Cramming more components onto integrated circuits," *Readings in computer architecture*, vol. 56, 2000.

[14] http://www.cringely.com/wp-content/uploads/2013/10/642px-Moores_law_1970-2011.png.

[15] http://spectrum.ieee.org/image/MTk1MTMzOA.

[16] J. D. Plummer, *Silicon VLSI technology: fundamentals, practice, and modeling*. Pearson Education India, 2009.

[17] www.itrs.net/.

[18] D. A. Miller, "Optical interconnects to electronic chips," *Applied Optics*, vol. 49, no. 25, pp. F59–F70, 2010.

[19] `http://www.cs.virginia.edu/kim/courses/cs3330/lec/cs3330-chap1-power.pdf`.

[20] R. Perez, *Handbook of electromagnetic compatibility*. Academic Press, 2013.

[21] D. Dai and J. E. Bowers, "Silicon-based on-chip multiplexing technologies and devices for peta-bit optical interconnects," *Nanophotonics*, vol. 3, no. 4-5, pp. 283–311, 2014.

[22] J. K. Doylend and A. P. Knights, "The evolution of silicon photonics as an enabling technology for optical interconnection," *Laser & Photonics Reviews*, vol. 6, no. 4, pp. 504–525, 2012.

[23] J. L. Malinge, "A view on the silicon photonics trends and market prospective.," 2014.

[24] G. T. Reed and A. P. Knights, *Silicon photonics*. Wiley Online Library, 2008.

[25] L. Pavesi and D. J. Lockwood, *Silicon photonics*, vol. 1. Springer Science & Business Media, 2004.

[26] M. Asghari and A. V. Krishnamoorthy, "Silicon photonics: Energy-efficient communication," *Nature Photonics*, vol. 5, no. 5, pp. 268–270, 2011.

[27] R. Soref and J. Lorenzo, "Single-crystal silicon: a new material for 1.3 and 1.6 μm integrated-optical components," *Electronics Letters*, vol. 21, no. 21, pp. 953–954, 1985.

[28] G. Abstreiter, "Engineering the future of electronics," *Physics World*, vol. 5, no. 3, p. 36, 1992.

[29] R. A. Soref, "Silicon-based optoelectronics," *Proceedings of the IEEE*, vol. 81, no. 12, pp. 1687–1706, 1993.

[30] R. Soref, "The past, present, and future of silicon photonics," *IEEE Journal of Selected Topics in Quantum Electronics*, vol. 12, no. 6, pp. 1678–1687, 2006.

[31] E. L. Wooten, K. M. Kissa, A. Yi-Yan, E. J. Murphy, D. A. Lafaw, P. F. Hallemeier, D. Maack, D. V. Attanasio, D. J. Fritz, G. J. McBrien, *et al.*, "A review of lithium niobate modulators for fiber-optic communications systems," *IEEE Journal of Selected Topics in Quantum Electronics*, vol. 6, no. 1, pp. 69–82, 2000.

[32] W. N. Ye and Y. Xiong, "Review of silicon photonics: history and recent advances," *Journal of Modern Optics*, vol. 60, no. 16, pp. 1299–1320, 2013.

[33] R. A. Soref and J. P. Lorenzo, "All-silicon active and passive guided-wave components for lambda= 1.3 and 1.6 microns," *IEEE Journal of Quantum Electronics*, vol. 22, pp. 873–879, 1986.

[34] G. T. Reed, W. R. Headley, and C. J. Png, "Silicon photonics: The early years," in *Integrated Optoelectronic Devices 2005*, pp. 1–18, International Society for Optics and Photonics, 2005.

[35] Y. Li, S. Verstuyft, G. Yurtsever, S. Keyvaninia, G. Roelkens, D. Van Thourhout, and R. Baets, "Heterodyne laser doppler vibrometers integrated on silicon-on-insulator based on serrodyne thermo-optic frequency shifters," *Applied optics*, vol. 52, no. 10, pp. 2145–2152, 2013.

[36] K. De Vos, I. Bartolozzi, E. Schacht, P. Bienstman, and R. Baets, "Silicon-on-insulator microring resonator for sensitive and label-free biosensing," *Optics express*, vol. 15, no. 12, pp. 7610–7615, 2007.

[37] F. B. Myers and L. P. Lee, "Innovations in optical microfluidic technologies for point-of-care diagnostics," *Lab on a Chip*, vol. 8, no. 12, pp. 2015–2031, 2008.

[38] B. Redding, S. F. Liew, R. Sarma, and H. Cao, "Compact spectrometer based on a disordered photonic chip," *Nature Photonics*, vol. 7, no. 9, pp. 746–751, 2013.

[39] N. Jokerst, M. Royal, S. Palit, L. Luan, S. Dhar, and T. Tyler, "Chip scale integrated microresonator sensing systems," *Journal of biophotonics*, vol. 2, no. 4, pp. 212–226, 2009.

[40] T. Van Vaerenbergh, M. Fiers, P. Mechet, T. Spuesens, R. Kumar, G. Morthier, B. Schrauwen, J. Dambre, and P. Bienstman, "Cascadable excitability in microrings," *Optics express*, vol. 20, no. 18, pp. 20292–20308, 2012.

[41] K. Vandoorne, P. Mechet, T. Van Vaerenbergh, M. Fiers, G. Morthier, D. Verstraeten, B. Schrauwen, J. Dambre, and P. Bienstman, "Experimental demonstration of reservoir computing on a silicon photonics chip," *Nature Communications*, vol. 5, 2014.

[42] C. Mesaritakis, V. Papataxiarhis, and D. Syvridis, "Micro ring resonators as building blocks for an all-optical high-speed reservoir-computing bit-pattern-recognition system," *Journal of the Optical Society of America B*, vol. 30, no. 11, pp. 3048–3055, 2013.

[43] IEEE International Conference on Group IV Photonics, held annually at various international locations.

[44] SPIE Photonics West symposium on Silicon Photonics, held annually in San Francisco.

[45] `http://www.intel.com/content/www/us/en/research/intel-labs-silicon-photonics-research.html`.

[46] `http://download.intel.com/pressroom/pdf/photonics/50G_Silicon_Photonics_Link.pdf?iid=pr_smrelease_vPro_materials1`.

[47] J. Gripp, J. Simsarian, J. LeGrange, P. Bernasconi, and D. Neilson, "Photonic terabit routers: The iris project," in *Optical Fiber Communication Conference*, Optical Society of America, 2010.

[48] G. Roelkens, L. Liu, D. Liang, R. Jones, A. Fang, B. Koch, and J. Bowers, "Iii-v/silicon photonics for on-chip and intra-chip optical interconnects," *Laser & Photonics Reviews*, vol. 4, no. 6, pp. 751–779, 2010.

[49] J. Michel, J. Liu, and L. C. Kimerling, "High-performance ge-on-si photodetectors," *Nature Photonics*, vol. 4, no. 8, pp. 527–534, 2010.

[50] W. Bogaerts, M. Fiers, and P. Dumon, "Design challenges in silicon photonics," *IEEE Journal of Selected Topics in Quantum Electronics*, vol. 20, no. 4, pp. 1–8, 2014.

[51] B. E. Saleh, M. C. Teich, and B. E. Saleh, *Fundamentals of photonics*, vol. 22. Wiley New York, 1991.

[52] C.-L. Chen, *Foundations for guided-wave optics*. John Wiley & Sons, 2006.

[53] R. Osgood, N. Panoiu, J. Dadap, X. Liu, X. Chen, I.-W. Hsieh, E. Dulkeith, W. Green, and Y. Vlasov, "Engineering nonlinearities in nanoscale optical systems: physics and applications in dispersion-engineered silicon nanophotonic wires," *Advances in Optics and Photonics*, vol. 1, no. 1, pp. 162–235, 2009.

[54] K. K. Lee, D. R. Lim, H.-C. Luan, A. Agarwal, J. Foresi, and L. C. Kimerling, "Effect of size and roughness on light transmission in a si/sio2 waveguide: Experiments and model," *Applied Physics Letters*, vol. 77, no. 11, pp. 1617–1619, 2000.

[55] L. Rowe, M. Elsey, N. Tarr, A. Knights, and E. Post, "Cmos-compatible optical rib waveguides defined by local oxidation of silicon," *Electronics Letters*, vol. 43, no. 7, p. 1, 2007.

[56] M. Gnan, S. Thoms, D. Macintyre, R. M. De La Rue, and M. Sorel, "Fabrication of low-loss photonic wires in silicon-on-insulator using hydrogen silsesquioxane electron-beam resist," *Electronics Letters*, vol. 44, no. 2, pp. 115–116, 2008.

[57] W. Bogaerts *et al.*, "Compact single-mode silicon hybrid rib/strip waveguide with adiabatic bends," *IEEE Photonics Journal*, vol. 3, no. 3, pp. 422–432, 2011.

[58] I. E. Day, I. Evans, A. Knights, F. Hopper, S. Roberts, J. Johnston, S. Day, J. Luff, H. K. Tsang, and M. Asghari, "Tapered silicon waveguides for low insertion loss highly-efficient high-speed electronic variable optical attenuators," in *Optical Fiber Communication Conference*, Optical Society of America, 2003.

[59] M. Pu, L. Liu, H. Ou, K. Yvind, and J. M. Hvam, "Ultra-low-loss inverted taper coupler for silicon-on-insulator ridge waveguide," *Optics Communications*, vol. 283, no. 19, pp. 3678–3682, 2010.

[60] W. S. Chang, *Fundamentals of guided-wave optoelectronic devices*. Cambridge University Press, 2009.

[61] D. Taillaert, F. Van Laere, M. Ayre, W. Bogaerts, D. Van Thourhout, P. Bienstman, and R. Baets, "Grating couplers for coupling between optical fibers and nanophotonic waveguides," *Japanese Journal of Applied Physics*, vol. 45, no. 8, p. 6071, 2006.

[62] L. Liu, M. Pu, K. Yvind, and J. M. Hvam, "High-efficiency, large-bandwidth silicon-on-insulator grating coupler based on a fully-etched photonic crystal structure," *Applied physics letters*, vol. 96, no. 5, p. 051126, 2010.

[63] Y. Tang, Z. Wang, L. Wosinski, U. Westergren, and S. He, "Highly efficient nonuniform grating coupler for silicon-on-insulator nanophotonic circuits," *Optics letters*, vol. 35, no. 8, pp. 1290–1292, 2010.

[64] S. K. Selvaraja, D. Vermeulen, M. Schaekers, E. Sleeckx, W. Bogaerts, G. Roelkens, P. Dumon, D. Van Thourhout, and R. Baets, "Highly efficient grating coupler between optical fiber and silicon photonic circuit," in *Conference on Lasers and Electro-Optics*, Optical Society of America, 2009.

[65] Y. Ding, C. Peucheret, H. Ou, and K. Yvind, "Fully etched apodized grating coupler on the soi platform with- 0.58 db coupling efficiency," *Optics letters*, vol. 39, no. 18, pp. 5348–5350, 2014.

[66] Y. Zhang, S. Yang, A. E.-J. Lim, G.-Q. Lo, C. Galland, T. Baehr-Jones, and M. Hochberg, "A compact and low loss y-junction for submicron silicon waveguide," *Optics express*, vol. 21, no. 1, pp. 1310–1316, 2013.

[67] L. B. Soldano and E. Pennings, "Optical multi-mode interference devices based on self-imaging: principles and applications," *Journal of Lightwave Technology*, vol. 13, no. 4, pp. 615–627, 1995.

[68] P. Trinh, S. Yegnanarayanan, and B. Jalali, "Integrated optical directional couplers in silicon-on-insulator," *Electronics Letters*, vol. 31, no. 24, pp. 2097–2098, 1995.

[69] A. W. Snyder and J. Love, *Optical waveguide theory*. Springer Science & Business Media, 2012.

[70] Y. Ding, J. Xu, F. Da Ros, B. Huang, H. Ou, and C. Peucheret, "On-chip two-mode division multiplexing using tapered directional coupler-based mode multiplexer and demultiplexer," *Optics express*, vol. 21, no. 8, pp. 10376–10382, 2013.

[71] M. Greenberg and M. Orenstein, "Multimode add-drop multiplexing by adiabatic linearly tapered coupling," *Optics express*, vol. 13, no. 23, pp. 9381–9387, 2005.

[72] S. Feng, T. Lei, H. Chen, H. Cai, X. Luo, and A. W. Poon, "Silicon photonics: from a microresonator perspective," *Laser & photonics reviews*, vol. 6, no. 2, pp. 145–177, 2012.

[73] M. Borghi, D. Gandolfi, M. Ghulinyan, R. Guider, M. Mancinell, G. Pucker, F. Ramiro Manzano, F. Turri, and L. Pavesi, *Plenary Lectures on Nanoscience and Engineering*, ch. 2. 2015.

[74] W. Bogaerts, P. De Heyn, T. Van Vaerenbergh, K. De Vos, S. Kumar Selvaraja, T. Claes, P. Dumon, P. Bienstman, D. Van Thourhout, and R. Baets, "Silicon microring resonators," *Laser & Photonics Reviews*, vol. 6, no. 1, pp. 47–73, 2012.

[75] M. Ghulinyan, D. Navarro-Urrios, A. Pitanti, A. Lui, G. Pucker, and L. Pavesi, "Whispering-gallery modes and light emission from a si-nanocrystal-based single microdisk resonator," *Optics express*, vol. 16, no. 17, pp. 13218–13224, 2008.

[76] Q. Xu, D. Fattal, and R. G. Beausoleil, "Silicon microring resonators with 1.5-μm radius," *Optics express*, vol. 16, no. 6, pp. 4309–4315, 2008.

[77] D. Armani, B. Min, A. Martin, and K. J. Vahala, "Electrical thermo-optic tuning of ultrahigh-q microtoroid resonators," *Applied physics letters*, vol. 85, no. 22, pp. 5439–5441, 2004.

[78] M. Mancinelli, R. Guider, P. Bettotti, M. Masi, M. R. Vanacharla, J.-M. Fedeli, D. Van Thourhout, and L. Pavesi, "Optical characterization of silicon-on-insulator–based single and coupled racetrack resonators," *Journal of Nanophotonics*, vol. 5, no. 1, p. 051705, 2011.

[79] M. Borghi, M. Mancinelli, F. Merget, J. Witzens, M. Bernard, M. Ghulinyan, G. Pucker, and L. Pavesi, "High-frequency electro-optic measurement of strained silicon racetrack resonators," *Optics letters*, vol. 40, no. 22, pp. 5287–5290, 2015.

[80] K. Hiremath, R. Stoffer, and M. Hammer, "Coupled mode theory and fdtd simulations of the coupling between bent and straight optical waveguides," IEEE Lasers and Electro-Optics Society, 2003.

[81] Y. M. Landobasa, S. Darmawan, and M.-K. Chin, "Matrix analysis of 2-d microresonator lattice optical filters," *Quantum Electronics, IEEE Journal of*, vol. 41, no. 11, pp. 1410–1418, 2005.

[82] M. M. Mancinelli, *Linear and non linear coupling effects in sequence of microresonators.* PhD thesis, University of Trento, 2013.

[83] F. Morichetti, C. Ferrari, A. Canciamilla, and A. Melloni, "The first decade of coupled resonator optical waveguides: bringing slow light to applications," *Laser & Photonics Reviews*, vol. 6, no. 1, pp. 74–96, 2012.

[84] A. Canciamilla, M. Torregiani, C. Ferrari, F. Morichetti, R. De La Rue, A. Samarelli, M. Sorel, and A. Melloni, "Silicon coupled-ring resonator structures for slow light applications: potential, impairments and ultimate limits," *Journal of Optics*, vol. 12, no. 10, p. 104008, 2010.

[85] A. Yariv, Y. Xu, R. K. Lee, and A. Scherer, "Coupled-resonator optical waveguide: a proposal and analysis," *Optics letters*, vol. 24, no. 11, pp. 711–713, 1999.

[86] J. K. Poon, J. Scheuer, Y. Xu, and A. Yariv, "Designing coupled-resonator optical waveguide delay lines," *Journal of the Optical Society of America B*, vol. 21, no. 9, pp. 1665–1673, 2004.

[87] M. Mancinelli, R. Guider, P. Bettotti, M. Masi, M. R. Vanacharla, and L. Pavesi, "Coupled-resonator-induced-transparency concept for wavelength routing applications," *Optics express*, vol. 19, no. 13, pp. 12227–12240, 2011.

[88] J. D. Joannopoulos, S. G. Johnson, J. N. Winn, and R. D. Meade, *Photonic crystals: molding the flow of light*. Princeton university press, 2011.

[89] M. Mancinelli, M. Borghi, P. Bettotti, J.-M. Fedeli, and L. Pavesi, "An all optical method for fabrication error measurements in integrated photonic circuits," *Journal of Lightwave Technology*, vol. 31, no. 14, pp. 2340–2346, 2013.

[90] S. K. Selvaraja, *Wafer-scale fabrication technology for silicon photonic integrated circuits*. PhD thesis, PhD thesis, Ghent University, 2011.

[91] W. Bogaerts, D. Van Thourhout, R. Baets, *et al.*, "Fabrication of uniform photonic devices using 193nm optical lithography in silicon-on-insulator," in *14th European Conference on Integrated Optics*, pp. 359–362, 2008.

[92] P. Dong, W. Qian, H. Liang, R. Shafiiha, D. Feng, G. Li, J. E. Cunningham, A. V. Krishnamoorthy, and M. Asghari, "Thermally tunable silicon racetrack resonators with ultralow tuning power," *Optics express*, vol. 18, no. 19, pp. 20298–20304, 2010.

[93] F. Gan, T. Barwicz, M. Popovic, M. Dahlem, C. Holzwarth, P. Rakich, H. Smith, E. Ippen, and F. Kartner, "Maximizing the thermo-optic tuning range of silicon photonic structures," in *Photonics in Switching*, pp. 67–68, 2007.

[94] Q. Xu, S. Manipatruni, B. Schmidt, J. Shakya, and M. Lipson, "12.5 gbit/s carrier-injection-based silicon micro-ring silicon modulators," *Optics express*, vol. 15, no. 2, pp. 430–436, 2007.

[95] L. Zhou and A. W. Poon, "Electrically reconfigurable silicon microring resonator-based filter with waveguide-coupled feedback," *Optics express*, vol. 15, no. 15, pp. 9194–9204, 2007.

[96] T. J. Johnson, M. Borselli, and O. Painter, "Self-induced optical modulation of the transmission through a high-q silicon microdisk resonator," *Optics express*, vol. 14, no. 2, pp. 817–831, 2006.

[97] R. A. Soref and B. R. Bennett, "Electrooptical effects in silicon," *IEEE Journal of Quantum Electronics*, vol. 23, no. 1, pp. 123–129, 1987.

[98] Q. Xu, B. Schmidt, S. Pradhan, and M. Lipson, "Micrometre-scale silicon electro-optic modulator," *nature*, vol. 435, no. 7040, pp. 325–327, 2005.

[99] M. Mancinelli, M. Borghi, F. Ramiro-Manzano, J. Fedeli, and L. Pavesi, "Chaotic dynamics in coupled resonator sequences," *Optics express*, vol. 22, no. 12, pp. 14505–14516, 2014.

[100] V. R. Almeida, C. A. Barrios, R. R. Panepucci, M. Lipson, M. A. Foster, D. G. Ouzounov, and A. L. Gaeta, "All-optical switching on a silicon chip," *Optics letters*, vol. 29, no. 24, pp. 2867–2869, 2004.

[101] C. Manolatou and M. Lipson, "All-optical silicon modulators based on carrier injection by two-photon absorption," *Journal of Lightwave Technology*, vol. 24, no. 3, pp. 1433–1439, 2006.

[102] D. Dimitropoulos, R. Jhaveri, R. Claps, J. Woo, and B. Jalali, "Lifetime of photogenerated carriers in silicon-on-insulator rib waveguides," *Applied Physics Letters*, vol. 86, no. 7, p. 071115, 2005.

[103] G. T. Reed, G. Mashanovich, F. Gardes, and D. Thomson, "Silicon optical modulators," *Nature Photonics*, vol. 4, no. 8, pp. 518–526, 2010.

[104] N. Sherwood-Droz, H. Wang, L. Chen, B. G. Lee, A. Biberman, K. Bergman, and M. Lipson, "Optical 4×4 hitless silicon router for optical networks-on-chip (noc)," *Optics express*, vol. 16, no. 20, pp. 15915–15922, 2008.

[105] M.-C. Estevez, M. Alvarez, and L. M. Lechuga, "Integrated optical devices for lab-on-a-chip biosensing applications," *Laser & Photonics Reviews*, vol. 6, no. 4, pp. 463–487, 2012.

[106] D. Duval, L. Lechuga, and A. Gonzalez, "Silicon photonic based biosensors: the future of lab-on-a-chip diagnostic devices," *IEEE Photonics Society*, vol. 26, pp. 5–8, 2012.

[107] D. Gandolfi, *On-chip photonic label-free biosensors*. PhD thesis, University of Trento, 2015.

[108] X. Liu, B. Kuyken, G. Roelkens, R. Baets, R. M. Osgood Jr, and W. M. Green, "Bridging the mid-infrared-to-telecom gap with silicon nanophotonic spectral translation," *Nature Photonics*, vol. 6, no. 10, pp. 667–671, 2012.

[109] A. C. Turner, M. A. Foster, A. L. Gaeta, and M. Lipson, "Ultra-low power parametric frequency conversion in a silicon microring resonator," *Optics express*, vol. 16, no. 7, pp. 4881–4887, 2008.

[110] P. Del Haye, A. Schliesser, O. Arcizet, T. Wilken, R. Holzwarth, and T. Kippenberg, "Optical frequency comb generation from a monolithic microresonator," *Nature*, vol. 450, no. 7173, pp. 1214–1217, 2007.

[111] T. J. Kippenberg, R. Holzwarth, and S. Diddams, "Microresonator-based optical frequency combs," *Science*, vol. 332, no. 6029, pp. 555–559, 2011.

[112] Y. Okawachi, K. Saha, J. S. Levy, Y. H. Wen, M. Lipson, and A. L. Gaeta, "Octave-spanning frequency comb generation in a silicon nitride chip," *Optics letters*, vol. 36, no. 17, pp. 3398–3400, 2011.

[113] J. S. Levy, A. Gondarenko, M. A. Foster, A. C. Turner-Foster, A. L. Gaeta, and M. Lipson, "Cmos-compatible multiple-wavelength oscillator for on-chip optical interconnects," *Nature Photonics*, vol. 4, no. 1, pp. 37–40, 2010.

[114] L. Razzari, D. Duchesne, M. Ferrera, R. Morandotti, S. Chu, B. Little, and D. Moss, "Cmos-compatible integrated optical hyper-parametric oscillator," *Nature Photonics*, vol. 4, no. 1, pp. 41–45, 2010.

[115] R. Salem, M. A. Foster, A. C. Turner, D. F. Geraghty, M. Lipson, and A. L. Gaeta, "Signal regeneration using low-power four-wave mixing on silicon chip," *Nature Photonics*, vol. 2, no. 1, pp. 35–38, 2008.

[116] V. R. Almeida, C. A. Barrios, R. R. Panepucci, and M. Lipson, "All-optical control of light on a silicon chip," *Nature*, vol. 431, no. 7012, pp. 1081–1084, 2004.

[117] Q. Xu and M. Lipson, "All-optical logic based on silicon micro-ring resonators," *Optics express*, vol. 15, no. 3, pp. 924–929, 2007.

[118] V. R. Almeida and M. Lipson, "Optical bistability on a silicon chip," *Optics letters*, vol. 29, no. 20, pp. 2387–2389, 2004.

[119] G. Priem, P. Dumon, W. Bogaerts, D. Van Thourhout, G. Morthier, and R. Baets, "Optical bistability and pulsating behaviour in silicon-on-insulator ring resonator structures," *Optics express*, vol. 13, no. 23, pp. 9623–9628, 2005.

[120] T. Van Vaerenbergh, M. Fiers, J. Dambre, and P. Bienstman, "Simplified description of self-pulsation and excitability by thermal and free-carrier effects in semiconductor microcavities," *Physical Review A*, vol. 86, no. 6, p. 063808, 2012.

[121] L. Liao, D. Samara-Rubio, M. Morse, A. Liu, D. Hodge, D. Rubin, U. D. Keil, and T. Franck, "High speed silicon mach-zehnder modulator," *Optics express*, vol. 13, no. 8, pp. 3129–3135, 2005.

[122] `http://www.ofcnfoec.org/conferenceprogram/2009/images/09-DAndrea.pdf`.

[123] A. Liu, L. Liao, D. Rubin, H. Nguyen, B. Ciftcioglu, Y. Chetrit, N. Izhaky, and M. Paniccia, "High-speed optical modulation based on carrier depletion in a silicon waveguide," *Optics express*, vol. 15, no. 2, pp. 660–668, 2007.

[124] T. Baba, S. Akiyama, M. Imai, N. Hirayama, H. Takahashi, Y. Noguchi, T. Horikawa, and T. Usuki, "50-gb/s ring-resonator-based silicon modulator," *Optics express*, vol. 21, no. 10, pp. 11869–11876, 2013.

[125] D. J. Thomson, F. Y. Gardes, J.-M. Fedeli, S. Zlatanovic, Y. Hu, B. P. P. Kuo, E. Myslivets, N. Alic, S. Radic, G. Z. Mashanovich, *et al.*, "50-gb/s silicon optical modulator," *IEEE Photonics Technology Letters*, vol. 24, no. 4, pp. 234–236, 2012.

[126] A. Liu, H. Rong, R. Jones, O. Cohen, D. Hak, and M. Paniccia, "Optical amplification and lasing by stimulated raman scattering in silicon waveguides," *Journal of Lightwave Technology*, vol. 24, no. 3, pp. 1440–1455, 2006.

[127] Q. Lin, O. J. Painter, and G. P. Agrawal, "Nonlinear optical phenomena in silicon waveguides: modeling and applications," *Optics express*, vol. 15, no. 25, pp. 16604–16644, 2007.

[128] O. Boyraz and B. Jalali, "Demonstration of a silicon raman laser," *Optics express*, vol. 12, no. 21, pp. 5269–5273, 2004.

[129] M. Ferrara, L. Sirleto, G. Nicotra, C. Spinella, and I. Rendina, "Enhanced gain coefficient in raman amplifier based on silicon nanocomposites," *Photonics and Nanostructures-Fundamentals and Applications*, vol. 9, no. 1, pp. 1–7, 2011.

[130] J. McMillan, M. Yu, D.-L. Kwong, and C. Wong, "Observation of spontaneous raman scattering in silicon slow-light photonic crystal waveguides," *Applied Physics Letters*, vol. 93, no. 25, p. 251105, 2008.

[131] R. Chen, T.-T. D. Tran, K. W. Ng, W. S. Ko, L. C. Chuang, F. G. Sedgwick, and C. Chang-Hasnain, "Nanolasers grown on silicon," *Nature Photonics*, vol. 5, no. 3, pp. 170–175, 2011.

[132] `/http://web.mit.edu/press/2010/germanium-laserS`.

[133] Y. Huo, H. Lin, R. Chen, Y. Rong, T. I. Kamins, and J. S. Harris, "Mbe growth of tensile-strained ge quantum wells and quantum dots," *Frontiers of Optoelectronics*, vol. 5, no. 1, pp. 112–116, 2012.

[134] B. Dutt, D. S. Sukhdeo, D. Nam, B. M. Vulovic, Z. Yuan, and K. C. Saraswat, "Roadmap to an efficient germanium-on-silicon laser: strain vs. n-type doping," *IEEE Photonics Journal*, vol. 4, no. 5, pp. 2002–2009, 2012.

[135] J. Bowers, D. Liang, A. Fang, H. Park, R. Jones, and M. Paniccia, "Hybrid silicon lasers: The final frontier to integrated computing," *Optics and Photonics News*, vol. 21, no. 5, pp. 28–33, 2010.

[136] H. Park, A. W. Fang, S. Kodama, and J. E. Bowers, "Hybrid silicon evanescent laser fabricated with a silicon waveguide and iii-v offset quantum wells," *Optics express*, vol. 13, no. 23, pp. 9460–9464, 2005.

[137] R. W. Boyd, *Nonlinear optics*. Academic press, 2003.

[138] P. Damas, X. Le Roux, D. Le Bourdais, E. Cassan, D. Marris-Morini, N. Izard, T. Maroutian, P. Lecoeur, and L. Vivien, "Wavelength dependence of pockels effect in strained silicon waveguides," *Optics express*, vol. 22, no. 18, pp. 22095–22100, 2014.

[139] B. Chmielak, M. Waldow, C. Matheisen, C. Ripperda, J. Bolten, T. Wahlbrink, M. Nagel, F. Merget, and H. Kurz, "Pockels effect based fully integrated, strained silicon electro-optic modulator," *Optics express*, vol. 19, no. 18, pp. 17212–17219, 2011.

[140] B. Chmielak, C. Matheisen, C. Ripperda, J. Bolten, T. Wahlbrink, M. Waldow, and H. Kurz, "Investigation of local strain distribution and linear electro-optic effect in strained silicon waveguides," *Optics express*, vol. 21, no. 21, pp. 25324–25332, 2013.

[141] M. W. Puckett, J. S. Smalley, M. Abashin, A. Grieco, and Y. Fainman, "Tensor of the second-order nonlinear susceptibility in asymmetrically strained silicon waveguides: analysis and experimental validation," *Optics letters*, vol. 39, no. 6, pp. 1693–1696, 2014.

[142] R. S. Jacobsen, K. N. Andersen, P. I. Borel, J. Fage-Pedersen, L. H. Frandsen, O. Hansen, M. Kristensen, A. V. Lavrinenko, G. Moulin, H. Ou, *et al.*, "Strained silicon as a new electro-optic material," *Nature*, vol. 441, no. 7090, pp. 199–202, 2006.

[143] J. Leuthold, C. Koos, and W. Freude, "Nonlinear silicon photonics," *Nature Photonics*, vol. 4, no. 8, pp. 535–544, 2010.

[144] T. Vallaitis, S. Bogatscher, L. Alloatti, P. Dumon, R. Baets, M. L. Scimeca, I. Biaggio, F. Diederich, C. Koos, W. Freude, *et al.*, "Optical properties of highly nonlinear silicon-organic hybrid (soh) waveguide geometries," *Optics express*, vol. 17, no. 20, pp. 17357–17368, 2009.

[145] B. Jalali, "Nonlinear optics in the mid-infrared," *Nature Photonics*, vol. 4, pp. 506–508, 2010.

[146] R. Soref, "Mid-infrared photonics in silicon and germanium," *Nature Photonics*, vol. 4, no. 8, pp. 495–497, 2010.

[147] I.-W. Hsieh, X. Chen, X. Liu, J. I. Dadap, N. C. Panoiu, C.-Y. Chou, F. Xia, W. M. Green, Y. A. Vlasov, and R. M. Osgood, "Supercontinuum generation in silicon photonic wires," *Optics express*, vol. 15, no. 23, pp. 15242–15249, 2007.

[148] B. Kuyken, X. Liu, R. M. Osgood, R. Baets, G. Roelkens, and W. M. Green, "Mid-infrared to telecom-band supercontinuum generation in highly nonlinear silicon-on-insulator wire waveguides," *Optics express*, vol. 19, no. 21, pp. 20172–20181, 2011.

[149] R. Claps, V. Raghunathan, D. Dimitropoulos, and B. Jalali, "Anti-stokes raman conversion in silicon waveguides," *Optics express*, vol. 11, no. 22, pp. 2862–2872, 2003.

[150] R. Claps, D. Dimitropoulos, V. Raghunathan, Y. Han, and B. Jalali, "Observation of stimulated raman amplification in silicon waveguides," *Optics express*, vol. 11, no. 15, pp. 1731–1739, 2003.

[151] L. Yin, Q. Lin, and G. P. Agrawal, "Soliton fission and supercontinuum generation in silicon waveguides," *Optics letters*, vol. 32, no. 4, pp. 391–393, 2007.

[152] J. Zhang, Q. Lin, G. Piredda, R. W. Boyd, G. P. Agrawal, and P. M. Fauchet, "Optical solitons in a silicon waveguide," *Optics express*, vol. 15, no. 12, pp. 7682–7688, 2007.

[153] B. Corcoran, C. Monat, C. Grillet, D. J. Moss, B. J. Eggleton, T. White, L. O'Faolain, and T. F. Krauss, "Green light emission in silicon through slow-light enhanced third-harmonic generation in photonic-crystal waveguides," *Nature Photonics*, vol. 3, no. 4, pp. 206–210, 2009.

[154] S. Azzini, D. Grassani, M. J. Strain, M. Sorel, L. Helt, J. Sipe, M. Liscidini, M. Galli, and D. Bajoni, "Ultra-low power generation of twin photons in a compact silicon ring resonator," *Optics express*, vol. 20, no. 21, pp. 23100–23107, 2012.

[155] S. Clemmen, K. P. Huy, W. Bogaerts, R. G. Baets, P. Emplit, and S. Massar, "Continuous wave photon pair generation in silicon-on-insulator waveguides and ring resonators," *Optics express*, vol. 17, no. 19, pp. 16558–16570, 2009.

[156] S. M. Spillane, M. Fiorentino, and R. G. Beausoleil, "Spontaneous parametric down conversion in a nanophotonic waveguide," *Optics express*, vol. 15, no. 14, pp. 8770–8780, 2007.

[157] M. Cazzanelli, F. Bianco, E. Borga, G. Pucker, M. Ghulinyan, E. Degoli, E. Luppi, V. Véniard, S. Ossicini, D. Modotto, *et al.*, "Second-harmonic generation in silicon waveguides strained by silicon nitride," *Nature materials*, vol. 11, no. 2, pp. 148–154, 2012.

[158] F. Bianco, K. Fedus, F. Enrichi, R. Pierobon, M. Cazzanelli, M. Ghulinyan, G. Pucker, and L. Pavesi, "Two-dimensional micro-raman mapping of stress and strain distributions in strained silicon waveguides," *Semiconductor Science and Technology*, vol. 27, no. 8, p. 085009, 2012.

[159] C. Schriever, F. Bianco, M. Cazzanelli, M. Ghulinyan, C. Eisenschmidt, J. de Boor, A. Schmid, J. Heitmann, L. Pavesi, and J. Schilling, "Second-order optical nonlinearity in silicon waveguides: Inhomogeneous stress and interfaces," *Advanced Optical Materials*, vol. 3, no. 1, pp. 129–136, 2015.

[160] C. L. Manganelli, P. Pintus, and C. Bonati, "Modeling of strain-induced pockels effect in silicon," *Optics express*, vol. 23, no. 22, pp. 28649–28666, 2015.

[161] P. Damas, D. Marris-Morini, E. Cassan, and L. Vivien, "Bond orbital description of the strain induced second order optical susceptibility in silicon," *arXiv preprint arXiv:1511.03041*, 2015.

[162] S. S. Azadeh, F. Merget, M. Nezhad, and J. Witzens, "On the measurement of the pockels effect in strained silicon," *Optics letters*, vol. 40, no. 8, pp. 1877–1880, 2015.

[163] R. Sharma, M. W. Puckett, H.-H. Lin, F. Vallini, and Y. Fainman, "Characterizing the effects of free carriers in fully etched, dielectric-clad silicon waveguides," *Applied Physics Letters*, vol. 106, no. 24, p. 241104, 2015.

[164] C. Hong and L. Mandel, "Theory of parametric frequency down conversion of light," *Physical Review A*, vol. 31, no. 4, p. 2409, 1985.

[165] M. Fiorentino, S. M. Spillane, R. G. Beausoleil, T. D. Roberts, P. Battle, and M. W. Munro, "Spontaneous parametric down-conversion in periodically poled ktp waveguides and bulk crystals," *Optics express*, vol. 15, no. 12, pp. 7479–7488, 2007.

[166] V. Giovannetti, S. Lloyd, and L. Maccone, "Quantum-enhanced measurements: beating the standard quantum limit," *Science*, vol. 306, no. 5700, pp. 1330–1336, 2004.

[167] N. Gisin, G. Ribordy, W. Tittel, and H. Zbinden, "Quantum cryptography," *Reviews of modern physics*, vol. 74, no. 1, p. 145, 2002.

[168] V. Giovannetti, S. Lloyd, and L. Maccone, "Quantum metrology," *Physical Review Letters*, vol. 96, no. 1, p. 010401, 2006.

[169] M. D'Angelo, M. V. Chekhova, and Y. Shih, "Two-photon diffraction and quantum lithography," *Physical Review Letters*, vol. 87, no. 1, p. 013602, 2001.

[170] J. L. O'Brien, "Optical quantum computing," *Science*, vol. 318, no. 5856, pp. 1567–1570, 2007.

[171] A. Politi, M. J. Cryan, J. G. Rarity, S. Yu, and J. L. O'Brien, "Silica-on-silicon waveguide quantum circuits," *Science*, vol. 320, no. 5876, pp. 646–649, 2008.

[172] B. L. Higgins, D. W. Berry, S. D. Bartlett, H. M. Wiseman, and G. J. Pryde, "Entanglement-free heisenberg-limited phase estimation," *Nature*, vol. 450, no. 7168, pp. 393–396, 2007.

[173] T. Nagata, R. Okamoto, J. L. O'Brien, K. Sasaki, and S. Takeuchi, "Beating the standard quantum limit with four-entangled photons," *Science*, vol. 316, no. 5825, pp. 726–729, 2007.

[174] Y. Kawabe, H. Fujiwara, R. Okamoto, K. Sasaki, and S. Takeuchi, "Quantum interference fringes beating the diffraction limit," *Optics express*, vol. 15, no. 21, pp. 14244–14250, 2007.

[175] T. Pittman, M. Fitch, B. Jacobs, and J. Franson, "Experimental controlled-not logic gate for single photons in the coincidence basis," *Physical Review A*, vol. 68, no. 3, p. 032316, 2003.

[176] J. L. O'Brien, G. J. Pryde, A. G. White, T. C. Ralph, and D. Branning, "Demonstration of an all-optical quantum controlled-not gate," *Nature*, vol. 426, no. 6964, pp. 264–267, 2003.

[177] P. Walther, K. J. Resch, T. Rudolph, E. Schenck, H. Weinfurter, V. Vedral, M. Aspelmeyer, and A. Zeilinger, "Experimental one-way quantum computing," *Nature*, vol. 434, no. 7030, pp. 169–176, 2005.

[178] C.-Y. Lu, X.-Q. Zhou, O. Gühne, W.-B. Gao, J. Zhang, Z.-S. Yuan, A. Goebel, T. Yang, and J.-W. Pan, "Experimental entanglement of six photons in graph states," *Nature Physics*, vol. 3, no. 2, pp. 91–95, 2007.

[179] J. C. Matthews, A. Politi, A. Stefanov, and J. L. O'Brien, "Manipulation of multiphoton entanglement in waveguide quantum circuits," *Nature Photonics*, vol. 3, no. 6, pp. 346–350, 2009.

[180] J. W. Silverstone, D. Bonneau, K. Ohira, N. Suzuki, H. Yoshida, N. Iizuka, M. Ezaki, C. M. Natarajan, M. G. Tanner, R. H. Hadfield, *et al.*, "On-chip quantum interference between silicon photon-pair sources," *Nature Photonics*, vol. 8, no. 2, pp. 104–108, 2014.

[181] M. Borselli, T. J. Johnson, and O. Painter, "Beyond the rayleigh scattering limit in high-q silicon microdisks: theory and experiment," *Optics express*, vol. 13, no. 5, pp. 1515–1530, 2005.

[182] T. J. A. Kippenberg, *Nonlinear optics in ultra-high-Q whispering-gallery optical microcavities*. PhD thesis, California Institute of Technology, 2004.

[183] P. Del'Haye, *Optical frequency comb generation in monolithic microresonators*. PhD thesis, lmu, 2011.

[184] N. Cazier, X. Checoury, L.-D. Haret, and P. Boucaud, "High-frequency self-induced oscillations in a silicon nanocavity," *Optics express*, vol. 21, no. 11, pp. 13626–13638, 2013.

[185] A. Armaroli, S. Malaguti, G. Bellanca, S. Trillo, A. de Rossi, and S. Combrié, "Oscillatory dynamics in nanocavities with noninstantaneous kerr response," *Physical Review A*, vol. 84, no. 5, p. 053816, 2011.

[186] `http://www-leti.cea.fr/`.

[187] M. Dinu, F. Quochi, and H. Garcia, "Third-order nonlinearities in silicon at telecom wavelengths," *Applied Physics Letters*, vol. 82, no. 18, pp. 2954–2956, 2003.

[188] A. Uchida, K. Amano, M. Inoue, K. Hirano, S. Naito, H. Someya, I. Oowada, T. Kurashige, M. Shiki, S. Yoshimori, *et al.*, "Fast physical random bit generation with chaotic semiconductor lasers," *Nature Photonics*, vol. 2, no. 12, pp. 728–732, 2008.

[189] A. Argyris, M. Hamacher, K. Chlouverakis, A. Bogris, and D. Syvridis, "Photonic integrated device for chaos applications in communications," *Physical review letters*, vol. 100, no. 19, p. 194101, 2008.

[190] J. Petracek, Y. Eksiglu, and A. Sterkhova, "Simulation of self-pulsing in kerr-nonlinear coupled ring resonators," *Optics Communications*, vol. 318, pp. 147–151, 2014.

[191] B. Maes, M. Fiers, and P. Bienstman, "Self-pulsing and chaos in short chains of coupled nonlinear microcavities," *Physical Review A*, vol. 80, no. 3, p. 033805, 2009.

[192] F. Takens, *Detecting strange attractors in turbulence*. Springer, 1981.

[193] A. M. Fraser and H. L. Swinney, "Independent coordinates for strange attractors from mutual information," *Physical Review A*, vol. 33, no. 2, p. 1134, 1986.

[194] J.-P. Eckmann and D. Ruelle, "Ergodic theory of chaos and strange attractors," *Reviews of modern physics*, vol. 57, no. 3, p. 617, 1985.

[195] M. Cencini, F. Cecconi, and A. Vulpiani, *Chaos: from simple models to complex systems*, vol. 17. World Scientific Publishing Company Incorporated, 2010.

[196] I. Kanter, Y. Aviad, I. Reidler, E. Cohen, and M. Rosenbluh, "An optical ultrafast random bit generator," *Nature Photonics*, vol. 4, no. 1, pp. 58–61, 2010.

[197] A. Rukhin, J. Soto, J. Nechvatal, M. Smid, and E. Barker, "A statistical test suite for random and pseudorandom number generators for cryptographic applications," tech. rep., DTIC Document, 2001.

[198] J. Chen, K. F. Lee, and P. Kumar, "Deterministic quantum splitter based on time-reversed hong-ou-mandel interference," *Physical Review A*, vol. 76, no. 3, p. 031804, 2007.

[199] C. Cohen-Tannoudji, J. Dupont-Roc, and G. Grynberg, "Photons and atoms: Introduction to quantum electrodynamics (wiley professional)," 1997.

[200] L. G. Helt, M. Liscidini, and J. E. Sipe, "How does it scale? comparing quantum and classical nonlinear optical processes in integrated devices," *Journal of the Optical Society of America B*, vol. 29, no. 8, pp. 2199–2212, 2012.

[201] A. Messiah, "Quantum mechanics," 1958.

[202] L.-W. Luo, N. Ophir, C. P. Chen, L. H. Gabrielli, C. B. Poitras, K. Bergmen, and M. Lipson, "Wdm-compatible mode-division multiplexing on a silicon chip," *Nature Communications*, vol. 5, 2014.

[203] M. Born and E. Wolf, *Principles of optics: electromagnetic theory of propagation, interference and diffraction of light*. CUP Archive, 2000.

[204] `www.fbk.eu/`.

[205] A. Rogalski, "Hgcdte infrared detector material: history, status and outlook," *Reports on Progress in Physics*, vol. 68, no. 10, p. 2267, 2005.

[206] P. Norton, "Hgcdte infrared detectors," *Optoelectronics review*, no. 3, pp. 159–174, 2002.

[207] J. S. Dam, P. Tidemand-Lichtenberg, and C. Pedersen, "Room-temperature mid-infrared single-photon spectral imaging," *Nature Photonics*, vol. 6, no. 11, pp. 788–793, 2012.

[208] P. A. Flinn, "Principles and applications of wafer curvature techniques for stress measurements in thin films," in *MRS Proceedings*, vol. 130, p. 41, Cambridge Univ Press, 1988.

[209] J. Ristein, "Surface transfer doping of semiconductors," *Science*, vol. 313, no. 5790, pp. 1057–1058, 2006.

[210] L. Alloatti, C. Koos, and J. Leuthold, "Optical loss by surface transfer doping in silicon waveguides," *Applied Physics Letters*, vol. 107, no. 3, p. 031107, 2015.

[211] P. Zhang, E. Tevaarwerk, B.-N. Park, D. E. Savage, G. K. Celler, I. Knezevic, P. G. Evans, M. A. Eriksson, and M. G. Lagally, "Electronic transport in nanometre-scale silicon-on-insulator membranes," *Nature*, vol. 439, no. 7077, pp. 703–706, 2006.

[212] S. M. Sze and K. K. Ng, *Physics of semiconductor devices*. John wiley & sons, 2006.

[213] S. Govorkov, V. EmelaYanov, N. Koroteev, G. Petrov, I. Shumay, and V. Yakovlev, "Inhomogeneous deformation of silicon surface layers probed by second-harmonic generation in reflection," *Journal of the Optical Society of America B*, vol. 6, no. 6, pp. 1117–1124, 1989.

[214] N. W. Ashcroft and N. D. Mermin, "Solid state physics," 1976.

[215] `www.covesion.com`.

[216] K. Koch, E. Cheung, G. T. Moore, S. H. Chakmakjian, and J. Liu, "Hot spots in parametric fluorescence with a pump beam of finite cross section," *IEEE Journal of Quantum Electronics*, vol. 31, no. 5, pp. 769–781, 1995.

[217] G. Fujii, N. Namekata, M. Motoya, S. Kurimura, and S. Inoue, "Bright narrowband source of photon pairs at optical telecommunication wavelengths using a type-ii periodically poled lithium niobate waveguide," *Optics express*, vol. 15, no. 20, pp. 12769–12776, 2007.

[218] `http://www.idquantique.com/instrumentation/id350-ppln.html`.

[219] L. Mandel and E. Wolf, *Optical coherence and quantum optics*. Cambridge university press, 1995.

[220] J. G. Rarity and P. Tapster, "Fourth-order interference in parametric downconversion," *Journal of the Optical Society of America B*, vol. 6, no. 6, pp. 1221–1226, 1989.

[221] J. Rarity, P. Tapster, E. Jakeman, T. Larchuk, R. Campos, M. Teich, and B. Saleh, "Two-photon interference in a mach-zehnder interferometer," *Physical Review Letters*, vol. 65, no. 11, p. 1348, 1990.

[222] R. A. Campos, B. E. Saleh, and M. C. Teich, "Fourth-order interference of joint single-photon wave packets in lossless optical systems," *Physical Review A*, vol. 42, no. 7, p. 4127, 1990.

[223] M. G. Paris, "Entanglement and visibility at the output of a mach-zehnder interferometer," *Physical Review A*, vol. 59, no. 2, p. 1615, 1999.

[224] A. Zeilinger, "General properties of lossless beam splitters in interferometry," *American Journal of Physics*, vol. 49, no. 9, pp. 882–883, 1981.

[225] S. M. Barnett, J. Jeffers, A. Gatti, and R. Loudon, "Quantum optics of lossy beam splitters," *Physical Review A*, vol. 57, no. 3, p. 2134, 1998.

[226] C. Hong, Z. Ou, and L. Mandel, "Measurement of subpicosecond time intervals between two photons by interference," *Physical Review Letters*, vol. 59, no. 18, p. 2044, 1987.

[227] R. Storn and K. Price, "Differential evolution–a simple and efficient heuristic for global optimization over continuous spaces," *Journal of global optimization*, vol. 11, no. 4, pp. 341–359, 1997.

[228] P. Kwiat, W. Vareka, C. Hong, H. Nathel, and R. Chiao, "Correlated two-photon interference in a dual-beam michelson interferometer," *Physical Review A*, vol. 41, no. 5, p. 2910, 1990.

[229] M. O. Scully and M. S. Zubairy, *Quantum optics*. Cambridge university press, 1997.

[230] Z. Ou and L. Mandel, "Observation of spatial quantum beating with separated photodetectors," *Physical Review Letters*, vol. 61, no. 1, p. 54, 1988.

[231] Y. Hibino, "Recent advances in high-density and large-scale awg multi/demultiplexers with higher index-contrast silica-based plcs," *IEEE Journal of Selected Topics in Quantum Electronics*, vol. 8, no. 6, pp. 1090–1101, 2002.

[232] F. Rana, "Quantization of radiation in cavities and free space."

[233] H. A. Haus, "Waves and fields in optoelectronics," 1983.